Free boundary problems in a Hele-Shaw cell

by

Ali Haseeb Khalid BSc, MSc DIC, ARAeS

A thesis submitted in conformity with the requirements

for the degree of Doctor of Philosophy

Department of Mathematics

Faculty of Mathematical & Physical Sciences

University College London

February, 2015

Disclaimer

I, Ali Haseeb Khalid, confirm that the work presented in this thesis is my own. Where information has been derived from other sources, I confirm that this has been indicated in the thesis.

Signature _____

Date _____

Abstract

The motion of a free boundary separating two immiscible fluids in an unbounded Hele-Shaw cell is considered. In the one-phase problem, a viscous fluid is separated from an inviscid fluid by a simple closed boundary. Preliminaries for a complex variable technique are presented by which the one-phase problem can be solved explicitly via conformal mappings. The Schwarz function of the boundary plays a major role giving rise to the so called Schwarz function equation which governs the evolution of exact solutions. The Schwarz function approach is used to study the stability of a translating elliptical bubble due to a uniform background flow, and the stability of a blob (or bubble) subject to an external electric field.

The one-phase problem of a translating free boundary and of a free boundary subject to an external field are studied numerically. A boundary integral method is formulated in the complex plane by considering the Cauchy integral formula and the complex velocity of a fluid particle on the free boundary. In the case of a free boundary subject to an external electric field due to a point charge, it is demonstrated that a stable steady state is achieved for appropriate charge strength. The method is also employed to study breakup of a single translating bubble in which the Schwarz function singularities (shown to be stationary) of the initial boundary play an important role.

The two-phase problem is also considered, where the free boundary now separates two viscous fluids, and the construction of exact solutions is studied. The one-phase numerical model is enhanced, where a boundary integral method is formulated to accommodate the variable pressure in both viscous phases. Some numerical experiments are presented with a comparison to analytical results, in particular for the case where the free boundary is driven by a uniform background flow.

This thesis was completed under the supervision of ***Professor Nicholas Robb McDonald*** *and* ***Professor Jean-Marc Vanden-Broeck****.*

Acknowledgments

It has been a pleasure and honour to have been supervised by Robb McDonald and Jean-Marc Vanden-Broeck, to whom I extend my deepest gratitude. I appreciate their support, as well as the time and mathematical training they have given me; I am hugely indebted to them both. I imagine that Robb's feelings, when proofreading my work, could be summarised by the quote '*Word-smithing is a much greater percentage of what I am supposed to be doing in life than I would have ever thought*'—Donald E. Knuth. Thank you Robb, for your patience and excellent wordsmanship.

The Department of Mathematics has funded my research through a Departmental Teaching Assistantship, an opportunity I am enormously grateful to have received. I would also like to thank Helen Higgins, Mumtaz Ghafoor, Soheni Francis, Bonita Carboo and Richard Hoyle for their support throughout my studies at UCL.

I take this opportunity to thank those who have invested in me and shaped my life significantly. Roy Baker and Antoine Touil, who gave me solid foundations to study mathematics at any level. The lecturers that have guided and inspired me whilst at UCL and Imperial College, in particular Frank Smith, Anatoly Ruban, Sergei Timoshin, Keith Ball, Richard Hillier and Ted Johnson. A heartfelt mention goes to my teacher, not just of mathematics—but of life lessons in general—the late Rashid Ahmed. I can only hope that I have done you proud.

I am eternally grateful to my mother, father and brother. Having always shown me unparalleled love and support throughout my entire life, without them this thesis would have been extremely difficult to realise. I also thank my friends, whom I

consider as family, for their championship and encouragement over the years. In particular Reena Patel, Xiao Han and Alastair Jones.

Thank you also to my colleagues and mentors who made my time as a research student enjoyable, and for providing many interesting and useful discussions over the years. A special thanks to Tom Ashbee, Gavin Esler, Oliver Southwick, Adam Townsend and Pietro Servini, whom helped with the proofreading of this thesis.

I have been incredibly lucky to have had the opportunity to meet with, experience talks by, and present research to some eminent researchers in the field of free boundary problems and fluid mechanics. I am grateful for numerous conversations and useful discussions with Giovani Vasconcelos, Mark Mineev-Weinstein, Darren Crowdy, Christopher Green, Jonathan Marshall and Michael Dallaston.

A special mention must go to The KLB. It's also known as $K\Lambda B$, and sometimes referred to as M201 Mathematics Mezzanine; where the fridge is always overflowing and the sink very rarely empty. The KLB manages to exhibit massively varying localised climates: recently, the West Wing akin to the Antarctic, and the East End very much like Northern Africa. As seasons change throughout the year in the UK, so do the localised climates of The KLB, but its inhabitants—even those who are experts in atmospheric flows—have not yet observed a predictable pattern, on any time scale! However, with a continuous supply of Yorkshire Tea from the 6^{th} floor of 25 Gordon Street, it has been an enjoyable setting, housing a wonderful bunch of mathematicians. It has provided a place to work at any time, to share ideas, to learn from others, to house sporting pastimes—such as book ball and table tennis—and, most importantly, an arena to enjoy the company of others. The KLB is a magical place which truly encompasses the character of UCL. It will be sorely missed.

Ali Khalid, *University College London*, February 2015

To the world of fluid mechanics. A subject that has afforded me the opportunity to conduct research in an area of applied mathematics I thoroughly enjoy studying.

Simplicity is the ultimate sophistication

—Leonardo da Vinci

Contents

List of Tables

List of Figures

Chapter 1

Introduction

1.1 Problem background

The list of authors that have contributed to the study of fluid mechanics is littered with some of the greatest minds of mathematics and philosophy, such as Aristotle, Archemedes, da Vinci, Newton, Euler, Lagrange and many more, with works recorded from as early as the 4^{th} century BC. The equations of motion for a 'frictionless fluid' were first introduced in differential form by Euler [42] in the mid 18^{th} century based on Newton's laws of motion [141]. The mathematical equations governing the flow of viscous fluids—taking into account friction—were established in the 19^{th} century, now known as the *Navier-Stokes equations* [105, 130]. Since the inception of the Navier-Stokes equations the topic of viscous fluid flow has flourished, becoming a core subject of interest in applied mathematics. The application of the equations covers a wide range of problems. In this thesis the focus is on an effectively two dimensional (2D) viscous flow produced by the constraints of an apparatus known as the Hele-Shaw cell [50,51], where the resulting equations of the underlying model also find application in complex geometrical flows, such as flows through porous media.

The Hele-Shaw cell—see figure 1.1—was first introduced in 1897 by a British engineer, scientist and inventor by the name of Henry Selby Hele-Shaw. Whilst a

professor at University College Liverpool, Hele-Shaw endeavoured to capture the imagination of his students by arranging experiments to showcase the characteristics of fluid flow past an object [150]—see figure 1.2. In doing so, the cell was formed, consisting of two solid plates with viscous fluid sandwiched between them. Hele-Shaw made the realisation that if the plates were sufficiently close together, the resulting flow between the plates will remain laminar at all velocities, a concept he described in the paper entitled 'Experiments on the flow of water' published in *Transactions of the Liverpool Engeneering Society* in 1897 [150]. Schematics and further discussion regarding the Hele-Shaw cell can be found in the widely known publications made in 1898 and 1899 by Hele-Shaw [50, 51]. Although the problems for which the cell was originally constructed contain areas of significant interest in fluid dynamics, e.g. laminar flow past an aerofoil, the Hele-Shaw cell also gave rise to another problem; the problem of a moving *free boundary* between two fluids in two dimensions. The Hele-Shaw cell provides a very useful tool to visualise such problems, and the mathematical treatment of patterns produced by the free boundary between a viscous and effectively inviscid fluid have merited a large research interest among the mathematical, physics and engineering community. In 1998, a bibliography was compiled by Howison [61] of over 500 articles on the topic of Hele-Shaw flow.

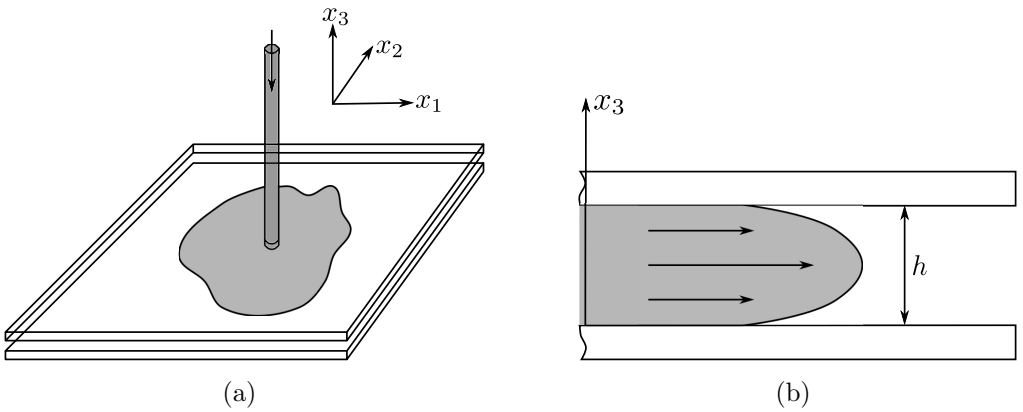

Figure 1.1: Schematics of a Hele-Shaw cell. The cross section in (b) depicts the assumption of laminar Poiseuille flow with parabolic velocity profile between two parallel plates, and (a) shows a sketch of the flow produced by injection through the upper cell wall.

Moving free boundaries make up a wide range of interesting physical problems in applied mathematics, engineering and physics. In particular, there has been considerable work on the motion of fluids and gasses in *porous media*, where the resulting macroscopic fluid flow obeys *Darcy's law*, derived by Darcy in 1856 [29, pp.137–184]. Although the fluid motion at microscopic scale is complex and interesting, the resounding question is; how does the boundary of the fluid evolve on a macroscopic scale as it moves through the porous media? It transpires that the equations of motion of porous media are analogous to those for flows in a Hele-Shaw cell, given by the *Stokes-Leibenzon* model (derived in section 1.2.1) in 2D. The *one-phase* free boundary problem in a Hele-Shaw cell can be described qualitatively as follows.

> *Consider a blob of viscous fluid surrounded by a secondary fluid of negligible viscosity, in a Hele-Shaw cell. Suppose that the two fluids are immiscible and also that the fluid blob grows via injection at a point through the upper cell wall—see figure 1.1(a). The resulting motion of the interface between the two fluids characterises the free boundary problem. Henceforth, the problem of finding the shape of the evolving interface will be known as the* ***Hele-Shaw free boundary problem*** [48, 107]*, also widely referred to as the* ***Laplacian growth problem*** [100].

Two fluids are considered *immiscible* if they do not mix at the molecular level and therefore there is no mixing at the macroscopic level. This implies that the two fluids are separated at all times by a distinct, sharp interface. In this thesis, the interface separating two fluids will usually refer to the free boundary, where *interface* and *free boundary* shall be considered synonymous. It shall also be assumed that the physical properties of density and viscosity in each fluid remain constant. It is well known in the literature that the Hele-Shaw free boundary problem can be categorised in the following ways [48].

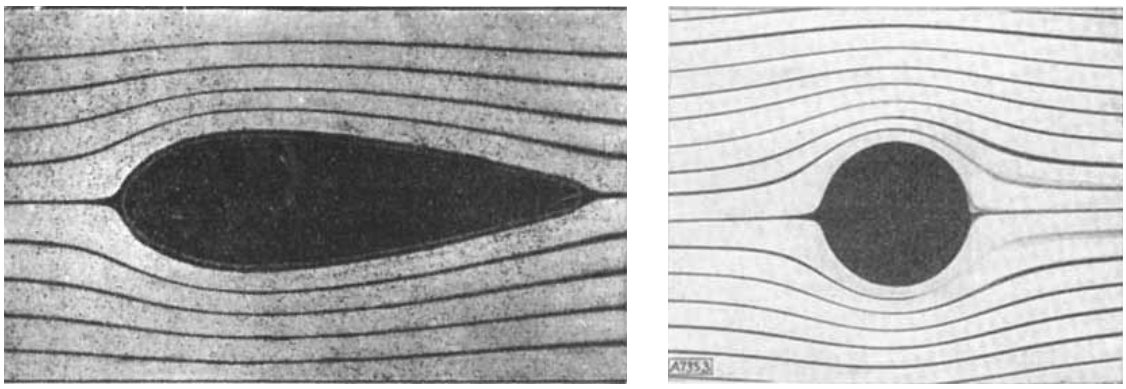

(a) (b)

Figure 1.2: Potential flow past (a) a screw strut and (b) a cylinder, produced by a Hele-Shaw cell where die is used to visualise streamlines. An almost perfect potential flow is observed, even behind the cylinder in (b). Pictures are from (a) the paper by Hele-Shaw [50] and (b) the paper Riegels [120].

(i) The *well-posed* problem, where the advancing fluid is *more* viscous than the surrounding fluid.

(ii) The *ill-posed* problem where the advancing fluid is *less* viscous than the surrounding fluid.

In this thesis, we will consider both well-, and ill-posed problems.

Free boundary problems of type (ii) are usually considered with additional physical effects on the interface, such as surface tension or kinetic undercooling, see e.g. [27, 28, 132, 145]. Such problems are referred to as *regularised* Hele-Shaw free boundary problems, where physical phenomena such as surface tension serve to smooth regions of high curvature on the interface, which primarily prevent breakdown of the mathematical solution. However, breakdown of the solution may still occur, see e.g. [139]. A one-phase Hele-Shaw free boundary problems with only a constant pressure condition on the interface is known as *unregularised*. Such a problem is known as a zero surface tension (ZST) Hele-Shaw free boundary problem, which will be the main focus of this thesis.

The main difficulty in solving the Hele-Shaw free boundary problem lies in the nonlinear nature of the mathematical problem. This is since an elliptic partial dif-

ferential equation (PDE) is to be solved in the domain describing the viscous fluid, given some boundary data, and the boundary of the domain must also be found. Here, the boundary data in the one-phase problem will be given by the constant pressure in the inviscid fluid region.

1.1.1 Historic overview, recent studies and applications

Since the 1940s, there has been plenteous effort devoted to the Hele-Shaw free boundary problem, described above, both analytically and numerically. There have been two main groups responsible for its development: one made by mathematicians in the east (e.g. Russia) and the other predominantly made by mathematicians in the west (e.g. Great Britain). The two streams converged in the late 1980s and early 1990s. Significant steps leading to exact solutions of the Hele-Shaw free boundary problem arose via *complex variable methods* and *conformal mapping* techniques, by which the problem can be recast as an initial value problem of a functional differential equation. This was first realised independently by the Russian mathematicians Polubarinova-Kochina [110, 111] and Galin [44] in 1945.

During the late 1950s, Saffman and Taylor tackled the now well known problem of viscous fingering in the Hele-Shaw cell, experimentally, theoretically and computationally [123, 138]. Their initial interest (similar to Polubarinova-Kochina and Galin) was due to the industrial application of oil recovery as a free boundary problem. Consider a pocket of oil surrounded by water forming a free boundary at their interface, in a porous medium. The problem is extracting a fluid with viscosity larger than the surrounding fluid (e.g. extracting oil from water). This is an ill-posed problem, i.e. a problem of type (ii) described above. This ill posedness gives rise to instabilities on the contracting interface which subsequently form long fingers. From the view of

oil recovery, this leads to unwanted water contamination in the recovered oil.

The works by Saffman and Taylor [123, 138] have lead to a vast array of study in Hele-Shaw free boundary problems and the viscous fingering effect. In [123], the main aim of the study is the selection of finger size in a channel geometry set-up in the Hele-Shaw cell, where air (a fluid of low viscosity) advances into glycerin (a viscous fluid of relatively high viscosity)—see figure 1.3. Saffman and Taylor [123] derived a family of solutions for the fingering phenomenon in an infinitely long channel in the Hele-Shaw cell. Following this work, Taylor and Saffman [138] also derived solutions for a translating air bubble, known today as the Taylor-Saffman bubble, in a channel geometry. From these solutions, the solution for a translating air bubble in an unbounded Hele-Shaw cell can be found as an asymptotic approximation, by taking the channel width to be infinite. The propagation of the air bubble is due to a uniform, bounded, background flow *and* the pressure gradient—due to the existence of the bubble—in the direction of the flow.

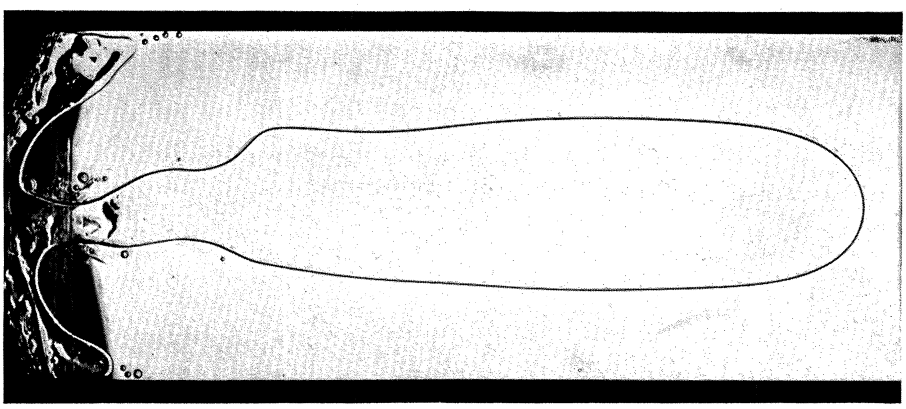

Figure 1.3: A Saffman-Taylor finger produced in a channel within a Hele-Shaw cell by the penetration of air into glycerine. Picture from [123].

An interesting outcome of the works of Saffman and Taylor [123, 138] is known as the *selection problem*, namely the selection of speed *or* bubble shape given the dynamics of the surrounding viscous fluid. Much of the work in this area relates the 'naturally' selected shape or speed of the bubble (observed by Taylor and Saffman

[123, 138]) from a family of possible solutions; the selection was since conjectured to be due to surface tension, i.e physical effects on the bubble interface, see e.g. [69,136] and references therein. However, more recently, the necessity of surface tension as the main selection mechanism has been questioned. It has been shown that selection of the Saffman-Taylor finger can be made in the absence of surface tension [96]. Moreover, for the translating Taylor-Saffman bubble in a channel, it is has recently been shown that the unique bubble shape corresponding to a bubble travelling at twice the speed of the background flow emerges as the stable solution for large times without surface tension [149]. This result was shown by virtue of the existence of an infinitely dimensional dynamical system for a parametric solution of the Hele-Shaw free boundary problem, resulting from the infinite conservation laws of Hele-Shaw flows. The stability of the free boundary and the selection of the interface shape in an unbounded Hele-Shaw cell is studied here, numerically, in chapter 4.

One of the most intriguing results, and features, of Hele-Shaw flows attracting the attention of the physics community is the existence of an infinite number of conservation laws[1]—the complex moments. These were first deduced by Richardson in 1972 [116]. Using this feature of Hele-Shaw flows proved particularly useful in finding exact solutions to the free boundary problem in terms of a parametric conformal map of the interface.

The methods presented by Polubarinova-Kochina [111], Galin [44] and Richardson [116], based on complex variable techniques, are of particular interest, mathematically, due to exact solutions that exhibit cusp formation on the physical interface. The cusps correspond to singularities of the set of ordinary differential equations (ODEs) that govern the evolution of the conformal map. Typically, in the ill-posed problem, breakdown of the mathematical solution occurs in finite time, for example,

[1]See appendix A for a derivation of the infinite conservation laws and short description of how these may be used to find exact solutions of the one-phase Hele-Shaw free boundary problem via a conformal mapping technique described in section 1.3.1.

in Hele-Shaw flows driven by a sink due to the formation of cusps on the free boundary [25, 56, 59], or complete extraction of the fluid. Furthermore, the exact solutions highlighted the property of time reversibility of ZST Hele-Shaw flows, for example, reversal in time of a sink driven Hele-Shaw flow is equivalent to replacing the sink by a source, in which the precise initial condition of the interface of the former solution is recovered.

On the basis of the complex variable methods described, more elaborate mapping functions were sought from which exact solutions have been derived describing a wide variety of physical situations. In particular, mathematically interesting solutions were found where higher order cusps can form in finite time on the free boundary, beyond which the solution can be continued—e.g. the 'special case' of radial fingers in the expanding bubble problem [56] and the expanding blob problem with specific initial condition [63].

The Hele-Shaw cell finds application in other significant areas of fluid flow theory such as potential flow through a porous media, where the governing equation describing the flow velocity is given by Darcy's law [53, 57]. The Hele-Shaw cell has also been used to model dendritic instabilities in crystallisation fronts, which can be studied via the dendritic growth of the Saffman-Taylor finger in a Hele-Shaw cell [17]. The Hele-Shaw model also finds application in the study of the evolving interface between viscous fluids and liquid crystals, e.g. the study of 2D solidification and melting in potential flows in porous media [24] where it turns out that the resulting motion of the interface is analogous to the case of ZST Hele-Shaw flow.

Hele-Shaw free boundary problems have been studied over the past seven decades for both the wide spread application in fluid problems, as well as the mathematical challenges embedded in its formulation. Mineev-Weinstein [93] has demonstrated the link between a system of ODEs, giving exact solutions to the Hele-Shaw free boundary problem, and the conserved moments of Richardson [116]. Mineev-Weinstein

derives the system of ODEs using conformal mapping techniques, where the mapping function on the unit circle (in an auxiliary mapping domain) represents a closed interface, i.e. the interface of a bubble, say. This realisation was a significant step in the development and understanding of the Hele-Shaw free boundary problem and its integrable structure, paving the way for interesting connections to other fields of mathematics and classical physics such as dynamical and integrable systems [48,100], in particular 2D quantum gravity [99] and random matrices [98].

For a further, in-depth account on the life of Hele-Shaw and the developments in the Hele-Shaw free boundary problem, the reader is directed to the article by Vasil'ev [150], and chapters 1 and 2 of the book by Gustafsson and Vasil'ev [48] where a brief overview of the Hele-Shaw free boundary problem and a historic overview of the development in finding exact solutions is presented.

The Hele-Shaw free boundary problem is characterised by a PDE (derived in the following section) whose solution we seek, given two boundary conditions, along with the unknown domain since the domains boundary is unrestricted. Like nonlinear waves, two solutions to the free boundary problem cannot be superimposed to provide another solution, hence, the problem is nonlinear.

1.2 Mathematical model

Let us begin by introducing the equations of motion governing fluid flow. In this work we consider all fluids to be Newtonian. In fluid mechanics, the motion of an incompressible inviscid fluid can be described by the well known Euler equations [42] given by

$$\rho \frac{\mathrm{D}\mathbf{u}}{\mathrm{D}t} = -\nabla p + \mathbf{f}_b, \tag{1.1a}$$

$$\nabla \cdot \mathbf{u} = 0, \tag{1.1b}$$

where $\mathrm{D}/\mathrm{D}t = \partial/\partial t + \mathbf{u}\cdot\nabla$ denotes the *material derivative*, the 3D operator $\nabla = (\partial_x, \partial_y, \partial_z)$, $\mathbf{u} = (u_1, u_2, u_3)$ is the 3D velocity vector following a fluid particle, ρ denotes fluid density, p denotes fluid pressure and $\mathbf{f}_b$ represents body forces on the fluid, e.g. gravity. Equation (1.1a) represents the momentum equation of the fluid, while (1.1b) describes conservation of mass.

Considering the shear and normal stresses on a volume of fluid, we introduce viscous forces on the right hand side of (1.1a), i.e. the governing equations become

$$\frac{\partial \mathbf{u}}{\partial t} + (\mathbf{u}\cdot\nabla)\,\mathbf{u} = -\frac{1}{\rho}\nabla p + \nu\nabla^2\mathbf{u} + \frac{1}{\rho}\mathbf{f}_b, \tag{1.2a}$$

$$\nabla\cdot\mathbf{u} = 0. \tag{1.2b}$$

Equations (1.2) are known as the Navier-Stokes equations which are used to model flow of a viscous fluid. The parameter $\nu = \mu/\rho$ denotes the kinematic viscosity, where μ denotes the dynamic viscosity of the fluid.

1.2.1 The Stokes-Leibenzon model

We will now derive the equation governing Hele-Shaw flows. The model considered is due to Leibenzon [81, 82], first developed as a theory of the motion of gases in porous media during the 1920s, and later employed by Muskat [104]. In this section all quantities presented are dimensional quantities. Let us consider slow uni-directional flow of an incompressible viscous fluid occupying some domain $\Omega(t)$, between two parallel plates fixed at a distance h apart, as shown in figure 1.1(b). Let the velocity $\mathbf{u}$ of the fluid be generated from some external mechanism, e.g. injection of fluid—see figure 1.1(a). The flow profile between the plates is that of Poiseuille flow since we have the no-slip condition on the surface of each plate. In this section we consider the Navier-Stokes equations, (1.2), where external body forces are

neglected for simplicity, i.e. $\mathbf{f}_b = 0$, thus

$$\frac{\partial \mathbf{u}}{\partial t} + (\mathbf{u} \cdot \nabla)\,\mathbf{u} = -\frac{1}{\rho}\nabla p + \nu \nabla^2 \mathbf{u}, \tag{1.3a}$$

$$\nabla \cdot \mathbf{u} = 0. \tag{1.3b}$$

Assume the injection of fluid is slow such that the flow remains approximately steady and parallel to the plates—in fact, Hele-Shaw discovered that the flow will remain laminar for any velocity given the two plates are sufficiently close together [49, 150]. That is, there is no vertical fluid motion, i.e. $u_3 = 0$, and $\partial \mathbf{u}/\partial t = 0$. Hence, the x_1, x_2 and x_3 momentum equations from (1.3a) give

$$u_1 \frac{\partial u_1}{\partial x_1} + u_2 \frac{\partial u_1}{\partial x_2} = -\frac{1}{\rho}\frac{\partial p}{\partial x_1} + \nu \nabla^2 u_1, \tag{1.4a}$$

$$u_1 \frac{\partial u_2}{\partial x_1} + u_2 \frac{\partial u_2}{\partial x_2} = -\frac{1}{\rho}\frac{\partial p}{\partial x_2} + \nu \nabla^2 u_2, \tag{1.4b}$$

$$0 = -\frac{1}{\rho}\frac{\partial p}{\partial x_3}, \tag{1.4c}$$

with the no-slip boundary condition at the upper and lower plates given by

$$u_1\big|_{x_3=0,h} = 0, \tag{1.5a}$$

$$u_2\big|_{x_3=0,h} = 0. \tag{1.5b}$$

Now we consider a dimensional analysis of (1.4). Let the typical velocity scale in the x_1 and x_2 directions be U_d, let the typical length scale in the x_1 and x_2 directions be L_d, and the typical length scale in the x_3 direction be h. Then, the inertial terms on the left hand side of (1.4a) and (1.4b) have orders of magnitude

$$\begin{aligned} u_1 \frac{\partial u_1}{\partial x_1} &\sim \frac{U_\mathrm{d}^2}{L_\mathrm{d}}, & u_2 \frac{\partial u_1}{\partial x_2} &\sim \frac{U_\mathrm{d}^2}{L_\mathrm{d}}, \\ u_1 \frac{\partial u_2}{\partial x_1} &\sim \frac{U_\mathrm{d}^2}{L_\mathrm{d}}, & u_2 \frac{\partial u_2}{\partial x_2} &\sim \frac{U_\mathrm{d}^2}{L_\mathrm{d}}, \end{aligned} \tag{1.6}$$

whilst the viscous terms on the right hand side of (1.4a) and (1.4b) have magnitude

$$\begin{aligned} \frac{\partial^2 u_1}{\partial x_1^2} &\sim \frac{U_\mathrm{d}}{L_\mathrm{d}^2}, & \frac{\partial^2 u_1}{\partial x_2^2} &\sim \frac{U_\mathrm{d}}{L_\mathrm{d}^2}, & \frac{\partial^2 u_1}{\partial x_3^2} &\sim \frac{U_\mathrm{d}}{h^2}, \\ \frac{\partial^2 u_2}{\partial x_1^2} &\sim \frac{U_\mathrm{d}}{L_\mathrm{d}^2}, & \frac{\partial^2 u_2}{\partial x_2^2} &\sim \frac{U_\mathrm{d}}{L_\mathrm{d}^2}, & \frac{\partial^2 u_2}{\partial x_3^2} &\sim \frac{U_\mathrm{d}}{h^2}. \end{aligned} \tag{1.7}$$

Hence, for $h/L_\mathrm{d} \ll 1$ the derivatives of u_1 and u_2 with respect to (w.r.t.) x_1 and x_2 are negligible as compared to the derivative w.r.t. x_3. Thus, (1.4) can be approximated as

$$\frac{\partial p}{\partial x_1} = \mu \frac{\partial^2 u_1}{\partial x_3^2}, \tag{1.8a}$$

$$\frac{\partial p}{\partial x_2} = \mu \frac{\partial^2 u_2}{\partial x_3^2}, \tag{1.8b}$$

$$0 = \frac{\partial p}{\partial x_3}. \tag{1.8c}$$

Equations (1.8a) and (1.8b) represent Stokes flow in two dimensions, whilst equation (1.8c) states that the pressure p is independent of x_3, i.e. $p = p(x_1, x_2, t)$. Hence, integrating (1.8a) and (1.8b) and applying the boundary condition given in (1.5) we have

$$u_1 = \frac{1}{2\mu} \frac{\partial p}{\partial x_1} \left(x_3^2 - h x_3 \right), \tag{1.9a}$$

$$u_2 = \frac{1}{2\mu} \frac{\partial p}{\partial x_2} \left(x_3^2 - h x_3 \right). \tag{1.9b}$$

Taking the mean (average volume flux per unit width of fluid layer) of (1.9) over the gap between the parallel plates yields

$$\overline{u}_1 = \frac{1}{h} \int_0^h u_1 \, \mathrm{d}x_3 = -\frac{h^2}{12\mu} \frac{\partial p}{\partial x_1}, \tag{1.10a}$$

$$\overline{u}_2 = \frac{1}{h} \int_0^h u_2 \, \mathrm{d}x_3 = -\frac{h^2}{12\mu} \frac{\partial p}{\partial x_2}. \tag{1.10b}$$

In vector form, (1.10) can be written as

$$\overline{\mathbf{u}} = -\frac{h^2}{12\mu}\nabla p, \tag{1.11}$$

where here and in the remainder of this thesis, ∇ will denote the 2D differential operator $(\partial_{x_1}, \partial_{x_2})$. Equation (1.11), describing a 2D *potential* velocity field, is known as the *Hele-Shaw equation* and the coefficient $k = h^2/12\mu$ is the *mobility* of the fluid. The flow field is identical to that of a hypothetical 2D flow of inviscid fluid with zero vorticity. The Hele-Shaw equation (1.11) is a useful analogue for the study of inviscid potential flow in porous media, where (1.11) is equivalent to *Darcy's law*, governing flow in 2D porous media with permeability $h^2/12$. Many references are made in the literature outlining the connection between Hele-Shaw flow and flow in porous media, see for example [123]. In what follows, we drop the bar notation for the mean velocity field in (1.11) and write $\overline{\mathbf{u}} = (\overline{u}_1, \overline{u}_2)$ as $\mathbf{u} = (u_1, u_2)$, for brevity.

The averaged velocity field (1.11) also satisfies the 2D continuity equation

$$\nabla \cdot \mathbf{u} = \frac{\partial u_1}{\partial x_1} + \frac{\partial u_2}{\partial x_2} \tag{1.12}$$

$$= 0. \tag{1.13}$$

Coupled with (1.11), (1.12) implies that the pressure p satisfies Laplace's equation, i.e.

$$\nabla^2 p = 0 \quad \text{in } \Omega(t), \tag{1.14}$$

and hence $p(x_1, x_2, t)$ is harmonic in $\Omega(t)$.

Finally, to close the system, we require boundary conditions on the free boundary $\partial\Omega(t)$. These are the *dynamic* and *kinematic* boundary conditions. We shall assume, for the moment, that the secondary fluid forming the interface with the fluid occupying $\Omega(t)$ is of negligible viscosity. Therefore, the pressure in the inviscid fluid is

constant, taken to be zero without loss of generality (w.l.o.g.), and so in the case of ZST, the dynamic boundary condition is

$$p = 0 \quad \text{on } \partial\Omega(t). \tag{1.15}$$

The dynamic boundary condition serves to determine the boundary data of $p(x_1, x_2, t)$. The resulting motion of the free boundary is given by the fluid velocity on the interface. The kinematic boundary condition states that fluid particles on the interface remain on the interface, and is given by

$$V_n = \mathbf{u} \cdot \mathbf{n} \quad \text{on } \partial\Omega(t), \tag{1.16}$$

where $\mathbf{n}$ is the unit normal vector on $\partial\Omega(t)$ pointing to the right if $\partial\Omega(t)$ is positively orientated (i.e. traversed in the anticlockwise direction) and V_n is the normal velocity of $\partial\Omega(t)$. That is, if the finite region enclosed by $\partial\Omega(t)$ describes a fluid *blob* then $\mathbf{n}$ points out of $\Omega(t)$, if it describes a *bubble* then $\mathbf{n}$ points into $\Omega(t)$—see figure 1.4. This choice is made for simplicity in the mathematical formulation of the numerical model presented in chapter 2.

1.2.2 The ZST Hele-Shaw free boundary problem

Writing $\phi(x_1, x_2, t) = -kp(x_1, x_2, t)$, the governing equation (1.14) and the boundary conditions (1.15) and (1.16) can be written in terms of the scalar potential function $\phi(x_1, x_2, t)$, i.e.

$$\nabla^2\phi = 0, \qquad \mathbf{x} \in \Omega(t), \tag{1.17a}$$

$$\phi = 0, \qquad \mathbf{x} \in \partial\Omega(t), \tag{1.17b}$$

$$V_n = \frac{\partial\phi}{\partial n}, \qquad \mathbf{x} \in \partial\Omega(t), \tag{1.17c}$$

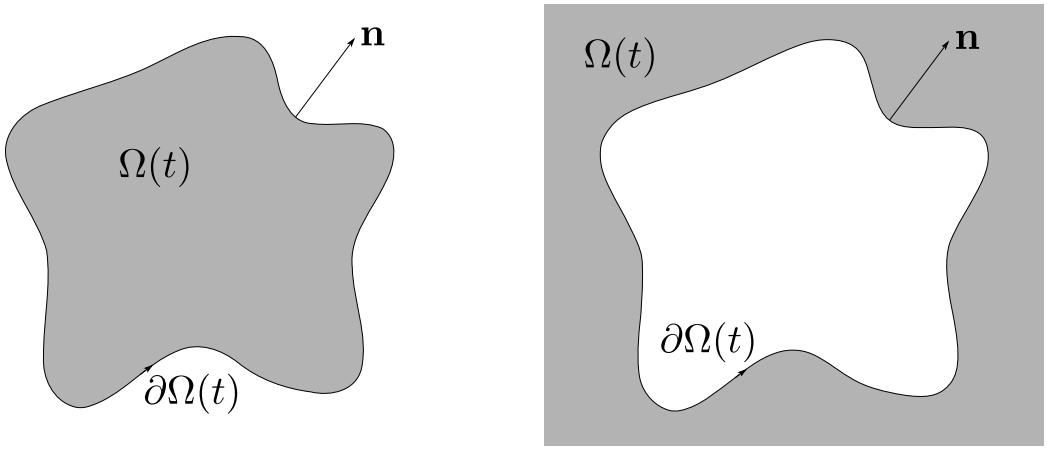

(a) (b)

Figure 1.4: The types of two fluid set-up considered in this thesis, displaying direction of the normal vector on the free boundary $\partial\Omega(t)$. In (a) we have a fluid blob and in (b) a bubble. In both cases, the outer fluid is of infinite expanse, i.e. an unbounded Hele-Shaw cell is considered.

where $\partial/\partial n = \mathbf{n} \cdot \nabla$ denotes the derivative in the normal direction on $\partial\Omega(t)$ and $\mathbf{x} = (x_1, x_2)$ is the 2D position vector. In this thesis we will refer to (1.17) as the *free boundary problem*[2].

The free boundary $\partial\Omega(t)$ in many Hele-Shaw flows is driven by hydrodynamic singularities, for example distributed sources or sinks in the case of injection or extraction of fluid mass. In this thesis we will mainly be concerned with two types of hydrodynamic singularities, described below.

(i) For finite fluid *blobs* occupying the domain $\Omega(t)$, we will consider cases where the interface $\partial\Omega(t)$ is driven by sources or sinks (or even higher order hydrodynamic singularities, e.g. dipoles, quadrupoles etc.). Conservation of mass adheres to the rate of injection or extraction of fluid, i.e. considering the flux integral of fluid mass over $\partial\Omega(t)$ and applying *Gauss' theorem* we find $\nabla \cdot \mathbf{u} = \sum_j Q_j \delta_0(\mathbf{x} - \mathbf{x}_j)$ for a combination of sources and sinks of strength Q_j [9, pp. 88–92]. Here, $\delta_0(\mathbf{x} - \mathbf{x}')$ denotes the *Dirac distribution* supported at

[2]A derivation of the free boundary problem with external background fields, i.e. $\mathbf{f}_b \neq 0$, is given in appendix B. The motion of $\partial\Omega(t)$ due specifically to background electric fields are studied in chapter 3.

the origin, i.e.

$$\delta_0(\mathbf{x}-\mathbf{x}') = \begin{cases} \infty & \text{if } \mathbf{x}=\mathbf{x}', \\ 0 & \text{if } \mathbf{x}\neq\mathbf{x}'. \end{cases} \tag{1.18}$$

Hence, the field equation (1.17a) in this case is given by

$$\nabla^2\phi = \sum_j Q_j\delta_0(\mathbf{x}-\mathbf{x}_j), \qquad \mathbf{x}\in\Omega(t), \tag{1.19}$$

where Q_j denotes the strength of the j-th hydrodynamic singularity at position $\mathbf{x}_j \in \Omega(t)\setminus\partial\Omega(t)$ and $\sum_j Q_j$ gives the rate of change of fluid mass due to the finite number of distributed hydrodynamic singularities. Using the *Green's function* for the Laplacian operator in 2D, we find[3]

$$\phi(x,y,t) \to \sum_j \frac{Q_j}{2\pi}\log|\mathbf{x}-\mathbf{x}_j|, \qquad \text{as } \mathbf{x}\to\mathbf{x}_j, \tag{1.20}$$

a supplementary condition that must be satisfied inside $\Omega(t)$.

(ii) In the case of a finite *bubble* surrounded by an infinite expanse of viscous fluid occupying the domain $\Omega(t)$ in an unbounded Hele-Shaw cell, we will consider the motion of the interface $\partial\Omega(t)$ due to a bounded uniform flow at infinity. That is, the free boundary problem (1.17) is supplemented with the condition

$$\phi \to Vx, \qquad \text{as } \mathbf{x}\to\pm\infty, \tag{1.21}$$

i.e. in this case the fluid is driven by a singularity at large distance from $\partial\Omega(t)$.

In this thesis, we shall constrain our focus to problems where the interface, $\partial\Omega(t)$, separating the two fluids is a *simple closed curve* in $\mathbb{R}^2$.

[3]Throughout this thesis, log denotes the natural logarithm, base e.

1.3 Preliminaries

As we are concerned with a 2D flow, in the remainder of this thesis we use the classical notation in $\mathbb{R}^2$ where $x \equiv x_1$, $y \equiv x_2$, $u \equiv u_1$ and $v \equiv u_2$. Since the flow is incompressible, there also exists a stream function $\psi(x, y, t)$, say, such that $\mathbf{u} = \nabla \times \psi \mathbf{k}$, where $\mathbf{k}$ is the unit vector in the x_3 direction, i.e.

$$u = \frac{\partial \psi}{\partial y}, \tag{1.22a}$$

and

$$v = -\frac{\partial \psi}{\partial x}. \tag{1.22b}$$

Combining (1.11) and (1.22) gives

$$\frac{\partial \phi}{\partial x} = \frac{\partial \psi}{\partial y}, \tag{1.23a}$$

and

$$\frac{\partial \phi}{\partial y} = -\frac{\partial \psi}{\partial x}, \tag{1.23b}$$

which can be viewed as the classical *Cauchy-Riemann* equations. This implies that there exists a complex potential

$$w(z, t) \equiv \phi(x, y, t) + i\psi(x, y, t), \tag{1.24}$$

which is an analytic function of the complex variable $z = x + iy$. This is a significant result as it suggests that Hele-Shaw flow can be investigated using the theory of analytic functions. Indeed, such methods based on complex variables will be utilised frequently in this research. In terms of the complex variable z, the free boundary

problem (1.17) is given by

$$\nabla_z^2 \phi = 0, \qquad z \in \Omega(t), \tag{1.25a}$$

$$\phi = 0, \qquad z \in \partial\Omega(t), \tag{1.25b}$$

$$V_n = \frac{\partial \phi}{\partial n}, \qquad z \in \partial\Omega(t), \tag{1.25c}$$

where $\partial/\partial n = \Re\{(n_1 + in_2)(\partial_x - i\partial_y)\}$, n_1 and n_2 are the x and y components of the unit normal vector $\mathbf{n}$ on $\partial\Omega(t)$, respectively, the harmonic function $\phi(x, y, t) \equiv \phi(z, \bar{z}, t)$ and $\nabla_z^2 = 4\partial^2/\partial z \partial \bar{z}$ is the complex form of the Laplacian operator $\nabla^2 = \partial^2/\partial x^2 + \partial^2/\partial y^2$.

1.3.1 Conformal mapping techniques

To tackle the Hele-Shaw free boundary problem, conformal mapping techniques have been used extensively in the literature, e.g. [25,48,59,89,99,111]. Due to the 2D nature of the Hele-Shaw free-boundary problem, one can take advantage of complex variable methods to seek the evolution of the free boundary, $\partial\Omega(t)$, by transforming (1.17) into an initial value problem of a functional equation. Here we shall briefly state some basic definitions and concepts of conformal mapping techniques and derive the so called *Schwarz function equation* which is used extensively throughout this research to find exact solutions to the Hele-Shaw free boundary problem.

Since $\partial\Omega(t)$ is considered to be a simple closed curve in $\mathbb{R}^2$, in the language of complex variables, $\partial\Omega(t)$ is *Jordan curve* in $\mathbb{C}$.

Definition 1.3.1 (Jordan Curve) Let an arc in the complex z-plane be defined by a parametric equation $z = z(s)$, where $s \in \mathbb{R}$. If the arc is finite, then $z(s) = x(s) + iy(s)$ is a continuous function on an interval $a \leq s \leq b$, say, whose orientation is fixed by its parameterisation, where z describes the arc in the positive sense as s increases from a to b. A Jordan curve is defined by the closed path $z(a) = z(b)$ such

that $z(s_1) \neq z(s_2)$ for $a \leq s_1 < s_2 \leq b$.

A complex function, $z = f(\zeta)$, say, where $f : A \to A'$, $\zeta \in A$, $z \in A'$ and A, $A' \subseteq \mathbb{C}$, is a function that maps a point $\zeta = \xi + i\eta$ in the ζ-plane (ξ, $\eta \in \mathbb{R}$) to a point $z = x + iy$ in the z-plane.

Definition 1.3.2 (Conformal map) A conformal map of a domain or surface is a map that preserves the magnitude of angles between curves.

That is, the map $f : A \to A'$ is said to be conformal if $f(\zeta)$ preserves angles, and their orientation, of smooth curves. A map $f : A \to A'$ is conformal at a point where the derivative exists and is non-zero, that is, any *analytic function* $f(\zeta)$ is conformal where $f'(\zeta) \neq 0$ in the complex plane[4].

Definition 1.3.3 (Analytic function) Let $f(\zeta)$ be a complex function on some domain $A \subseteq \mathbb{C}$. If $f(\zeta)$ is single-valued and differentiable at each point $\zeta \in A$, then $f(\zeta)$ is called *analytic*. An analytic function is also referred to as a *regular* function, where *analytic* and *regular* may be used interchangeably throughout this thesis.

Definition 1.3.4 (Univalent map) Let B, $B' \subset \mathbb{C} \cup \{\infty\}$, then a map is called univalent in B if it is *injective* (one-to-one) in B, i.e. $f(\zeta_1) \neq f(\zeta_2)$ if $\zeta_1 \neq \zeta_2$, where ζ_1, $\zeta_2 \in B$ and $z_1 = f(\zeta_1)$, $z_2 = f(\zeta_2) \in B'$. If $f : B \to B'$ is univalent in B, it is also univalent in all subdomains of B.

The set $\mathbb{C} \cup \{\infty\}$ is known as the *Riemann sphere* or *extended complex plane*. A univalent map is a conformal homemorphism (topological isomorphism). The inverse of a univalent map, i.e. $\zeta = f^{-1}(z)$, is also univalent.

The basis of applying conformal mapping techniques in the complex plane to find exact solutions to the Hele-Shaw free boundary problem is the *Riemann Mapping Theorem*. This important result states that *any* simply connected domain in the

[4]In this thesis, the prime used in conjunction with a function shall always denote differentiation w.r.t. the first argument.

complex plane can be obtained via a conformal map from the unit disc in an auxiliary 'mapping domain' [48].

In this thesis we will consider time-dependent univalent mappings from the interior *or* exterior of the unit ζ-disc (the mapping domain) in the ζ-plane, to the viscous fluid domain $\Omega(t)$ in the z-plane, i.e.

$$z = f(\zeta, t). \tag{1.26}$$

The interior and exterior of the unit ζ-disc are defined as

$$D \coloneqq \{\zeta : |\zeta| \leq 1\} \tag{1.27a}$$

and

$$D_{\text{ext}} \coloneqq \{\zeta : |\zeta| \geq 1\}, \tag{1.27b}$$

respectively. That is, the interface separating the two fluids in the z-plane, i.e. the free boundary $\partial\Omega(t)$, is mapped from the unit ζ-circle in the ζ-plane. The unit ζ-circle is defined as

$$\partial D := \{\zeta : |\zeta| = 1\}. \tag{1.28}$$

1.3.2 The Schwarz function and its properties

By use of the *Schwarz reflection principle* (symmetry principle) [106], the Schwarz function (defined below) can be used to construct a functional equation relating the free boundary, $\partial\Omega(t)$, to the hydrodynamics (and even external body force effects) which drive its evolution.

Definition 1.3.5 (Schwarz function) The uniquely defined function $g(z, t)$, which is analytic in the neighbourhood $\Omega_\epsilon(t)$, say, of a simple curve $\partial\Omega(t)$ in the complex

plane such that

$$\bar{z} = g(z,t), \qquad z \in \partial\Omega(t), \tag{1.29}$$

is called the Schwarz function.

If the curve $\partial\Omega(t)$ is given by $h(x,y,t) = 0$, then the Schwarz function of the curve $\partial\Omega(t)$ can, in principle, be obtained by setting $x = (z+\bar{z})/2$ and $y = (z-\bar{z})/2$ and re-arranging $h([z+\bar{z}]/2, [z-\bar{z}]/2i) = 0$ for $\bar{z}$.

Let $z = f(\zeta,t)$ be a time-dependent conformal map from the interior of the unit ζ-disc, D, to $\Omega(t)$ in the z-plane. Then the Schwarz function of the curve $\partial\Omega(t)$ is given by

$$\begin{aligned} g(z,t) &= \bar{z} \\ &= \overline{f(\zeta,t)} \\ &= \bar{f}(1/\zeta,t), \end{aligned} \tag{1.30}$$

since $|\zeta|^2 = \zeta\bar{\zeta} = 1$, where the points $z = f(\zeta,t) \in \partial\Omega(t)$ are mapped from the unit ζ-circle ∂D—see figure 1.5.

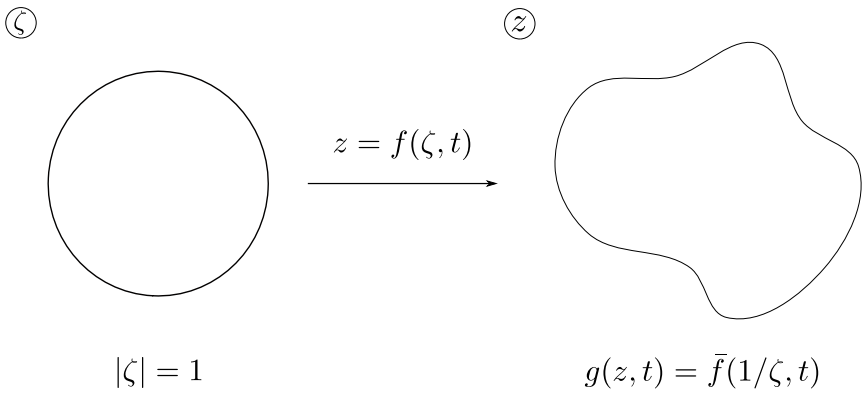

Figure 1.5: A conformal map from the unit ζ-circle, ∂D, in the ζ-plane, to the free boundary, $\partial\Omega(t)$, in the z-plane.

Note that on ∂D we have that $\bar{\zeta} = 1/\zeta$, and therefore

$$\overline{f(1/\zeta,t)} = \overline{f}(\zeta,t). \tag{1.31}$$

Since $\partial\Omega(t)$ is mapped from ∂D by $f(\zeta,t)$, it can be shown that $f(\zeta,t)$ is regular on ∂D, and that $\bar{f}(\zeta,t)$ and $f(1/\zeta,t)$ are analytic continuations of one another. Furthermore, (1.31) does not just hold on ∂D, but for all analytic continuations of $\bar{f}(\zeta,t)$. Taking the complex conjugate of (1.31), we see that the point $f(1/\zeta,t)$ is the reflection of the point $\bar{f}(\zeta,t)$ with respect to $\partial\Omega(t)$ [106], a useful fact when deriving the Schwarz function equation for the Hele-Shaw free boundary problem.

Before deriving the Schwarz function equation, we derive three useful properties of the Schwarz function.

(a) Let the curve $\partial\Omega(t)$ be parameterised by its arc length, which is denoted by s, then

$$\begin{aligned} \mathrm{d}s^2 &= \mathrm{d}x^2 + \mathrm{d}y^2 \\ &= (\mathrm{d}x + i\mathrm{d}y)(\mathrm{d}x - i\mathrm{d}y) \\ &= \mathrm{d}z\mathrm{d}\bar{z}. \end{aligned} \tag{1.32}$$

Let $\bar{z} = g(z,t)$ be the Schwarz function of the curve $\partial\Omega(t)$, then from (1.32) we have

$$\begin{aligned} \frac{\partial g}{\partial z} &= \frac{\partial \bar{z}}{\partial z} \\ &= \left(\frac{\partial s}{\partial z}\right)^2, \end{aligned} \tag{1.33}$$

hence, taking the positive root, (1.33) yields

$$\frac{\partial z}{\partial s} = \left(\frac{\partial g}{\partial z}\right)^{-1/2}. \tag{1.34}$$

(b) Let $\partial\Omega(t)$ be given by $h(x,y,t) \equiv h(z,\bar{z},t) = 0$. Recall the kinematic boundary condition (1.16), which states that a fluid particle on the boundary stays on the boundary, i.e. the boundary is formed by the same set of particles for

all time. This implies that the material derivative following a fluid particle on $\partial\Omega(t)$ must be equal to zero in the normal direction, and since the normal velocity of the interface must be equal to the normal velocity of fluid on $\partial\Omega(t)$, the material derivative on $\partial\Omega(t)$ is

$$\frac{\partial h}{\partial t} + V_n \mathbf{n} \cdot \nabla h = 0, \tag{1.35}$$

where $\mathbf{n} = (\mathrm{d}y/\mathrm{d}s, -\mathrm{d}x/\mathrm{d}s)$ is the unit normal vector on $\partial\Omega(t)$. The unit normal to $\partial\Omega(t)$ can also be written in terms of $h(x, y, t)$ as $\mathbf{n} = \nabla h/|\nabla h|$, and so (1.35) becomes

$$\begin{aligned} \frac{\partial h}{\partial t} + V_n \frac{\nabla h \cdot \nabla h}{|\nabla h|} &= \frac{\partial h}{\partial t} + V_n |\nabla h| \\ &= 0. \end{aligned} \tag{1.36}$$

Using the relations

$$\frac{\partial}{\partial x} = \frac{\partial}{\partial z} + \frac{\partial}{\partial \bar{z}}, \tag{1.37a}$$

$$\frac{\partial}{\partial y} = i\frac{\partial}{\partial z} - i\frac{\partial}{\partial \bar{z}}, \tag{1.37b}$$

and $h(x, y, t) \equiv h(z, \bar{z}, t)$, we may write

$$\begin{aligned} |\nabla h| &= (\nabla h \cdot \nabla h)^{1/2} \\ &= \left[\left(\frac{\partial h}{\partial x} \right)^2 + \left(\frac{\partial h}{\partial y} \right)^2 \right]^{1/2} \\ &= \left(4 \frac{\partial h}{\partial z} \frac{\partial h}{\partial \bar{z}} \right)^{1/2}. \end{aligned} \tag{1.38}$$

Using the definition of the Schwarz function (1.29), it can be seen that $\partial\Omega(t)$

is given by $h(z,\bar{z},t) = \bar{z} - g(z,t) = 0$, and so (1.38) yields

$$\begin{aligned} |\nabla h| &= 2\left(\frac{\partial h}{\partial z}\frac{\partial h}{\partial \bar{z}}\right)^{1/2} \\ &= 2i\left(\frac{\partial g}{\partial z}\right)^{1/2}, \end{aligned} \tag{1.39}$$

since $\partial h/\partial z = -\partial g/\partial z$ and $\partial h/\partial \bar{z} = 1$. Taking the partial derivative w.r.t. time of $h(z,\bar{z},t) = \bar{z} - g(z,t)$, we obtain

$$\frac{\partial h}{\partial t} = -\frac{\partial g}{\partial t}. \tag{1.40}$$

Substituting (1.39) and (1.40) into (1.36), we deduce that[5]

$$V_n = -\frac{i}{2}\frac{\dot{g}}{(g')^{1/2}}. \tag{1.41}$$

(c) From the definition of the Schwarz function (1.29), it can easily be verified that the Schwarz function satisfies the consistency condition

$$g(\overline{g(z,t)},t) \equiv \bar{z}. \tag{1.42}$$

1.3.3 The Schwarz function equation

Exact solutions of the Hele-Shaw free boundary problem are rare and often difficult to come by owing to the nonlinearity of the problem. The general solution for an arbitrary shaped blob forced by a single source has not been found. However, some exact solutions can be found using complex variable methods, an idea first employed by Polubarinova-Kochina [110, 111] and Galin [44] in 1945. In [44, 110, 111] the so called *Polubarinova-Galin equation* (P-G equation) is formulated[6], the designation

[5]Here, and in the remainder of this thesis, the dot shall represent derivative w.r.t. time.
[6]A derivation of the P-G equation is given in appendix C.

appearing in a paper by Howison [59]. More recently, the application of the Schwarz function to find explicit solutions to the Hele-Shaw free boundary problem has been seen, e.g. [25, 59, 89].

Here we derive the governing equation based on the Schwarz function approach to find exact solutions to the Hele-Shaw free boundary problem (1.25). Let us consider the case of a viscous fluid blob occupying a simply connected domain, $\Omega(t)$. Suppose the domain $\Omega(t)$ is mapped from the interior of the unit ζ-disc[7], D, via a time-dependent univalent conformal map $z = f(\zeta, t)$. Then the free boundary $\partial\Omega(t)$ has Schwarz function (1.30). The dynamic boundary condition (1.25b) implies that the free boundary is an *isobar* (a surface of constant pressure), in particular $\phi(z, \bar{z}, t) = 0$. From (1.30) the free boundary can be described by $\phi(z, \bar{z}, t) = \bar{z} - g(z, t)$. Now, let us consider the derivative of the complex potential $w(z, t)$, defined in (1.24), along $\partial\Omega(t)$, i.e. tangent to the free boundary. If the curve $\phi(z, \bar{z}, t) = 0$ is parameterised w.r.t. arc length, denoted by s, we have

$$\begin{aligned} \frac{\partial w}{\partial z} &= \frac{\partial w}{\partial s}\frac{\partial s}{\partial z} \\ &= \left(\frac{\partial \phi}{\partial s} + i\frac{\partial \psi}{\partial s}\right)\frac{\partial s}{\partial z}. \end{aligned} \tag{1.43}$$

Hence, since the pressure is constant along $\partial\Omega(t)$, $\partial\phi/\partial s = 0$. The velocity potential and stream function satisfy the Cauchy-Riemann equations w.r.t. the tangential and normal derivatives, i.e.

$$\frac{\partial \phi}{\partial n} = \frac{\partial \psi}{\partial s}, \tag{1.44a}$$

$$\frac{\partial \phi}{\partial s} = -\frac{\partial \psi}{\partial n}, \tag{1.44b}$$

where $v_\tau = \partial\phi/\partial s$ and $v_n = \partial\phi/\partial n$ denote the tangential and normal velocity components on $\partial\Omega(t)$, respectively. On the free boundary v_n must satisfy the boundary

[7]It is not necessary for $\Omega(t)$ to be mapped specifically from D, it can also be mapped, for example, from D_{ext}, as is the case when studying translating bubbles in chapter 4.

condition (1.25c). Therefore, (1.43) becomes

$$\begin{aligned}\frac{\partial w}{\partial z} &= i\frac{\partial \phi}{\partial n}\frac{\partial s}{\partial z} \\ &= iV_n\frac{\partial s}{\partial z},\end{aligned} \tag{1.45}$$

and finally, employing properties (a) and (b) from section 1.3.2, namely (1.34) and (1.41), we have

$$\frac{\partial w}{\partial z} = \frac{1}{2}\frac{\partial g}{\partial t}. \tag{1.46}$$

In this thesis we will refer to (1.46) as the *Schwarz function equation*. This equation is implicit in the work of Richardson [116] and was first derived explicitly by Lacey [77] (in a different form) where it is stated to hold on the free boundary $\partial\Omega(t)$, which follows the derivation given above[8]. It can also be found in the work of Millar [91, 92] and was popularised by Howison [59].

So far, (1.46) has been derived on the interface, $\partial\Omega(t)$. In this respect, (1.46) is not immediately useful since the complex potential $w(z,t)$ is unknown on $\partial\Omega(t)$. However, since both sides of (1.46) are analytic functions in the neighbourhood of $\partial\Omega(t) \subset \Omega(t)$, i.e. $\Omega_\epsilon(t)$, both sides of (1.46) may be be analytically continued away from the free boundary and so (1.46) holds over the entire domain $\Omega(t)$. In this light, (1.46) is now useful since it must hold in the limit where any singularities of $w(z,t)$ are approached, providing a basis from which exact solutions may be derived.

Example 1.3.1 (Flows due to a point source or sink)

Suppose that the free boundary, $\partial\Omega(t)$, is driven by single singularity, such as a hydrodynamic source or a sink of strength Q_1, say, located arbitrarily at $z_1 = x_1 + iy_1$. In a small vicinity of the point z_1 we have $\nabla_z^2\phi = Q_1$ and so the Hele-Shaw free

[8] An alternative derivation, also including external fields (as discussed in section 1.3.5), is given in appendix D following the derivation given by McDonald [89].

boundary problem in this case is given by

$$\nabla_z^2 \phi = Q_1 \delta_0(z - z_1), \qquad z \in \Omega(t), \tag{1.47a}$$

$$\phi = 0, \qquad z \in \partial\Omega(t), \tag{1.47b}$$

$$v_n = \frac{\partial \phi}{\partial n}, \qquad z \in \partial\Omega(t), \tag{1.47c}$$

where $\delta_0(z - z_1)$ is the Dirac distribution defined in (1.18) with 2D position vectors replaced by their complex variable counterparts, and so

$$\phi(z, \bar{z}, t) \to \frac{Q_1}{2\pi} \log|z - z_1|, \qquad \text{as } z \to z_1. \tag{1.48}$$

The complex potential, $w(z,t)$, has only one singularity, which corresponds to the source or sink, that drives the flow. The driving singularities and the initial boundary shape given by $g(z,0)$ are fixed, completing the initial description of the problem.

From the equality in (1.46), the singularities of $w'(z,t)$ and $\dot{g}(z,t)$ must match, that is, the hydrodynamic singularities driving the flow give singularities of $\dot{g}(z,t)$ within $\Omega(t)$ and so in this sense singularities of $g(z,t)$ evolve in a predictable way. In the case of a single point source or sink, $w'(z,t)$ has a simple pole at $z = z_1$ with residue $Q_1/2\pi$, where $Q_1 > 0$ corresponds to a source, and $Q_1 < 0$ to a sink. The Schwarz function equation (1.46) then implies $\dot{g}(z,t)$ must also have the same singular behaviour.

For a point source or sink, considering (1.48), we may deduce that in the vicinity of the hydrodynamic singularity the complex potential takes the form

$$w = \frac{Q_1}{2\pi} \log(z - z_1) + W(z), \tag{1.49}$$

where $W(z)$ can be expressed as an analytic power series of z, hence, from (1.46) we

have

$$\frac{\partial g}{\partial t} = \frac{Q_1}{\pi}\frac{1}{z - z_1} + G(z), \tag{1.50}$$

where $G(z)$ can also be expressed as an analytic power series of z. Equation (1.50) coupled with (1.30) provides a method with which to solve the physical problem described by (1.47). More precisely, first employing (1.30), the Laurent expansion of the Schwarz function, $g(z,t)$, about the singular point z_1 can be found. Then, matching the coefficients in the Schwarz function equation, which in the current example is given by (1.50), determines the time-dependent parameters of the univalent conformal map $z = f(\zeta, t)$. Thus, the parameters are usually given by a set of coupled ODEs.

To summarise, complex variable methods and conformal mappings are used to reformulate the ZST Hele-Shaw free boundary problem as a nonlinear initial value problem in a fixed canonical domain (e.g. D in the ζ-plane).

1.3.4 Exact solutions of one-phase Hele-Shaw flow

Here we display the procedure by which exact solutions can be found to the Hele-Shaw free boundary problem by virtue of the Schwarz function equation (1.46).

Example 1.3.2 (Expanding circular fluid blob)

Let us consider the trivial example of a circular fluid blob growing due to a point source located at its centre, $z = z_1$, say. The area of the viscous domain, $\Omega(t)$, will grow at the rate of injection, Q_1. By the symmetry of the problem, it is expected that the boundary will remain circular for all time. Since the blob is circular, on the free boundary $\partial\Omega(t)$, we have

$$z\bar{z} = a^2, \tag{1.51}$$

where $a = a(t)$ is the radius of the circular blob at time t. Therefore, the Schwarz

function is easily found and is given by

$$g = \frac{a^2}{z}. \tag{1.52}$$

Here, the radius of the fluid blob ($a \in \mathbb{R}$) is a time varying parameter to be found.

Near the source the complex potential takes the form (1.49). Thus, the conjugate complex velocity, $w'(z,t) = u - iv$, is

$$\frac{\partial w}{\partial z} = \frac{Q_1}{2\pi}\frac{1}{z - z_1} + W'(z), \quad \text{as } z \to z_1, \tag{1.53}$$

which has a simple pole at $z = z_1$. Considering the Schwarz function equation (1.46) with (1.50), (1.52) and (1.53), equating terms of $O((z - z_1)^{-1})$ we have

$$\frac{Q_1}{2\pi} = \frac{1}{2}\frac{\mathrm{d}}{\mathrm{d}t}(a^2). \tag{1.54}$$

Integrating (1.54) yields

$$a = \sqrt{\frac{Q_1 t}{\pi} + a(0)^2}, \tag{1.55}$$

i.e. $a(t) \sim t^{1/2}$. Note that re-arranging (1.54) gives

$$Q_1 = \frac{\mathrm{d}}{\mathrm{d}t}(\pi a^2), \tag{1.56}$$

which states that the rate of change of area of the circular blob is equal to the rate of change of fluid mass, Q_1, as expected. Thus, the evolution of the free boundary $\partial\Omega(t)$ can be described via the differential equation (1.56) with the initial condition $a(0) = a_0$, say. In the case of a point source, i.e. $Q_1 > 0$, (1.55) is well-defined, i.e. $a \in \mathbb{R}$ for all t, as expected.

Consider the problem in which $\partial\Omega(t)$ is driven by a sink at $z = z_1$. Solution (1.55) holds, however, since $Q_1 < 0$, it is expected that (1.55) will give an imaginary solution

beyond some time, $t = t^*$, say, where the solution breaks down in the physical sense. The time t^* can be calculated by setting

$$\frac{Q_1 t^*}{\pi} + a_0^2 = 0, \tag{1.57}$$

and re-arranging we have

$$t^* = -\frac{\pi a_0^2}{Q_1}. \tag{1.58}$$

This is precisely the time for all the fluid to be extracted by the sink. In practice, Hele-Shaw sink flows are ill-posed, and typically cusps form on the free boundary in finite time, before all the fluid is extracted [56, 62, 63]. This is demonstrated in the next example.

Example 1.3.3 (Shrinking perturbed circular blob)

Consider the non-trivial case of an initially perturbed circular blob of fluid whose free boundary is driven by a source or a sink. It is well known that the interior of a circle with $n-1$ perturbations can be mapped from the unit disc. Therefore, consider the following simple mapping function from D to the fluid domain $\Omega(t)$ (employed by Cummings et al. [25]) given by the polynomial map

$$z = a\left(\zeta - \frac{b}{n}\zeta^n\right), \tag{1.59}$$

where $n \geq 2$, $n \in \mathbb{N}$. We may assume $a = a(t)$ and $b = b(t)$ are real, positive parameters for all time that are to be found. Note that (1.59) is univalent if and only if $|b(0)| < 1$. For $b(0) \neq 0$, the shape of the initial boundary, $\partial\Omega(0)$, is a limaçon.

The Schwarz function of (1.59) is found by employing (1.30) and using the fact $\bar{\zeta} = \zeta^{-1}$ on $\partial\Omega(t)$, which gives

$$g = a\left(\frac{1}{\zeta} - \frac{b}{n\zeta^n}\right). \tag{1.60}$$

The derivative of the complex potential, $w'(z,t)$, takes the form (1.53) as $z \to z_1$, and from (1.59) we have

$$\frac{1}{\zeta} = \frac{1}{z}\left(a - \frac{ab}{n}\zeta^{n-1}\right). \tag{1.61}$$

Without loss of generality, assume that the source is located at the origin, i.e. $z_1 = 0$. As $\zeta \to 0$, we approximate

$$\zeta = \frac{z}{a} + \mathcal{O}(z^n), \tag{1.62}$$

and we can write

$$\frac{1}{\zeta} = \frac{a}{z} - \frac{ab}{na^{n-1}}z^{n-2} + \mathcal{O}(z^{2n-2}). \tag{1.63}$$

To complete the expansion of $g(z,t)$ about the location of the source, $z = 0$, the expansion of $1/\zeta^n$ is also required as $\zeta \to 0$. This is achieved by the binomial expansion of (1.63), giving

$$\frac{1}{\zeta^n} = \frac{a^n}{z^n} - \frac{ab}{z} + \mathcal{O}(z^{n-2}). \tag{1.64}$$

Hence, the Schwarz function has the expansion

$$g = -\frac{a^{n+1}b}{n}\frac{1}{z^n} + a^2\left(1 + \frac{b^2}{n}\right)\frac{1}{z} + \mathcal{O}(z^{n-2}), \quad \text{as } z \to 0. \tag{1.65}$$

Applying (1.46) and comparing terms of $\mathcal{O}(z^{-n})$ and $\mathcal{O}(z^{-1})$, we have a set of coupled differential equations for $a(t)$ and $b(t)$ given by

$$\frac{\mathrm{d}}{\mathrm{d}t}\left[a^{n+1}b\right] = 0, \tag{1.66a}$$

$$\frac{\mathrm{d}}{\mathrm{d}t}\left[a^2\left(1 + \frac{b^2}{n}\right)\right] = \frac{Q_1}{\pi}, \tag{1.66b}$$

which, in turn, describe the evolution of the free boundary $\partial\Omega(t)$. Integrating we

have

$$a^{n+1}b = a_0^{n+1}b_0, \tag{1.67a}$$

$$a^2\left(1+\frac{b^2}{n}\right) = \frac{Q_1 t}{\pi} + a_0^2\left(1+\frac{b_0^2}{n}\right), \tag{1.67b}$$

where $a_0 = a(0)$ and $b_0 = b(0)$. The solution (1.67) was also derived by Galin [44] and Polubarinova-Kochina [112] using a different method—see appendix C.

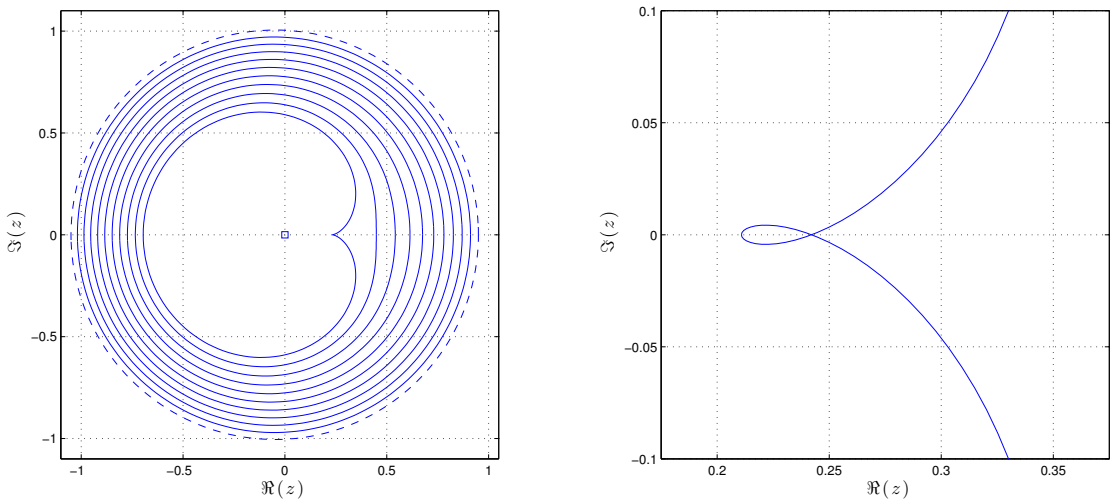

(a) (b)

Figure 1.6: Cusp formation on the free boundary, $\partial\Omega(t)$, at $t = t_c \approx 0.6825$, beyond which the solution breaks down—close up after breakdown shown in (b) where $t > t_c$. The initial boundary (dashed), $\partial\Omega(0)$, is given by (1.59) with $a_0 = 1$, $b_0 = 0.1$. Snapshots of the evolution of $\partial\Omega(t)$, in (a), are shown $t = 0$, 0.0683, 0.1365, 0.2046, 0.273, 0.3413, 0.4095, 0.4778, 0.546, 0.6143 and 0.6825. The flow is driven by a sink of strength $Q_1 = -\pi$, marked by a square.

In the case of a point source, i.e. $Q_1 > 0$, the fluid blob grows such that $\partial\Omega(t)$ eventually becomes a circle centred at $z = 0$, where the solution (1.67) is valid for all time. For a sink driven flow, i.e. $Q_1 < 0$, a cusp forms on the free boundary at time $t = t_c$, say, beyond which (1.59) is no longer univalent and the solution breaks down—see figure 1.6. Physically, the assumption of a simply connected domain $\Omega(t)$ is violated beyond this time [25]. At $t = t_c$, we have $b(t_c) = 1$ and $\partial\Omega(t)$ becomes a cardioid, as shown in figure 1.6(a), where the shape of $\partial\Omega(t)$ comprises a 3/2-power cusp, at which point the speed of the free boundary at the cusp tip is of

$\mathcal{O}((t-t_c)^{-1/2})$, i.e. infinite [56].

Example 1.3.4 (Growing circular blob near a wall)

Example 1.3.3 may be generalised to accommodate any number of sources or sinks distributed in $\Omega(t)$. In some cases it may be useful to have more than one singularity driving the free boundary, for example the problem of a fluid blob expanding near a straight wall. To model the flow when a fluid blob is in contact with the wall, the method of images can be employed, e.g. [117], reflecting the free boundary and any sources or sinks in the wall to satisfy the zero flux boundary condition on the wall—see figure 1.7.

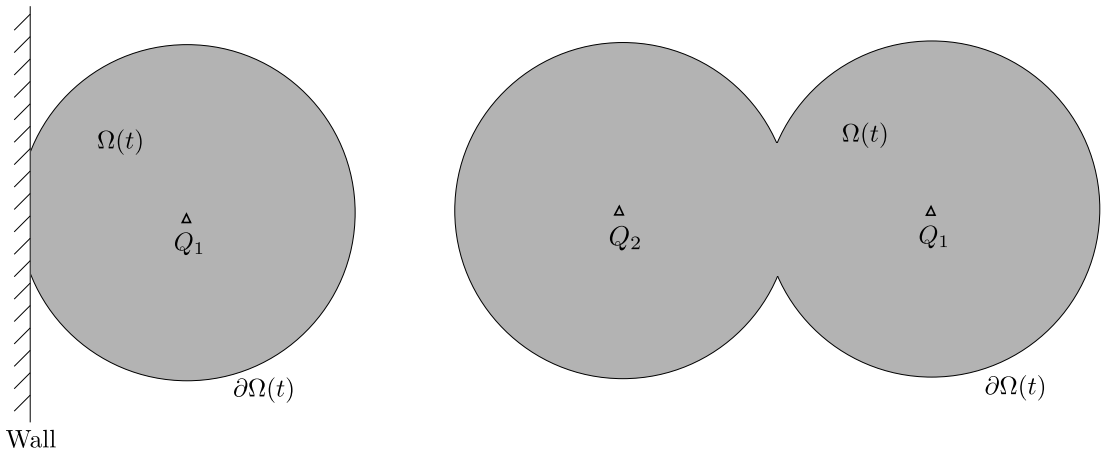

Figure 1.7: Employing the method of images to solve the problem of a Hele-Shaw flow near a wall where the free boundary, $\partial\Omega(t)$, is driven by a point source of strength Q_1, marked by a triangle, depicted in (a). The equivalent scenario in which the boundary is that of a Neumann oval is shown in (b) where $Q_1 \equiv Q_2$.

Consider the rational map from D, in the ζ-plane, to $\Omega(t)$, in the z-plane, such that $\partial\Omega(t)$ has the same shape as that shown in figure 1.8(b) given by

$$z = \frac{R\zeta}{\zeta^2 - \zeta_1^2}, \tag{1.68}$$

where $R \in \mathbb{R}$ gives the required symmetry in the $\Im(z)$ axis. $R = R(t)$ and $\zeta_1 = \zeta_1(t)$ are real, time varying parameters to be found. Assume that we want to model the

evolution of $\partial\Omega(t)$ driven by two sources, as shown in 1.8(b), such that the line of symmetry coincides with the imaginary axis. Hence, the sources lie on the real axis located at $z = z_1$ and $z = z_2 \equiv -z_1$, say. Without loss of generality, let us take $z_1 = 1$. Taking the complex conjugate of (1.68) and using the fact $\overline{\zeta} = \zeta^{-1}$ on ∂D, we have the Schwarz function for the free boundary given by

$$\begin{aligned} g &= \frac{R\overline{\zeta}}{\overline{\zeta}^2 - \zeta_1^2} \\ &= -\frac{R}{2\zeta_1^2}\left(\frac{1}{\zeta + \zeta_1^{-1}} - \frac{1}{\zeta - \zeta_1^{-1}}\right), \end{aligned} \tag{1.69}$$

which has simple poles at $\zeta = \zeta_1^{-1}$ and $\zeta = -\zeta_1^{-1}$. Given the sources or sinks are located at $z = \pm 1$, choosing to map the poles of (1.69) to $z = \pm 1$, i.e. $z(\pm\zeta_1^{-1}) = \pm 1$, then, from (1.68) we have the relation

$$R\zeta_1 = (1 - \zeta_1^4). \tag{1.70}$$

Now consider the expansion of (1.68) about $\zeta = a^{-1}$, i.e.

$$z = z(\zeta_1^{-1}, t) + (\zeta - \zeta_1^{-1})z'(\zeta_1^{-1}, t) + \mathcal{O}((\zeta - \zeta_1^{-1})^2), \tag{1.71}$$

and so we have

$$\frac{1}{\zeta - \zeta_1^{-1}} = \frac{1}{z - 1}z'(\zeta_1^{-1}, t) + \mathcal{O}(1), \tag{1.72}$$

hence

$$\frac{1}{\zeta - \zeta_1^{-1}} = \frac{1 + \zeta_1^{-4}}{R\zeta_1^{-2}}\frac{1}{z - 1} + \mathcal{O}(1). \tag{1.73}$$

Considering the complex potential, we find that

$$\frac{\partial w}{\partial z} \to \frac{Q_1}{2\pi}\frac{1}{z - 1}, \qquad \text{as } z \to 1. \tag{1.74}$$

Therefore, employing the the Schwarz function equation (1.46) and comparing terms of order $\mathcal{O}((z-1)^{-1})$ yields

$$\frac{\mathrm{d}}{\mathrm{d}t}\left[\frac{1}{2}\left(\frac{1+\zeta_1^{-4}}{\zeta_1^{-2}}\right)\right] = \frac{Q_1}{\pi}. \tag{1.75}$$

Integrating (1.75) gives

$$\zeta_1^4 - \left(2\frac{Q_1 t}{\pi} + \frac{1+\zeta_{10}^{-4}}{\zeta_{10}^{-2}} - 2\right)\zeta_1^2 + 1 = 0, \tag{1.76}$$

where $\zeta_{10} = \zeta_1(\pi/Q_1)$, and at $t = \pi/Q_1$ the circular blob has unit radius (and just touches the wall). The parameters $\zeta_1(t)$ and $R(t)$ are found by solving (1.76) and (1.70), where $|\zeta_1(t)| \geq 1$, and both $\zeta_1(t)$ and $R(t)$ are real for (1.68) to be univalent. Figure 1.8 shows solution to (1.76) and (1.70) for $t > \pi/Q_1$ where $\zeta_{10} = 1$ and $R_0 = R(\pi/Q_1) = 0$. As $t \to \infty$, $\partial\Omega(t)$ tends to a circle.

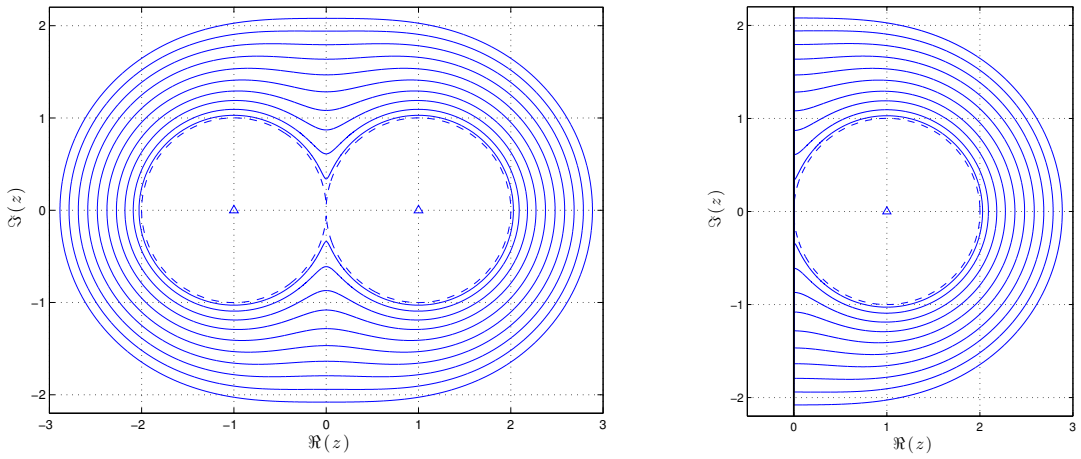

(a) (b)

Figure 1.8: Time evolution of $\partial\Omega(t)$ of a fluid blob growing under the influence of a point source (marked by a triangle) near a solid wall coinciding with $\Re(z) = 0$, shown in (b). The initial boundary (dashed), $\partial\Omega(0)$, is given by (1.68) with $\zeta_1(\pi/Q_1) = 1$ and $R(\pi/Q_1) = 0$, where $Q_1 = 1$. Evolution of $\partial\Omega(t)$ is shown at $t = 3.142$, 4.084, 5.027, 5.969, 6.912, 7.854, 8.796, 9.739, 10.681, 11.624, 12.566. The equivalent problem of a dumbbell shaped boundary evolving under the action of two sources of the same strength (marked by triangles) in each lobe is shown in (a).

Examples 1.3.1–1.3.4 outline a useful method by which exact solutions to the one-phase Hele-Shaw free boundary problem can be found, a method which will be used extensively to study the evolution of the free boundary, $\partial\Omega(t)$, in chapters 3 and 4.

1.3.5 The generalised Schwarz function equation

The Schwarz function equation (1.46) can be generalised to include background conservative body force effects in one-phase Hele-Shaw flows [39, 89]. For flows including body forces, the Hele-Shaw free boundary problem is given by (B.11) in appendix B, where the dynamic boundary condition now reads

$$\phi = \Psi, \qquad \mathbf{x} \in \partial\Omega(t), \tag{1.77}$$

and the background force can be described as the gradient of a scalar potential function $\Psi(x, y, t)$ such that $\mathbf{f}_b = -\nabla\Psi/k$. Therefore, the free boundary $\partial\Omega(t)$ can be described by the function $\phi(x, y, t) - \Psi(x, y, t) = 0$. Making the substitution $x = (z + \bar{z})/2$, $y = (z - \bar{z})/2$, and using the definition of the Schwarz function (1.30) of $\partial\Omega(t)$, on the free boundary we must have $\phi((z + \bar{z})/2, (z - \bar{z})/2, t) - \Psi((z + \bar{z})/2, (z - \bar{z})/2, t) \equiv \phi(z, \bar{z}, t) - \Psi(z, \bar{z}, t) = \bar{z} - g(z, t) = 0$. Since the pressure along the free boundary is given by (1.77), taking the tangential derivative along $\partial\Omega(t)$ gives $\partial\phi/\partial s = \partial\Psi/\partial s$. Therefore, using (1.44a), (1.43) along $\partial\Omega(t)$ gives

$$\frac{\partial w}{\partial z} = \left(\frac{\partial \Psi}{\partial s} + i\frac{\partial \phi}{\partial n}\right)\frac{\partial s}{\partial z}. \tag{1.78}$$

Finally, employing (1.25c), (1.34) and (1.41), we have

$$\frac{\partial w}{\partial z} = \frac{\partial \Psi}{\partial z} + \frac{1}{2}\frac{\partial g}{\partial t}. \tag{1.79}$$

The analytic continuation of (1.46), as descried in section 1.3.3, also applies to (1.79), which we shall call the *generalised Schwarz function equation*, and so is valid over the entire domain $\Omega(t)$. Therefore, (1.79) can be used to construct exact solutions to the Hele-Shaw free boundary problem including external potentials, if the structure of singularities of $\partial w/\partial z$ and $\partial \Psi/\partial z$ are known.

Example 1.3.5 (Elliptical bubble in a rotating cell)

Consider an elliptical bubble surrounded by an infinite fluid region, $\Omega(t)$, in a rotating Hele-Shaw cell [19,41,89]. For a rotating Hele-Shaw cell, the centrifugal potential in the entire plane is given by

$$\Psi = \omega \frac{z\bar{z}}{2}, \tag{1.80}$$

where ω is constant, denoting the speed of angular rotation. Therefore, since $\bar{z} = g$ on the free boundary $\partial\Omega(t)$, (1.80) gives

$$\frac{\partial \Psi}{\partial z} = \omega \left(g + z \frac{\partial g}{\partial z} \right). \tag{1.81}$$

Let us consider the map from the interior of the unit ζ-disc, D, to the fluid region exterior to the elliptical bubble, $\Omega(t)$, by

$$z = \frac{a}{\zeta} + b\zeta, \tag{1.82}$$

where $a(t)$ and $b(t)$ are real, time varying parameters to be found. Note, from (1.82), it is clear that as $\zeta \to 0$, $z \to \infty$. Taking the complex conjugate of (1.82), and using (1.82) to approximate $1/\zeta$ as $\zeta \to 0$, the Schwarz function of $\partial\Omega(t)$, as $z \to \infty$, has the expansion

$$g = \frac{b}{a} z + \frac{a^2 - b^2}{z} + \mathcal{O}(z^{-3}). \tag{1.83}$$

Since there are no hydrodynamic singularities within $\Omega(t)$, $\partial w/\partial z$ is analytic in $\Omega(t)$. Hence, considering terms of $\mathcal{O}(z)$ and $\mathcal{O}(z^{-1})$, the generalised Schwarz function

equation (1.79) gives

$$\frac{\mathrm{d}}{\mathrm{d}t}\left(\frac{b}{a}\right) + 2\omega\left(\frac{b}{a}\right) = 0, \tag{1.84a}$$

$$\frac{\mathrm{d}}{\mathrm{d}t}(a^2 - b^2) = 0, \tag{1.84b}$$

a set of coupled ODEs governing the evolution of a and b. The second of these equations, (1.84b), is equivalent to conservation of bubble area, as expected, since there is no flux of fluid mass through $\partial\Omega(t)$. Solving (1.84), the exact solution for the elliptical bubble in a rotating Hele-Shaw cell is given by the map (1.82) with

$$a = \frac{a_0\sqrt{a_0^2 - b_0^2}}{\sqrt{a_0^2 - b_0^2\exp(-4\omega t)}}, \tag{1.85a}$$

$$b = \frac{b_0\sqrt{a_0^2 - b_0^2}\exp(-2\omega t)}{\sqrt{a_0^2 - b_0^2\exp(-4\omega t)}}, \tag{1.85b}$$

where $a_0 = a(0)$ and $b_0 = b(0)$. Without loss of generality, we can choose

$$a_0^2 - b_0^2 = 1, \tag{1.86}$$

fixing the area of the elliptical bubble for all time.

Evolution of an initially elliptical bubble for positive and negative ω are shown in figure 1.9. For $\omega > 0$, the flow is stable, where the elliptical bubble tends to a circle as $t \to \infty$, whereas for $\omega < 0$, the flow is unstable and the solution (1.85) breaks down in finite time, $t = t_c$, say, at which point the elliptical bubble collapses onto the real axis [89].

Example 1.3.6 (Translating circular bubble)

Consider a circular bubble of initial radius R_0 centred at $z = C_0$ (where R_0, $C_0 \in \mathbb{R}$), surrounded by an infinite expanse of viscous fluid occupying the domain $\Omega(t)$. Assume that the bubble is driven by a uniform steady flow of speed V in the positive

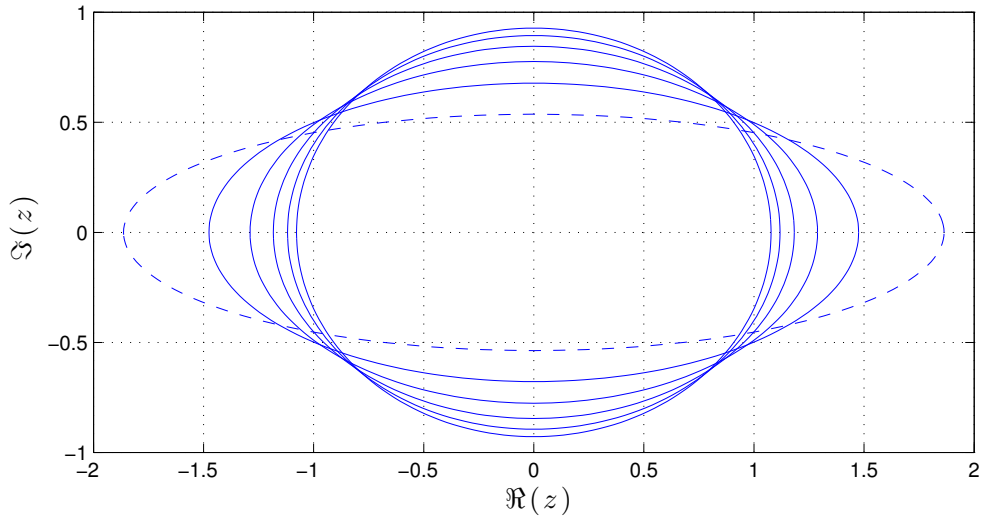

(a)

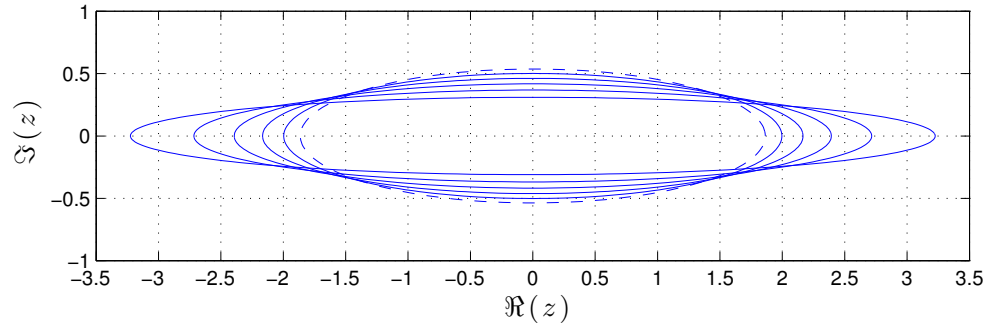

(b)

Figure 1.9: Time evolution of an initially elliptical bubble interface (dashed line) in a rotating Hele-Shaw cell, with $a_0 = 1.2$, $b_0 = \sqrt{1.2^2 - 1}$ and $0 \leq t \leq 1$. In (a) the evolution of $\partial\Omega(t)$ for $\omega = -1$ is shown at $t = 0$, 0.2, 0.4, 0.6, 0.8 and 1.0, and in (b) for $\omega = 1$, the interface is shown at $t = 0$, 0.04, 0.08, 0.12, 0.16 and 0.2.

x direction [138]. That is, as $z \to \infty$, $w(z,t) \to Vz$.

Let us consider the conformal map from the interior of the unit ζ-disc, D, to the fluid region exterior to the circular bubble given by

$$z = \frac{R}{\zeta} + C, \tag{1.87}$$

where $R(t)$, $C(t) \in \mathbb{R}$ are time-dependent parameters to be found. The Schwarz function of $\partial\Omega(t)$ behaves like

$$g \to \frac{R^2}{z} + C, \qquad \text{as } z \to \infty. \tag{1.88}$$

Therefore, applying the Schwarz function equation (1.46) as $z \to \infty$, we find

$$V = \frac{R\dot{R}}{z} + \frac{\dot{C}}{2}, \tag{1.89}$$

and so, comparing terms of $\mathcal{O}(z^{-1})$ and $\mathcal{O}(1)$ in (1.89), we have

$$R\frac{\mathrm{d}R}{\mathrm{d}t} = 0, \tag{1.90a}$$

$$\frac{\mathrm{d}C}{\mathrm{d}t} = 2V. \tag{1.90b}$$

Hence, if $R(0) = R_0$ and $C_0 = C(0)$, the solution to (1.90) is $R = R_0 =$ constant and $C = 2Vt + C_0$, which implies the circular bubble will translate as a circle of constant radius at speed twice that of the background flow, in the same direction.

1.4 Thesis structure

The research presented in this thesis is arranged around three topics, two of which are problems studied in one-phase Hele-Shaw flows, in chapters 3–4, and the third is based on the study of two-phase Hele-Shaw flows given in chapter 5. The Hele-Shaw free boundary problem in both one-, and two-phase are investigated using two approaches: analytically, via the Schwarz function approach presented in sections 1.3.3–1.3.5 of this chapter, and numerically. Earlier in this chapter, the Hele-Shaw free boundary problem was introduced and a review of some of the literature, which will be relevant throughout the subsequent chapters, was presented. Some exact solutions obtained via the Schwarz function approach were also presented, serving as introductory material for the following chapters.

In chapter 2, the mathematical formulation and algorithm for the numerical method, developed as part of the current research, is presented for the one-phase problem. A brief account on the formulation of existing numerical methods is given

in section 2.1. In section 2.2.2 the mathematical formulation is presented, based on complex variable techniques, namely contour integration, by which a boundary integral equation (BIE) is derived. The distinguishing factor between bubbles and blobs in the mathematical formulation is discussed in section 2.6. The numerical method is tested against some known, exact solutions to one-phase Hele-Shaw flows, like those presented in sections 1.3.4 and 1.3.5. Finally, the numerical method is extended to consider multiple interface problems, e.g. flows with multiple bubbles, after which, some concluding remarks are made.

Chapter 3 is concerned with flow of conducting fluids subject to an external electric field. The underlying assumptions and field equations governing the electromagnetic effects are set forth in section 3.1, and the resulting free boundary problem is presented in section 3.2. In the following section, analytical results are derived for a steady solution after which a temporal solution is given which tends to the former steady state solution. The stability of the free boundary under the action of the external field is discussed in section 3.3.2. In section 3.4 the numerical results (computed using the method presented in chapter 2) are compared with the analytical results. Given the excellent agreement between analytical and numerical results, additional numerical simulations are presented with some discussion, and finally some conclusions are drawn.

The unsteady motion of a translating bubble, due to a uniform background flow, is considered in chapter 4. Details of the Taylor-Saffman bubble and the selection problem [138] are given. In section 4.2 the steady elliptical bubble is revisited and the propagation speed of the rotated elliptical bubble is derived using the Schwarz function approach. Numerical simulations of a translating bubble are shown in section 4.3 and the attraction to the circular bubble with propagation speed twice the background flow is discussed. The breakup of a single bubble is investigated numerically in section 4.3.2 where the singularities of the Schwarz function of the initial

bubble interface play a significant role. The stability of an elliptical bubble is studied analytically in section 4.4. Details of exact solutions that breakdown in finite time and unsteady solutions that exist for all time are studied in section 4.4.1. Furthermore, in chapter 6, the problem of a single bubble near a wall of infinite length, subject to a uniform flow, is considered numerically.

In Chapter 5, the two-phase Hele-Shaw free boundary problem is considered, where two fluids of non-zero, finite viscosity are separated by a simple closed interface. The construction of exact solutions are discussed in section 5.3 and are used to test numerical results in section 5.2.3. The formulation and algorithm of the numerical method to solve the two-phase Hele-Shaw free boundary problem are presented in sections 5.2.1 and 5.2.2. An exact solution for a rotated elliptical inclusion is presented in section 5.3.2 using an existing solution technique for two-phase flow, and a relationship between viscosity ratio and the speed of propagation of a circular inclusion is given in section 5.3.3. Remarks made by Taylor and Saffman [138] are revisited in section 5.3.4 with some discussion, and some concluding remarks are made.

In the final chapter—chapter 6—the conclusions of the work presented in this thesis are summarised and some avenues of future research are discussed.

1.5 Contribution to literature

As a result of the research carried out during the term of the author's PhD studentship, two complete research articles have been written and submitted, one to the *European Journal of Applied Mathematics*, and the other to *Physics of Fluids* [71,72]. The first article was published online in October 2013 (later published in the 25^{th} volume of the journal in August 2014), and the second paper is currently under the review process. Below we give the abstracts of each paper. The majority of the

research published (or submitted) is presented in chapters 3 and 4, respectively.

Article title

Hele-Shaw flow driven by an electric field (*European Journal of Applied Mathematics*, 25(4): 425–447, 2014).

Article abstract

The behaviour of two-dimensional finite blobs of conducting viscous fluid in a Hele-Shaw cell subject to an electric field is considered. The time-dependent free boundary problem is studied both analytically using the Schwarz function of the free boundary, and numerically using a boundary integral method.

Various problems are considered including: (i) the behaviour of an initially circular blob of conducting fluid subject to an electric point charge located arbitrarily within the blob, (ii) the delay in cusp formation on the free boundary in sink driven flow due to a strategically placed electric charge and (iii) stability of exact steady solutions having both hydrodynamic and electric forcing.

Article title

On the motion of unsteady translating bubbles in an unbounded Hele-Shaw cell (*Physics of Fluids*, 27(1): 1–21).

Article abstract

Unsteady propagating bubbles in an unbounded Hele-Shaw cell are considered numerically in the case of zero surface tension. The instability of elliptical bubbles and their evolution toward a stable circular boundary, with speed twice that of the fluid speed at infinity, is studied numerically and by stability analysis. Numerical

simulations of bubbles demonstrate the important role played by singularities of the Schwarz function of the bubble boundary in determining the evolution of the bubble. When the singularity lies close to the initial bubble, two types of topological change are observed: (i) the bubble splitting into multiple bubbles and (ii) a finite fluid blob pinching off inside the bubble region.

Chapter 2

A numerical model for one-phase Hele-Shaw flows

2.1 Boundary Integral Methods

The solutions of Hele-Shaw free boundary problems including various boundary effects, for example constant pressure, surface tension or kinetic undercooling, have been the subject of numerical study with a large emphasis on *Boundary Intergral Methods* (BIMs) in the literature[1], see e.g. [1, 14, 15, 26, 28, 68]. The use of a BIM is appealing as the main interest lies in computing the motion of the interface, hence, formulating the problem in terms of quantities of interest such as velocity potential, stream function or fluid velocity on the interface is sufficient and efficient. BIMs usually consist of an integral equation formulated along the interface, as we do in this thesis, known as a *Boundary Integral Equation* (BIE). In some cases the equations on the interface may be derived in the form of an integro-differential system, see e.g. [14]. The formulations of BIEs are either based on complex variable methods, e.g. [90, 146], or a Green's identity approach, formulated by virtue of Green's third

[1]For a further in-depth discussion and historical perspective on BIMs and their application to fluid dynamic problems, the reader is referred to the paper by Hou et al. [55] and references therein.

identity, e.g. [68, 126].

McLean and Saffman [90]—whose work concerns the time-dependent problem of predicting the shape of a finger in a channel, where surface tension effects are included, and the stability of the steady Saffman-Taylor finger—formulate the Hele-Shaw free boundary problem as an integro-differential system where a BIE (which in fact is a Cauchy principal value integral) is formulated using free streamline techniques due to Helmholtz [52] and Kirchhoff [74] by considering the complex conjugate velocity and the complex potential along the interface. More recently, the same BIE formulation is also used by Chapman and King [15] and Dallaston [26] to study the effects of kinetic undercooling on particular Hele-Shaw flow problems, e.g. selection of the Saffman-Taylor finger, where asymptotic expansion techniques are also employed to investigate the stability and asymptotic behaviour of the interface, whereby the expansions are truncated and the resulting equations can be treated numerically.

A BIE can also be formulated via a vortex sheet method for Hele-Shaw flows which can be treated numerically using spectral methods, see e.g. [14, 55, 143], which follow closely the numerical method for computing the motion of a vortex sheet, for example used in the studies by Baker [8] and Krasny [76]. Such boundary integrals are based on an integro-differential equation known as the Birkhoff-Rott equation [11, 121] in which the velocity of the free boundary is related to the strength of the vortex sheet. In particular, Ceniceros et al. [14] follow the algorithm of Strain [131], where the governing equations are recast in a curvilinear coordinate system, and the time stepping algorithm is based on an explicit-implicit method. Furthermore, Ceniceros et al. [14] establish a small scale decomposition to reduce stiffness of the resulting system of equations. The formulation allows clustering of mesh points in regions of high curvature and therefore allows to accurately predict the formation of a cusp of an exact solution such as example 1.3.3. Although the numerical method is elaborate and accounts for the stiffness of the system of equations, stability issues, similar to

those presented here and by Aitchison and Howison [1], still occur, and a filtering process is applied. The filtering process employed is based on that of Krasny [76], where Fourier modes, satisfying a given tolerance condition, are set to zero, i.e. the Fourier series is truncated.

In a similar way to the vortex sheet method, where the strength of the 'vortex sheet' is found as part of the formulation at any instance, a method of distributed sources can also be used. Here sources are distributed along the free boundary and the source strengths must be determined as part of the formulation, see e.g. [34]. In the method presented by Degregoria and Schwarz [34], a conformal map is used to transform the problem to a simpler domain before solving numerically to find the complex potential which is then differentiated w.r.t. the complex variable to give the conjugate complex velocity of the free boundary.

Green's identity can also be used to formulate a BIE in $\mathbb{R}^2$ as opposed to $\mathbb{C}$, where in particular, Green's third identity is used giving a formulation whereby the stream function and its normal derivative are related through an integral equation, see e.g. [67, 68, 126]. Such a formulation has proven popular in recent years and a similar line integral formulation has also been used to study other free boundary problems in fluid mechanics such as Contour Dynamics [33, 35], the equations of which can also be reformulated in the complex plane [23].

Another numerical method closely related to the Contour Dynamics method has also been employed in [88] to study Hele-Shaw flows near obstacles, where the Hele-Shaw free boundary problem can be recast as a pseudo vortex patch problem via a Baiocchi transform. The objective then becomes to find a steady patch of uniform vorticity by a combination of Contour Dynamics and Newton's method to compute the varying strength of vorticity for such equilibria. Again, quantities of interest are computed on the free boundary only.

Solution methods are not restricted to BIMs: Volume of Fluids methods, e.g.

[151], immersed interface methods, e.g. [54], or finite difference methods, e.g [108], have also been employed to solve Hele-Shaw free boundary problems numerically. In the Volume of Fluids method, for example, the pressure field is computed in the viscous phase using finite difference approximations, and the continuity equation is given in terms of a flux integral over the interface which is approximated numerically using well known quadrature rules, e.g. the trapezium rule. However, even today, the downside to such methods is the dramatic increase in computational complexity as the entire phase domain (or an area surrounding the interface in immersed interface methods) is discretised, as compared with 'pure' BIMs where the interface alone is discretised.

2.2 Numerical model

Here we give, in detail, a formulation of a boundary integral method which differs to those discussed in section 2.1. The formulation presented here is similar to the method introduced by Vanden-Broeck [146, 147] in which a complex contour integral on the free boundary is constructed such that the integrand is a function of the complex conjugate fluid velocity (which is an analytic function). Considering such an integral gives an equation which can be solved directly for the fluid velocity on—and therefore the velocity of—the interface.

In section 2.2.2 we present the numerical model for a finite fluid blob enclosed by an anticlockwise contour describing the interface. Section 2.3 describes the numerical procedure. In section 2.4 the stability of the numerical model is discussed and in section 2.5 the model is modified to incorporate external fields. In section 2.6 the equations are presented for the bubble problem where the contour describing the bubble interface is also orientated in the anticlockwise direction. Numerical results are tested against exact solutions in section 2.7, and we finally end by presenting an

extension to the numerical model to study problems with more than one distinct, simple, closed interface in section 2.8.

The Cauchy integral formula and Cauchy principal value

Before we proceed, we state two important mathematical concepts, namely the *Cauchy integral formula* and the definition of the *Cauchy principal value* for specific real integrals, that form the basis of the numerical model and allow us to compute the solution.

The Cauchy integral formula for an integrand with at most a simple pole can be stated as follows. Let $f(z)$ be analytic everywhere in the domain $\Omega(t)$, say, then for any simply connected closed contour $\mathscr{C}$ within $\Omega(t)$, with positive orientation, i.e. traversed in the anticlockwise direction, then

$$\frac{1}{2i\pi}\int_{\mathscr{C}}\frac{f(z)}{z-z_m}\,\mathrm{d}z=\begin{cases}0, & \text{if } z_m \text{ is outside of } \mathscr{C},\\ f(z_m), & \text{if } z_m \text{ is inside of } \mathscr{C},\\ \frac{1}{2}f(z_m), & \text{if } z_m \text{ is on } \mathscr{C}.\end{cases} \tag{2.1}$$

When evaluating a real integral, the assumption is that the integrand is well-defined over the entire domain of integration, i.e. when evaluating $\int_a^b f(s)\,ds$, it is assumed $f(s)$ is well-defined over $[a,b]$, a, $b\in\mathbb{R}$. An integral can be evaluated if $f(s)$ is undefined at some point over the domain of integration and the integral is convergent, in the following sense.

Definition 2.2.1 (Cauchy principle value) Let $f(s)$ be a real function that is undefined at a point $s_0\in[a,b]$, then the value of the integral

$$\fint_a^b f(s)\,\mathrm{d}s=\lim_{\epsilon\to 0^+}\left\{\int_a^{s_0-\epsilon} f(s)\,\mathrm{d}s+\int_{s_0+\epsilon}^b f(s)\,\mathrm{d}s\right\} \tag{2.2}$$

is called the *Cauchy principal value* if the limits on the right hand side of (2.2) exist. Convergent integrals with a Cauchy principal value are denoted by a dashed integral sign, as in the left hand side of (2.2).

2.2.1 Decomposition of the velocity potential

To present the numerical method for finite viscous domains $\Omega(t)$ (i.e. finite blobs of fluid), we choose the particular case where the free boundary is driven by a point source or sink located at $(x_1, y_1) \in \Omega(t) \setminus \partial\Omega(t)$. The velocity potential of the flow is decomposed as $\phi = \widetilde{\phi} + \widehat{\phi}$ where the velocity potential due to the given background flow (i.e. due to the point source or sink) is $\widehat{\phi}(x, y, t)$, and $\widetilde{\phi}(x, y, t)$ is the potential part due to the presence of the free boundary (i.e. the interface with the inviscid domain $\mathbb{C} \setminus \Omega(t)$). The velocity $\widetilde{\mathbf{u}} = \nabla\widetilde{\phi}(x, y, t)$ is a solenoidal, irrotational vector field which describes the local evolution of the interface as a result of the background flow, $\widehat{\mathbf{u}} = \nabla\widehat{\phi}$, and so $\widetilde{\phi}(x, y, t)$ is regular in $\Omega(t)$. The total fluid velocity is given by the sum $\mathbf{u} = \widetilde{\mathbf{u}} + \widehat{\mathbf{u}}$. In order to solve (1.47) numerically, the free boundary problem is written in terms of $\widetilde{\phi}$ for which the governing equations are

$$\nabla^2\widetilde{\phi} = 0, \qquad \mathbf{x} \in \Omega(t), \tag{2.3a}$$

$$\widetilde{\phi} = -\widehat{\phi}, \qquad \mathbf{x} \in \partial\Omega(t), \tag{2.3b}$$

$$V_n = \frac{\partial}{\partial n}\left(\widetilde{\phi} + \widehat{\phi}\right), \qquad \mathbf{x} \in \partial\Omega(t), \tag{2.3c}$$

where, in the case $\partial\Omega(t)$ is driven by a point source or sink, the background potential is $\widehat{\phi} = (Q_1/4\pi)\log\left[(x - x_1)^2 + (y - y_1)^2\right] \equiv (Q_1/2\pi)\log|z - z_1|$.

The numerical method is to first solve (2.3a) and (2.3b) to find the velocity due to $\widetilde{\phi}$ on $\partial\Omega(t)$ at any instance given $\Omega(t)$, and then to advect the interface by the kinematic condition (2.3c).

2.2.2 Mathematical formulation

Suppose two fluids are separated by a simple closed curve, $\partial\Omega(t)$, in a Hele-Shaw cell. Suppose also that one of the fluids is viscous and the other is a fluid with negligible viscosity, e.g. oil and air. Let the viscous fluid domain occupy the finite region $\Omega(t)$. Since we consider $\partial\Omega(t)$ to be a simple closed curve in $\mathbb{R}^2$, in the language of complex variables, we consider $\partial\Omega(t)$ to be a contour in $\mathbb{C}$ traversed in the positive direction in the normal sense[2]. That is, following convention—the same convention used in section 1.2.1—when traversing along $\partial\Omega(t)$ in the anticlockwise direction we take the (outward) unit normal vector pointing to the right, i.e. we take the mass of fluid occupying $\Omega(t)$ to lie to the left [66, pp. 98–99]. Therefore, in the case of a fluid blob, $\partial\Omega(t)$ is traversed in the anticlockwise direction and we stick to this convention throughout the derivation of any subsequent equations. Let us parameterise $\partial\Omega(t)$ with arc length, s. Let the total arc length of $\partial\Omega(t)$ be $L(t)$. Then, in $\mathbb{C}$, $z(s) = x(s) + iy(s)$ describes $\partial\Omega(t)$ in the anticlockwise direction with s increasing from 0 to $L(t)$, i.e. $0 \leq s \leq L(t)$.

Now let us define the unit normal and tangent vectors on $\partial\Omega(t)$ as

$$\mathbf{n} = \left(\frac{\mathrm{d}y}{\mathrm{d}s}, -\frac{\mathrm{d}x}{\mathrm{d}s}\right), \tag{2.4a}$$

$$\boldsymbol{\tau} = \left(\frac{\mathrm{d}x}{\mathrm{d}s}, \frac{\mathrm{d}y}{\mathrm{d}s}\right), \tag{2.4b}$$

respectively. That is, according to the convention described above, travelling in the positive direction on $\partial\Omega(t)$, (2.4a) fixes the direction of $\mathbf{n}$ towards the right—see figure 2.1. Let the normal and tangential fluid velocity on the interface $\partial\Omega(t)$ be denoted by v_τ and v_n, respectively. If $\mathbf{u} = (u, v)$ denotes the fluid velocity vector

[2]Recall, the Hele-Shaw free boundary problem can be recast in terms of the complex variable $z = x + iy$ such that $\phi(x, y, t) \equiv \phi(z, \bar{z}, t)$, as presented in section 1.3—c.f. (1.25).

inside $\Omega(t)$ in Cartesian coordinates, then on the interface, v_τ and v_n are

$$\begin{aligned} v_n &= \mathbf{u}\cdot\mathbf{n} \\ &= u\frac{\mathrm{d}y}{\mathrm{d}s} - v\frac{\mathrm{d}x}{\mathrm{d}s}, \end{aligned} \tag{2.5}$$

$$\begin{aligned} v_\tau &= \mathbf{u}\cdot\boldsymbol{\tau} \\ &= u\frac{\mathrm{d}x}{\mathrm{d}s} + v\frac{\mathrm{d}y}{\mathrm{d}s}. \end{aligned} \tag{2.6}$$

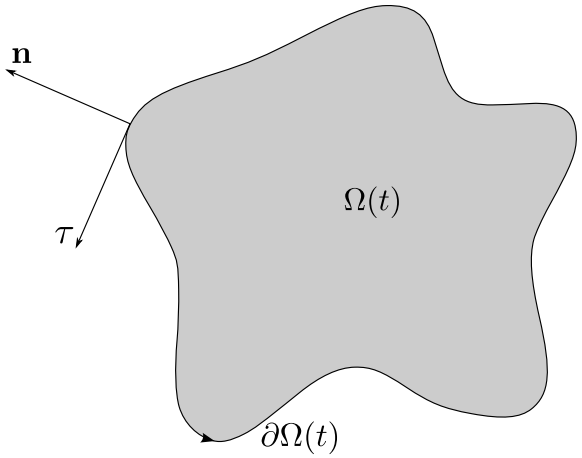

Figure 2.1: Displaying the parameterisation of the interface, $\partial\Omega(t)$, of a finite fluid blob occupying $\Omega(t)$, and the direction of the normal and tangential vectors on the interface.

Since we are interested in formulating the free boundary problem directly for the velocity of the interface, let us write the dynamic boundary condition (2.3b) in terms of the tangential velocity on $\partial\Omega(t)$. Taking the tangential derivative of (2.3b) gives

$$\frac{\partial\widetilde{\phi}}{\partial\tau} = -\frac{\partial\widehat{\phi}}{\partial\tau}, \qquad \mathbf{x}\in\partial\Omega(t), \tag{2.7}$$

i.e.

$$\widetilde{v}_\tau = -\widehat{v}_\tau, \qquad \mathbf{x}\in\partial\Omega(t). \tag{2.8}$$

Now let us turn our attention to the kinematic condition (2.3c). Since the normal

velocity on $\partial\Omega(t)$ must be continuous, we write (2.3c) as

$$V_n = v_n, \qquad \mathbf{x} \in \partial\Omega(t), \tag{2.9}$$

where the total normal fluid velocity is

$$v_n = \widetilde{v}_n + \widehat{v}_n, \qquad \mathbf{x} \in \partial\Omega(t). \tag{2.10}$$

Now we reformulate the field equation (2.3a) in terms of a complex contour integral. In order to do so, we first construct a complex function $F(z,t)$. The complex potential, an analytic function in $\Omega(t)$, for the regular part of the flow field can be defined as

$$\widetilde{w}(z,t) = \widetilde{\phi}(z,\bar{z},t) + i\widetilde{\psi}(z,\bar{z},t), \tag{2.11}$$

where $\widetilde{\psi}(x,y,t) \equiv \widetilde{\psi}(z,\bar{z},t)$ is the stream function and so $\partial\widetilde{w}/\partial z = \widetilde{u} - i\widetilde{v}$ is the conjugate complex velocity, which is also analytic in $\Omega(t)$. Since it is required that $\operatorname{div}(\widetilde{\mathbf{u}}) = \operatorname{div}(\nabla\widetilde{\phi}) = 0$, in terms of the function $\partial\widetilde{w}/\partial z$, we must have that

$$\oint_{\partial\Omega(t)} \frac{\partial\widetilde{w}}{\partial z}\,\mathrm{d}z = 0, \tag{2.12}$$

i.e. there are no residues in $\Omega(t)$. Now, let the function $F(z,t)$ in $\Omega(t)$ be defined as

$$F(z,t) \coloneqq \frac{\partial\widetilde{w}/\partial z}{z - z_m}, \tag{2.13}$$

where $z_m \in \Omega(t)$ and so $F(z,t)$ is a well-defined analytic function in $\Omega(t)$ except at the simple pole $z = z_m$. If $z_m \in \partial\Omega(t)$, considering the contour integral of $F(z,t)$ over $\partial\Omega(t)$, we have

$$\frac{1}{2i\pi}\oint_{\partial\Omega(t)} F(z,t)\,\mathrm{d}z = \frac{1}{2}\left.\frac{\partial\widetilde{w}}{\partial z}\right|_{z_m}, \tag{2.14}$$

by Cauchy's integral formula—see (2.1). Writing (2.14) explicitly in terms of $\widetilde{u}$ and

$\widetilde{v}$, we have

$$\oint_{\partial\Omega(t)} \frac{\widetilde{u} - i\widetilde{v}}{z - z_m}\,\mathrm{d}z = i\pi\,(\widetilde{u} - i\widetilde{v})|_{z_m}\,. \tag{2.15}$$

Equation (2.15) gives a direct relation between the regular part of the fluid velocity, $\widetilde{\mathbf{u}}$, and the geometry of the interface, $\partial\Omega(t)$. Since $\partial\Omega(t)$ can be parameterised w.r.t. arc length, s, (2.15) can be written as

$$\int_0^{L(t)} \frac{\widetilde{u}(s) - i\widetilde{v}(s)}{z(s) - z(s_m)}\frac{\mathrm{d}z}{\mathrm{d}s}\,\mathrm{d}s = i\pi\,(\widetilde{u} - i\widetilde{v})|_{s_m}\,, \tag{2.16}$$

where $0 < s_m < L(t)$ is such that $z_m = z(s_m)$, and the integral on the left hand side of (2.16) is a Cauchy principal value integral. We note that, on $\partial\Omega(t)$, we have the identity

$$\begin{aligned}(\widetilde{u} - i\widetilde{v})\frac{\mathrm{d}z}{\mathrm{d}s} &= (\widetilde{u} - i\widetilde{v})\left(\frac{\mathrm{d}x}{\mathrm{d}s} + i\frac{\mathrm{d}y}{\mathrm{d}s}\right)\\ &= \widetilde{u}\frac{\mathrm{d}x}{\mathrm{d}s} + \widetilde{v}\frac{\mathrm{d}y}{\mathrm{d}s} + i(\widetilde{u}\frac{\mathrm{d}y}{\mathrm{d}s} - \widetilde{v}\frac{\mathrm{d}x}{\mathrm{d}s})\\ &= \widetilde{\mathbf{u}}\cdot\boldsymbol{\tau} + i\widetilde{\mathbf{u}}\cdot\mathbf{n}\\ &= \widetilde{v}_\tau + i\widetilde{v}_n.\end{aligned} \tag{2.17}$$

Using (2.17) we can express (2.16) in terms of the tangential and normal velocity on the interface, i.e.

$$\int_0^{L(t)} \frac{\widetilde{v}_\tau(s) + i\widetilde{v}_n(s)}{z(s) - z(s_m)}\,\mathrm{d}s = i\pi\,(\widetilde{v}_\tau + i\widetilde{v}_n)\left(\frac{\mathrm{d}z}{\mathrm{d}s}\right)^{-1}\Bigg|_{s_m}. \tag{2.18}$$

Equations (2.8), (2.9) and (2.18) describe the Hele-Shaw free boundary problem. Since the free boundary $\partial\Omega(t)$ moves in the normal direction and is governed by the kinematic boundary condition (2.9), using the dynamic condition (2.8) along $\partial\Omega(t)$, we are able to solve (2.18) for $\widetilde{v}_n$. That is, direct substitution of (2.8) into (2.18)

yields

$$-\!\!\!\!\!\!\int_0^{L(t)} \frac{-\widehat{v}_\tau(s) + i\widetilde{v}_n(s)}{z(s) - z(s_m)}\,\mathrm{d}s = i\pi\,(-\widehat{v}_\tau + i\widetilde{v}_n)\left(\frac{\mathrm{d}z}{\mathrm{d}s}\right)^{-1}\Bigg|_{s_m}, \tag{2.19}$$

and re-arranging gives

$$\left.\frac{\mathrm{d}z}{\mathrm{d}s}\right|_{s_m} -\!\!\!\!\!\!\int_0^{L(t)} \frac{i\widetilde{v}_n(s)}{z(s) - z(s_m)}\,\mathrm{d}s + \pi\widetilde{v}_n(s_m) = r(s_m), \tag{2.20}$$

where the right hand side of (2.20) is given by

$$r(s_m) = \left.\frac{\mathrm{d}z}{\mathrm{d}s}\right|_{s_m} -\!\!\!\!\!\!\int_0^{L(t)} \frac{\widehat{v}_\tau(s)}{z(s) - z(s_m)}\,\mathrm{d}s - i\pi\widehat{v}_\tau(s_m). \tag{2.21}$$

Since $\widehat{v}_\tau$ is known on the interface, $r(s_m)$ is a known function on $\partial\Omega(t)$.

Given the background potential $\widehat{\phi}$, the tangential velocity, $\widehat{v}_\tau = \boldsymbol{\tau}\cdot\nabla\widehat{\phi}$, and normal velocity, $\widehat{v}_n = \mathbf{n}\cdot\nabla\widehat{\phi}$, are known on $\partial\Omega(t)$. For example, in the case of a point source we have $\widehat{\phi} = (Q_1/4\pi)\log\left[(x-x_1)^2 + (y-y_1)^2\right]$, then the background tangent and normal velocities on the interface are

$$\widehat{v}_\tau = \frac{Q_1}{2\pi}\frac{x_s(x-x_1) + y_s(y-y_1)}{(x-x_1)^2 + (y-y_1)^2} \tag{2.22a}$$

and

$$\widehat{v}_n = \frac{Q_1}{2\pi}\frac{y_s(x-x_1) - x_s(y-y_1)}{(x-x_1)^2 + (y-y_1)^2}, \tag{2.22b}$$

respectively, where the subscript s denotes differentiation w.r.t. arc length. Equation (2.20) can then be solved for $\widetilde{v}_n$, from which the normal velocity of $\partial\Omega(t)$, V_n, can be inferred since $V_n = \widetilde{v}_n + \widehat{v}_n$. Since $\partial\Omega(t)$ moves in the normal direction, the velocity of $\partial\Omega(t)$ in Cartesian coordinates is given by

$$\mathbf{V} = V_n\mathbf{n}, \qquad \mathbf{x} \in \partial\Omega(t), \tag{2.23}$$

and so $\partial\Omega(t)$ is advected according to the kinematic condition

$$\frac{\mathrm{d}\mathbf{x}}{\mathrm{d}t} = \mathbf{V}, \qquad \mathbf{x} \in \partial\Omega(t), \tag{2.24}$$

and the tangential velocity on $\partial\Omega(t)$ is zero.

This completes the formulation of the Hele-Shaw free boundary problem as a BIM, where the solution to the BIE (2.20) gives the unknown normal velocity on $\partial\Omega(t)$ at any instance t, where $\Omega(t)$ and $\widehat{\phi}(x, y, t)$ are given, and (2.24) allows $\partial\Omega(t)$ to be advected forwards in time.

2.3 Numerical procedure

The BIE (2.20) and (2.24) can be discretised in space and time which allows us to compute the evolution of $\partial\Omega(t)$ over time. Here we outline the numerical procedure in computing the interface at each time step. In what follows explicit time notation is suppressed for brevity. At time $t = t_j$, the numerical solution to the BIE (2.20) is considered when the interface $\partial\Omega$ has total arc length L. All quantities are taken at time t_j unless stated otherwise. On the interval $[0, L]$, $N+1$ equispaced mesh points are constructed such that

$$S_1 = 0, \tag{2.25a}$$

$$S_{i+1} = S_i + \Delta S, \quad i = 1, \ldots, N, \tag{2.25b}$$

where the mesh size is given by

$$\begin{aligned} \Delta S &= \frac{L}{N} \\ &= \frac{S_{N+1}}{N}, \end{aligned} \tag{2.26}$$

and N midpoints are defined as

$$S_{i+1/2} = S_i + \frac{\Delta S}{2}, \quad i = 1, \ldots, N. \tag{2.27}$$

The point s_m in (2.20) and (2.21) is chosen to coincide with $S_{m+1/2}$—see figure 2.2.

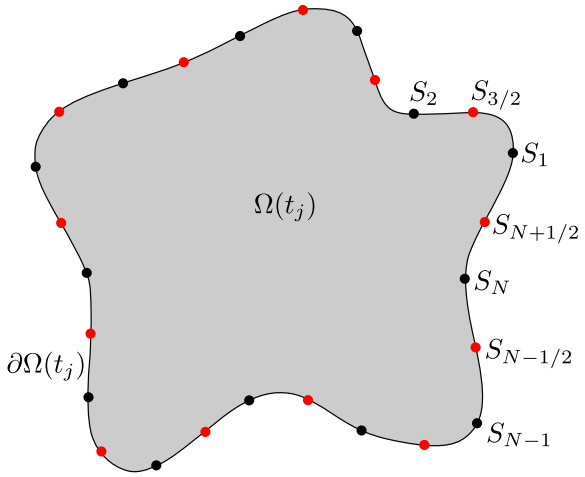

Figure 2.2: Discretisation of the interface $\partial\Omega$ at time $t = t_j$, displaying both mesh points and midpoints given by (2.25) and (2.27), respectively.

New variables for the discretisation of $\partial\Omega$ are defined as

$$Z_i = z(S_i), \quad i = 1, \ldots, N+1, \tag{2.28}$$

and the unknown quantities to be found are

$$\alpha_i = \widetilde{v}_n(S_i), \quad i = 1, \ldots, N+1. \tag{2.29}$$

The periodic conditions

$$Z_{N+1} = Z_1, \tag{2.30a}$$

and

$$\alpha_{N+1} = \alpha_1, \tag{2.30b}$$

hold since $\partial\Omega$ is assumed to be a simple closed contour at each time step. Let the right hand side of (2.21) be discretised such that $R_i = r(S_{i+1/2})$. The value of $z(s_m) = z(S_{i+1/2}) = Z_{i+1/2}$ are found via a four point formula given by

$$Z_{i+1/2} = \frac{1}{16}\left(-Z_{i-1} + 9Z_i + 9Z_{i+1} - Z_{i+2}\right). \tag{2.31}$$

The quantity $\widetilde{v}_n(S_{i+1/2}) = \alpha_{i+1/2}$ is approximated linearly between neighbouring points on $\partial\Omega$ for $i = 1, \ldots, N$, i.e.

$$\alpha_{i+1/2} = \frac{1}{Z_{i+1} - Z_i} \left[\left(Z_{i+1} - Z_{i+1/2} \right) \alpha_i + \left(Z_{i+1/2} - Z_i \right) \alpha_{i+1} \right]. \tag{2.32}$$

The integrals in (2.20) and (2.21) are approximated using the trapezium rule. Since the singular points, s_i, are taken to coincide with the midpoints of the mesh, $S_{i+1/2}$, the integral is evaluated by ignoring the singularities[3] with an accuracy no less than that of a non-singular integral [8, 146]. Taking into account the periodicity on the interface, the integral is approximated as

$$\int_0^L \frac{i\widetilde{v}_n(s)}{z(s) - z(s_m)} \, \mathrm{d}s \approx \sum_{j=1}^{N} \frac{i\alpha_j}{Z_j - Z_{m+1/2}} \Delta S, \quad m = 1, \ldots, N. \tag{2.33}$$

Baker [8] gives the approximation to the integrand of the type given in (2.1), as s approaches s_m, to be (after making the change of variable from z to s)

$$\frac{f(s) z_s(s)}{z(s) - z(s_m)} = \frac{f(s_m)}{|s - s_m|} + f_s(s_m) + \frac{f(s_m)(z_m)_{ss}}{2(z_m)_s} + \mathcal{O}(|s - s_m|), \tag{2.34}$$

where here the subscript s denotes differentiation. Considering the integral over the k-th (singular) panel of the integrand of type given above (under an equispaced discretisation), then approximation by the trapezium rule gives

$$\begin{aligned} I_k &= \int_{S_k}^{S_{k+1}} \frac{f(s) z_s(s)}{z(s) - z(S_{k+1/2})} \, \mathrm{d}s \\ &\approx \frac{1}{2} \left[\frac{f(S_k) z_s(S_k)}{z(S_k) - z(S_{k+1/2})} + \frac{f(S_{k+1}) z_s(S_{k+1})}{z(S_{k+1}) - z(S_{k+1/2})} \right] \Delta S. \end{aligned} \tag{2.35}$$

Since $S_k = S_{k+1/2} - \Delta S/2$ and $S_{k+1} = S_{k+1/2} + \Delta S/2$, expanding the first term in

[3] For supplementary discussion on the evaluation of integrals by ignoring singularities, specifically for Cauchy principal value integrals, the reader is directed to the book by Davis and Rabinowitz [31, pp.180–187].

the brackets on the right hand side about $S_{k+1/2}$ yields

$$\frac{f(S_k)z_s(S_k)}{z(S_k)-z(S_{k+1/2})} = \frac{f(S_{k+1/2})}{\Delta S/2} + f_s(S_{k+1/2}) + \frac{f(S_{k+1/2})z_{ss}(S_{k+1/2})}{2z_s(S_{k+1/2})} + \mathcal{O}(\Delta S), \quad (2.36)$$

hence, expanding the second term in a similar way, the integral I_k is approximated as

$$I_k \approx \Delta S \left[f_s(S_{k+1/2}) + \frac{f(S_{k+1/2})z_{ss}(S_{k+1/2})}{2z_s(S_{k+1/2})} \right]. \quad (2.37)$$

That is, the trapezium rule on the equispaced mesh takes into account the 'error' in the terms enclosed by square brackets in (2.35), in approximating the integrand close to the singularity, so the approximation can be made in the same way as for a non-singular integrand. Therefore, the discretisation and quadrature in (2.33) gives a good approximation, where the integrand is singular at $z = z_m$, i.e. the accuracy of the approximation is the same as a non-singular integral, and in this case is $\mathcal{O}((\Delta S)^2)$ accurate. This also applies to the integral in (2.21).

The derivatives in (2.21), i.e. $z_s(s_m)$, are approximated via a four point average of the fourth order centred finite difference approximation of $z_s(s)$, i.e.

$$\frac{\mathrm{d}}{\mathrm{d}s} Z_i \approx \frac{1}{12\Delta S} \left(Z_{i-2} - 8Z_{i-1} + 8Z_{i+1} - Z_{i+2} \right), \quad (2.38a)$$

and

$$\frac{\mathrm{d}}{\mathrm{d}s} Z_{i+1/2} \approx \frac{1}{16} \left(-\frac{\mathrm{d}Z_{i-1}}{\mathrm{d}s} + 9\frac{\mathrm{d}Z_i}{\mathrm{d}s} + 9\frac{\mathrm{d}Z_{i+1}}{\mathrm{d}s} - \frac{\mathrm{d}Z_{i+2}}{\mathrm{d}s} \right). \quad (2.38b)$$

Thus, employing (2.32) and (2.33) in (2.21), and taking the real part, gives a system of N linear algebraic equations for the unknown α_i, for $i = 1, \ldots, N$, which can be written in matrix form as

$$\boldsymbol{M}\boldsymbol{\alpha} = \mathbf{R}. \quad (2.39)$$

The matrix equation (2.39) is solved, giving the normal velocity (the vector $\boldsymbol{\alpha}$) of

fluid particles on $\partial\Omega$ coinciding with the mesh at time $t = t_j$.

Net flux across $\partial\Omega(t)$ is zero for all time. Therefore, the solution $\boldsymbol{\alpha}$ can be purged at each time step following the method given by Kelly and Hinch [68], where we set

$$\begin{aligned} \alpha_i &= \alpha_i - \left(\oint_{\partial\Omega} \widetilde{v}_n(s)\,\mathrm{d}s\right) \Big/ \left(\oint_{\partial\Omega} \mathrm{d}s\right) \\ &\approx \alpha_i - \frac{1}{N}\sum_{j=1}^{N} \alpha_j, \end{aligned} \tag{2.40}$$

for $i = 1, \ldots, N$, since the mesh points on $\partial\Omega$ are equispaced. Largely, the use of (2.40) has little effect since the solution to (2.39) conserves mass to a good approximation[4].

It remains to compute the evolution of $\partial\Omega$ in time given the vector $\boldsymbol{\alpha}$. The evolution can be approximated at the following time step, $t_{j+1} = t_j + \Delta t$, as

$$\begin{aligned} z(S_i(t_j + \Delta t), t_j + \Delta t) &\approx z(S_i, t_j) + \Delta t \left[\frac{\partial z}{\partial s}(S_i, t_j)\frac{\mathrm{d}S_i}{\mathrm{d}t} + \frac{\partial z}{\partial t}(S_i, t_j)\right] \\ &= z(S_i, t_j) + \Delta t \frac{\mathrm{d}z}{\mathrm{d}t}(S_i, t_j), \end{aligned} \tag{2.41}$$

where $\dot{z}$ is the complex velocity of the interface. Since (2.3c) must be satisfied, and the interface evolves according to its normal velocity, the normal interface velocity V_n is constructed from the total normal fluid velocity, i.e. $V_n(S_i, t_j) = \widetilde{v}_n(S_i, t_j) + \widehat{v}_n(S_i, t_j)$. This normal interface velocity is resolved into the x and y components of the Cartesian coordinate system as $\mathcal{U}(S_i, t_j) = \Im\{V_n(S_i, t)\mathrm{d}Z_i/\mathrm{d}s\}$ and $\mathcal{V}(S_i, t_j) = -\Re\{V_n(S_i, t)\mathrm{d}Z_i/\mathrm{d}s\}$, respectively. The mesh points $Z_i = z(S_i, t) \in \partial\Omega$ can be treated as Lagrangian particles and (2.41) is written in the form

$$\Re(Z_i^{\text{new}}) = \Re(Z_i) + \mathcal{U}(S_i, t_j)\Delta t, \quad i = 1, \ldots, N, \tag{2.42}$$

$$\Im(Z_i^{\text{new}}) = \Im(Z_i) + \mathcal{V}(S_i, t_j)\Delta t, \quad i = 1, \ldots, N, \tag{2.43}$$

[4]In appendix E, an argument for an observed constant error in approximating (2.21), in particular $\widehat{v}_\tau(s)$, and the effect on the solution $\widetilde{v}_n(s)$ is given, where the use of (2.40) is highlighted in the study of translating bubbles in chapter 4.

where $Z_i^{\text{new}} \in \partial\Omega^{\text{new}}$, which is the new position of the interface $\partial\Omega$ at $t = t_j + \Delta t$. A modified Euler (i.e. a second order Runge-Kutta) method is employed, as in [8], such that the time stepping method is approximately $\mathcal{O}((\Delta t)^2)$ accurate.

Once $\partial\Omega^{\text{new}}$ is found, the new total arc length L^{new} is computed from the mesh points Z_i^{new}, $i = 1, \ldots, N+1$, which are then redistributed to an equispaced mesh by cubic spline interpolation. Setting $Z_i = Z_i^{\text{new}}$ (i.e. $\partial\Omega = \partial\Omega^{\text{new}}$ and $L = L^{\text{new}}$) and applying the above procedure again completes the algorithm for computing the interface at later times. Since the time stepping procedure is explicit in time, a stability constraint applies in the form $\Delta t \leq c(\Delta S)^n$, for some positive numbers c and n [14].

2.3.1 Computing elements of the resulting matrix equation

By discretising the interface w.r.t. arc length, the BIE (2.20) can be approximated using a combination of a linear approximation for the value of the solution at the midpoint, (2.32), and the trapezium rule for the Cauchy principal value integral, (2.33). According to these approximations, when the problem is written in matrix form (2.39), the elements of the matrix $\boldsymbol{M}$ are given by

$$M_{jk} = \frac{i\Delta S}{Z_k - Z_{j+1/2}} \frac{\mathrm{d}}{\mathrm{d}s} Z_{j+1/2}, \qquad k \neq j,\ k \neq j+1, \tag{2.44a}$$

$$M_{jk} = \frac{i\Delta S}{Z_k - Z_{j+1/2}} \frac{\mathrm{d}}{\mathrm{d}s} Z_{j+1/2} + \frac{Z_{j+1} - Z_{j+1/2}}{Z_{j+1} - Z_j}, \qquad k = j, \tag{2.44b}$$

$$M_{jk} = \frac{i\Delta S}{Z_k - Z_{j+1/2}} \frac{\mathrm{d}}{\mathrm{d}s} Z_{j+1/2} + \frac{Z_{j+1/2} - Z_j}{Z_{j+1} - Z_j}, \qquad k = j+1, \tag{2.44c}$$

for $j = 1, \ldots, N-1$, $k = 1, \ldots, N$, and when $j = N$

$$M_{Nk} = \frac{i\Delta S}{Z_k - Z_{N+1/2}} \frac{\mathrm{d}}{\mathrm{d}s} Z_{N+1/2}, \qquad k = 2, \ldots, N-1, \tag{2.45a}$$

$$M_{Nk} = \frac{i\Delta S}{Z_k - Z_{N+1/2}} \frac{\mathrm{d}}{\mathrm{d}s} Z_{N+1/2} + \frac{Z_1 - Z_{N+1/2}}{Z_1 - Z_N}, \qquad k = N, \tag{2.45b}$$

$$M_{Nk} = \frac{i\Delta S}{Z_k - Z_{N+1/2}} \frac{\mathrm{d}}{\mathrm{d}s} Z_{N+1/2} + \frac{Z_{N+1/2} - Z_N}{Z_1 - Z_N}, \qquad k = 1, \tag{2.45c}$$

due to the periodic conditions (2.30). The right hand side of the matrix system is given by

$$R_j = -i\pi \widehat{v}_\tau(S_{j+1/2}) + \sum_{k=1}^{N} \frac{\widehat{v}_\tau(S_k)}{Z_k - Z_{j+1/2}} \Delta S, \tag{2.46}$$

where $\widehat{v}_\tau(S_i)$ and $\widehat{v}_\tau(S_{i+1/2})$ are known quantities when given the background potential $\widehat{\phi}$. For example, when the interface is driven by a point source the background tangential velocity in discrete form is

$$\widehat{v}_\tau(S_i) = \frac{Q_1}{2\pi} \frac{\Re\{(\mathrm{d}Z_i/\mathrm{d}s)\overline{(Z_i - z_1)}\}}{|Z_i - z_1|^2}, \tag{2.47}$$

where $z_1 \in \Omega(t) \setminus \partial\Omega(t)$ and Q_1 denote the location of the point source and strength, respectively.

2.4 Numerical instability of the discretised equations

Many authors have employed BIEs to solve a range of 2D fluid dynamic problems where numerical instabilities due to 'round off error' are a common occurrence, see e.g. [1, 14, 76, 85]. These errors, usually referred to as 'spurious oscillations' in the literature, in most cases arise when a solution to a discretised integral equation, similar to the form presented here, is required. Since the free boundary problem is physically ill-posed (e.g. in the case of a point sink, i.e. when $Q_1 < 0$) and is unregularised (ZST), and the solution to a singular integral equation is required for a temporal problem, it is difficult to distinguish the underlying cause of numerical

oscillations to the solution of (2.39). In the present work, it was noted that errors in the solution were largely due to the discretisation of the integral equation and similar to those reported previously, see e.g. [1, 71, 85].

The solution to the BIE (2.20) at each 'evaluation point', $z(s_m)$, governs the function $\widetilde{v}_n(s)$ on the interface and requires a solution satisfying an integral over the entire interface, $\partial\Omega$. The integral equation is discretised and the points s_m are chosen to coincide with the midpoints of the equispaced mesh on $\partial\Omega$. This gives rise to numerical instabilities if one was to solve the discretised problem, i.e. (2.39), directly. This can be seen by investigating more closely the discretisation of the integral equation (2.20). In matrix form, this equation becomes (2.39). The matrix $\boldsymbol{M}$ is the discretisation of an effective linear operator. The vector $\boldsymbol{\alpha}$ is the desired solution, i.e. $\alpha_i = \widetilde{v}_n(S_i)$ and $\mathbf{R}$ the approximation of $r(S_{i+\frac{1}{2}})$, given in (2.21), i.e. the right hand side of (2.20).

Following the analysis of Phillips [109] and Twomey [144] on the discretisation of integral equations, the right hand side of (2.20), i.e. (2.21), can strictly be written (at the discrete midpoints) as $\mathbf{r} = \mathbf{R} + \mathbf{e}$ where $\mathbf{e}$ represents the error in approximating $r(S_{i+\frac{1}{2}})$, and so the discretised integral equation in matrix form can be written as

$$\boldsymbol{M}\boldsymbol{\alpha} = \mathbf{R} + \mathbf{e}. \tag{2.48}$$

Phillips [109] shows that if a smooth solution is superimposed with some undulations, then the resulting superposition will also satisfy the integral equation. Similar arguments can be applied to the discrete equation (2.39). The undulations of the solution occur in the discretised problem as a result of the errors in approximating $r(S_{i+\frac{1}{2}})$, i.e. in calculating $\mathbf{r}$, giving rise to an oscillatory solution to $\boldsymbol{\alpha}$.

Phillips [109] suggests a method to solve (2.48) by introducing a minimisation problem for the integral of the square of the second derivative of the solution $\widetilde{v}_n(s)$, since the solution $\widetilde{v}_n$ of the BIE (2.20) is assumed to be smooth. That is, it is

assumed the function does not undergo sudden change in gradient, a good assumption for the physical quantity of normal velocity on a smooth continuous interface, $\partial\Omega$. Otherwise, oscillatory solutions are valid for (2.48) and so some knowledge from a physical aspect should be applied. In the method proposed by Phillips [109], the inversion of two matrices is required in finding the smooth solution solving (2.39). However, Twomey [144] suggests an improvement where only one matrix inversion is necessary. This method is described below.

The discrete matrix equation (2.48) can be written as

$$\sum_{k=1}^{N} M_{jk}\alpha_k = R_j + e_j, \tag{2.49}$$

where M_{jk} are given by (2.44)–(2.45). The quantity to be minimised, chosen here to be

$$\int_0^L \left(\frac{\partial^2 \widetilde{v}_n}{\partial s^2}\right)^2 \mathrm{d}s, \tag{2.50}$$

can be written in discrete form (see e.g. [109]) as

$$\sum_{k=1}^{N}(\alpha_{k-1} - 2\alpha_k + \alpha_{k+1})^2, \tag{2.51}$$

and an equation for the square of the errors can be written as

$$\sum_{k=1}^{N} e_k^2 = \varepsilon^2. \tag{2.52}$$

Therefore, a function H can be constructed, given by

$$H = \sum_{k=1}^{N}(\alpha_{k-1} - 2\alpha_k + \alpha_{k+1})^2 + \gamma\left(\sum_{k=1}^{N} e_k^2 - \varepsilon^2\right), \tag{2.53}$$

where γ is known as the Lagrange multiplier. From (2.48) it can be seen that e_j is

a linear function of the unknown discrete solution α_k, and so

$$\frac{\partial e_k}{\partial \alpha_j} = M_{kj}. \tag{2.54}$$

Hence, differentiating H with respect to α_j, critical points are given by the solutions to the set of linear equations

$$0 = \sum_{k=1}^{N} (\alpha_{k-2} - 4\alpha_{k-1} + 6\alpha_k - 4\alpha_{k+1} + \alpha_{k+2}) + \gamma M_{kj} e_k, \tag{2.55}$$

which in matrix form is written as

$$\mathbf{0} = \boldsymbol{H}\boldsymbol{\alpha} + \gamma \boldsymbol{M}^\top \mathbf{e}, \tag{2.56}$$

where $\boldsymbol{H}$ is the matrix representation of a third order difference operator [144]. Eliminating $\mathbf{e}$ between (2.56) and (2.48) gives

$$(\boldsymbol{M}^\top \boldsymbol{M} + \gamma^{-1} \boldsymbol{H})\boldsymbol{\alpha} = \boldsymbol{M}^\top \mathbf{R}. \tag{2.57}$$

From (2.56) it is clear that the errors $\mathbf{e}$ and the smoothness of the solution $\boldsymbol{\alpha}$ depend on the parameter γ. Therefore, γ serves as a smoothing parameter, where, given different estimates to the error $\mathbf{e}$, γ should be chosen such that the solution is sufficiently smooth [109]. That is, we solve for the smooth solution, $\boldsymbol{\alpha}$, where γ is known (chosen) and error $\mathbf{e}$ is unknown. It is expected that $e_k = \mathcal{O}((\Delta S)^P)$, $k = 1, \ldots, N$, where $P \geq 1$ is a positive integer denoting the order of spacial error arising from the approximations (2.32) and (2.33). For example, we expect error of $\mathcal{O}((\Delta S)^3)$ for trapezium rule approximation on a periodic domain and error of $\mathcal{O}((\Delta S)^4)$ arising from the centred finite difference formula (2.38a) employed for approximating derivatives. Thus, for non-zero, finite value of γ, inverting the matrix on the left hand side

of (2.57), the desired approximate smooth solution to (2.20) is given by

$$\alpha = (\boldsymbol{M}^\top \boldsymbol{M} + \gamma^{-1}\boldsymbol{H})^{-1}\boldsymbol{M}^\top \mathbf{R}, \tag{2.58}$$

where usually decreasing values of γ increases the smoothing effect on the solution. In general $0 < \gamma < \infty$ and (2.57) gives a sufficiently accurate solution compared with an otherwise oscillatory solution from (2.39). The filtering technique employed here is analogous to that of spectral methods, e.g. [14], where the Fourier series is truncated and modes of the high frequency, small amplitude oscillations are neglected. The affects of the filtering technique on the discrete solution are displayed in figure 2.8(a) in example 2.7.1 on page 97.

Since the discrete solution to the BIE (2.20) is susceptible to oscillatory solutions through errors in approximating the right hand side, i.e. $r(S_{i+1/2})$, these errors may grow in time as the interface evolves. Aitchison and Howison [1] have reported on the growth of errors in solutions to Hele-Shaw free boundary problems, where a boundary integral method is employed. They show that the growth rate of numerical errors over time are related to the local linear stability of the interface, given by Saffman and Taylor [123]. In [123] it is shown that a fluid penetrating a more viscous fluid is physically unstable and that the growth rate of the physical instability increases with shorter wave length disturbances on the interface.

Aitchison and Howison [1] make a note on the introduction of small wave length instabilities into the solution of the numerical problem as a result of rounding errors and approximate solution techniques. The difficulty being, the more mesh points that are included (i.e. increasing N), shorter wavelength errors are permitted which grow fastest with time. However, in [1], the cause of the errors from the approximations and their oscillatory nature are not elaborated. These have been addressed above, specifically for the BIE (2.20), and the frequency of the oscillations in the error scale with N, as expected. Since these oscillatory errors grow rapidly in time, the solution

requires filtering. Filtering is carried out at each time step by solving the modified matrix equation (2.57), in which a sufficiently smooth solution is required to the physical problem. Since this filtering process is coupled with the numerical solution to the physical problem, it provides a better approximation to the solution than the filtering technique which was employed previously during this research and is recorded in [71], where the solution may be susceptible to 'unwanted' smoothing or changes, e.g. in areas where curvature of the interface may vary rapidly[5].

The filtering technique presented in this section provides a regularisation such that solutions to the ZST Hele-Shaw free boundary problem can be computed numerically. This filtering technique may be akin to the limit of vanishing surface tension in the sense that it provides a regularisation effect. However, instead of introducing surface tension we impose directly smoothness of the solution by an appropriate filter, i.e. here we have a mathematical requirement as apposed to the physical imposition of, for example, a surface tension condition on the interface.

2.5 Including external potential fields

When the fluid flow is subject to an external potential field, $\Psi(x, y, t)$, the Hele-Shaw free boundary problem can be written in the form

$$\nabla^2 \phi = 0, \qquad \mathbf{x} \in \Omega(t), \tag{2.59a}$$

$$\phi = \Psi, \qquad \mathbf{x} \in \partial\Omega(t), \tag{2.59b}$$

$$v_n = \frac{\partial \phi}{\partial n}, \qquad \mathbf{x} \in \partial\Omega(t), \tag{2.59c}$$

[5]In the article published in the *European Journal of Applied Mathematics* as part of this research—see [71]—a rudimentary matrix system is solved to calculate the velocity of fluid particles on the interface, where the background potential is *not* decomposed, as suggested in section 2.2.1. The filtering technique employed there is similar to the filtering technique suggested by Longuet-Higgins and Cokelet [85], where the desired effect is similar, but not as robust as the filtering technique suggested in this section.

where $\phi(x,y,t) \equiv \phi(z,\bar{z},t)$ and $\Psi(x,y,t) \equiv \Psi(z,\bar{z},t)$ are scalar potential functions—c.f. appendix B. Decomposing the velocity potential ϕ as in section 2.2.1, the free boundary problem in terms of $\widetilde{\phi}(x,y,t) \equiv \widetilde{\phi}(z,\bar{z},t)$ becomes

$$\nabla^2 \widetilde{\phi} = 0, \qquad \mathbf{x} \in \Omega(t), \tag{2.60a}$$

$$\widetilde{\phi} = \Psi - \widehat{\phi}, \qquad \mathbf{x} \in \partial\Omega(t), \tag{2.60b}$$

$$v_n = \frac{\partial}{\partial n}\left(\widetilde{\phi} + \widehat{\phi}\right), \qquad \mathbf{x} \in \partial\Omega(t), \tag{2.60c}$$

where $\Psi(x,y,t)$ and $\widehat{\phi}(x,y,t)$ are known functions on $\partial\Omega(t)$. Taking the tangential derivative of (2.60b) along $\partial\Omega(t)$, the dynamic boundary condition (2.8), in the case of applied external fields, becomes

$$\widetilde{v}_\tau = \Psi_\tau - \widehat{v}_\tau, \qquad \mathbf{x} \in \partial\Omega(t), \tag{2.61}$$

where $\Psi_\tau = \partial\Psi/\partial\tau = \boldsymbol{\tau}\cdot\nabla\Psi$. Hence, the BIE (2.20), for a fluid blob, becomes

$$\left.\frac{\mathrm{d}z}{\mathrm{d}s}\right|_{s_m} \fint_0^{L(t)} \frac{i\widetilde{v}_n(s)}{z(s)-z(s_m)}\,\mathrm{d}s + \pi\widetilde{v}_n(s_m) = - \left.\frac{\mathrm{d}z}{\mathrm{d}s}\right|_{s_m} \fint_0^{L(t)} \frac{\Psi_\tau(s)-\widehat{v}_\tau(s)}{z(s)-z(s_m)}\,\mathrm{d}s + i\pi\left[\Psi_\tau(s_m)-\widehat{v}_\tau(s_m)\right]. \tag{2.62}$$

Equation (2.62) can be discretised and solved numerically in a similar manner to that presented in sections 2.3 and 2.4—see example 2.7.3, where (2.62) is employed and the interface is driven solely by an external potential field.

2.6 A boundary integral formulation for a finite bubble in an unbounded Hele-Shaw cell

Here, the BIE in the case of a bubble surrounded by a viscous fluid of infinite extent is derived. First we assume that the viscous fluid domain, $\Omega(t)$, is of finite extent, extending from the interface of the bubble to a circular contour of radius R, say, centred at the origin (we can take the origin to coincide with the centre of mass of the bubble region w.l.o.g.). Let the bubble interface be given by a simple closed contour, $\partial\Omega(t)$. Taking the usual convention of fluid lying towards the left of the contour defining the interface (as described in section 2.2.2) implies $\partial\Omega(t)$ should be traversed in the clockwise direction—see figure 2.3. Therefore, the outer contour, which we denote by Γ_R, is a circle of radius R, traversed in the anticlockwise direction and $\Omega(t)$ is bounded by the two curves $\partial\Omega(t)$ and Γ_R. In this case, taking the definition of the normal and tangent on $\partial\Omega(t)$ as in (2.4a) and (2.4b), respectively, then the normal vector on $\partial\Omega(t)$ points in to the bubble region. If the pressure on the exterior of Γ_R is taken to be the same as the pressure in the bubble, i.e. $\phi = 0$, then (2.3) hold with the additional conditions

$$\phi = 0, \qquad \mathbf{x} \in \Gamma_R, \tag{2.63a}$$

$$V_{\Gamma n} = \frac{\partial}{\partial n}(\widehat{\phi} + \widetilde{\phi}), \qquad \mathbf{x} \in \Gamma_R, \tag{2.63b}$$

where $V_{\Gamma n}$ is the normal velocity of the interface marked by Γ_R.

Here, the velocity field due to $\widetilde{\phi}$, i.e. $\widetilde{\mathbf{u}}$, is still a solenoidal vector field and so $\mathrm{div}(\widetilde{\mathbf{u}}) = 0$ still holds over $\Omega(t)$. This implies that if $z = z_m \in \Omega(t)$, the function $F(z)$ defined in (2.13) is analytic everywhere in $\Omega(t)$ except at the simple pole $z = z_m$.

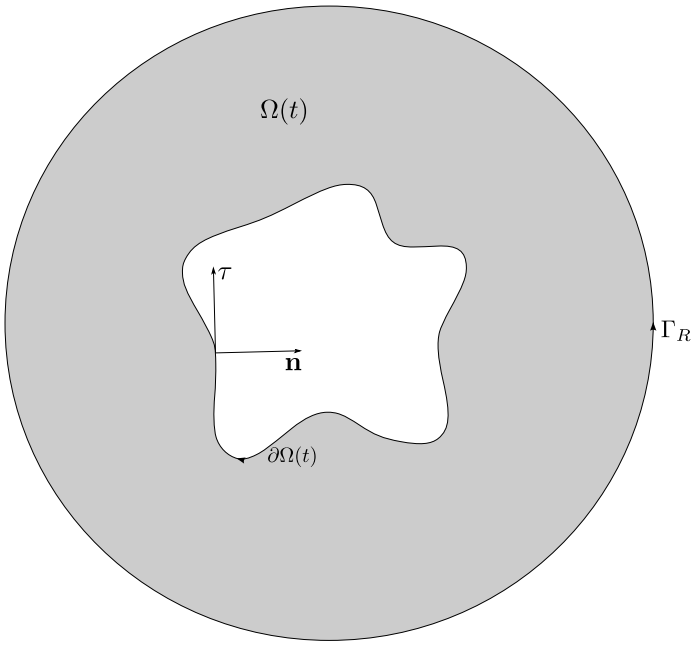

Figure 2.3: A bubble in a Hele-Shaw cell surrounded by a finite fluid region, $\Omega(t)$, which is bounded by the curves $\partial\Omega(t)$ and Γ_R. The normal and tangential vectors along $\partial\Omega(t)$ are displayed.

Let $z = z_A$ and $z = z_B$ be two points lying on $\partial\Omega(t)$ and Γ_R, respectively, and let the arc $z_A z_B$ be a straight path between z_A and z_B with positive sign, in $\Omega(t)$, as shown in figure 2.4. Following the above statement with $z_m \in \Omega(t)$, then

$$\begin{aligned}
\left.\frac{\partial \widetilde{w}}{\partial z}\right|_{z_m} &= \left(\int_{z_A z_B} + \oint_{\Gamma_R} + \int_{z_B z_A} + \oint_{\partial\Omega(t)}\right) F(z,t)\,\mathrm{d}z \\
&= \left(\int_{z_A z_B} + \oint_{\Gamma_R} - \int_{z_A z_B} + \oint_{\partial\Omega(t)}\right) F(z,t)\,\mathrm{d}z \\
&= \left(\oint_{\Gamma_R} + \oint_{\partial\Omega(t)}\right) F(z,t)\,\mathrm{d}z
\end{aligned} \tag{2.64}$$

must hold.

It can be assumed that the contour integral around Γ_R of $F(z,t)$ is equal to zero for sufficiently rapidly decaying $F(z,t)$ as $z \to \infty$. This is true for $F(z,t)$ as defined in (2.13) since it is a function of the 'residual' field, i.e. $\widetilde{u} - i\widetilde{v}$, which exhibits no singularities in $\Omega(t)$. Hence, taking the limit $R \to \infty$, in the case of an unbounded Hele-Shaw cell—see figure 2.5(a)—where $\Omega(t)$ is of infinite extent, and

letting $z_m \in \partial\Omega(t)$, (2.64) becomes

$$\oint_{\partial\Omega(t)} F(z,t)\,\mathrm{d}z = \frac{1}{2}\left.\frac{\partial\widetilde{w}}{\partial z}\right|_{z_m}, \tag{2.65}$$

i.e.

$$\frac{1}{2i\pi}\oint_{\partial\Omega(t)} \frac{\widetilde{u}(z) - i\widetilde{v}(z)}{z - z_m}\,\mathrm{d}z = \left.\frac{\widetilde{u} - i\widetilde{v}}{2}\right|_{z_m}. \tag{2.66}$$

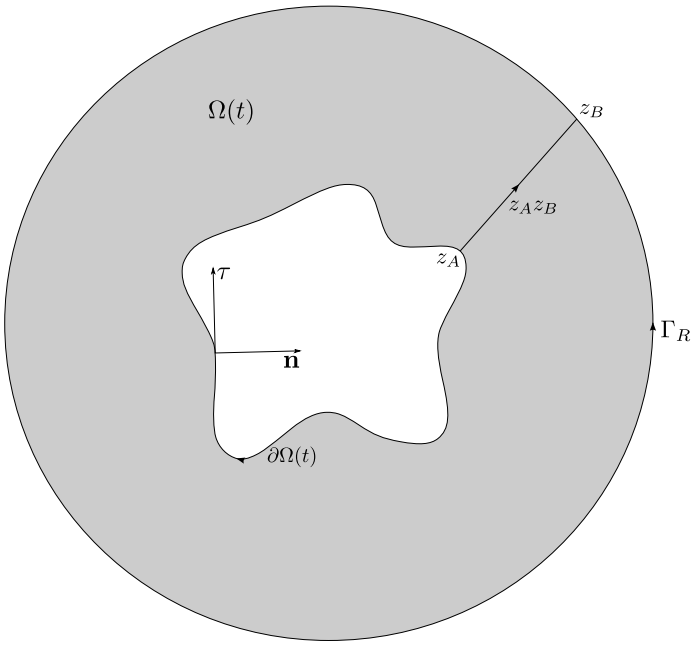

Figure 2.4: Choice of contours taken in the calculation of the integral in (2.64), where the orientation is displayed along each contour.

Now suppose that we traverse the contours in figure 2.4 in the opposite direction, i.e. considering $\partial\Omega(t) \cup z_A z_B \cup \Gamma_R \cup z_B z_A$ to be a simple closed curve in $\mathbb{C}$ traversed in the clockwise direction, and if $z_m \in \Omega(t)$, then (2.64) becomes

$$\left(\oint_{\Gamma_R} + \oint_{\partial\Omega(t)}\right) F(z,t)\,\mathrm{d}z = -\left.\frac{\partial\widetilde{w}}{\partial z}\right|_{z_m}. \tag{2.67}$$

Therefore, changing the orientation of the contour describing the bubble from clockwise in figure 2.5(a) to anticlockwise as in figure 2.5(b), in the unbounded Hele-Shaw

cell, and letting $z_m \in \partial\Omega(t)$, the equation that must hold on $\partial\Omega(t)$ reads

$$\frac{1}{2i\pi}\oint_{\partial\Omega(t)} \frac{\widetilde{u} - i\widetilde{v}}{z - z_m}\,\mathrm{d}z = -\left.\frac{\widetilde{u} - i\widetilde{v}}{2}\right|_{z_m}. \tag{2.68}$$

Since the vectors $\mathbf{n}$ and $\boldsymbol{\tau}$ are defined in (2.4a) and (2.4b) and are thus given by the choice of parameterisation, i.e. the direction in which $\partial\Omega(t)$ is traversed, in terms of the tangential and normal velocities on $\partial\Omega(t)$, (2.68) becomes

$$\frac{1}{2i\pi}\int_0^{L(t)} \frac{\widetilde{v}_\tau(s) + i\widetilde{v}_n(s)}{z(s) - z(s_m)}\,\mathrm{d}s = -\left.\frac{\widetilde{v}_\tau + i\widetilde{v}_n}{2}\left(\frac{\mathrm{d}z}{\mathrm{d}s}\right)^{-1}\right|_{s_m}. \tag{2.69}$$

Using the dynamic boundary condition (2.8), (2.69) can be written as

$$\left.\frac{\mathrm{d}z}{\mathrm{d}s}\right|_{s_m}\int_0^{L(t)} \frac{-\widehat{v}_\tau(s) + i\widetilde{v}_n(s)}{z(s) - z(s_m)}\,\mathrm{d}s = -i\pi\,\left(-\widehat{v}_\tau + i\widetilde{v}_n\right)|_{s_m}, \tag{2.70}$$

and re-arranging gives

$$\left.\frac{\mathrm{d}z}{\mathrm{d}s}\right|_{s_m}\int_0^{L(t)} \frac{i\widetilde{v}_n(s)}{z(s) - z(s_m)}\,\mathrm{d}s - \pi\widetilde{v}_n(s_m) = \left.\frac{\mathrm{d}z}{\mathrm{d}s}\right|_{s_m}\int_0^{L(t)} \frac{\widehat{v}_\tau(s)}{z(s) - z(s_m)}\,\mathrm{d}s + i\pi\widehat{v}_\tau(s_m). \tag{2.71}$$

Equation (2.71) is the BIE equation for a bubble in an unbounded Hele-Shaw, which differs from the BIE equation for the case of a fluid blob by a crucial change in sign—c.f. (2.20).

The BIE (2.71) can be approximated via the approximations (2.32) and (2.33), and therefore can be written in matrix form (2.39), which can be solved in the form according to (2.58) giving a smooth solution.

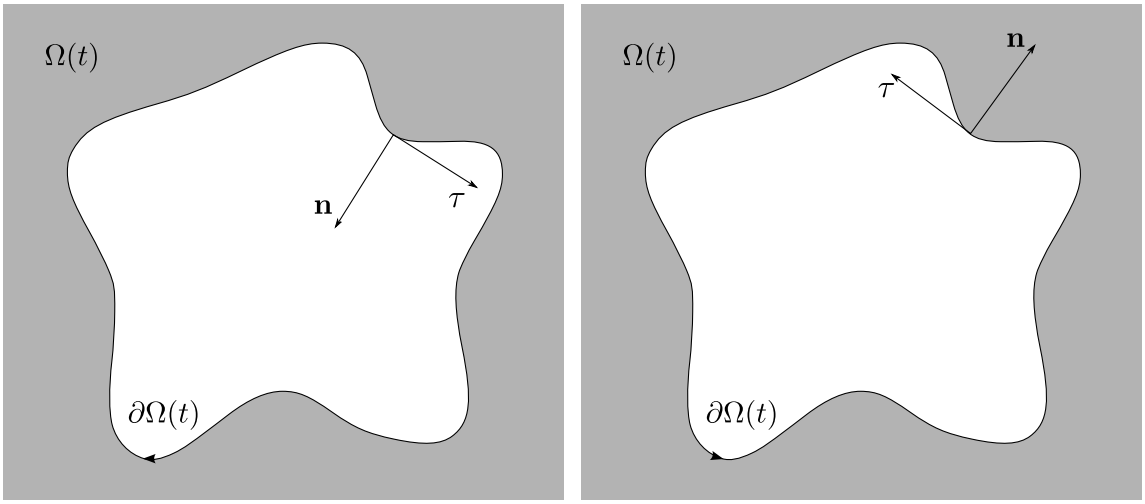

(a) (b)

Figure 2.5: A bubble in an unbounded Hele-Shaw cell with interface $\partial\Omega(t)$ traversed in the clockwise direction in (a) and anticlockwise direction in (b). Displaying the direction of the normal and tangential vectors along $\partial\Omega(t)$ as defined by (2.4a) and (2.4b), respectively.

2.7 Testing and results

The numerical method outlined above was tested against some exact, known solutions of the Hele-Shaw flow problem. These include the growth of finite fluid blobs by hydrodynamic singularities, e.g. sources or sinks (where the background flow potential $\widehat{\phi}$ is modified appropriately), and for flows driven by external background fields. The numerical results give excellent agreement with the exact solutions. Furthermore, in the unstable regime, e.g. when the interface (given by a polynomial map) of a fluid blob is driven by a sink, the numerical solutions agree with exact solutions before cusp formation. In all the numerical results presented here, the smoothing parameter $\gamma = 1$ gives sufficiently smooth and accurate results.

Example 2.7.1 (Circular translating bubble)

The numerical method is tested against the exact solution for a translating circular bubble in a uniform flow given in example 1.3.6. In this case, the background velocity potential is given by $\widehat{\phi} = Vx$, i.e. $\widehat{\mathbf{u}} = (V, 0)$. The exact normal velocity on the interface is $\mathbf{u} \cdot \mathbf{n} = (u, v) \cdot (y_s, -x_s)$, where the circular interface is parametrised with

arc length, traversed in the anticlockwise direction. Subtracting the velocity due to the background flow on the interface gives the exact solution for the normal velocity due to the existence of the bubble, i.e.

$$\begin{aligned}\widetilde{V}_n &= (\mathbf{u} - \widehat{\mathbf{u}}) \cdot \mathbf{n} \\ &= ((2V, 0) - (V, 0)) \cdot (y_s, -x_s) \\ &= V y_s \\ &= V \cos\Theta,\end{aligned} \tag{2.72}$$

where $s \equiv \Theta$ for a circular bubble, and the initial circular bubble of unit radius is given by $z = e^{i\Theta}$, i.e. centred at the origin. The numerical solution of (2.71) is denoted by $\alpha_i = \widetilde{v}_n(S_i)$. Figure. 2.6 shows the convergence of the solution $\alpha(\Theta)$ towards the exact solution $\widetilde{V}_n(S_i)$, as the number of mesh points, N, is increased, over one time step. The root mean square error (RMSE) is given by

$$\frac{1}{N}\left(\sqrt{\sum_{i}^{N}\left[\alpha_i - \widetilde{V}_n(S_i)\right]^2}\right). \tag{2.73}$$

Here, the background flow speed is set to be $V = 1$. As expected, the errors decrease approximately as $\mathcal{O}(1/N^3)$, as measured by the RMSE. This is because the largest errors occur in approximating the integrals in (2.71) by the trapezium rule (2.33).

The affect of filtering on the numerical solution in this case is presented in figure 2.7, where the numerical solution is given as a function of the angle $\Theta_i = \arg(z(S_i))$, i.e. $\alpha_i = \widetilde{v}_n(\Theta_i)$. In the absence of filtering, the errors in approximating the right hand side of (2.71) give oscillatory solution (as discussed in section 2.4) about the corresponding smooth solution. When the filter is applied—by choosing finite value of γ in (2.57)—the smooth solution gives excellent agreement with the expected solution, in this case given by (2.72).

Figure 2.8(a) shows a superposition of the interface at the last time step and

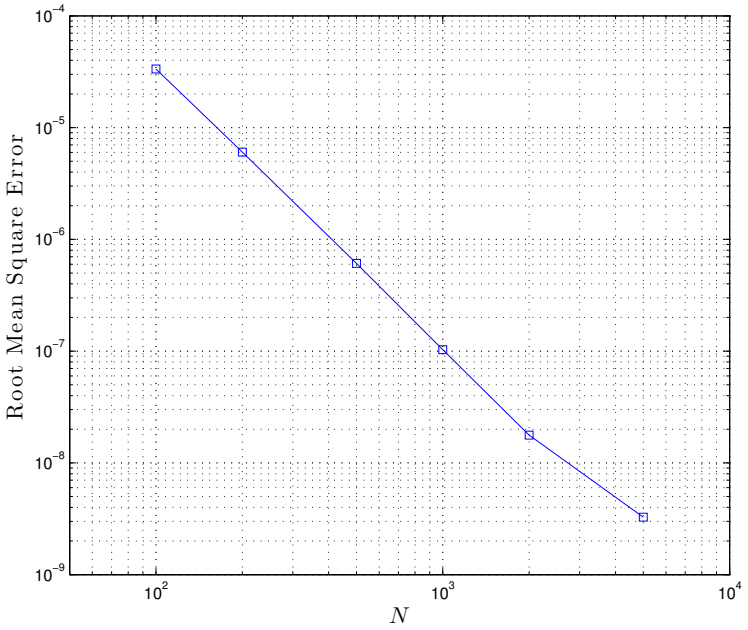

Figure 2.6: The decrease in RMSE of the normal velocity of a circular bubble of unit radius in a uniform background flow, as the number of mesh points is increased from $N = 100$ to $N = 5000$. In all tests, the algorithm is run for one fixed time step $\Delta t = 0.001$.

the interface given by the exact solution, given in example 1.3.6, at $t = 10$. There is excellent agreement between the numerical and exact solutions. The area of the bubble is calculated at each time step as follows. Consider the integral

$$A(t) = \iint_{\Omega(t)} \mathrm{d}x\mathrm{d}y, \tag{2.74}$$

where applying Green's theorem and parameterising with respect to arc length, s, (2.74) becomes

$$A(t) = \frac{1}{2} \oint_{\partial\Omega(t)} \left(x\frac{\mathrm{d}y}{\mathrm{d}s} - y\frac{\mathrm{d}x}{\mathrm{d}s} \right) \mathrm{d}s. \tag{2.75}$$

Since the mesh points are equispaced at each time step according to (2.28), we have at time $t = t_j$, the discrete form of (2.75) given by

$$A_{\mathrm{num}}(t_j) = \frac{1}{2} \sum_{i=1}^{N} \left(\Re(Z_i)\Im\left(\frac{\mathrm{d}Z_i}{\mathrm{d}s}\right) - \Im(Z_i)\Re\left(\frac{\mathrm{d}Z_i}{\mathrm{d}s}\right) \right) \Delta S, \tag{2.76}$$

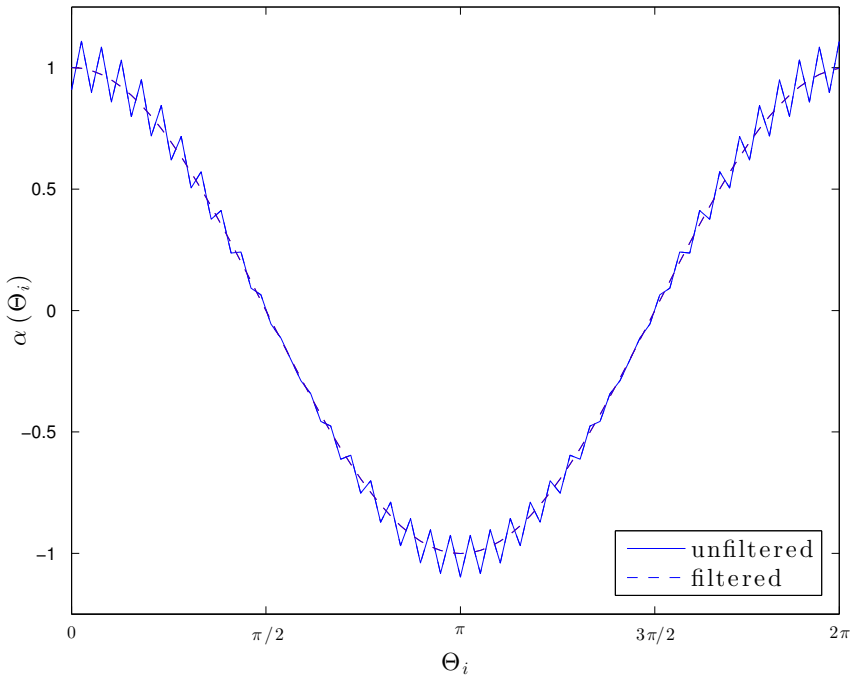

Figure 2.7: An example of oscillations in the (unfiltered) numerical solution of $\widetilde{v}_n$ after one time step with $N = 78$, $\Delta t = 0.001$, superimposed on the smooth (filtered) solution. The smoothing parameter is $\gamma = \infty$ (unfiltered) and $\gamma = 1$ (filtered), respectively. The solutions presented are for a circular bubble of unit radius in a uniform background flow such that $\widehat{\mathbf{u}} = (V, 0)$.

obtained using the trapezium rule. The bubble area of the exact solution can be calculated using complex variables, where in this example $z \in \partial\Omega(t)$ is given by the map (1.87) and so the bubble area A is

$$\begin{aligned} A(t) &= \left| \frac{1}{2i} \oint_{\partial D} \overline{z(\zeta,t)} z'(\zeta,t) \mathrm{d}\zeta \right| \\ &= \left| \frac{1}{2i} \oint_{\partial D} -\frac{cR}{\zeta^2} - \frac{R^2}{\zeta} \mathrm{d}\zeta \right| \\ &= \pi R^2, \end{aligned} \tag{2.77}$$

as expected, for a circle, where here R = constant represents the radius in the parametric map of the exact solution. The area of the numerical solution, (2.76), and the area of the exact solution, (2.77), are used to calculate a relative error at

any time step by the expression

$$\frac{A(t_j) - A_{\text{num}}(t_j)}{A(t_j)}, \tag{2.78}$$

and for the current example is shown in figure 2.8(b). The maximum observed error, given by (2.78), is $\mathcal{O}(10^{-4})$ for the results shown in figure 2.8.

Example 2.7.2 (Growing circular blob along a wall)

Consider a circular fluid blob growing along a straight wall (after contact is made), as presented in example 1.3.4, where the method of images is employed. Figure 2.9(a) shows the superposition of numerical results with analytical results, where in the numerical method, an initial Neumann Oval interface is used (obtained from (1.68) with $\zeta_1 = 0.7071$ and $R = 1.0607$ at initial time $t = 0.25 + \pi/Q$) with two sources of equal strength, $Q_1 = \pi$, in each lobe. There is excellent agreement between the numerical and exact solutions.

For a fluid blob whose interface is driven by a distribution of sources and sinks in $\Omega(t)$, the area can be calculated at any time t_j as

$$A(t_j) = A_0 + \sum_{i=1}^{K} Q_i t_j, \tag{2.79}$$

where A_0 is the initial area of the fluid blob, and K is the total number of hydrodynamic sources and sinks of strength Q_i. Hence, in this example, the area of the total fluid blob can be computed as

$$A(t_j) = A_0 + 2Q_1 t_j, \tag{2.80}$$

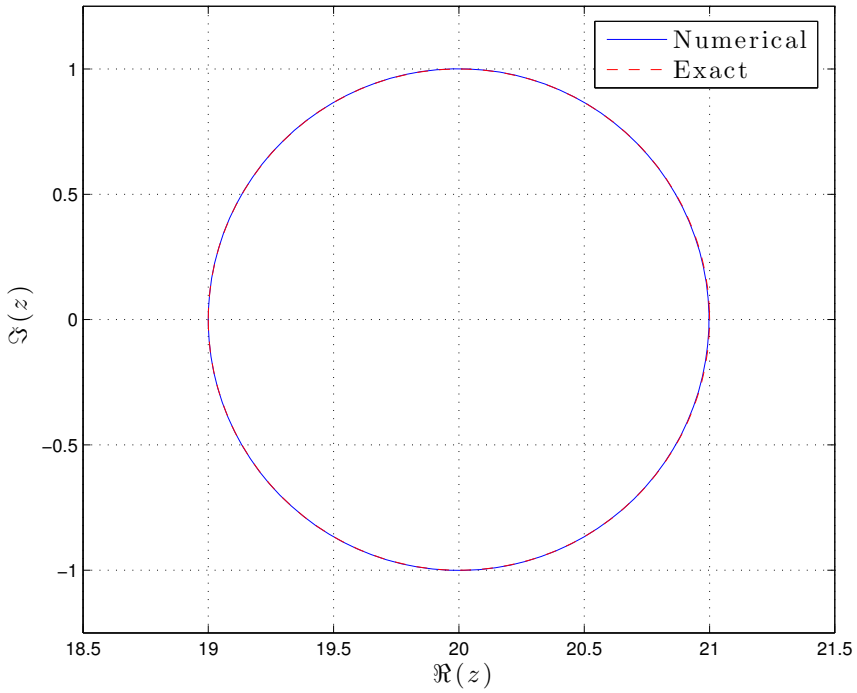

(a)

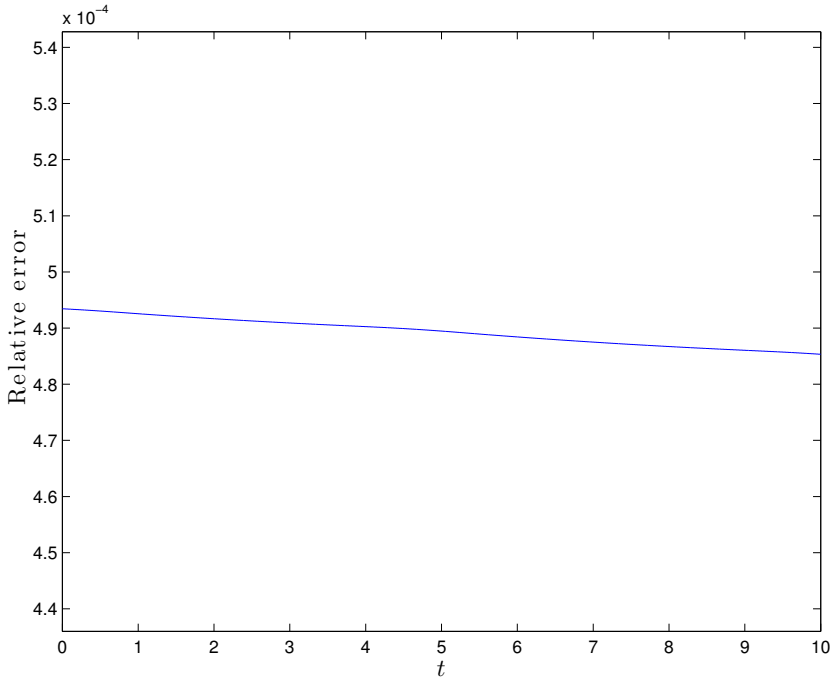

(b)

Figure 2.8: Superposition of the numerical and exact solutions of (a) the interface at time $t = 10$, and (b) the relative error of bubble area (2.78), $0 \leq t \leq 10$, for a translating circular bubble of unit radius in a uniform background flow of speed $V = 1$. Here there are $N = 100$ mesh points on the free boundary and step-size $\Delta t = 10^{-3}$.

and the initial area is given by

$$\begin{aligned} A_0 &= \left| \frac{1}{2i} \oint_{\partial D} \frac{R_0 \zeta}{(1-\zeta^2\zeta_{10}^2)} \left(\frac{R_0}{\zeta^2 - \zeta_{10}^2} - \frac{2R_0\zeta^2}{(\zeta^2-\zeta_{10}^2)^2} \right) \mathrm{d}\zeta \right| \\ &= \frac{\pi R_0^2 (1+\zeta_{10}^4)}{(1-\zeta_{10})^2(\zeta_{10}+1)^2(1+\zeta_{10}^2)^2}. \end{aligned} \tag{2.81}$$

Figure 2.9(b) shows relative error of the area of the fluid blob, calculated according to (2.78). Again, there is excellent agreement between the results. In (2.81), R_0 and ζ_{10} represent parameters of the map in the exact solution presented in example 1.3.4.

Example 2.7.3 (Elliptical bubble in a rotating cell)

The numerical results shown in this example were computed using the adaptation of the BIM presented in section 2.2, shown in appendix F. Figure 2.10(a) shows a superposition of the numerical results and the explicit results obtained from example 1.3.5 in section 1.3.5, for an elliptical bubble in a rotating Hele-Shaw cell. The initial interface is given by (1.82) with $a = 1.2$ and $b = \sqrt{0.44}$ at $t = 0$. The only forcing of the interface is due to the external potential field, and the dynamic boundary condition given in section 2.5 is employed. Figure 2.10(b) shows relative error between numerical and exact results for the area of the bubble, where the area can be calculated numerically and explicitly as in examples 2.7.1 and 2.7.2. There is excellent agreement between numerical and exact solutions.

2.8 Extension to multiple interface problems

The BIEs (2.20) and (2.71) formulated for a single blob or bubble, respectively, can be extended to consider Hele-Shaw free boundary problems with multiple blobs or bubbles. Here we derive the BIE in the case of multiple bubbles in an unbounded

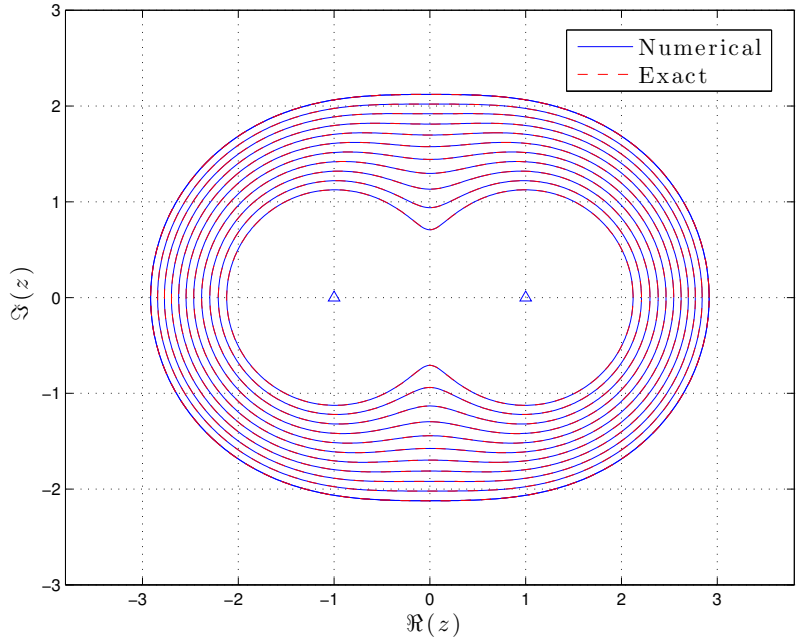

(a)

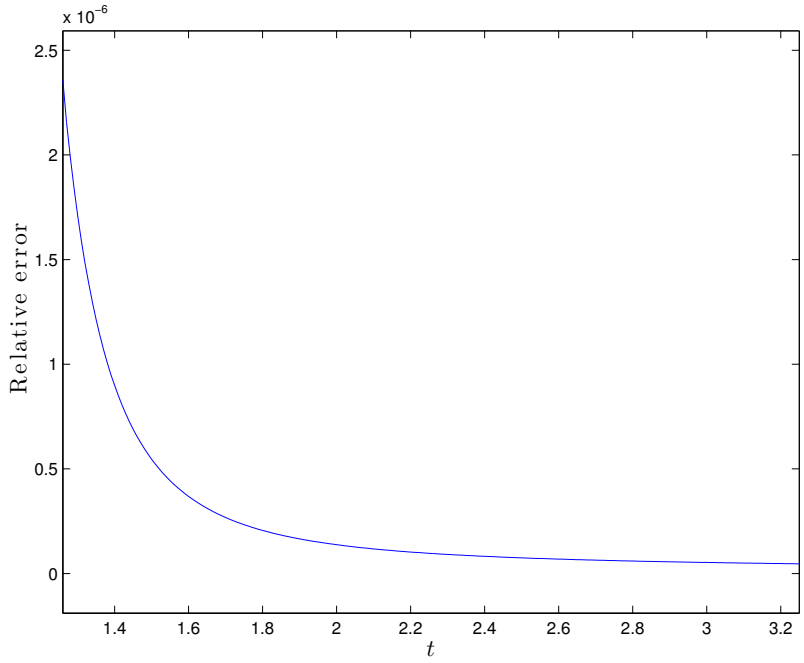

(b)

Figure 2.9: Superposition of the numerical and exact solutions of (a) the interface at time $t = 1.25, 1.44, 1.64, 1.84, 2.04, 2.24, 2.44, 2.64, 2.84, 3.04, 3.24$, and (b) the relative error of blob area (2.78), $0.25+\pi/Q \le t \le 2.25+\pi/Q$, for a dumbbell shaped fluid blob with two sources of strength $Q = Q_1 = Q_2 = \pi$ at $z = \pm 1$, marked by triangles in (a). Here there are $N = 500$ mesh points on the free boundary and step-size $\Delta t = 10^{-2}$. The initial interface is given by (1.68) with $\zeta_1(0.25 + \pi/Q) = 0.7071$ and $R(0.25 + \pi/Q) = 1.0607$.

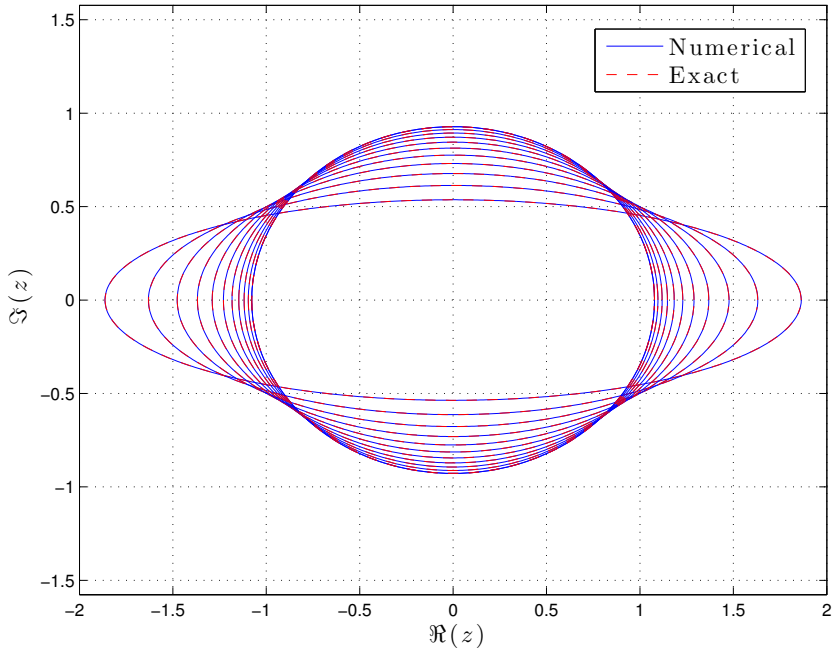

(a)

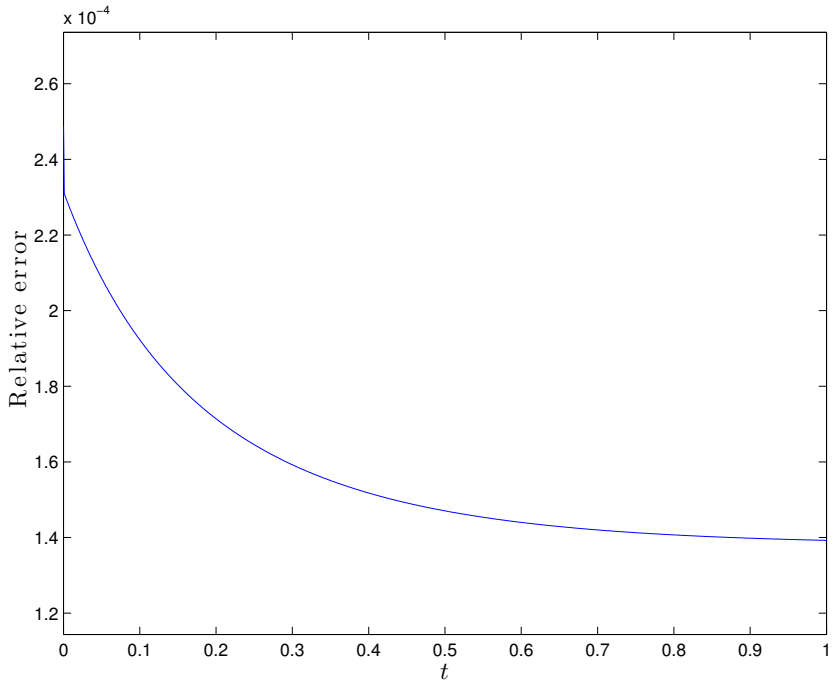

(b)

Figure 2.10: Superposition of the numerical and exact solutions of (a) the interface at time $t = 0$, 0.1, 0.2, 0.3, 0.4, 0.5, 0.6, 0.7, 0.8, 0.9, 1.0, and (b) the relative error of bubble area (2.78), $0 \leq t \leq 1$, for an elliptical bubble in a rotating Hele-Shaw cell with external centrifugal potential given by (1.80) with $\omega = 1$. Here there are $N = 500$ mesh points on the free boundary and step-size $\Delta t = 10^{-3}$. The initial interface is given by (1.82) with $a(0) = 1.2$ and $b(0) = \sqrt{0.44}$.

Hele-Shaw cell.

Suppose two fluids are separated by multiple simple closed curves, $\partial\Omega_\ell(t)$, $\ell = 1, \ldots, \Upsilon$, in a Hele-Shaw cell, where Υ is the total number of simple closed curves describing each interface. For simplicity, let us first consider the case of two bubbles, i.e. $\Upsilon = 2$, surrounded by a viscous fluid—see figure 2.11. Taking the average fluid velocity over the cell gap, the fluid velocity in the viscous phase is governed by (1.11). Assuming the pressure in each bubble is equal, i.e. we shall assume $p_1 = p_2 = 0$ where the subscript denotes each bubble, then the Hele-Shaw free boundary problem can be written as

$$\nabla^2\phi = 0, \qquad \mathbf{x} \in \Omega(t), \tag{2.82a}$$

$$\phi = 0, \qquad \mathbf{x} \in \partial\Omega_\ell(t), \tag{2.82b}$$

$$V_{n\ell} = \frac{\partial\phi}{\partial n_\ell}, \qquad \mathbf{x} \in \partial\Omega_\ell(t). \tag{2.82c}$$

where $\mathbf{n}_\ell$ is the unit normal vector on each bubble interface and $V_{n\ell}$ is the normal velocity of the ℓ-th interface.

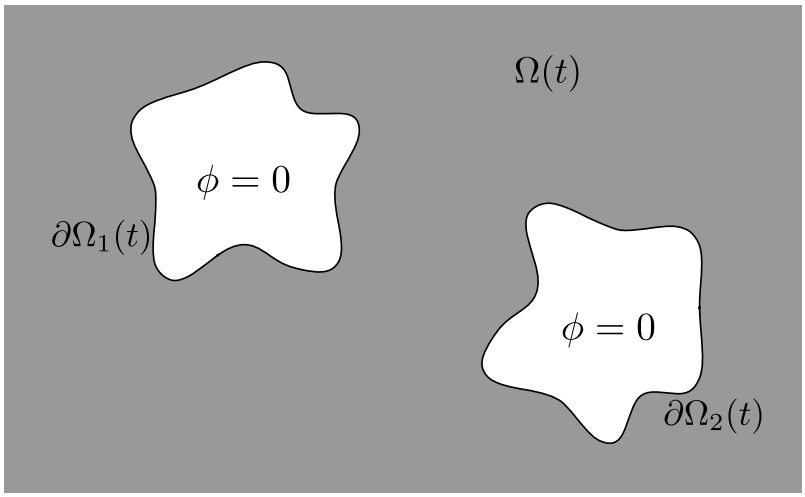

Figure 2.11: Two finite bubble regions described by simple closed curves $\partial\Omega_1(t)$ and $\partial\Omega_2(t)$, in an unbounded Hele-Shaw cell, where the viscous domain $\Omega(t)$ is of infinite extent.

Parameterising each interface with arc length s such that $\partial\Omega_\ell(t)$ are traversed in the anticlockwise direction (see figure 2.12), taking the tangential derivative of the

dynamic boundary condition (2.82b) gives

$$\frac{\partial \phi}{\partial \tau_\ell} = 0, \qquad \mathbf{x} \in \partial\Omega_\ell(t), \tag{2.83}$$

i.e.

$$v_{\tau\ell} = 0, \qquad \mathbf{x} \in \partial\Omega_\ell(t), \tag{2.84}$$

where $\boldsymbol{\tau}_\ell$ is the unit tangent vector along $\partial\Omega_\ell(t)$ and $v_{\tau\ell}$ is the tangential velocity on the ℓ-th interface. Since the normal velocity on $\partial\Omega_\ell(t)$ must be continuous, the kinematic boundary condition (2.82c) can be written as

$$V_{n\ell} = v_{n\ell}, \qquad \mathbf{x} \in \partial\Omega_\ell(t), \tag{2.85}$$

where $v_{n\ell}$ is the normal fluid velocity on the ℓ-th interface.

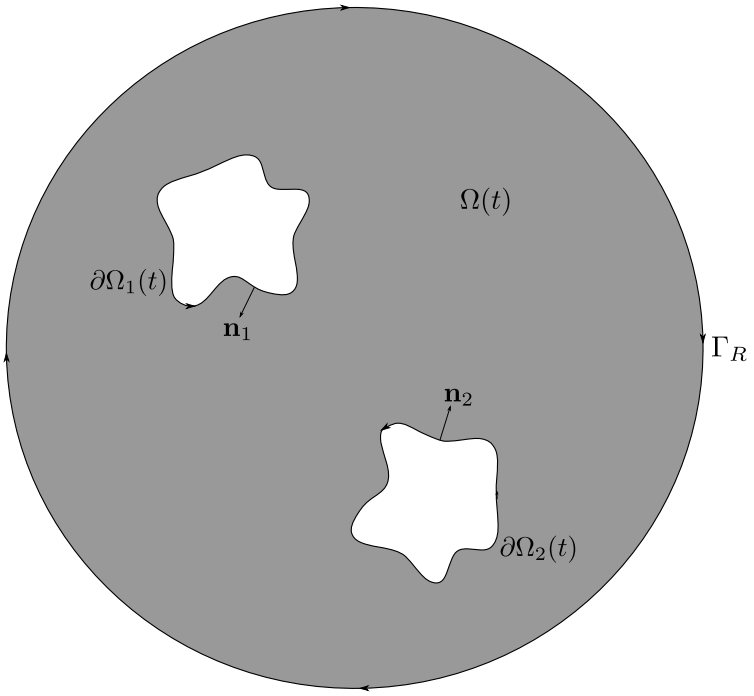

Figure 2.12: The contours bounding the viscous domain $\Omega(t) \subset \mathbb{C}$. In the limiting case $R \to \infty$, the scenario of finite bubbles in an infinite expanse of viscous fluid (in an unbounded Hele-Shaw cell) is achieved.

Decomposing the velocity potential of the viscous phase as in section 2.2.1, the

Hele-Shaw free boundary problem in terms of $\widetilde{\phi}$ becomes

$$\nabla^2\widetilde{\phi} = 0, \qquad \mathbf{x} \in \Omega(t), \tag{2.86a}$$

$$\widetilde{\phi} = -\widehat{\phi}, \qquad \mathbf{x} \in \partial\Omega_\ell(t), \tag{2.86b}$$

$$V_{n\ell} = \frac{\partial}{\partial n_\ell}\left(\widetilde{\phi} + \widehat{\phi}\right), \qquad \mathbf{x} \in \partial\Omega_\ell(t) \tag{2.86c}$$

and the conditions (2.84) and (2.85) can be written as

$$\widetilde{v}_{\tau\ell} = -\widehat{v}_{\tau\ell}, \qquad \mathbf{x} \in \partial\Omega_\ell(t), \tag{2.87}$$

and

$$V_{n\ell} = \widetilde{v}_{n\ell} + \widehat{v}_{n\ell}, \qquad \mathbf{x} \in \partial\Omega_\ell(t), \tag{2.88}$$

respectively.

A boundary integral equation for the regular part of the flow field can be constructed over the interfaces of the bubbles in a similar manner to the BIE for a single bubble derived in section 2.6 by first assuming the domain $\Omega(t)$ is bounded by an outer contour Γ_R traversed in the clockwise direction—see figure 2.13. Choosing the points z_{A1} and z_{A2} on Γ_R, and z_{B1} and z_{B2} on $\partial\Omega_1(t)$ and $\partial\Omega_2(t)$, respectively, defining the straight paths $z_{A\ell}z_{B\ell}$ to be the arcs joining the points $z_{A\ell}$ and $z_{B\ell}$, then the BIE, corresponding to (2.68) in the single bubble case, now for multiple bubbles, becomes

$$-\frac{1}{2i\pi}\sum_{\ell=1}^{\Upsilon}\oint_{\partial\Omega_\ell(t)}\frac{\widetilde{u}(z) - i\widetilde{v}(z)}{z - z_m}\,\mathrm{d}z = \left.\frac{\widetilde{u} - i\widetilde{v}}{2}\right|_{z_m}, \tag{2.89}$$

in the limit $R \to \infty$ and z_m is a point lying on $\partial\Omega_\ell(t)$, $\ell \in \{1, \ldots, \Upsilon\}$, i.e. $z_m \in$

$\cup_{\ell=1}^{\Upsilon}\partial\Omega_\ell(t)$. Using the identity

$$(\widetilde{u} - i\widetilde{v})\,\frac{\mathrm{d}z}{\mathrm{d}s} = \widetilde{v}_{\tau\ell} + i\widetilde{v}_{n\ell}, \tag{2.90}$$

where $z \in \partial\Omega_\ell(t)$, then the boundary integral equation (2.89) can be formulated in terms of the normal and tangential components of the regular part of the fluid velocity on each interface, i.e.

$$-\sum_{\ell=1}^{\Upsilon} \fint_0^{L_\ell(t)} \frac{\widetilde{v}_{\tau\ell}(s) + i\widetilde{v}_{n\ell}(s)}{z(s) - z(s_m)}\,\mathrm{d}s = i\pi\,(\widetilde{v}_{\tau\jmath} + i\widetilde{v}_{n\jmath})\left(\frac{\mathrm{d}z}{\mathrm{d}s}\right)^{-1}\Bigg|_{s_m}, \tag{2.91}$$

when $z_m \in \partial\Omega_\jmath(t)$, $\jmath \in \{1, \ldots, \Upsilon\}$, and $L_\ell(t)$ is the total arc length of the closed interface $\partial\Omega_\ell(t)$. Using the dynamic boundary condition in the form (2.87), the BIE (2.91) can be written in terms of the unknown normal velocity on each interface, i.e.

$$\begin{aligned} -\left(\frac{\mathrm{d}z}{\mathrm{d}s}\right)\Big|_{z_m} \sum_{\ell=1}^{\Upsilon} \fint_0^{L_\ell(t)} \frac{i\widetilde{v}_{n\ell}}{z - z_m}\,\mathrm{d}s + \pi\,\widetilde{v}_{n\jmath}|_{z_m} = \\ -\left(\frac{\mathrm{d}z}{\mathrm{d}s}\right)\Big|_{z_m} \sum_{\ell=1}^{\Upsilon} \fint_0^{L_\ell(t)} \frac{\widehat{v}_{\tau\ell}}{z - z_m}\,\mathrm{d}s - i\pi\,\widehat{v}_{\tau\jmath}|_{z_m}\,. \end{aligned} \tag{2.92}$$

Given the background potential, $\widehat{\phi}$, the tangential velocity $\widehat{v}_{\tau\ell}$ on any interface $\partial\Omega_\ell(t)$ is known. Equation (2.92) can be solved for $\widetilde{v}_{n\ell}$, from which the normal velocity of the of the interfaces, $V_{n\ell}$, can be inferred since $V_{n\ell} = \widetilde{v}_{n\ell} + \widehat{v}_{n\ell}$. The normal velocity on each interface can be written in Cartesian form as

$$\mathcal{U}_\ell = V_{n\ell}\mathbf{n}_\ell, \qquad \mathbf{x} \in \partial\Omega_\ell(t). \tag{2.93}$$

Therefore, since the interfaces move in their respective normal directions, each interface is advected according to

$$\frac{\mathrm{d}\mathbf{x}}{\mathrm{d}t} = \mathcal{U}_\ell, \qquad \mathbf{x} \in \partial\Omega_\ell(t). \tag{2.94}$$

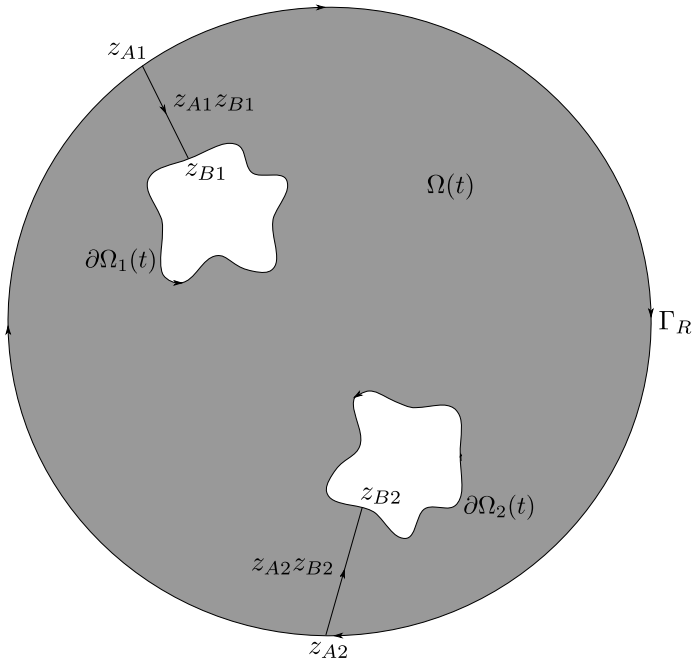

Figure 2.13: The choice of contours and their directions in the formulation of the BIE (2.89) in which the limit $R \to \infty$ is taken, for the case of multiple bubbles in an unbounded Hele-Shaw cell filled with a viscous fluid.

Following the approximations set out in section 2.3, the boundary integral equation (2.92) can be discretised, giving a set of algebraic equations which can be written as a matrix system in the form (2.39), i.e. $\boldsymbol{M}\boldsymbol{\alpha} = \mathbf{R}$. If each interface $\partial\Omega_\ell(t)$ is discretised into N_ℓ distinct mesh points, then we can choose N_ℓ distinct midpoints, z_m, on each interface, and so due to (2.92) there exist $\sum_{\ell=1}^{\Upsilon} N_\ell$ algebraic equations. Let us construct the solution vector $\boldsymbol{\alpha}$ such that

$$\boldsymbol{\alpha} = \left(\boldsymbol{\alpha}^{(1)}, \ldots, \boldsymbol{\alpha}^{(\Upsilon)}\right)^\top, \tag{2.95}$$

where $\alpha_k^{(\ell)} = \widetilde{v}_{n\ell}(S_k)$, $k = 1, \ldots, N_\ell$, is the unknown normal velocity at the k-th mesh point on the ℓ-th interface. Using the approximations (2.32) and (2.33), (2.92), in

discrete form, can be approximated as

$$-\frac{\mathrm{d}}{\mathrm{d}s}Z^{(\jmath)}_{m+1/2}\sum_{\ell=1}^{\Upsilon}\sum_{k=1}^{N_\ell}\frac{i\alpha^{(\ell)}_k}{Z^{(\ell)}_k-Z^{(\jmath)}_{m+1/2}}\Delta S^{(\ell)} +\pi\left[\frac{Z^{(\jmath)}_{m+1}-Z^{(\jmath)}_{m+1/2}}{Z^{(\jmath)}_{m+1}-Z^{(\jmath)}_{m}}\alpha^{(\jmath)}_m+\frac{Z^{(\jmath)}_{m+1/2}-Z^{(\jmath)}_{m}}{Z^{(\jmath)}_{m+1}-Z^{(\jmath)}_{m}}\alpha^{(\jmath)}_{m+1}\right]= -\frac{\mathrm{d}}{\mathrm{d}s}Z^{(\jmath)}_{m+1/2}\sum_{\ell=1}^{\Upsilon}\sum_{k=1}^{N_\ell}\frac{\widehat{v}_{\tau\ell}(S^{(\ell)}_k)}{Z^{(\ell)}_k-Z^{(\jmath)}_{m+1/2}}\Delta S^{(\ell)}-i\pi\widehat{v}_{\tau\jmath}\left(S^{(\jmath)}_{m+1/2}\right), \tag{2.96}$$

for $m=1,\ldots,N_\jmath$, $\jmath=1,\ldots,\Upsilon$ and the vector $\mathbf{R}=(\mathbf{R}^{(1)},\ldots,\mathbf{R}^{(\Upsilon)})^\top$ is such that $R^{(\jmath)}_m$ is given by the right hand side of (2.96). Hence, the matrix $\boldsymbol{M}$ is a $\left(\sum_{\ell=1}^{\Upsilon}N_\ell\right)\times\left(\sum_{\ell=1}^{\Upsilon}N_\ell\right)$ matrix. In this way, any number of interfaces or bubbles can be considered in the numerical method presented, where the computational complexity of the system grows linearly with the total number of discrete mesh points of all the interfaces combined.

Following the filtering method proposed in section 2.4 for the single interface problem, the matrix system, $\boldsymbol{M}\boldsymbol{\alpha}=\mathbf{R}$, is modified to the form (2.57) by considering errors in approximating the right hand side of (2.96). Assuming $\widetilde{v}_{n\ell}(s)$ are smooth periodic functions on each interface $\partial\Omega_\ell(t)$, the modification incorporates the condition that the integral of the square of the second derivative of $\widetilde{v}_{n\ell}(s)$ on each interface must be minimised, independently. The modified matrix equation in the case of multiple bubbles then reads

$$(\boldsymbol{M}^\top\boldsymbol{M}+\boldsymbol{P})\boldsymbol{\alpha}=\boldsymbol{M}^\top\mathbf{R}, \tag{2.97}$$

where $\boldsymbol{P}$ is a $\left(\sum_{\ell=1}^{\Upsilon} N_\ell\right) \times \left(\sum_{\ell=1}^{\Upsilon} N_\ell\right)$ block diagonal matrix given by

$$\boldsymbol{P} = \begin{pmatrix} \gamma_1 \boldsymbol{H}_1 & \mathbf{0} & \mathbf{0} \\ \mathbf{0} & \ddots & \mathbf{0} \\ \mathbf{0} & \mathbf{0} & \gamma_\Upsilon \boldsymbol{H}_\Upsilon \end{pmatrix}. \tag{2.98}$$

Here, $\boldsymbol{H}_\ell$ are the $N_\ell \times N_\ell$ matrix representations of a third order difference operator [144] and γ_ℓ denotes the smoothing parameter for the solution $\boldsymbol{\alpha}^{(\ell)}$ of each interface, where $0 < \gamma_\ell < \infty$ and $\ell = 1, \ldots, \Upsilon$.

The restriction here is that the pressure in all bubbles is considered equal. To introduce an extra parameter of the problem specifying the pressure in each bubble, the boundary integral method should be formulated for the solution of the stream function on each interface—c.f. appendix F—instead of solving directly for the fluid velocity. Taking the derivative of the stream function with respect to arc length will provide the normal velocity on each interface. Solving the problem of varying pressure bubbles, numerically, is not done in this doctoral research.

2.9 Summary

In section 2.2 a BIE is presented which is formulated by constructing a meromorphic function, $F(z,t)$, on the viscous fluid domain $\Omega(t)$, and considering the Cauchy integral formula with integration along the free boundary $\partial\Omega(t)$. The numerical procedure and the numerical instabilities encountered are described in section 2.3 and 2.4, respectively. An appropriate smooth solution for the normal velocity of the fluid on $\partial\Omega(t)$ is sought. The model is also presented for flows with external fields in section 2.5, and is extended to multiple independent interfaces in section 2.8. In section 2.7, numerical results are compared with known exact solutions for which excellent agreement is found.

Chapter 3

Hele-Shaw flows of conducting fluids

The main results from this chapter have been published in the paper entitled 'Hele-Shaw flow driven by an electric field' [71].

The results presented in this chapter may find applications in problems involving fluid extraction and in the theory of fluid flows in microfluidic devices, where the main interest lies in the manipulation of fluid blobs via electric fields. Entov and Etingof [39] raise the idea of the application of Hele-Shaw free boundary flows in electrokinetics, where flow is induced by applying electric fields, resulting in what is known as 'electro-osmotic flow'. The use of electro-osmotic flow in microfluidic devices, where flow in narrow gaps or channels are driven by electric potential fields, is mentioned in [83,152]. More recently, controlling fluid blobs or bubbles in advanced microfluidic devices has also become an area of interest in bio-chemical processes and fluid logical devices [16, 86, 113]. A method known as electrowetting has become a widely used tool through a surge in so called 'lab-on-chip' devices for applications such as DNA analysis and medical diagnostics; where electrowetting, first introduced by Lippmann in 1875 (English translation [102]), allows the manipulation of small drops or blobs of fluid on small surfaces, usually surrounded by air.

In section 3.1, the assumptions of the model are presented for Hele-Shaw flow of a conducting fluid due to a static point charge, where the assumption of non-conducting cell walls is important, and the governing equations are presented in section 3.2. New analytical results are derived in section 3.3 and some numerical results are presented in section 3.4. In section 3.4.3, the stability of known exact solutions are tested, numerically, and some concluding remarks are made in section 3.5.

3.1 Electromagnetic field equations

An electric current is a flow of electric charges. Such currents exist in conducting media. It will be assumed that the viscous fluid considered here has the same properties as a dielectric: a medium in which a constant current cannot flow. In general, if a conducting fluid flows in a magnetic or electric field, the electric field is modified due to the fluid motion, and is often described by the resulting 'streaming potential'. That is, electric currents are induced in the flow and the currents themselves affect the magnetic field [79]. In many cases, such a phenomenon occurs when the conducting fluid is in contact with a conducting solid boundary, which gives rise to the streaming potential in the conducting fluid. Although the study of such physical scenarios are relevant and apparent in the literature, specifically in engineering applications (see e.g. [73,115,129]), here it will be assumed for simplicity that the walls of the Hele-Shaw cell are non-conducting. The motivation and application of the model presented here is in the manipulation of fluid blobs (or bubbles) in 'simplified' lab-on-chip devices, similar to those that already exist (see for example [32]) but with non-conducting surfaces.

It is well known that an electric field, $\mathbf{E}$, in a conducting medium can be described

as the gradient of a scalar *electric potential* such that

$$\mathbf{E} = \nabla \Psi_e. \tag{3.1}$$

Electric displacement in a linear material is defined as

$$\mathbf{D} = c_e \mathbf{E}, \tag{3.2}$$

where c_e denotes the electric permittivity of the material. Here we shall restrict ourselves to homogenous fluids, where c_e remains constant throughout. The equations governing the electric and magnetic fields in a conducting medium are given by *Maxwell's equations*. In a fixed (i.e. Eulerian) frame of reference, these are

$$\nabla \cdot \mathbf{D} = \rho_e, \tag{3.3a}$$

$$\nabla \cdot \mathbf{B} = 0, \tag{3.3b}$$

$$\nabla \times \mathbf{E} = -\frac{\partial \mathbf{B}}{\partial t}, \tag{3.3c}$$

$$\nabla \times \mathbf{B} = -c_m \left(\mathbf{I} + c_e \frac{\partial \mathbf{E}}{\partial t} \right). \tag{3.3d}$$

Here, the vector $\mathbf{B}$ represents the magnetic field and c_m represents the magnetic permeability of the medium, i.e the fluid. The distribution of electric charge in the medium is given by ρ_e. *Ohm's law* states that the current, $\mathbf{I}$, in a conducting medium is proportional to the electric potential difference. That is, for a fluid of conductivity σ_e, the current is related to the electric field by

$$\mathbf{I} = \sigma_e \mathbf{E}. \tag{3.4}$$

Here we assume that the viscous fluid is a homogenous conductor, i.e. σ_e is constant. Then (3.4) implies that the conducting fluid is isotropic.

In a moving frame of reference (i.e. in the Lagrangian frame moving with a fluid particle), via the so called *Lorentz transformation*, Ohm's law reads [78, 79]

$$\mathbf{I} = \sigma_e \mathbf{E}', \tag{3.5}$$

where $\mathbf{E}'$ is the electric field in the moving frame given by

$$\mathbf{E}' = \mathbf{E} + \mathbf{u} \times \mathbf{B}. \tag{3.6}$$

It is assumed that the speed of the conducting fluid, $|\mathbf{u}|$, is small compared with the speed of light. Under this approximation, the field equations are (3.3) with the electric current given by (3.5) [114].

For an electrostatic potential field produced by a point charge of strength E, the body force acting on a conducting mass is given by

$$\mathbf{f}_b = \rho_e \mathbf{E} + \mathbf{I} \times \mathbf{B}, \tag{3.7}$$

where the first term is known as *Coulomb's force* and the second as the *Lorentz force*. For the electric field given in (3.1), the body force can be described in terms of the electric potential Ψ_e as

$$\mathbf{f}_b = \rho_e \nabla \Psi_e + \mathbf{I} \times \mathbf{B}. \tag{3.8}$$

An electro-osmotic flow is a flow induced by an electric potential differential in a conducting fluid. This phenomena arises in different physical applications; those that are relevant to the present work are flows in thin gaps in micro-fluidic devices or even flows through porous media [101] (the similarity between Hele-Shaw flows and those governed by Darcy's law have been previously discussed in section 1.2.1). The equations governing fluid flow are therefore given by (1.2) with $\mathbf{f}_b$ given in (3.8).

Electrokinetic coupling in a fluid is the relationship between hydrodynamics and

electric fields. Fluid flow and electric current become coupled when a conducting fluid is in contact with electrically conducting solid boundaries, e.g. a conducting wall. In the case when the solid boundaries are considered to be uncharged (precisely the assumption we make here), the pressure gradient of the flow and electric field remain decoupled [73, p. 64].

3.2 The Hele-Shaw free boundary problem for a conducting fluid subject to an external electric field

For a highly conducting fluid, the time scale on which the fluid evolves is much larger than the time scale for any charge to move around on its surface and thus the flow effect on the electric current is negligible. Here, the surface is described by the free boundary $\partial\Omega(t)$. This implies that for an applied external electric potential field, $\mathbf{E}$, we have an electrostatic problem [36]. For highly conducting materials, ρ_e is assumed to be zero throughout the material, i.e. throughout the viscous fluid domain $\Omega(t)$ [73, 78]. In this case, considering the applied external electric field, the mean effect of electric energy is assumed to be much larger than that of any magnetic effects. That is, here we shall also assume the magnetic effects are negligible, i.e. we set $\mathbf{B} = 0$ [73, 115].

3.2.1 Flow driven by an isolated static point charge

Consider the case in which a viscous fluid is driven by an isolated static electric point charge of strength $E =$ constant. Initially, we shall consider the case in which the point charge is located inside the viscous fluid region, $\Omega(t)$. Therefore, (3.3) gives

$$\nabla \cdot \mathbf{E} = E\delta(\mathbf{x} - \mathbf{x}_0), \tag{3.9a}$$

$$\nabla \times \mathbf{E} = 0, \tag{3.9b}$$

$$\mathbf{I} = -c_e \frac{\partial \mathbf{E}}{\partial t}. \tag{3.9c}$$

Equation (3.9b) implies that $\mathbf{E}$ is an irrotational vector field, $\mathbf{x} = (x, y)$ is the 2D position vector and $\mathbf{x}_0 \in \Omega(t)$ is the location of the point charge. Taking the divergence of (3.9c) and employing (3.9a) implies

$$\nabla \cdot \mathbf{I} = 0. \tag{3.10}$$

Since magnetic effects are assumed to be negligible, the Lorentz force in (3.8) is effectively zero. Therefore, in a Newtonian, instantaneously responsive, isotropic fluid this leaves the force on the fluid mass, i.e. on the domain $\Omega(t)$, to be simply a Coulomb force due to the point charge, given by

$$\mathbf{f}_b = E\nabla\Psi_e. \tag{3.11}$$

It is assumed that the inviscid fluid, exterior to $\Omega(t)$, has the same conductivity as the viscous fluid such that the electric field is able to permeate through it. In this case, the electric potential $\Psi_e(x, y)$ is governed by (3.9a) in the entire plane. The hydrodynamic pressure in the inviscid fluid is constant and we set this to zero, arbitrarily. Since both fluids are considered to be perfectly conducting fluids, all excess charge lies at the interface separating the fluids, i.e. on $\partial\Omega(t)$. Therefore, any applied electric field exerts a pressure on the interface by its action on the charge at the free boundary, giving the dynamic boundary condition. Following the derivation of Hele-Shaw flows with external potential fields, discussed in section 1.3.5

and presented in appendix B, setting $\Psi(x,y) \equiv E\Psi_e(x,y)$, the dynamic boundary condition is given by (B.9) and the Hele-Shaw free boundary problem subject to an external electric field due to a static point charge is then given by

$$\nabla^2\phi = 0, \qquad \mathbf{x} \in \Omega(t), \tag{3.12a}$$

$$\phi = \Psi, \qquad \mathbf{x} \in \partial\Omega(t), \tag{3.12b}$$

$$v_n = \frac{\partial\phi}{\partial n}, \qquad \mathbf{x} \in \partial\Omega(t), \tag{3.12c}$$

where $\phi(x,y,t)$ is a scalar potential function proportional to the pressure in $\Omega(t)$.

Since both fluids have the same conductivity, from (3.9a), it can be seen that $\Psi(x,y)$ must satisfy the equation

$$\nabla^2\Psi = E\delta_0(\mathbf{x}-\mathbf{x}_0), \tag{3.13}$$

in the entire plane, where $\delta_0(\mathbf{x}-\mathbf{x_0})$ is the Dirac distribution as defined in (1.18). Therefore, using the Green's function for the Laplacian operator in 2D, we find

$$\Psi(x,y) = \frac{E}{2\pi}\log|\mathbf{x}-\mathbf{x}_0|, \tag{3.14}$$

which describes the electric field, due to a static point charge, induced in the viscous fluid region $\Omega(t)$, and which extends to the entire plane.

3.3 Analytical results

The task is to find $\partial\Omega(t)$ of a fluid blob evolving under the influence of a background potential field given the initial boundary $\partial\Omega(0)$. Here we shall apply the complex variable techniques described in section 1.3.1, in particular the generalised Schwarz function equation (1.79). Since there are no hydrodynamic singularities

driving the flow, the derivative of the complex potential, $w'(z,t)$, has no singularities in the fluid domain $\Omega(t)$ and hence the left hand side of (1.79) is regular. As presented in section 1.3.1, the unknown boundary $\partial\Omega(t)$ is parameterised by a conformal map $z = f(\zeta, t)$ from the *interior* of the unit ζ-disc, D, to the *interior* of the fluid blob, $\Omega(t)$. By balancing singular terms of (1.79), the aim is to deduce ODEs for the unknown, time-dependent parameters of the conformal map, and subsequently determine the evolution of the free boundary $\partial\Omega(t)$. This approach is used to investigate the stability and behaviour of initially circular blobs of fluid when the external field is due to an electric point charge, given in (3.14).

In the complex plane, writing $z = x + iy$, the Schwarz function of the free boundary is defined as $g(z,t) = \bar{z}$ on $z \in \partial\Omega(t)$ (see section 1.3.2), where g is an analytic function in the neighbourhood of $\partial\Omega(t)$. Let us re-write the governing equation (1.79) as

$$\frac{\partial w}{\partial z} = \frac{1}{2}\frac{\partial g}{\partial t} + \frac{\partial M}{\partial z}, \tag{3.15}$$

which holds over the entire domain $\Omega(t)$, where

$$M(z) = \Psi((z + g(z))/2, (z - g(z))/(2i)), \tag{3.16}$$

which is an analytic function in the neighbourhood of $\partial\Omega(t)$ and $w(z,t)$ is the complex potential of the flow (defined in (1.24)) [89]. In the absence of any background fields, i.e. $M \equiv 0$, (3.15) reduces to the well-known Schwarz function equation (1.46) governing the evolution of the free boundary [25, 89].

3.3.1 Steady solution for an initially circular fluid blob with a point charge at its centre

Consider a circular blob of conducting viscous fluid with radius R centred at the origin enclosing a point charge located at $z = 0$, i.e. within the initial fluid domain $\Omega(0)$. By symmetry it is expected that this is an exact steady solution. The external potential owing to the point charge of strength E centred at $z = 0$ is given by $\Psi = (E/2\pi)\log r = M(z)$ on $\partial\Omega(t)$, where $r = (x^2 + y^2)^{1/2}$ and

$$M = \frac{E}{4\pi}\log(zg). \tag{3.17}$$

Employing (3.17), the Schwarz function equation (3.15) becomes

$$\frac{\partial w}{\partial z} = \frac{1}{2}\frac{\partial g}{\partial t} + \frac{E}{4\pi}\left(\frac{1}{z} + \frac{g'}{g}\right). \tag{3.18}$$

The boundary of a circular blob of radius $R(t)$ centred at $z = 0$ has Schwarz function $g(z,t) = R^2/z$. Using (3.18) and considering the singular structure of terms as $z \to 0$, recalling that there is no singularity in w since there are no hydrodynamic sources, it follows that $\dot{R} = 0$. This gives, as expected, a steady solution in which the fluid blob remains circular with constant radius $R_0 = R(0)$, irrespective of the sign of E.

3.3.2 Stability of blobs subject to an electric point charge

The stability of the circular blob equilibria is now studied with $R_0 = 1$, where a small perturbation to the circular boundary is imposed. Consider the conformal map from the unit ζ-disc to a nearly-circular fluid blob with a small disturbance to

the initial boundary, $\partial\Omega(0)$, given by (see e.g. [25, 40, 48])

$$z = \zeta + \alpha\zeta^n, \tag{3.19}$$

where n is an integer such that $n \geq 2$ and $\alpha(t)$ is a real time varying coefficient such that $|\alpha| \ll 1$. In polar coordinates with $r = |z|$, (3.19) is equivalent to $r = 1 + \alpha\cos(n-1)\theta + \mathcal{O}(\alpha^2)$, $0 \leq \theta < 2\pi$. Using $\overline{\zeta} = \zeta^{-1}$ on ∂D and the inversion of (3.19), the Schwarz function has the form

$$g = \frac{\alpha}{z^n} + \frac{n\alpha^2 + 1}{z} + \mathcal{O}(z^{n-2}), \quad \text{as } z \to 0. \tag{3.20}$$

Ignoring terms of $\mathcal{O}(\alpha^2)$ and considering the structure of the singularities of $\mathcal{O}(z^{-n})$ in (3.18), the following ODE for $\alpha(t)$ is obtained:

$$\frac{\mathrm{d}\alpha}{\mathrm{d}t} = \frac{E}{2\pi}(n-1)\alpha, \tag{3.21}$$

which has an exponentially decaying solution for a negative point charge E. For $E > 0$, the amplitude of the disturbances grow exponentially with time, and the assumption of small α breaks down. Hence, the flow is stable only if the point charge within the fluid domain is negative. Physically, this stability property owes itself to the following characteristic fluid behaviour: anomalous fluid outside $|z| = 1$ is attracted inward by a negative point charge, while a fluid deficit inside $|z| = 1$ is pushed outward. Together, these processes re-symmetrise a perturbed circular blob. For a positive point charge an anomaly for $|z| = 1$ is pushed further outward leading to instability. This stability prediction is tested numerically in section 3.4.1—see Figure 3.1.

It is worth noting that exact, time-dependent solutions which combine both hydrodynamic singularities and point charges have not yet been found. A prime can-

didate for generating such solutions is to use maps of the type (3.19) since these yield explicit solutions in the case driven by hyrodynamic singularities when point charges are absent (e.g. see [25, 48]). However, when combined with point charges, this map does not yield solutions with, for example, the correct rate of change of area. Finding a class of maps which admits such exact solutions is an open question.

3.3.3 A circular fluid blob with an off-centre point charge

Suppose the circular blob in section 3.3.1 is off-set by a small amount ϵ so that it is now centred at $z = \epsilon$, with the point charge E located at $z = 0$ which lies within the fluid domain $\Omega(t)$. Without loss of generality ϵ is assumed to be real. Making the approximation that, to leading order, the blob remains circular throughout its evolution, consider the conformal map from the unit ζ-disc to the fluid blob given by

$$z = \epsilon + R\zeta, \tag{3.22}$$

where $\epsilon(t)$ and $R(t)$ are real, time-dependent coefficients to be found. The validity of the approximation that the blob remains circular during its evolution is tested by comparing the analytical results of this section with numerical results in section 3.4.1. The map (3.22) implies $\partial\Omega(t)$ has the Schwarz function

$$g = \epsilon + \frac{R^2}{z - \epsilon}. \tag{3.23}$$

Expanding (3.23) for small ϵ yields

$$g = \epsilon + \frac{R^2}{z} + \frac{R^2\epsilon}{z^2} + \mathcal{O}(\epsilon^2). \tag{3.24}$$

Considering the structure of the singularities of $\mathcal{O}(z^{-1})$ and $\mathcal{O}(z^{-2})$ on both sides of (3.18), the following pair of ODEs are obtained for $R(t)$ and $\epsilon(t)$:

$$R\frac{\mathrm{d}R}{\mathrm{d}t} = 0, \tag{3.25a}$$

$$\frac{R^2}{2}\frac{\mathrm{d}\epsilon}{\mathrm{d}t} + \epsilon R\frac{\mathrm{d}R}{\mathrm{d}t} - \frac{E}{4\pi}\epsilon = 0. \tag{3.25b}$$

Hence, (3.25a) gives $R(t)$ is constant, which we denote by R_0 (the radius of the initial fluid blob) which is consistent with conservation of mass. Therefore, (3.25b) gives

$$\epsilon = \epsilon_0 \exp\left(\frac{E}{2R_0^2\pi}t\right), \tag{3.26}$$

where ϵ_0 denotes the abscissa of the centre of the initial circular fluid blob. Again, it is clear that for a negative point charge, $E < 0$, the resulting flow is stable and the blob moves through a series of near-circular domains $\Omega(t)$ until a steady state is achieved where $\epsilon(t) \to 0$. That is, the blob approaches a state in which it is circular and has its centre coinciding with the location of the point charge. In the case of a positive charge, $E > 0$, the flow is unstable, since $\epsilon(t)$ grows exponentially, the asymptotic analysis breaks down and it is unlikely that the blob remains near-circular. These predictions are tested numerically in section 3.4.1.

3.4 Numerical results

The numerical results shown here are based on the numerical method presented in chapter 2, section 2.5, where details regarding the inclusion of external fields in the numerical model can be found.

3.4.1 A circular blob subject to an electric point charge

The stability of a circular fluid blob subject to a point charge, discussed in section 3.3.2, is tested numerically. The boundary given by the map (3.19) is considered, with $\alpha = 0.1$, $n = 6$ and an electric point charge is located at the origin. Figure 3.1(a) demonstrates stability for a negative point charge, where disturbances on the boundary are suppressed and the boundary approaches a circle. In figure 3.1(b), on the other hand, for a positive point charge the instability is clear with the disturbances on the boundary growing and the solution rapidly breaking down, as predicted. For this reason only the stable case of $E < 0$ is investigated in the following numerical experiments.

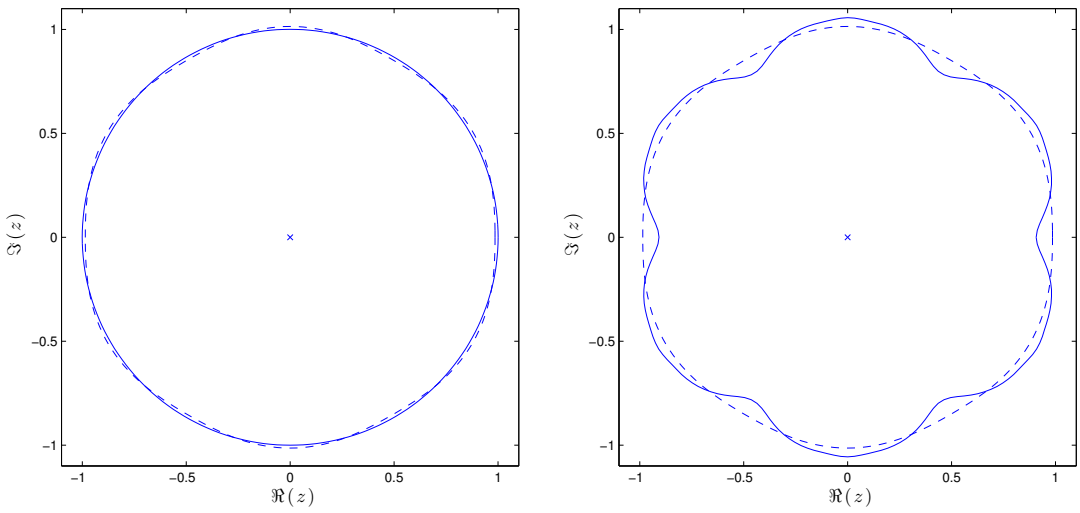

Figure 3.1: Stability of a perturbed circular blob for (a) $E = -\pi$ and (b) $E = \pi$. Initial boundary (dashed) given by (3.19) with $\alpha = 0.1$ and $n = 6$. Boundary shapes are shown at later times (solid) given at (a) $t = 4$ and (b) $t = 0.5$. Here, results are presented for $N = 200$ and step-size $\Delta t = 1.25 \times 10^{-4}$

The analytic solutions presented in section 3.3.3 are also compared with numerical results. At time $t = 0$, a circular blob with radius $R_0 = 1$ centred at $(\epsilon_0, 0)$ is allowed to evolve owing to a fixed electric point charge at the origin with strength $E < 0$.

Here, the main interest is in the quantity $\epsilon(t)$ given in (3.26), i.e. the x-coordinate

of the centre of the circular fluid blob. For comparison purposes, the centre of mass $\bar{\epsilon}$ of the numerically computed blob is defined as

$$\bar{\epsilon}(t) = \frac{1}{A}\iint_{\Omega(t)} x \, \mathrm{d}x\mathrm{d}y, \tag{3.27}$$

where A is the area of the fluid blob which is computed numerically by the formula (2.76). The analytic solution, $\epsilon(t)$, is compared with the numerical results for $\bar{\epsilon}(t)$.

The behaviour of $\bar{\epsilon}(t)$ with t is shown in figure 3.2 for different values of electric point charge, E, with $N = 125$ mesh points on the boundary and step-size $\Delta t = 10^{-4}$. Initially $\epsilon_0 = 0.1$ and $E = -\pi/2$, $-\pi$ and -2π. The numerical and exact solutions are superimposed in figure 3.2 and are in excellent agreement. Plots of $\partial\Omega(t)$ (not shown) establish that the boundary remains very close to circular throughout its motion.

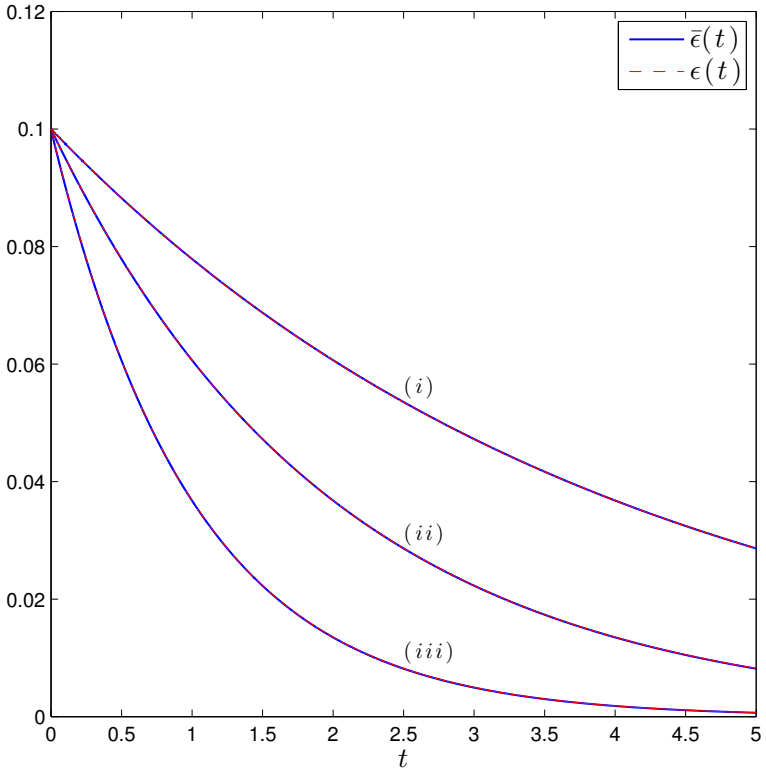

Figure 3.2: Evolution of the centre of mass, $\bar{\epsilon}(t)$, superimposed with the analytic solution (3.26) for the centre of the circle, $\epsilon(t)$, of a circular fluid blob with initial centre $(\epsilon_0, 0)$ such that $\epsilon_0 = 0.1$ and radius $R_0 = 1$. Three cases for increasing point charge strength are shown: (i) $E = -\pi/2$, (ii) $E = -\pi$ and (iii) $E = -2\pi$.

The numerical method is used to investigate the evolution of the boundary for larger choices of ϵ_0 for which the analytical result (being a small-ϵ theory) does not necessarily hold. Figure 3.3 shows the evolution of the centre of mass, $\bar{\epsilon}(t)$, compared with the prediction from the analytic solution, $\epsilon(t)$, in the cases $\epsilon_0 = 0.25$ and $\epsilon_0 = 0.5$. It is apparent that there is no longer excellent agreement between the analytical and numerical solutions, as expected, since the assumption of small ϵ was made in section 3.3.3. Nevertheless, even in this non-asymptotic regime the comparison is good. Figures 3.4 and 3.5 show snap shots of the evolving boundary corresponding to the results of figure 3.3. It is clear that the boundary shape remains closely circular during its evolution and that by $t = 10$ the blob is circular with centre coinciding with the point charge.

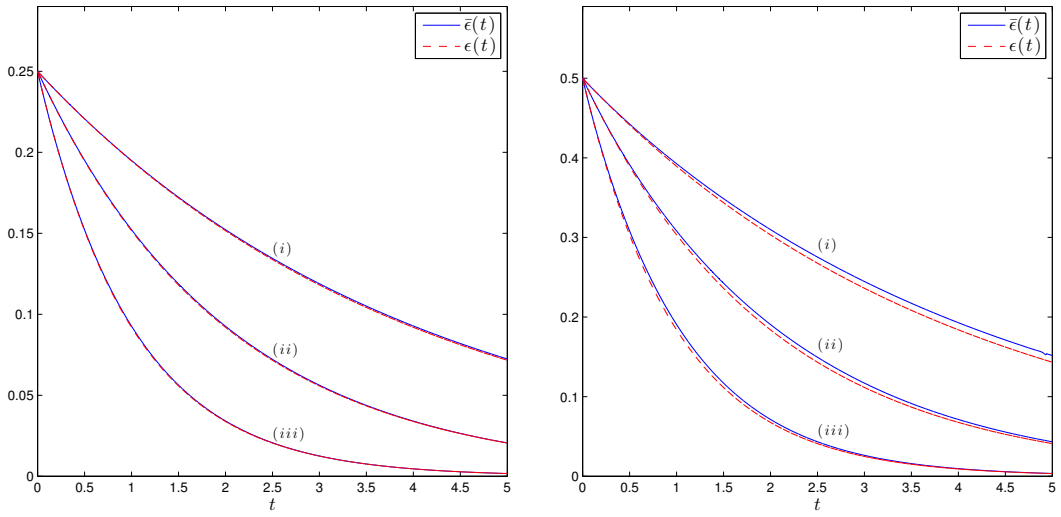

(a) $\epsilon_0 = 0.25$. (b) $\epsilon_0 = 0.5$.

Figure 3.3: Evolution of the centre of mass, $\bar{\epsilon}(t)$, superimposed with the analytic solution (3.26) for the centre of the circle, $\epsilon(t)$, of an initially circular fluid blob centred at $(\epsilon_0, 0)$ with radius $R_0 = 1$. Three cases for increasing point charge strength are shown: (i) $E = -\pi/2$, (ii) $E = -\pi$ and (iii) $E = -2\pi$.

The case in which ϵ_0 is chosen such that the electric point charge is close to the initial boundary (i.e. ϵ_0 is comparable to R_0), but still within the fluid domain, is also studied. For such a set-up the evolution of the boundary is shown in figure 3.6. Initially, a 'pinching' of the boundary can be seen near the point charge—see

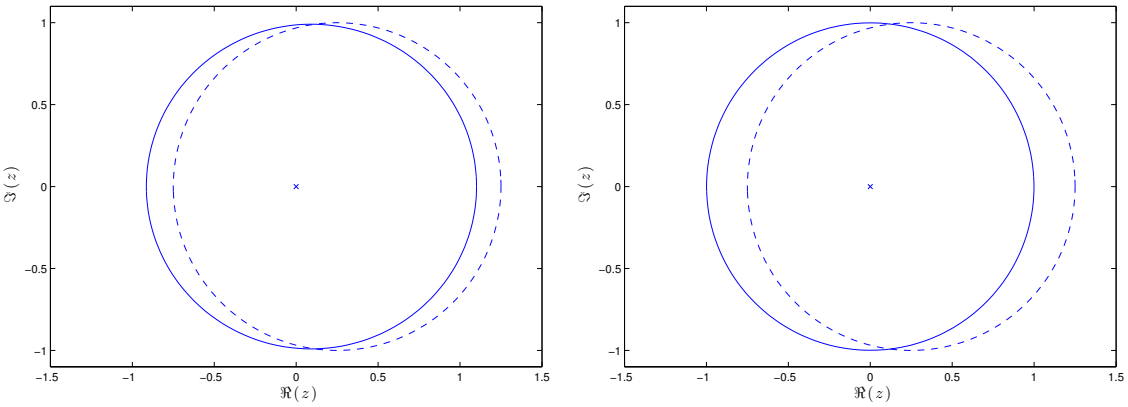

(a) $t = 1$. (b) $t = 10$.

Figure 3.4: Snapshots of the evolving boundary (solid) of an initially circular fluid blob (dashed) of radius $R_0 = 1$ centred at $(\epsilon_0, 0)$ with $\epsilon_0 = 0.25$. An electric point charge of strength $E = -\pi$ is located at the origin (marked by the cross).

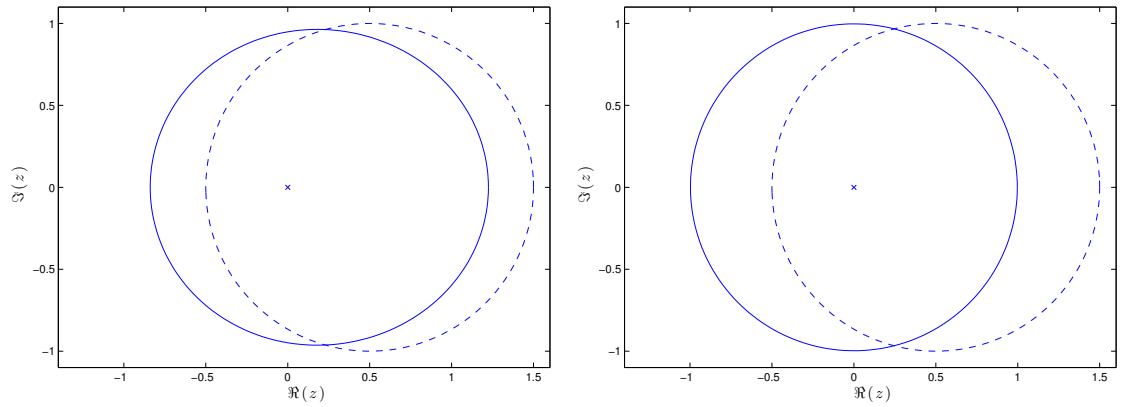

(a) $t = 1$. (b) $t = 10$.

Figure 3.5: Snapshots of the evolving boundary (solid) of initially circular fluid blob (dashed) of radius $R_0 = 1$ centred at $(\epsilon_0, 0)$ with $\epsilon_0 = 0.5$. An electric point charge of strength $E = -\pi$ is located at the origin (marked by the cross).

figure 3.6(b)—after which the blob evolves through a smooth sequence of elliptical and egg-like domains. Finally, for large time, the fluid blob tends to the same steady state as for small ϵ_0. That is, the fluid blob becomes symmetrised about the location of the point charge, adopting a circle of radius R_0 centred at the origin.

A 'random' boundary shape, $\partial\Omega(0)$, of area π is generated using [142]. The numerical procedure is used to compute the evolution of the blob with a negative point charge located within the closed boundary. The expected symmetrising of the fluid blob to a unit circle about the point charge is demonstrated in figure 3.7.

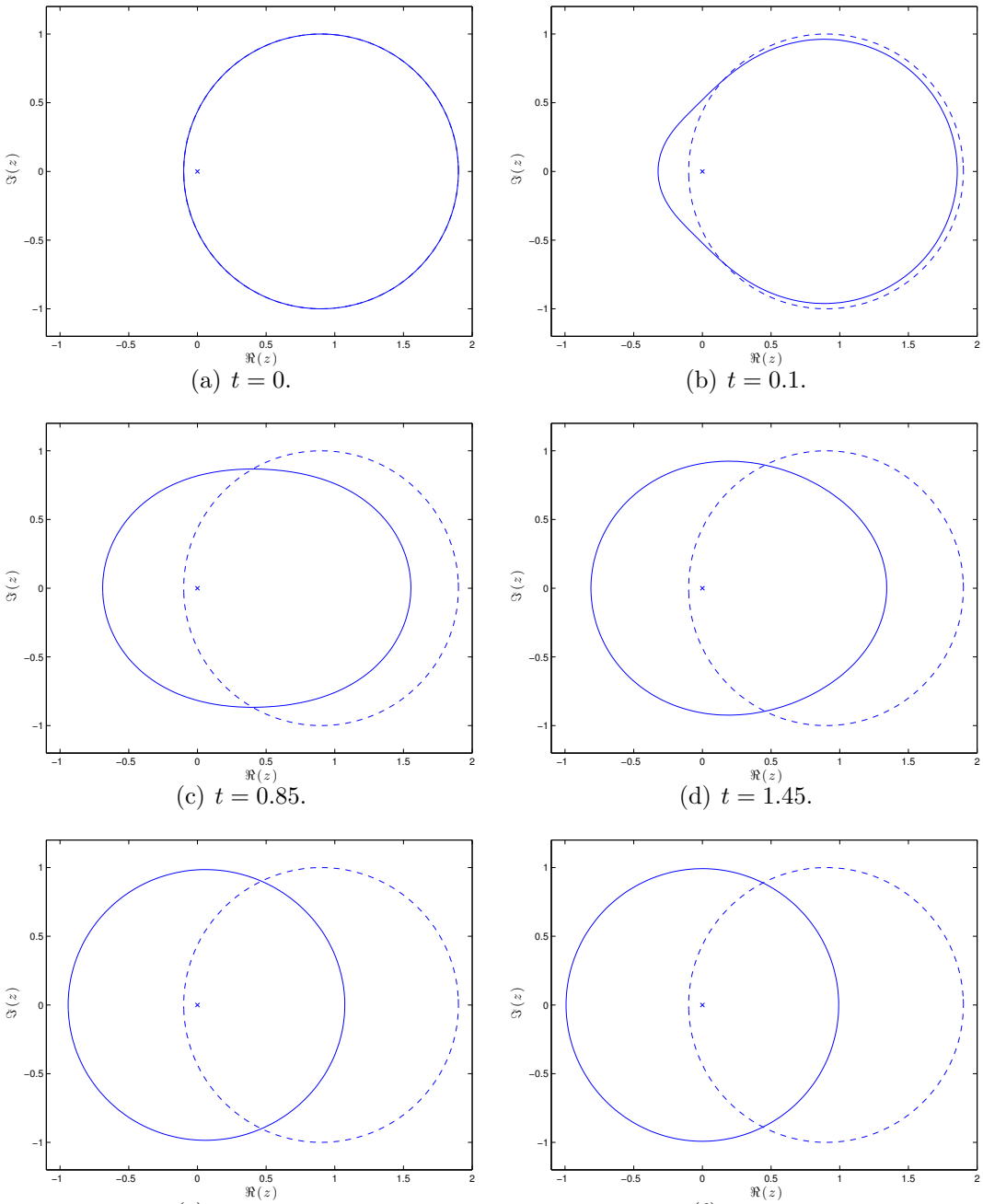

(a) $t = 0$. (b) $t = 0.1$.

(c) $t = 0.85$. (d) $t = 1.45$.

(e) $t = 2.85$. (f) $t = 10$.

Figure 3.6: Snapshots showing the evolution of the free boundary (solid) of an initially circular fluid blob (dashed) centred at $(\epsilon_0, 0)$ with $\epsilon_0 = 0.9$ and radius $R_0 = 1$. An electric point charge of strength $E = -2\pi$ is located at the origin (marked by a cross).

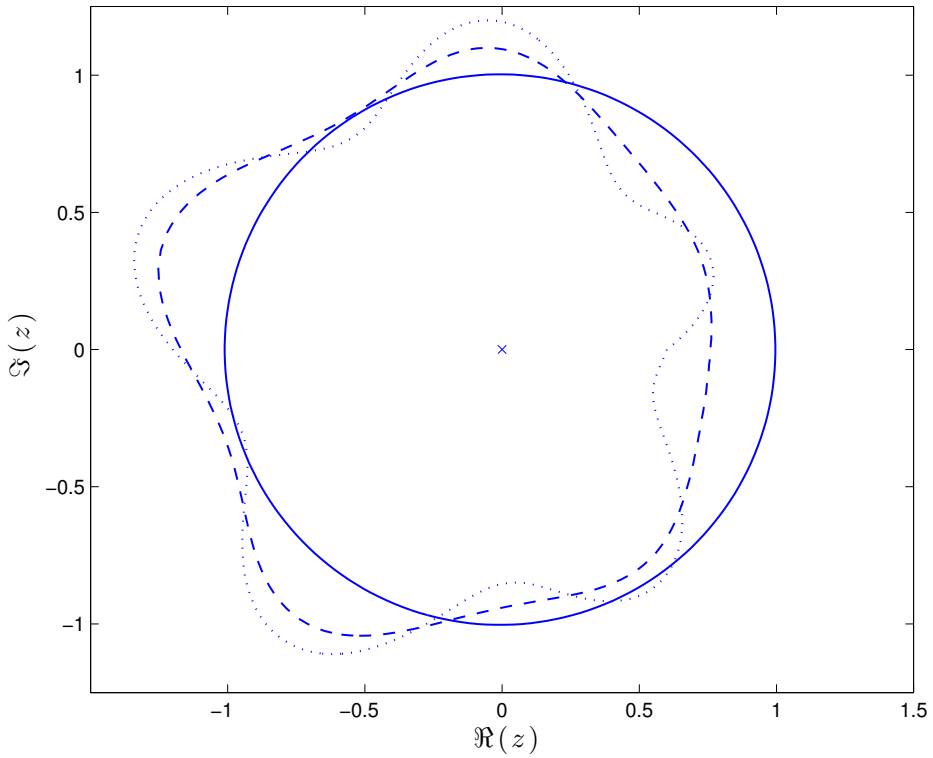

Figure 3.7: An initially 'random' boundary shape (dotted) with an electric point charge of strength $E = -\pi$ located at the origin (marked by the cross). Evolution of the boundary is shown at $t = 1.2$ (dashed) and $t = 22$ (solid). Here, the results are presented for $N = 200$ and step-size $\Delta t = 4.89 \times 10^{-4}$.

3.4.2 Delaying cusp formation in sink driven flows using an electric point charge

The formation of cusps in time-dependent Hele-Shaw flows have been, and still are, of particular interest, see e.g. [14, 25, 56, 62]. For example, it aids understanding of practical applications such as the extraction of oil which can be modelled by a Hele-Shaw flow driven by a hydrodynamic sink singularity within the oil region [75].

Consider a fluid blob with free boundary, $\partial\Omega(t)$, given by the following polynomial map from the unit ζ-disc:

$$z = a\zeta + b\zeta^n, \tag{3.28}$$

where $a(t)$ and $b(t)$ are real, time-dependent coefficients, with a point sink located at the origin. For this map it is known that the free boundary evolves through a series

of limaçon shapes, eventually leading to cusp formation—see figure 3.8(a)—in finite time, t^*, beyond which the boundary map no longer remains univalent [25, 48].

Suppose now that an electric point charge of strength $E < 0$ is placed within the fluid domain, with the aim of delaying the formation of the cusp on the boundary, thus enabling a greater proportion of fluid to be withdrawn before the solution breaks down. In section 3.4.1 it is shown that a negative point charge within the fluid domain provides a symmetrising effect on the boundary about the point charge. A domain with disturbances on its boundary would typically produce cusps over time in a sink driven flow. On the other hand the point charge, through its symmetrising effect, would be expected to suppress the development of cusps.

To assess this competition, a fluid blob with initial shape given by (3.28) with $a(0) = 1$, $b(0) = 0.1$ and $n = 2$, and a point sink of strength $Q = -1$ at $z = 0$, is allowed to evolve for the two cases when (a) there is no electric charge at $z = 0$ (analytic solution shown), and (b) $E = -5\pi$. As expected, $E = 0$ leads to a breakdown of the solution after finite time $t^* \approx 1.67$. For $E < 0$, the solution lasts far longer ($t > 3$) enabling most of the fluid to be withdrawn—see figure 3.8(b). The boundary can be made to enclose an arbitrarily small region depending on the numerical parameters (i.e. time-step and resolution) chosen. Here, there are $N = 100$ mesh points on the boundary and step-size $\Delta t = 10^{-4}$.

3.4.3 Stability of steady solutions

Some non-trivial steady exact solutions of the problem given by (3.12) have previously been found by Entov and Etingof [39] and McDonald [89] involving combinations of hydrodynamic singularities and electric point charges. Such solutions can be derived, as shown in [89] and example 1.3.5, by considering the balance between the terms $\partial w/\partial z$ and $\partial M/\partial z$ of (3.15) as singularities inside $\Omega(t)$ are approached. The stability of the steady solutions found in [39, 89] is an open question and is

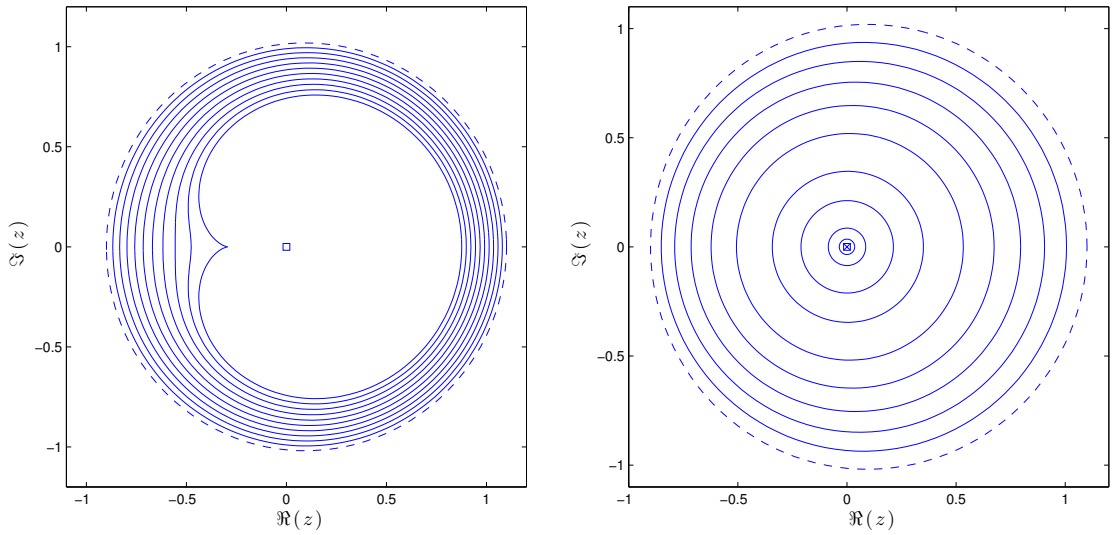

(a) (b)

Figure 3.8: Comparison between the time evolution of free boundaries for (a) cusp formation due to a sink driven flow (analytic solution) with sink strength $Q = -1$ (marked by the square), and (b) a superposition of a sink and an electric charge (numerical solution) with $Q = -1$ and $E = -5\pi$ (marked by a square and a cross respectively). A cusp forms at $t^* \approx 1.67$ in (a), the final time is shown. The final time shown in (b) is $t = 3.17$. In both (a) and (b) the initial boundary (dashed) is given by the map (3.28) with $a(0) = 1$, $b(0) = 0.1$ and $n = 2$.

investigated numerically in this section.

Consider the exact steady solution of Entov and Etingof [39] given by the boundary map from the unit ζ-disc to the blob in the z-plane given by

$$z = \sqrt{ab}\left(\frac{1-\alpha\zeta}{1+\alpha\zeta}\right)^{1/\lambda}, \tag{3.29}$$

where $\lambda = E/2Q$ and

$$\alpha = \sqrt{\frac{1-(a/b)^{\lambda/2}}{1+(a/b)^{\lambda/2}}}. \tag{3.30}$$

Here, the flow is driven by a point source of strength Q located at $z = a$, a point sink of strength $-Q$ at $z = b$ ($a, b \in \mathbb{R}$, $b > a$) and an electric point charge of strength E located at $z = 0$, which is outside the fluid domain. The stability of the steady solution is demonstrated numerically for large time—see figure 3.9(a). Simulations are run for $t = T$, where T is a characteristic time scale for the flow calculated as

$T \sim L^2/Q$, where L is taken to be the maximum blob width in the x-direction. There is little deviation between initial and final blob shapes after this long time.

The stability of the free boundary subject to an electric point charge lying within the fluid domain is analysed in section 3.3.2. Since here the electric point charge lies on the exterior of the fluid domain, it is expected that the flow is unstable for negative point charge strength. Reversing the sign of the source and sink strengths and point charge, the stability of the above steady solution (which is still a steady solution under change of sign of Q and E) is tested using the time-dependent numerical solution. Figure 3.9(b) shows the rise of an instability on the free boundary close to the electric point charge in much shorter time as compared to the characteristic time T, and the solution rapidly breaks down. Therefore, the numerical results suggest the solution given by (3.29) is only stable for positive point charge strength, E. The change in stability properties when swapping signs of E and Q is consistent with (3.15), which implies that the two resulting evolutions are time reversals of each other. Figures 3.9(c) and 3.9(d) show the free boundary at time immediately before breakdown of the solution. The numerical breakdown of the solution could possibly be due to the formation of high curvature leading to a cusp on the free boundary. Alternatively, the breakdown could result from the numerical formulation, as a point charge lying on the free boundary, $\partial\Omega(t)$, would provide a singularity in the discretisation formulae if a mesh point and the point charge were to coincide.

Figures 3.10 and 3.11 show instabilities arising on the boundaries for steady solutions given in [89] by

$$z(\zeta) = -a \tanh\left(\sqrt{\frac{-\mu}{aE}}\zeta\right), \tag{3.31}$$

for a dipole of strength μ located at $z = 0$ and electric point charges $\pm E$ at $z = \pm a$

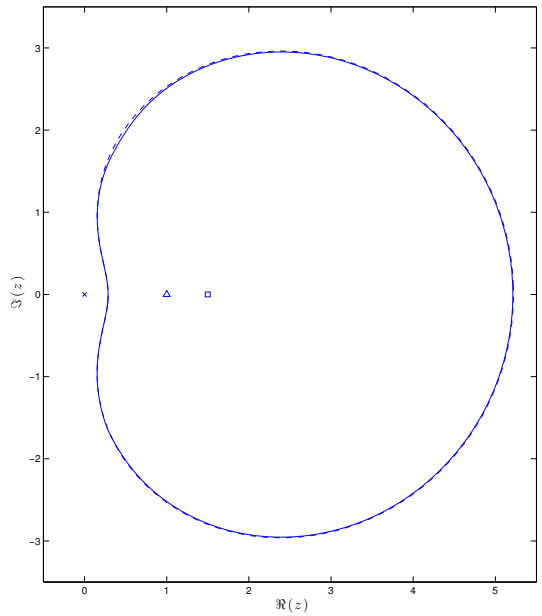

(a) $t_e = 25$, $E = 0.3909$.

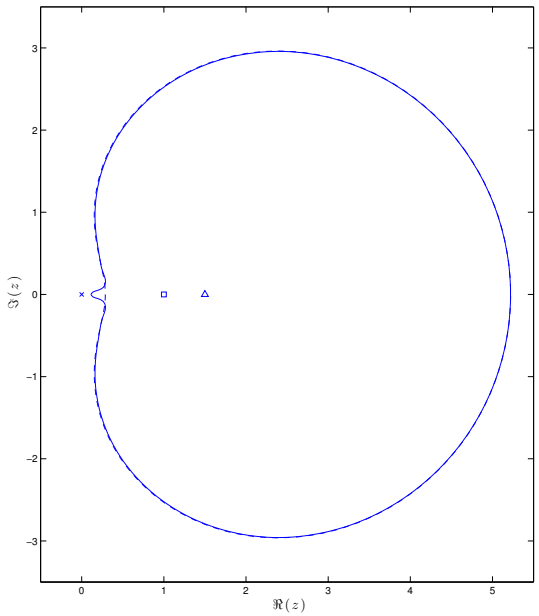

(b) $t_e = 4.2496$, $E = -0.3909$.

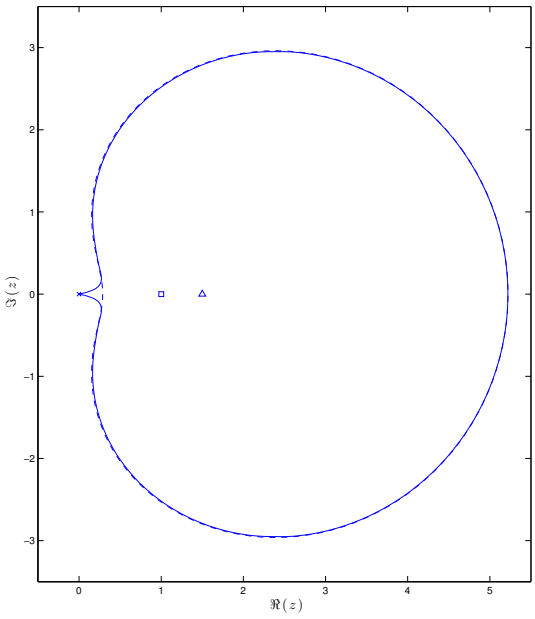

(c) $t_e = 4.5696$, $E = -0.3909$.

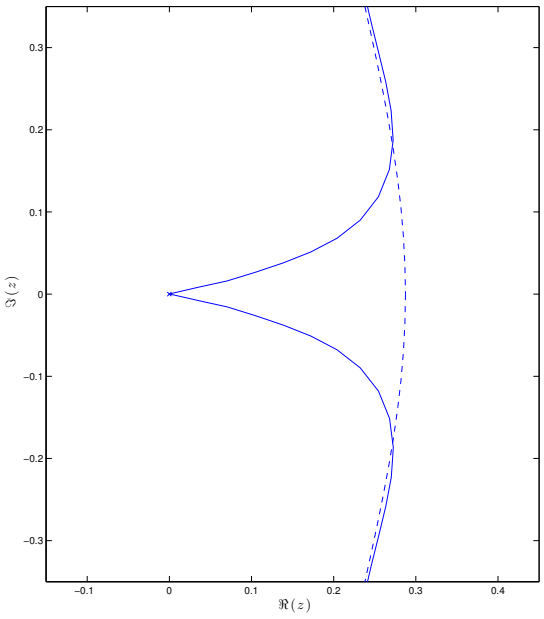

(d) Close up of (c).

Figure 3.9: Testing the stability of the steady solution boundary shape given by (3.29) for $a = 1$ and $b = 1.5$, where (a) $E = 0.3909$, $Q = 1$. In (b), (c) and (d) $E = -0.3909$, $Q = -1$. The boundary shape at initial time $t = 0$ (dashed) and at later time $t = t_e$ (solid) are shown. The electric point charge, source and sink are marked by a cross, triangle and square, respectively. In the results presented $N = 500$, step-size $\Delta t = 5 \times 10^{-4}$ and $L = 4.9331$

($a \in \mathbb{R}$), and

$$z = a\sqrt{\frac{1-\exp\left(-\sqrt{\frac{2\delta}{E}}\frac{\sqrt{a^2+b^2}}{ab}\zeta^2\right)}{1+\frac{a^2}{b^2}\exp\left(-\sqrt{\frac{2\delta}{E}}\frac{\sqrt{a^2+b^2}}{ab}\zeta^2\right)}}, \tag{3.32}$$

with a quadrupole of strength δ at $z = 0$ and electric point charges $-E$ at $z = \pm a$ and E at $z = \pm ib$ ($a, b \in \mathbb{R}$), respectively. Since in both of these exact steady solutions there are negative point charges lying outside of the fluid domain, the flow is unstable. It is evident (within short time) that the instabilities on the free boundary are prominent in regions closest to the negative point charges. Figures 3.10(c) and 3.10(d) show the free boundary at time immediately before breakdown of the solution when a mesh point lying on the horizontal axis and the point charge coincide. The solution of the free boundary in figure 3.11 eventually breaks down in a similar manner.

McDonald [89], also gives a family of exact steady solutions for an electric point charge of strength E, lying within the fluid domain, superimposed on a hydrodynamic n-pole of strength M at $z = 0$, given by

$$z = \beta\zeta\exp\left(\frac{2M}{E\beta^n}\zeta^n\right), \tag{3.33}$$

for some parameter β. The stability of the solution is demonstrated for negative charge E in figure 3.12(a), which shows the case for a hydrodynamic dipole ($n = 1$). The characteristic time scale for the flow is $T \sim L^3/M$. The case for positive charge is also tested, and the solution no longer remains steady, developing instabilities on the free boundary and then the solution breaks down rapidly, as expected—see figure 3.12(b). This is due to the aforementioned unstable nature of a positive point charge lying within the fluid blob (c.f. section 3.4.1). Note again that swapping the signs of the forcing and electric charge changes the stability properties.

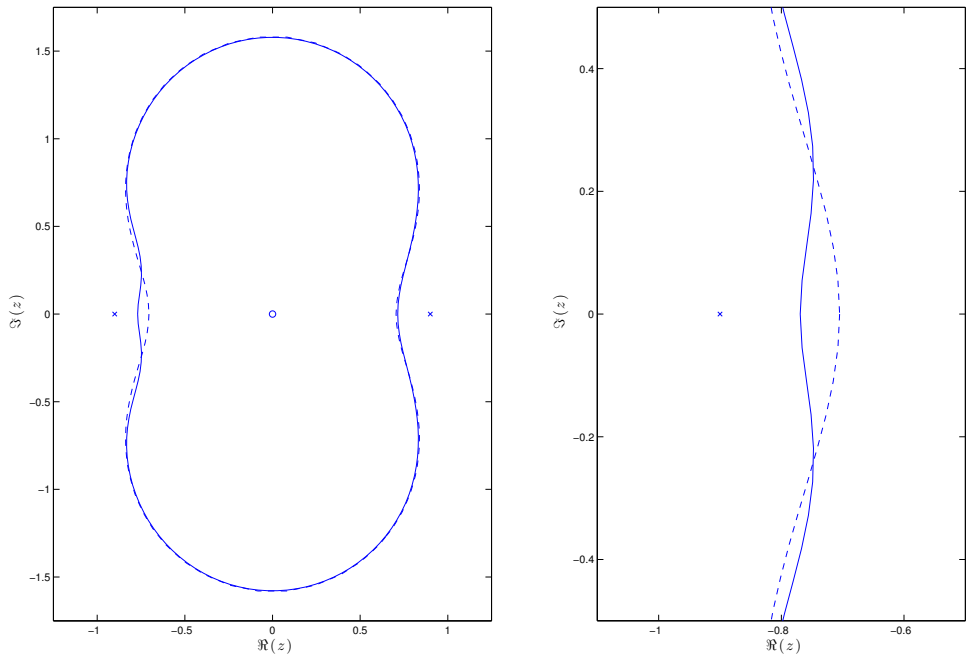

(a) $t_e = 0.5$. (b) Close up of (a).

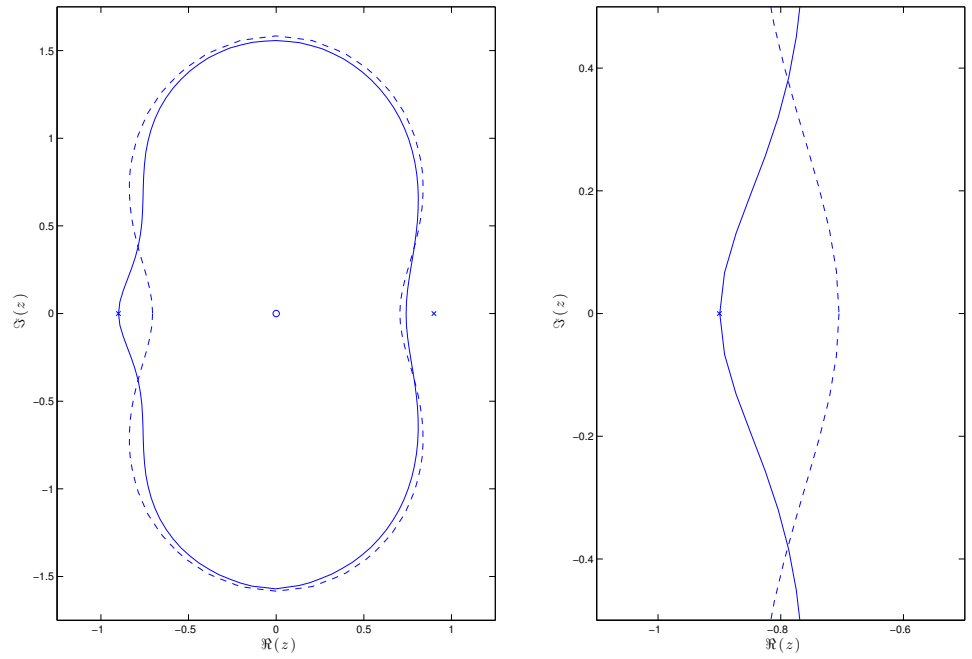

(c) $t_e = 1.04$. (d) Close up of (c).

Figure 3.10: Testing the stability of the steady solution boundary shape given by (3.31) for $a = 0.9$, $\mu = -1$ with $E = \pm 1$ at $z = \pm a$. The boundary shape at initial time $t = 0$ (dashed) and at time $t = t_e$ (solid) are shown. The dipole and electric point charges are marked by a circle and crosses, respectively. In the results presented $N = 100$ and step-size $\Delta t = 1.25 \times 10^{-5}$.

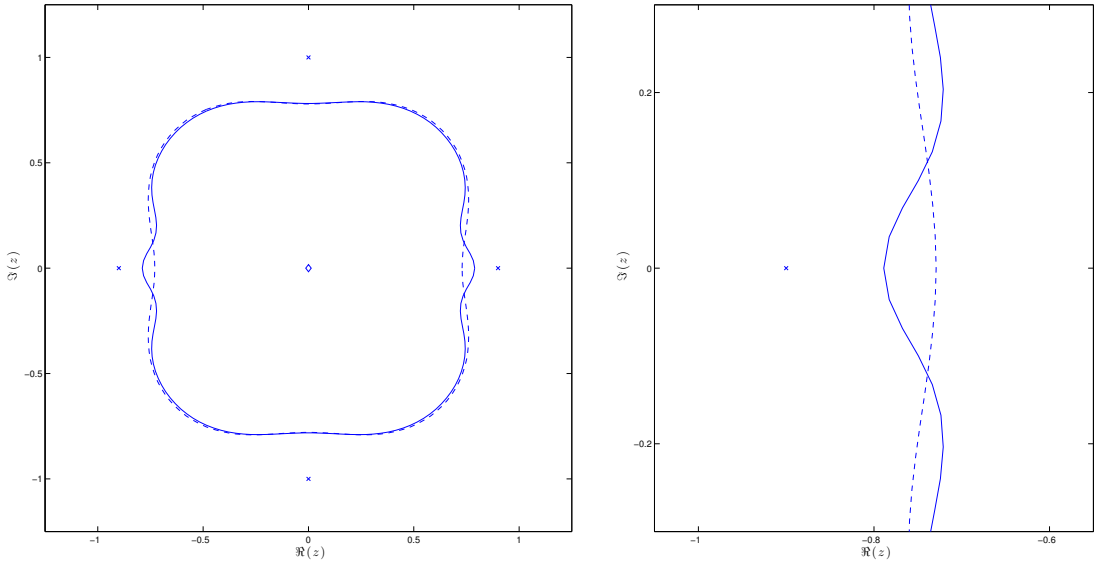

(a) (b)

Figure 3.11: Testing the stability of the steady solution boundary shape given by (3.32) for $a = 0.9$, $b = 1$, $\delta = 0.5$ with $E = -1$ at $z = \pm a$ and $E = 1$ at $z = \pm ib$. The boundary shape at initial time $t = 0$ (dashed) and at time $t = 0.5$ (solid) are shown. The quadrupole and electric point charges are marked by a diamond and crosses, respectively. In the results presented $N = 100$ and step-size $\Delta t = 1.25 \times 10^{-5}$.

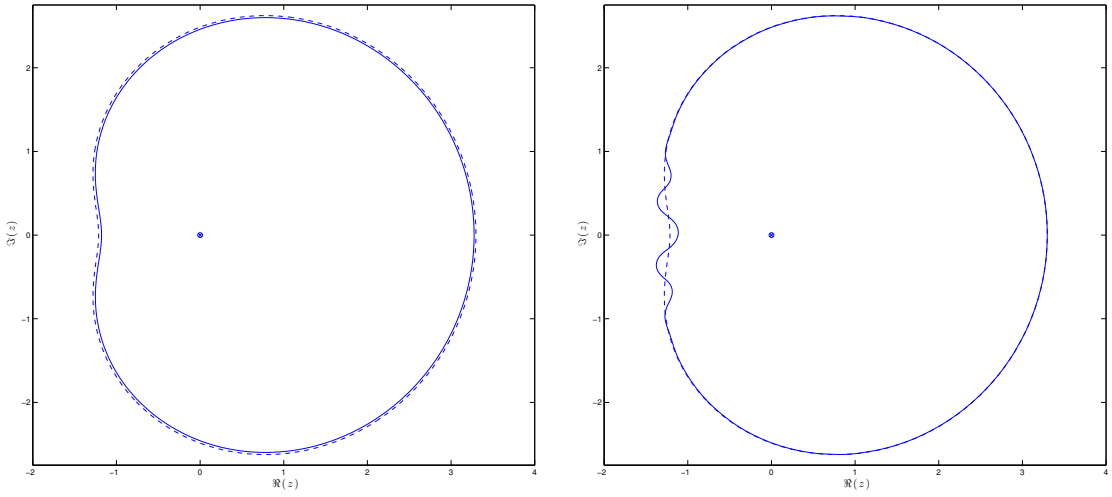

(a) $t_e = 90$, $E = -1$. (b) $t_e = 9$, $E = 1$.

Figure 3.12: Testing the stability of the steady solution boundary shape given by (3.33) for $\beta = 2.0$, $M = E/2$ and $n = 1$, where (a) $E = -1$ and (b) $E = 1$. The boundary shape at initial time $t = 0$ (dashed) and at later time $t = t_e$ (solid) are shown. The quadrupole and electric point charge are marked by a circle and cross, respectively. In the results presented $N = 500$, step-size $\Delta t = 3.33 \times 10^{-4}$ and $L = 4.4669$.

3.5 Summary

It has been shown that for a Hele-Shaw free boundary flow, if a negative electric point charge lies inside the fluid domain $\Omega(t_0)$, where its boundary $\partial\Omega(t_0)$ is a simple, smooth curve such as a circle, the resulting evolution of the free boundary $\partial\Omega(t)$ is stable. Furthermore, the boundary remains smooth for all time and tends to a steady state which is circular and centred about the point charge. The family of curves through which the boundary evolves depends on the location of the point charge relative to the initial boundary, as displayed in section 3.4.1. It has been shown analytically, in section 3.3.3, that if the location of the point charge is sufficiently close to the centre of a circular fluid blob, the family of curves the boundary evolves through are approximately circular, for which the numerical results (based on a boundary integral method) show excellent agreement.

It has been shown that for a positive point charge lying within the fluid domain, the evolution of the free boundary is unstable. In section 3.4.3, the stability of some exact solutions were tested numerically, where electric point charges of strength E lay outside of the fluid domain. The numerical results suggest that for $E > 0$, the evolution of the boundary is stable, whilst for $E < 0$, it is unstable.

For the exact steady solutions given by (3.29) and (3.33), numerical results show no instability on the free boundary after some characteristic time scale, provided that the sign of electric charge is negative within the fluid blob, and positive when lying outside the fluid blob. Although this does not prove stability or otherwise, by demonstrating that a solution stays close to the original exact, steady solution on some characteristic time scale, we conjecture that such solutions are likely to be stable. It is important to note that the solution breaks down in much shorter time (compared to the characteristic time) in the corresponding unstable cases.

Chapter 4

Unsteady translating bubbles in a Hele-Shaw cell

The main results from this chapter have been submitted for publication in the paper entitled 'On the motion of unsteady translating bubbles in an unbounded Hele-Shaw cell' [72].

The motion of a traveling bubble in a Hele-Shaw cell is a long-standing free boundary problem, which was first considered mathematically and experimentally by Saffman and Taylor [123, 138] in the late 1950s. The motion of a single travelling bubble has proven to be a difficult problem which yields a rich class of solutions, and the literature is littered with plenteous work regarding the *selection problem*—see section 4.1. Here, we consider a simpler problem of a travelling bubble in an unbounded Hele-Shaw cell as compared with that of the original works of Saffman and Taylor [123,138] where the flow domain is constrained by a parallel sided channel.

Bubble breakup (or blob pinch-off) and the associated change in topology has been of interest in Hele-Shaw flow. The breakup of a bubble, mainly due to contraction (by the suction of air from the bubble domain) has been previously considered [38, 80]. In [38], a system of contracting bubbles are also considered where breakdown of the solution is due to the formation of a cusp on one of the bubble

interfaces. The Schwarz function of the interface is used to study, in detail, the form of the interface when bubble breakup occurs (local to the point of breakup) in [80]. In particular, left-right symmetry about the point of bubble breakup is considered in the case of ZST Hele-Shaw flows and the connection of the governing equation to the dispersionless string equation of soliton theory is also explored.

Blob pinch-off has also been studied, see e.g. [4], where the interplay of centrifugal and capillary forces are considered and it is found that an initially dumbbell shaped blob in a rotating Hele-Shaw cell may pinch-off into two disconnected parts (as well as possibly stretching to infinity or becoming circular—c.f. example 1.3.5). Similar topological evolution, i.e. pinch-off of a viscous blob into the inviscid domain is considered in [97] in the case of ZST Hele-Shaw flow. The deformation of blobs and bubbles, including surface tension effects, have also been considered in 2D flows of ideal fluids induced by circulation [18], which may be applicable to Hele-Shaw flows given the effective 2D potential nature of the Hele-Shaw equation (1.11). In [18], steady equiliberia interface shapes are found which exist up to the point of steady pinch-off or breakup of a blob or bubble respectively.

The breakup of a stream of bubbles rising in a Hele-Shaw cell has also been considered experimentally, where a stack of bubbles rising in a Hele-Shaw cell may split in two streams by individual bubbles in the stack breaking up in a symmetric fashion [87]. There, the shape of a single bubble rising in a Hele-Shaw cell at different inclination angles to the horizontal are also considered, however, the breakup of a single travelling bubble is not observed.

Notwithstanding the work described above, the relatively simple but fundamental problem of a single travelling bubble in an unbounded Hele-Shaw cell does not appear to have been studied previously in the literature. The aim of the latter part of this chapter will be to consider the break up, or pinch-off, for various initial bubble shapes in ZST Hele-Shaw flows. It is shown in sections 4.3.2 and 4.3.3 that singularities of

the Schwarz function of the initial interface play an important role in the evolution of the interface, in that the bubble 'avoids' contact with the singular point.

In section 4.1 we discuss briefly the travelling finger and bubble solutions of Saffman and Taylor [123, 138]. The steady (rotated) elliptical solution of Tian and Vasconcelos [140] is revisited in section 4.2 using the Schwarz function approach, and the stability of the elliptical solution is tested numerically in section 4.3. The stability is also discussed analytically by considering a perturbed ellipse in section 4.4. We end this chapter with a summary in section 4.5.

4.1 The Taylor-Saffman bubble in an unbounded Hele-Shaw cell

Taylor and Saffman [138] considered the now well-known problem of a translating bubble, symmetric about the channel centreline in a Hele-Shaw cell, in which the viscous fluid region is constrained by a parallel sided channel. They found a family of solutions governed by the bubble speed and maximum bubble width. Previous to this, Saffman and Taylor [123] considered the motion of an infinitely long bubble in the channel (the Saffman-Taylor finger), where the observed 'selected' solution is half the width of the channel. The so called 'selection' of these particular width fingers can be explained by introducing surface tension and then taking the limit as surface tension tends to zero [133, 145].

Taylor and Saffman [138] conjectured that in the case of a small bubble in a channel (or equivalently an arbitrary sized bubble in an unbounded cell), surface tension effects are comparable with changes in fluid pressure near the bubble interface and it is the surface tension that makes the perimeter of the bubble as short as possible, therefore the bubbles evolves into a circle, which travels at speed twice that of the background flow, i.e. $U = 2V$, where U denotes the speed of the propagating

bubble and V the speed of the uniform background flow. Following the works of Taylor and Saffman [123, 138], much work has been carried out on the selection problem numerically, experimentally and theoretically, some of which are cited here [58, 70, 96, 128, 133–136, 145, 149] (see also references therein).

More recently, the selection of particular solutions of the solution family has been proposed as a fundamental stability property of ZST Hele-Shaw flows [96, 99, 149]. In this sense, surface tension can be viewed as a perturbation on the free boundary that forces the interface to the selected shape (observed in [123, 138]) whilst regularising high curvatures. In [96], the selection of the infinitely long finger travelling in the channel was considered. It was shown, using stability analysis, that when the selection problem is solved in the absence of surface tension for a particular class of solutions, the travelling finger with half the channel width is still selected. That selection is determined entirely by the ZST dynamics has led to much debate in the literature [3, 13, 70, 94, 95, 124]. Moreover, the ZST problem is ill-posed in the sense that small perturbations may cause large effects in the resulting interface evolution [128, 136]. The present work uses numerical smoothing to regularise the problem enabling convergent numerical results to be computed. The choice to use smoothing rather than surface tension offers an alternative way to understand the selection problem for bubbles in an unbounded Hele-Shaw cell.

The result of [96] has recently been extended to a finite bubble travelling in a channel [149], where it is demonstrated that the bubble with propagation speed $U = 2V$ is selected as it is a fixed point attractor of the ZST translating bubble problem. In an unbounded Hele-Shaw cell, or equivalently, the small bubble limit in a channel geometry, the attractor is the circular bubble. In this thesis, the ZST problem for unsteady bubbles in an unbounded cell is studied numerically. The selection problem is considered as well as cases of bubble breakup.

For a bubble in the presence of a uniform steady background flow with speed V,

the free boundary problem (1.17) is supplemented with the condition

$$\phi \to Vx, \quad \text{as } |\mathbf{x}| \to \infty, \tag{4.1}$$

i.e. there exists a uniform background flow, taken to be parallel to the x-axis w.l.o.g. Therefore, due to the pressure gradient, the bubble translates downstream at speed $U(t)$ which needs to be determined along with the bubble shape, $\partial\Omega(t)$. In the following section we use the Schwarz function approach to demonstrate how the speed and direction of propagation of a bubble may be calculated, in particular for a rotated ellipse. An alternative method has been presented by Tian and Vasconcelos [140] for the same problem.

4.2 Steady elliptical solution and rotational invariance

The elliptical bubble is a steady solution of the Hele-Shaw free boundary problem in an unbounded cell, and so is any rotation of the ellipse due to the rotational invariance of steady Hele-Shaw flows [140]. That is, the map given by

$$z = C + e^{i\theta_e}\left(a\zeta + \frac{b}{\zeta}\right) \tag{4.2}$$

is a solution to the Hele-Shaw problem, where the time-varying parameters a, b and θ_e (later shown to be constant) are real such that $b \neq 0$, and in general C is complex valued. Here, (4.2) represents a conformal map from the interior of the unit ζ-disc, D, to the exterior of the bubble, i.e. the flow domain $\Omega(t)$. The interface $\partial\Omega(t)$ is mapped from the unit ζ-circle, i.e. ∂D. The speed of the bubble can be found using the Schwarz function approach as follows. First, considering the map (4.2),

the Schwarz function of $\partial\Omega(t)$ is given by

$$\begin{aligned} g &= \bar{z}(1/\zeta, t) \\ &= \overline{C} + e^{-i\theta_e}\left(\frac{a}{\zeta} + b\zeta\right). \end{aligned} \tag{4.3}$$

As $\zeta = 0$ maps to infinity, from (4.2) we see that

$$\zeta = \frac{be^{i\theta_e}}{z - C} + \mathcal{O}((z-C)^{-3}), \qquad \text{as } z \to \infty, \tag{4.4}$$

and thus the time derivative of the Schwarz function in (4.3) as $z \to \infty$ is given by

$$\frac{\partial g}{\partial t} = \frac{\mathrm{d}\overline{C}}{\mathrm{d}t} + \frac{a}{b}(z-C)\frac{\mathrm{d}}{\mathrm{d}t}(e^{-2i\theta_e}) + e^{-2i\theta_e}\frac{\mathrm{d}}{\mathrm{d}t}\left(\frac{a}{b}(z-C)\right) + \mathcal{O}((z-C)^{-1}). \tag{4.5}$$

If the background flow is given by a uniform flow of speed V, then as $z \to \infty$ the complex potential takes the form $w = Vz$. Since the Schwarz function equation (1.46) must hold over $\Omega(t)$, using (4.5), as $z \to \infty$ at $\mathcal{O}(1)$ and $\mathcal{O}(z)$ we find

$$\frac{\mathrm{d}}{\mathrm{d}t}\left(\overline{C} - e^{-2i\theta_e}\frac{a}{b}C\right) = 2V, \tag{4.6a}$$

$$\frac{\mathrm{d}}{\mathrm{d}t}\left(e^{-2i\theta_e}\frac{a}{b}\right) = 0. \tag{4.6b}$$

In addition to (4.6a) and (4.6b), the bubble area, A, must also be constant where

$$\begin{aligned} A &= \left|\frac{1}{2i}\oint_{\partial D}\bar{z}z'\mathrm{d}\zeta\right| \\ &= \pi\left|a^2 - b^2\right|, \end{aligned} \tag{4.7}$$

and is calculated using the complex form of Green's theorem. That is, $|a^2 - b^2| = A/\pi$ = constant and together with (4.6b) implies that a, b and θ_e are constant.

Employing (4.6b) in (4.6a), and taking the real and imaginary parts gives

$$\dot{C}_R - \frac{a}{b}\left(\dot{C}_R\cos(2\theta_e) + \dot{C}_I\sin(2\theta_e)\right) = 2V, \tag{4.8a}$$

$$-\dot{C}_I - \frac{a}{b}\left(\dot{C}_I\cos(2\theta_e) - \dot{C}_R\sin(2\theta_e)\right) = 0, \tag{4.8b}$$

where C_R and C_I denote the real and imaginary parts of $C(t)$, respectively. Here, the dot denotes derivative with respect to time. Solving $\dot{C}_R$ and $\dot{C}_I$ from (4.8), and integrating with the initial condition $C(0) = 0$, yields

$$C(t) = \frac{2Vt}{1 - a^2/b^2}\left(1 + \frac{a}{b}\cos(2\theta_e) + i\frac{a}{b}\sin(2\theta_e)\right), \tag{4.9}$$

where $U = \dot{C}$ gives the bubble velocity. That is, the angle at which the bubble propagates steadily is given by $\tan^{-1}\left([(a/b)\sin(2\theta_e)]/[1 + (a/b)\cos(2\theta_e)]\right)$, measured from $\Re(z)$, which agrees with the result given by Tian and Vasconcelos [140]. In [140], a complex variable technique is used where, by considering an appropriate frame of reference, the kinematic condition is used to write down the velocity potential. Note that for a circular bubble $a = 0$ and from (4.8a) and (4.8b) $U = 2V$, i.e. the bubble propagates in the purely real direction with speed twice that of the background flow.

4.3 Numerical simulations of a translating bubble

The stability of the steady elliptical solution given by (4.2) is tested numerically in section 4.3.1. In section 4.3.2, numerical experiments are carried out which lead to the breakup of a single bubble in to multiple bubbles in an unbounded Hele-Shaw cell. In section 4.3.3, a different type of topological change is observed where a fluid blob is seen to pinch off inside a bubble which initially has a simple closed interface.

4.3.1 Attraction of an elliptical bubble to a circular bubble

Consider an initially elliptical bubble given by the conformal map (4.2) from D in the ζ-plane to the exterior of the bubble $\Omega(0)$ in the z-plane, in an unbounded Hele-Shaw cell. The evolution of the interface computed by the numerical procedure described in chapter 2 is given in figure 4.1 for three values of θ_e, all with same area, and aspect ratio (of 1/2). In all cases, the bubble evolves rapidly (within a distance of 2–3 major axis lengths) to the circular solution, and then translates steadily with speed $U = 2V$.

The velocity of the centre of mass of the bubble can be calculated given the normal velocity on the interface by [137]

$$\dot{z}_{cm} = \frac{1}{A}\int_0^{L(t)} z\mathbf{u}.\mathbf{n}\,\mathrm{d}s, \tag{4.10}$$

where $\dot{z}_{cm}$ denotes the velocity of the of the centre of mass in complex form, and $\mathbf{u}$ and $\mathbf{n}$ are the velocity and normal vectors on $\partial\Omega(t)$, s denotes the arc length parameter and $L(t)$ is the total arc length of $\partial\Omega(t)$. The speed of the centre of mass can thus be calculated as $v_{cm} = |\dot{z}_{cm}|$. The velocity in (4.10) is computed numerically at each time step. The real and imaginary (i.e. x and y) components of $\dot{z}_{cm}$, and the speed of the centre of mass v_{cm} are plotted as functions of time in figure 4.2. As expected, elliptical bubbles with semi-major axis aligned in the direction of the background flow (i.e. $\theta_e = 0$) decelerate to the steady solution $U = 2V$ as they become circular. It was noted by Taylor and Saffman [138] that bubbles elongated in the direction of the flow travel with increased speed, i.e. greater than $2V$. Elliptical bubbles with semi-major axis perpendicular to the background flow accelerate (c.f. figure 4.2, $\theta_e = \pi/2$) to $U = 2V$ while becoming circular.

If $0 < \theta_e < \pi/2$, then the bubble interface adjusts to the steady circular solution

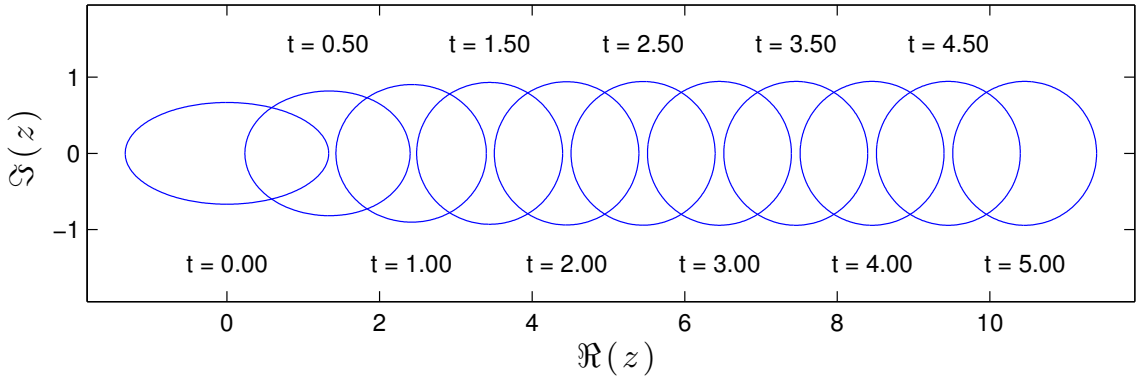

(a) $\theta_e = 0$

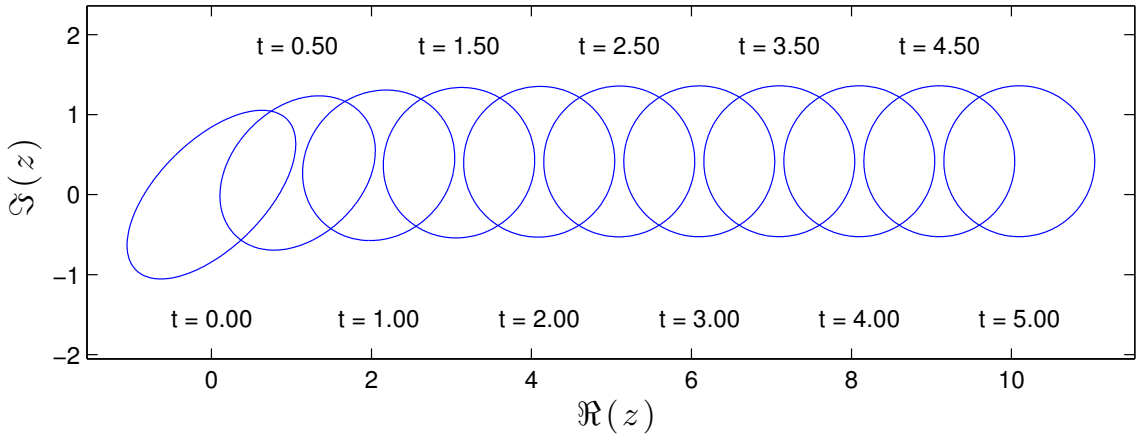

(b) $\theta_e = \frac{\pi}{4}$

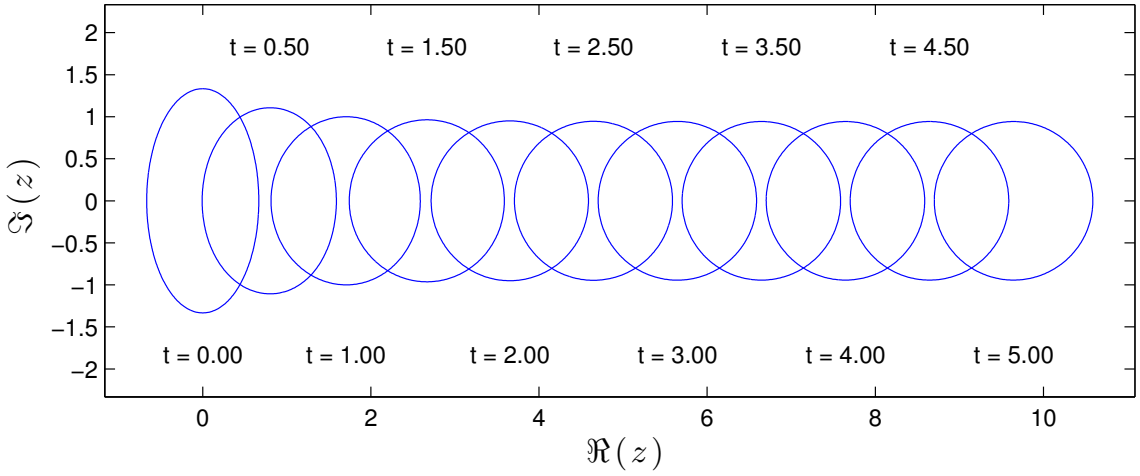

(c) $\theta_e = \frac{\pi}{2}$

Figure 4.1: Evolution of initially elliptical bubbles with semi-major axis inclined at three different angles θ_e to the positive real axis. In each case the interface evolves into a circle. The initial interface is given by (4.2) with $a = 1$, $b = 1/3$ and $C = 0$. The results presented are for $N = 400$, $\Delta t = 10^{-3}$ and $V = 1$. The corresponding time of the interface is displayed below and above the snapshots.

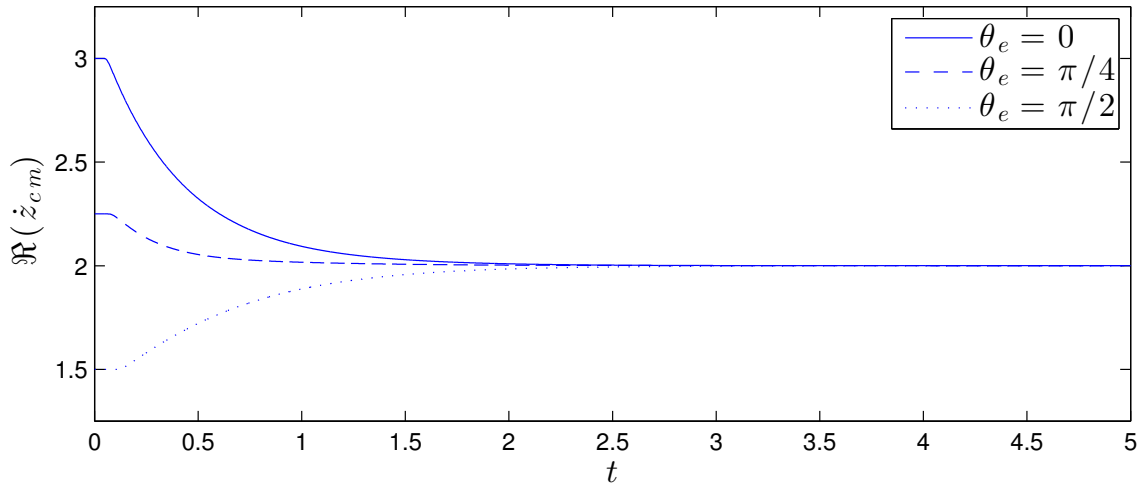

(a)

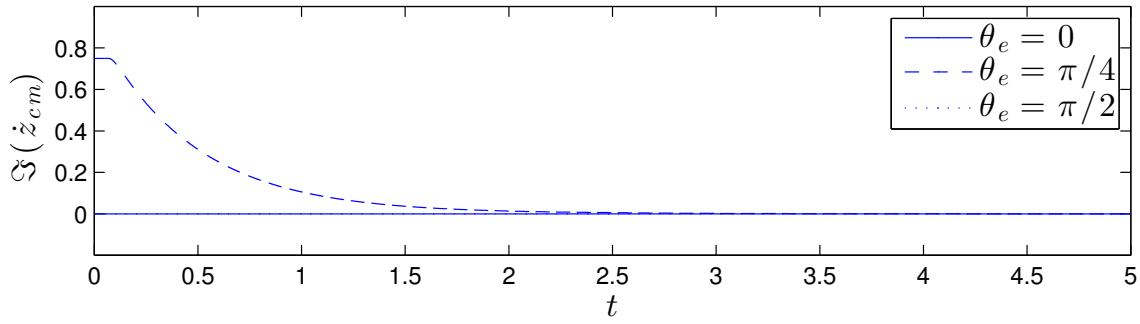

(b)

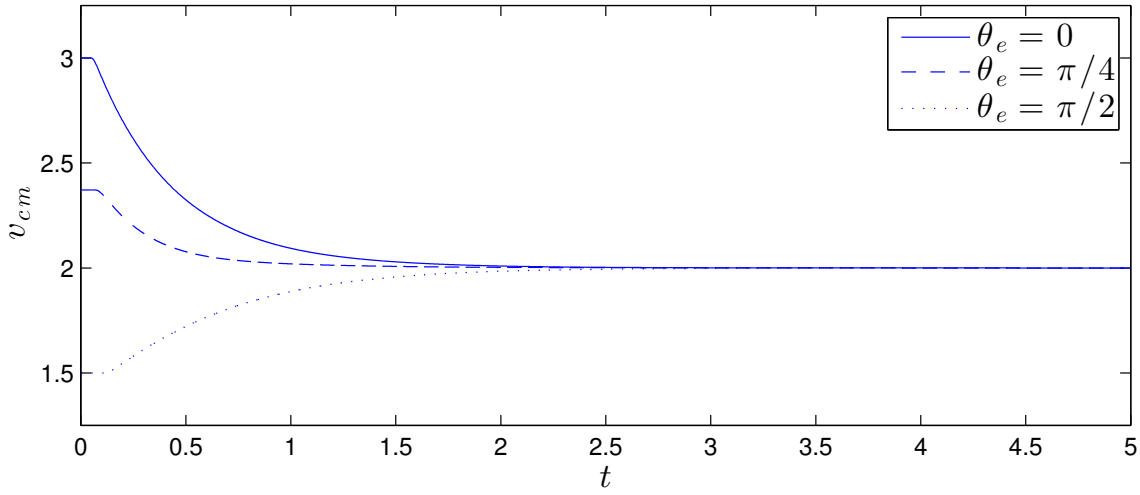

(c)

Figure 4.2: Velocity of the centre of mass in the (a) real and (b) imaginary directions, and (c) overall speed v_{cm} corresponding to the numerical solution presented in figure 4.1, for the different elevation angles θ_e of initially elliptical bubbles.

as $\Im(\dot{z}_{cm}) \to 0$. Therefore, starting with an initially elliptical interface with arbitrary inclination to the uniform background flow, the bubble evolves to the steady circular solution as $t \to \infty$ travelling with speed $U = 2V$, parallel to the background flow—see curves in figure 4.2 with $\theta_e = \pi/4$.

It is interesting to note that for a short time after $t = 0$ the bubble speed adjusts only slowly as the interface remains approximately elliptical before instability sets in. Figures 4.3(a) and 4.3(b) show a close-up of the evolution of $v_{cm}(t)$ for small time and corresponding snapshots of the interface, respectively. This delay before instability is possibly a numerical effect and is now investigated. Figure 4.4 shows dependence of bubble speed for various values of mesh points, N. When N is increased (keeping time step Δt fixed), the solution approaches the circular solution more rapidly. This may seem counter intuitive, however, Aitchison and Howison [1] speculate that increasing N introduces shorter wavelength instabilities which grow the fastest, thus increasing resolution leads to a more rapid growth in instability. This result holds true for increasing N with $\Delta t/\Delta S$ fixed, where ΔS is the mesh size defined in section 2.3.

4.3.2 Initial conditions leading to bubble breakup

Here we consider bubbles with 'simple' but non-elliptical initial fluid-bubble interfaces in a uniform background flow, and show how the initial geometry of the bubble may predict breakup by considering singularities of the Schwarz function of the initial interface.

Recall, the evolution of the interface can be expressed in complex form by the Schwarz function equation (1.46). It is well known (as demonstrated later in this section) that (1.46) implies that the singularities of the Schwarz function of the initial map remain fixed in the fluid domain [59] and that these cannot cross the boundary of the bubble. This will lead to bubble deformation as the singular points are approached. Next, the bubble deformation process is investigated numerically.

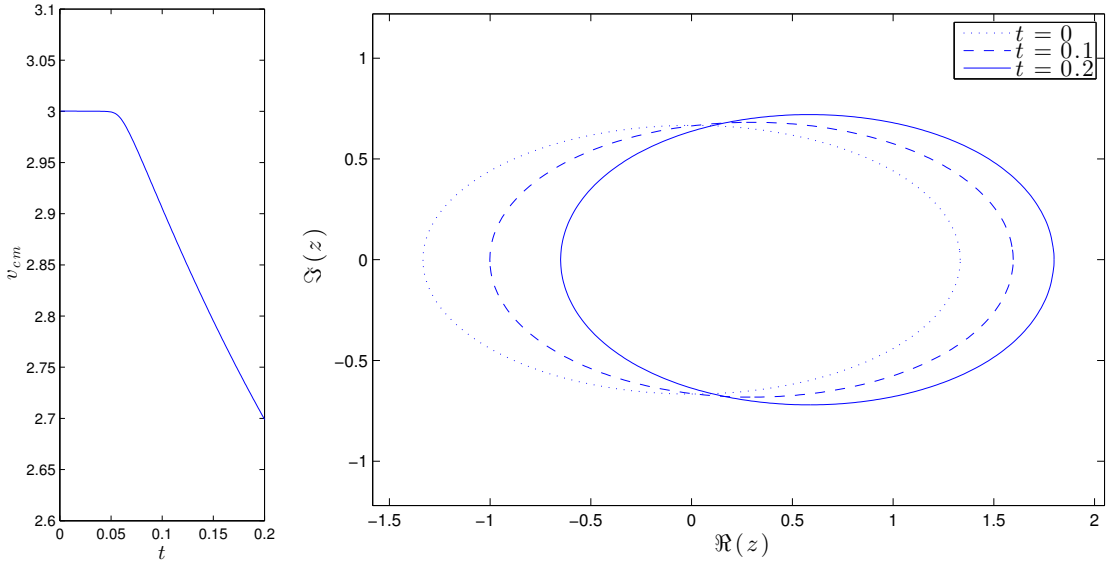

(a) (b)

Figure 4.3: Small time evolution of an initially elliptical bubble. The initial interface is given by (4.2) with $a = 1$, $b = 1/3$, $C = 0$ and with $\theta_e = 0$. The results presented are for $N = 400$, $\Delta t = 10^{-3}$ and $V = 1$. Evolution of the speed of the centre of mass of the bubble is shown in (a) with snapshots of the bubble interface shown in (b).

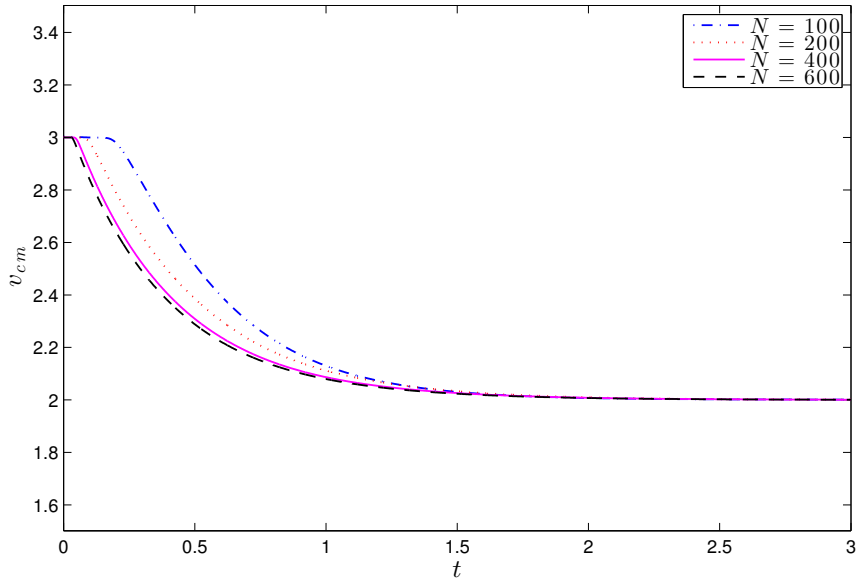

Figure 4.4: The effect of increasing the number of mesh points, N, on v_{cm} of an initially elliptical bubble as the interface evolves to the stable circular bubble travelling with speed $U = 2V$. The initial bubble is given by (4.2) with $a = 1$, $b = 1/3$, $C = 0$ and $\theta_e = 0$. For the results presented, $\Delta t = 10^{-3}$ and the background flow has speed $V = 1$.

Consider a bubble in a uniform flow with initial interface given by the rational map

$$z = \frac{a_0 + a_1\zeta + a_2\zeta^2}{\zeta + b_0}, \tag{4.11}$$

which for particular parameters a_i and b_i, $i = 0, 1, 2$, gives a univalent map from D to the exterior of a crescent shaped bubble. Here we will take a_i and b_i, to be real valued so that the bubble is symmetric about $\Re(z)$. For simplicity, we fix the coefficients $a_0 = -0.375$, $a_1 = -0.15$, $a_2 = 0.25$ and vary b_0 in order to generate different initial shapes. It is required that $|b_0| < 1$ for univalency. The map (4.11) has a singularity at $\zeta = -b_0$, which is mapped to infinity in the z-plane.

Since $\overline{\zeta}\zeta = 1$ on ∂D, the Schwarz function of the initial interface, $\partial\Omega(0)$, is given by

$$g = \frac{a_0\zeta^2 + a_1\zeta + a_2}{\zeta + b_0\zeta^2}. \tag{4.12}$$

The function (4.12) has two singularities. Here, the only relevant singularity is at $\zeta = 0$ since it is the only one that lies inside D, i.e. it is mapped to the fluid domain as displayed in figure 4.5. Note that this singular point is downstream of the initial bubble position in the z-plane.

As $\zeta \to 0$, the map (4.11) gives

$$z = \frac{a_0}{b_0}\left(1 + \left[\frac{a_1}{a_0} - \frac{1}{b_0}\right]\zeta\right) + \mathcal{O}(\zeta^2), \tag{4.13}$$

hence, expanding g to leading order yields

$$\begin{aligned} g &= \frac{a_2}{\zeta} + (a_1 - a_2 b_0) + \mathcal{O}(\zeta) \\ &= \frac{a_0 a_2}{b_0}\left(\frac{a_1}{a_0} - \frac{1}{b_0}\right)\frac{1}{(z - a_0/b_0)} + (a_1 - a_2 b_0) + \mathcal{O}(z - a_0/b_0). \end{aligned} \tag{4.14}$$

It is clear that the Schwarz function has a singularity at the point $z_0 = a_0/b_0 = z(0)$,

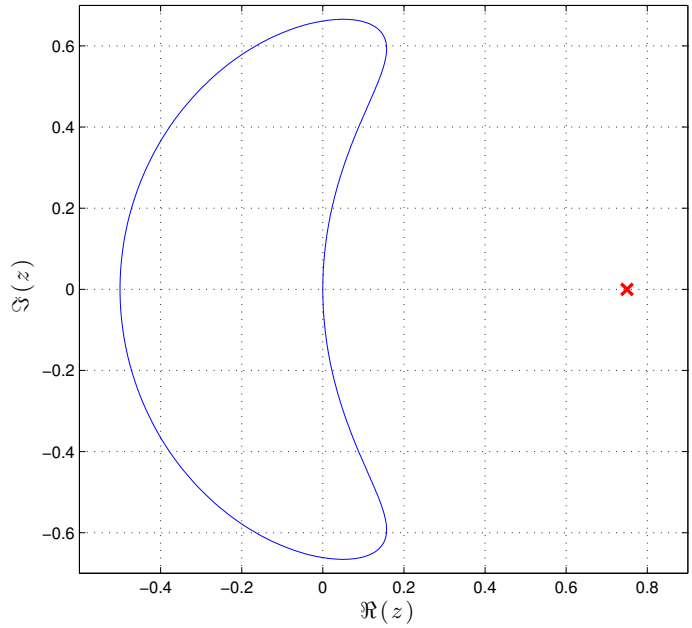

Figure 4.5: Initial bubble shape given by (4.11) and location of the singularity of the Schwarz function (4.12) with $a_0 = -0.375$, $a_1 = 0$, $a_1 = -0.15$, $a_2 = 0.25$, and $b_0 = -0.5$. The singularity (marked by a cross) is mapped from the interior of D to the initial fluid domain, $\Omega(0)$.

as expected. Differentiating (4.14) w.r.t. time gives

$$\frac{\partial g}{\partial t} = \left(\frac{a_0 a_2}{b_0}\left[\frac{a_1}{a_0} - \frac{1}{b_0}\right]\right)\frac{\mathrm{d}}{\mathrm{d}t}\left(\frac{a_0}{b_0}\right)\frac{1}{(z-z_0)^2} + \frac{\mathrm{d}}{\mathrm{d}t}\left(\frac{a_0 a_2}{b_0}\left[\frac{a_1}{a_0} - \frac{1}{b_0}\right]\right)\frac{1}{(z-z_0)} + \frac{\mathrm{d}}{\mathrm{d}t}\left(a_1 - a_2 b_0\right) + \mathcal{O}(z-z_0), \quad (4.15)$$

i.e. $\dot{g}$ has singularities at z_0 of first and second order. Since the background flow is a steady uniform flow (no sources, sinks or dipoles), $\partial w/\partial z$ is analytic in $\Omega(t)$, and since (1.46) holds away from $\partial\Omega(t)$, (4.15) implies $\mathrm{d}\left[(a_1 a_2/b_0) - (a_0 a_2/b_0^2)\right]/\mathrm{d}t = 0$ and $\mathrm{d}(a_0/b_0)/\mathrm{d}t = 0$. The latter implies $\dot{z}_0 = 0$, i.e. $z_0 =$ constant, and so the singularity of g remains stationary. Since this point must always lie in the fluid domain, the bubble boundary cannot cross z_0. That is, the interface must avoid z_0 as it evolves in time.

Figure 4.6 shows the evolution of initial crescent shaped bubbles given by the map (4.11) for various values of b_0, where the background flow speed $V = 1$ in each case. In all cases the front and rear of the bubble interface become progressively

close until they collide after which it is expected that the bubble will 'split' symmetrically. We do not extend the numerical solutions beyond this time. As the front of the starting bubble becomes less convex with respect to the interior of the bubble (and direction of the flow) the bubble splits at more than one location, as can be seen in figure 4.6(e). Furthermore, as the front of the initial bubble shape changes from convex to concave, the numerical results suggest the bubble no longer splits, as is the case in figure 4.7 where $b_0 = -0.1$. In the same limit of (4.14) the singularity of g is located further away from the starting location of the bubble. Instead of splitting, the bubble evolves to a circle, similar to the behaviour of the elliptical bubble observed in section 4.3.1 (which have Schwarz function singularities at infinity). That is, in figure 4.7 the interface passes over the location of the Schwarz function singularity. Mathematically, this is not permitted but it may be explained because of numerical instabilities which force the solution rapidly to a circular interface and so the numerical effects (e.g. instabilities and filtering) cause information on the initial Schwarz function singularity to be lost. The larger the distance the bubble has to travel before encountering the Schwarz function singularity the greater these effects are.

Now consider an initially crescent shaped bubble which is asymmetric in $\Re(z)$. Figure 4.8 shows the evolution of a bubble with initial interface given by (4.11) rotated through an angle $\theta_r = -\pi/4$ (i.e. we replace z by $e^{-i\theta_r}z$) with $b_0 = -0.8$. Although the singularity of the corresponding Schwarz function of the initial interface lies directly downstream of a portion of the bubble, it can be seen that the bubble evolves to the circular solution in a manner so as to avoid contact with the singularity z_0. If the angle of rotation is reduced to $\theta_r = -\pi/8$, as in figure 4.9, the bubble will split asymmetrically before the interface reaches z_0.

It is possible to use (4.11) to find an exact solution for the evolution of a Hele-Shaw bubble. The four unknown parameters a_0, a_1, a_2 and b_0 are governed by four

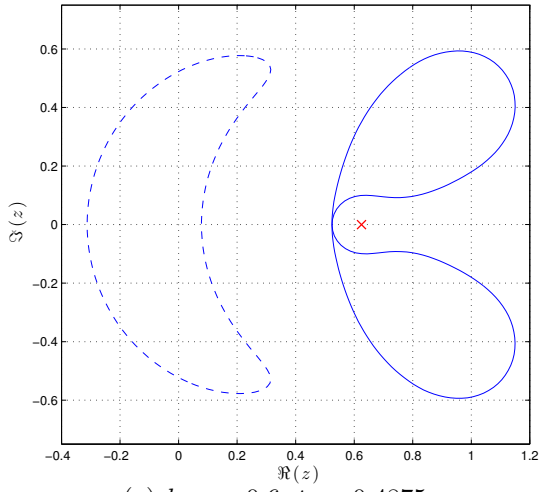

(a) $b_0 = -0.6$, $t_e = 0.4875$

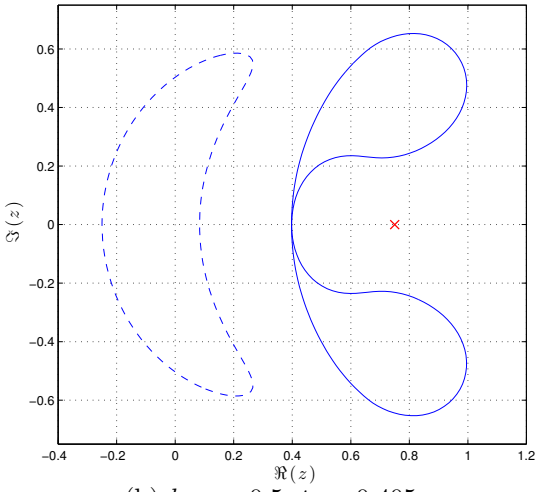

(b) $b_0 = -0.5$, $t_e = 0.405$

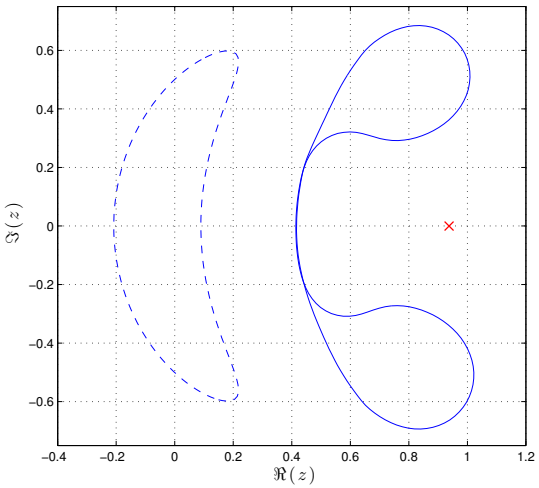

(c) $b_0 = -0.4$, $t_e = 0.43$

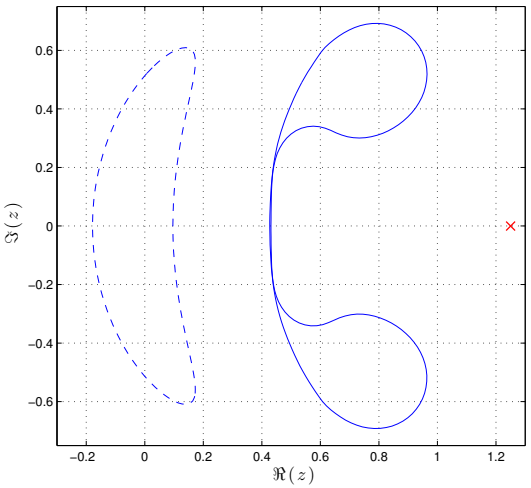

(d) $b_0 = -0.3$, $t_e = 0.43$

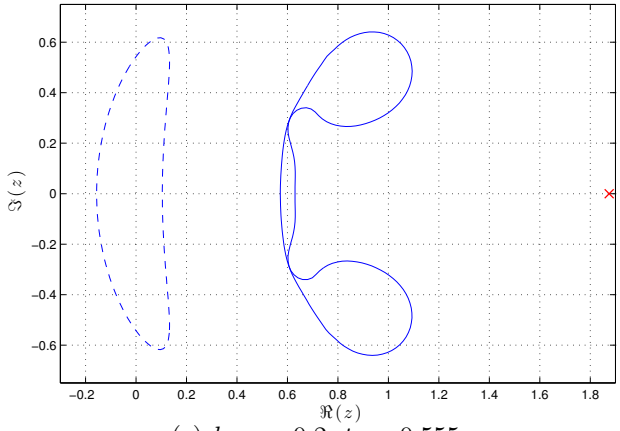

(e) $b_0 = -0.2$, $t_e = 0.555$

Figure 4.6: Snapshots of the bubble interface at the initial time $t = 0$ (dashed) and when the interface collides with itself at time $t = t_e$ (solid). Here, the results presented are for $N = 400$, $\Delta t = 5 \times 10^{-4}$ and $V = 1$. The Schwarz function singularity of the initial bubble shapes are marked by a cross.

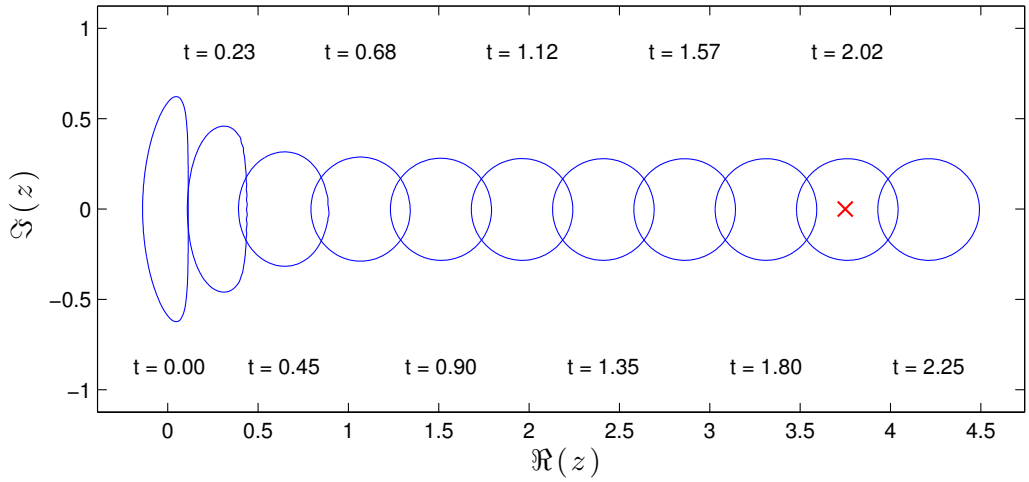

Figure 4.7: Evolution of an initially crescent shaped bubble given by the map (4.11) with $b_0 = -0.1$ and corresponding Schwarz function singularity in $\Omega(0)$ is marked by a cross. The results presented are for $N = 400$, $\Delta t = 5 \times 10^{-4}$ and $V = 1$. The corresponding time of the interface is displayed below and above the snapshots.

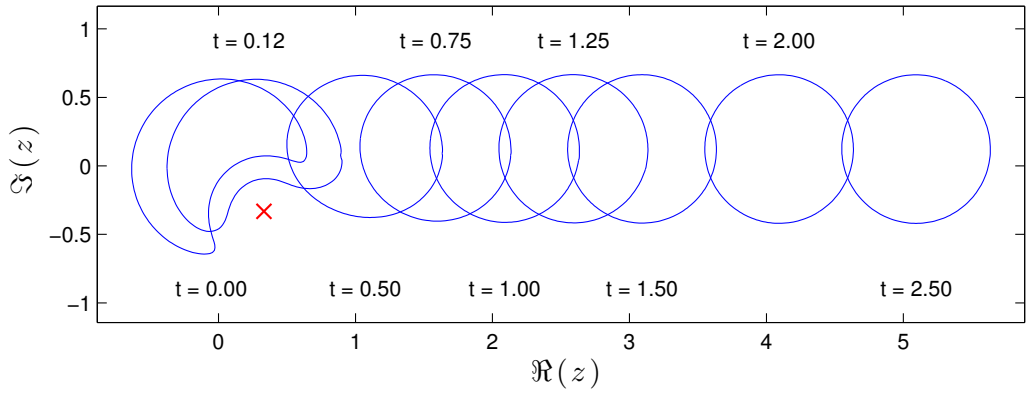

Figure 4.8: Evolution of an initially crescent shaped bubble given by the map (4.11) with $b_0 = -0.8$ rotated by angle $\theta_r = -\pi/4$. The results presented are for $N = 400$, $\Delta t = 5 \times 10^{-4}$ and $V = 1$. The corresponding time of the interface is displayed below and above the snapshots. The Schwarz function singularity in $\Omega(0)$ is marked by a cross.

ODEs, two of which come from (4.15); namely that the strength and location of the singularity of the Schwarz function at $z = z_0$ are constant. A further two independent ODEs can be derived by considering the behaviour of the Schwarz function (4.12) as $z \to \infty$ and applying (1.46) with $\partial w/\partial z \to V + \mathcal{O}(z^{-2})$ in the same limit. Equating terms of $\mathcal{O}(1)$ and $\mathcal{O}(z^{-1})$ yields the additional two ODEs, the latter of which is equivalent to bubble area conservation (see also section 4.4 for a similar derivation). These ODEs can then be integrated numerically to find a_0, a_1, a_2 and b_0 given their initial values. This has, in fact, been done and the results (see appendix G)

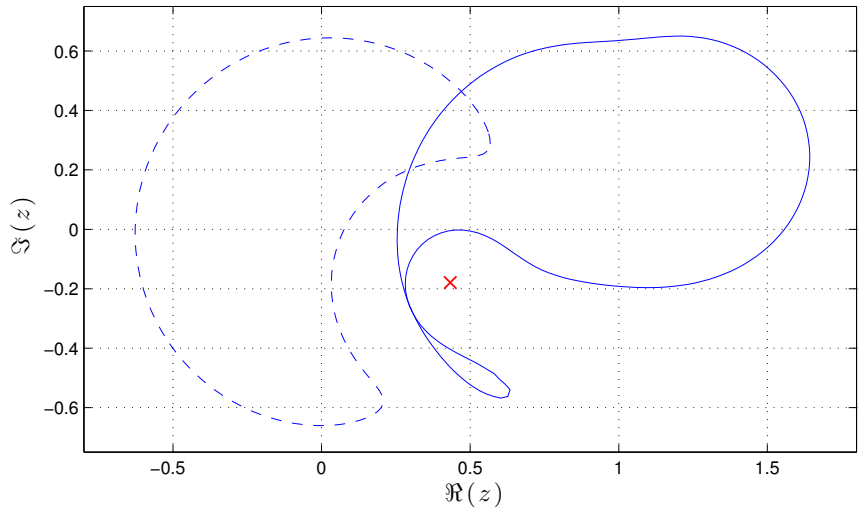

Figure 4.9: Snapshot of the bubble interface at $t = 0$ (dashed) and $t = 0.445$ (solid), where the initial interface is given by the map (4.11) with $b_0 = -0.8$, rotated by angle $\theta_r = -\pi/8$. The corresponding Schwarz function singularity in $\Omega(0)$ is marked by a cross. The results presented are for $N = 400$, $\Delta t = 5 \times 10^{-4}$ and $V = 1$.

differ from those in figures 4.6–4.8: while they confirm that the Schwarz function singularity plays an important role in the bubble evolution in that they are avoided by the bubble boundary, cusps form and the solution breaks down in finite time. It is evident that the present numerical procedure provides sufficient 'smoothing' to prevent such cusps forming and that instead breakdown here occurs via bubble breakup. As such, the numerical scheme can be viewed as providing a regularisation effect, so that the behaviour is closer to that of the case of vanishing small surface tension, as opposed to the ideal ZST problem—see section 2.4.

4.3.3 Finite blob pinch-off within a bubble

Here we present numerical results showing a different type of change in bubble topology. Consider the map given by

$$z = \frac{\alpha_0 + \alpha_1 \zeta}{(\zeta + \beta_1)(\zeta + \beta_2)}, \tag{4.16}$$

giving a crescent shape shown by the dashed line in figure 4.10(a). The coefficients α_i, β_i, $i = 0, 1, 2$, are real and such that (4.16) maps D to the exterior of the bubble. Here, the map has a singular point lying inside D, namely $\zeta = -\beta_1$, where $-1 < \beta_1 < 1$ so that the map remains univalent on D, and one singular point outside D at $\zeta = -\beta_2$, i.e. $|\beta_2| > 1$.

The Schwarz function of $\partial\Omega(0)$ in this case is given by

$$g = \frac{\alpha_0\zeta + \alpha_1}{(1 + \beta_1\zeta)(1 + \beta_2\zeta)}, \tag{4.17}$$

which gives one singularity for g in the fluid domain at position $z(-1/\beta_2)$ lying on the real axis, downstream of the initial bubble, shown in figure 4.10(a) marked by a cross. Again, we denote this point by z_0, and it can be shown using a similar argument presented in section 4.3.2 that $z_0 =$ constant.

Figure 4.10 shows the evolution of a bubble with initial interface given by the map (4.16) with $\alpha_0 = \alpha_1 = -0.25$, $\beta_1 = -0.3$ and $\beta_2 = 1.15$ subject to a background uniform flow of unit speed, i.e. $V = 1$. As the bubble translates downstream, the 'horns' of the crescent become smoother and begin to close at the front of the bubble. Subsequently, a region of fluid is trapped by the engulfing bubble and the interface of the bubble collides with itself, beyond which it is expected that the trapped fluid blob pinches off, with the bubble forming a ring around a disconnected fluid blob in its interior. The interior blob is centred on the Schwarz function singularity, $z_0 = z(-1/\beta_2)$—see figure 4.10(b). Since the pressure in the bubble region remains constant, the blob inside the bubble is expected to remain stationary once pinched off as no information of the background flow reaches its interface, whilst the outer interface is expected to translate downstream until the interior blob collides with the rear of the bubble and the blob will then reattach to the main body of fluid. As $t \to \infty$, we speculate that the bubble attracts to the aforementioned circular solution, travelling at speed twice the background flow.

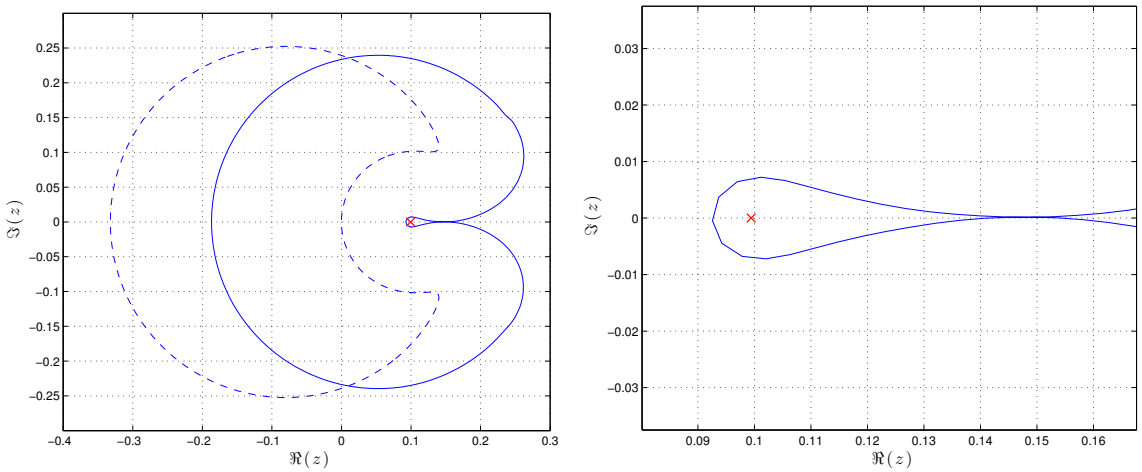

(a) (b)

Figure 4.10: Snapshot of the bubble interface at $t = 0$ (dashed) and $t = 0.06625$ (solid), where the initial interface is given by the map (4.16) with $\alpha_0 = -1$, $\alpha_1 = -1$, $\beta_1 = -0.3$ and $\beta_2 = 1.15$. The corresponding singularity of the Schwarz function in $\Omega(0)$ is marked by a cross. Close-up of the blob pinched off by the surrounding bubble is shown in (b). Results are presented for $N = 400$, $\Delta t = 2.5 \times 10^{-4}$ and $V = 1$.

4.4 Stability of elliptical bubbles

Here we will study, analytically, the stability of an elliptical bubble in a uniform background flow. As noted in section 4.1, Vasconcelos and Mineev-Weinstein [149] have given a stability analysis for time-dependent solutions (which survive for all time) describing bubbles in finite width channels. They show that the bubble with speed $U = 2V$ is the only stable attractor for these solutions. In the small bubble limit, in which the bubble is far from the channel walls, this corresponds to a circular bubble (in an unbounded Hele-Shaw cell). In this section an alternative stability analysis is given in which an elliptical bubble is shown to be unstable to a particular type of perturbation (this being sufficient to guarantee that it is unstable) and that it evolves toward a circle.

Consider the stability of the steady translating elliptical bubble solutions to a

certain class of perturbations having the form

$$z = c + a\zeta + \frac{b}{\zeta - \epsilon}, \tag{4.18}$$

where, now, the *exterior* of the unit ζ-disc, D_{ext}, is mapped to the exterior of the perturbed elliptical bubble (i.e. the flow domain $\Omega(t)$), and the time-varying parameters are such that ϵ is small, $a \neq 0$, b and c are real. If $\epsilon = 0$, note that (4.18) is the map describing an elliptical bubble, in which case a, b, and c are constant. The Schwarz function of the interface is given by

$$g = c + \frac{a}{\zeta} - \frac{b}{\epsilon} + \frac{b}{\epsilon}\frac{1}{1 - \epsilon\zeta}. \tag{4.19}$$

In the limit $z \to \infty$ it can be shown from (4.18) and (4.19) that

$$g = c - \frac{b}{\epsilon} + \frac{1}{z}\left(a^2 - \frac{ab}{\epsilon^2}\right) + \mathcal{O}(z^{-2}). \tag{4.20}$$

Applying the Schwarz function equation (1.46) as $z \to \infty$ yields

$$\frac{\mathrm{d}}{\mathrm{d}t}\left(c - \frac{b}{\epsilon}\right) + \frac{\mathrm{d}}{\mathrm{d}t}\left(a^2 - \frac{ab}{\epsilon^2}\right)\frac{1}{z} + \mathcal{O}(z^{-2}) = 2V, \tag{4.21}$$

which gives at $\mathcal{O}(1)$ and $\mathcal{O}(z^{-1})$

$$\frac{\mathrm{d}}{\mathrm{d}t}\left(c - \frac{b}{\epsilon}\right) = 2V, \tag{4.22a}$$

$$\frac{\mathrm{d}}{\mathrm{d}t}\left(a^2 - \frac{ab}{\epsilon^2}\right) = 0. \tag{4.22b}$$

Now, g has a singularity lying at $\zeta = 1/\epsilon$ exterior to the unit ζ-circle (i.e. in the pre-image fluid domain), about which the Schwarz function has leading order behaviour as $z \to z_0$

$$g = -\left(\frac{ab}{\epsilon^2} - \frac{b^2}{(1-\epsilon^2)^2}\right)\frac{1}{(z-z_0)} + c + a\epsilon - \frac{b}{\epsilon} - \frac{b^2\epsilon}{a(1-\epsilon^2)^3 - b\epsilon^2(1-\epsilon^2)} + \mathcal{O}(z-z_0), \tag{4.23}$$

where $z_0 = z(\epsilon^{-1}) = c + a/\epsilon + b\epsilon/(1-\epsilon^2)$. Differentiating (4.23) w.r.t. time yields

$$\frac{\partial g}{\partial t} = -\frac{\mathrm{d}z_0}{\mathrm{d}t}\left(\frac{ab}{\epsilon^2} - \frac{b^2}{(1-\epsilon^2)^2}\right)\frac{1}{(z-z_0)^2} - \frac{\mathrm{d}}{\mathrm{d}t}\left(\frac{ab}{\epsilon^2} - \frac{b^2}{(1-\epsilon^2)^2}\right)\frac{1}{(z-z_0)} + \frac{\mathrm{d}}{\mathrm{d}t}\left(c + a\epsilon - \frac{b}{\epsilon} - \frac{b^2\epsilon}{a(1-\epsilon^2)^3 - b\epsilon^2(1-\epsilon^2)}\right) + \mathcal{O}(z-z_0). \tag{4.24}$$

Since the velocity potential must be analytic in the fluid domain $\Omega(t)$, i.e. there exist no hydrodynamic singularities in the flow, and since the Schwarz function equation, $\partial g/\partial t = 2\partial w/\partial z$, must hold over the fluid domain, taking $\zeta \to 1/\epsilon$ gives

$$\frac{\mathrm{d}}{\mathrm{d}t}\left(\frac{ab}{\epsilon^2} - \frac{b^2}{(1-\epsilon^2)^2}\right) = 0, \tag{4.25a}$$

$$\frac{\mathrm{d}}{\mathrm{d}t}\left(c + \frac{a}{\epsilon} + \frac{b\epsilon}{1-\epsilon^2}\right) = 0. \tag{4.25b}$$

Along with the above equations, the area of the bubble must also be conserved. The area can be calculated using Green's theorem, with integration around the unit ζ-circle, ∂D, to yield

$$\begin{aligned} A &= \frac{1}{2i}\oint_{\partial D} \bar{z}z'\mathrm{d}\zeta \\ &= \pi\left(a^2 - \frac{b^2}{(1-\epsilon^2)^2}\right). \end{aligned} \tag{4.26}$$

Note that (4.25a) is a linear combination of (4.22b) and (4.26), and so provides no new information on the evolution of the parameters ϵ, a, b and c. Therefore, there are four equations, namely (4.22a), (4.22b), (4.25b) and (4.26) governing the evolution of the map (4.18) for the perturbed ellipse.

Now consider the case where the Schwarz function singularity of the initial bubble

interface may not lie on the real axis. This can be achieved in the case that $\Im(\epsilon) \neq 0$ initially, and so ϵ and b are no longer real in general and the set of equations governing the evolution of the time-dependent parametric map (4.18) become

$$\frac{\mathrm{d}}{\mathrm{d}t}\left(\overline{c} - \frac{\overline{b}}{\overline{\epsilon}}\right) = 2V, \tag{4.27a}$$

$$\frac{\mathrm{d}}{\mathrm{d}t}\left(a^2 - \frac{a\overline{b}}{\overline{\epsilon}^2}\right) = 0, \tag{4.27b}$$

$$\frac{\mathrm{d}}{\mathrm{d}t}\left(c + \frac{a}{\overline{\epsilon}} + \frac{b\overline{\epsilon}}{1-|\epsilon|^2}\right) = 0, \tag{4.27c}$$

$$a^2 - \frac{|b|^2}{(1-|\epsilon|^2)^2} = \frac{A}{\pi}. \tag{4.27d}$$

Therefore, (4.27) give a set of three complex equations and one real equation for the complex parameters c, b and ϵ, and the real parameter a. Now, as the bubble travels in the positive $\Re(z)$ direction, as $t \to \infty$, $c \to \infty$. From (4.27c), $\overline{\epsilon} \to 0$ as $t \to \infty$ to balance c terms. The alternative possibility of a and $b \to \infty$ can be ruled out by virtue of (4.27b) and (4.27d). Equation (4.27b) in turn implies that $\overline{b} \to 0$ and hence (4.27d) implies $a \to$ constant as $t \to \infty$. Using (4.27a), (4.27c) further implies that $\overline{\epsilon} \to -a/(\overline{c} + [b\overline{\epsilon}/(1-|\epsilon|^2)] - K) \sim -a/t$, where $K =$constant, i.e. ϵ approaches zero from below. Equation (4.27b) implies that $b \sim \epsilon^2$ as $t \to \infty$, that is b must approach zero at least as t^{-2} as $t \to \infty$. Finally, (4.27a) implies $c \to 2Vt$ as $t \to \infty$. Thus, the bubble becomes circular, travelling at speed twice the background flow.

Figure 4.11 shows the evolution of an initially elliptical, perturbed bubble given by the map (4.18) where the time-dependent coefficients are found by solving the nonlinear set of coupled equations (4.27a), (4.27b), (4.27c) and (4.27d), numerically.

The numerical simulations in section 4.3.1 demonstrate the evolution of an initially elliptical bubble to a circular bubble where the transition of shape takes place over a short distance, no more than 2–3 semi-major axis lengths of the initial bubble shape. That is, an otherwise steady shape solutions evolves to the circular bubble due to the numerical instabilities, which are implicit at each time step of the

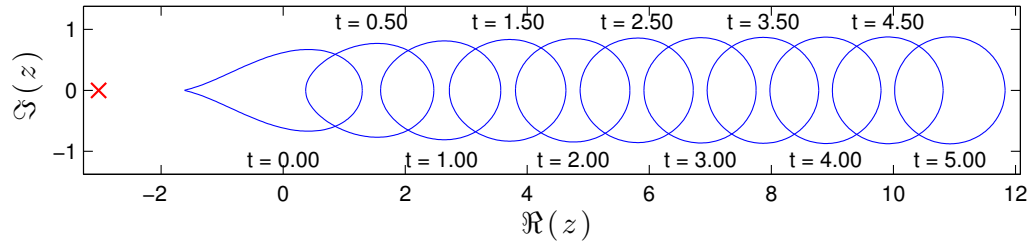

Figure 4.11: Evolution of an initially perturbed elliptical bubble given by the map (4.18) with $c(0) = 0$, $a(0) = 1$, $b(0) = 1/3$, $\epsilon = -0.3803$, where the background flow has speed $V = 1$. The cross denotes the location of the Schwarz function singularity of the initial interface. The corresponding time of the interface is displayed below and above the snapshots.

numerical algorithm (c.f. section 2.4). The rapid evolution towards the steadily translating circular bubble, beginning as soon as the numerical instability perturbs the interface, can be seen in figure 4.4. Therefore, with the added effects of numerical instability, it is expected that numerical simulations with initial bubble interface given by (4.18) would exhibit an enhanced rate of evolution to the circular bubble as compared with evolution governed by the set of coupled equations (4.27). Figure (4.12) shows a comparison between numerical results and evolution governed by the set of equations (4.27). It is observed that the numerical simulation evolves to the circular bubble more quickly, as expected. However, it is important to emphasise that in both cases, the dynamics of the interface are such that the bubble perimeter becomes circular, i.e. the parameters b and ϵ of (4.18) decay to zero as $t \to \infty$.

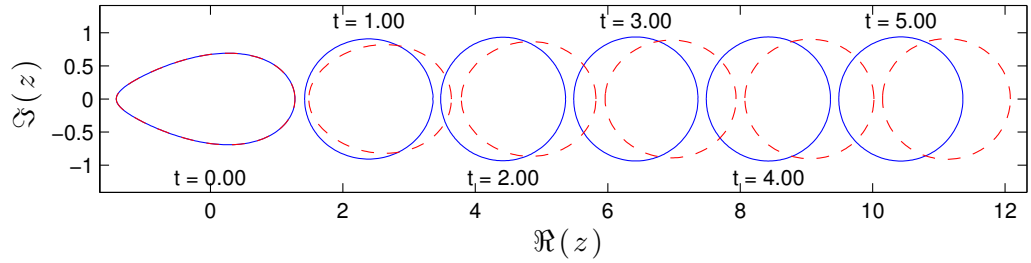

Figure 4.12: Evolution of an initially perturbed elliptical bubble given by (4.18) with $c(0) = 0$, $a(0) = 1$, $b(0) = 1/3$ and $\epsilon(0) = -0.2113$. Comparison between numerical simulation (solid) and solution to the set of equations (4.27) (dashed) are shown at multiple snapshots. The corresponding time is displayed below and above the interface snapshot pairs. Numerical results (solid) are presented for $N = 200$, $\Delta t = 10^{-3}$. The background flow speed is set to $V = 1$.

4.4.1 Unsteady perturbed solutions that exist for all time

In section 4.4 it is noted that when $\Im(\epsilon) \neq 0$, then the long time behaviour of ϵ is such that $\bar{\epsilon} \to -a/(\bar{c} + [b\bar{\epsilon}/(1-|\epsilon|^2)] - K) \sim -a/t$ where $K =$ constant and a is real, i.e. ϵ approaches zero from below, along the real axis. Here we investigate the set of initial conditions such that $\Re(\epsilon) > 0$, for which the solution exists for all time—tending to a circular interface as $t \to \infty$.

Let $z(\zeta, t)$ given by (4.18) be a conformal map from the *exterior* of the unit circle, D_{ext}, to the exterior of the bubble, $\Omega(t)$, in an unbounded Hele-Shaw cell. The interface of the bubble is mapped from the unit circle ∂D. For simplicity, we shall assume that b is also real and the parameter ϵ is such that $|\epsilon| < 1$ so that (4.18) has one singularity inside D, namely at $\zeta = \epsilon$. Note, the Schwarz function of the bubble interface, given by (4.19), has a singularity in D_{ext}, i.e. the pre-image of $\Omega(t)$.

Taking the derivative of z in (4.18) with respect to ζ yields

$$z'(\zeta, t) = a - \frac{b}{(\zeta - \epsilon)^2}. \tag{4.28}$$

Now consider the critical points of (4.18), i.e. the points ζ_* such that $z'(\zeta_*, t) = 0$. The reader is reminded that if the pre-image domain contains critical points, the map $z(\zeta, t)$ is not univalent [64]. From (4.28), we find that the critical points of (4.18) are given by

$$\zeta_* = \epsilon \pm \sqrt{\frac{b}{a}}. \tag{4.29}$$

Therefore, if both critical points lie outside D_{ext}, it is required that $|\zeta_*| < 1$ for (4.18)

to be univalent. Writing $\epsilon(t) = \epsilon_R(t) + i\epsilon_I(t)$, this implies

$$\begin{aligned} 1 &> \left| \epsilon \pm \sqrt{\frac{b}{a}} \right| \\ &= \left[\left(\epsilon_R \pm \sqrt{\frac{b}{a}} + i\epsilon_I \right) \left(\epsilon_R \pm \sqrt{\frac{b}{a}} - i\epsilon_I \right) \right]^{1/2}. \end{aligned} \tag{4.30}$$

Hence, assuming a and b are real positive numbers, at any instance, the curves which describe the extent of the regions in which ϵ would satisfy the inequality $|\zeta_*| < 1$ are given by

$$1 = \left[\left(\epsilon_R \pm \sqrt{\frac{b}{a}} + i\epsilon_I \right) \left(\epsilon_R \pm \sqrt{\frac{b}{a}} - i\epsilon_I \right) \right]^{1/2}. \tag{4.31}$$

Expanding and rearranging the above expression gives

$$\left(\epsilon_R \pm \sqrt{\frac{b}{a}} \right)^2 + \epsilon_I^2 = 1, \tag{4.32}$$

i.e. two circles centred at $(\sqrt{b/a}, 0)$ and $(-\sqrt{b/a}, 0)$.

The regions satisfying the inequalities (4.30) in the complex plane are given by the interior of each circle. Hence, the region satisfying both inequalities simultaneously for possible values of ϵ such that (4.18) remains univalent is described by the overlapping (shaded) region shown in figure 4.13, inside the unit ζ-disc, D.

A radial grid of 600 points is shown in figure 4.14, such that $\pi/4 \leq \arg(\epsilon(0)) \leq \pi/2$, where the evolution of c, a, b and ϵ satisfy (4.27). The initial ϵ, i.e. $\epsilon(0)$, are split up into two groups, those which lie to the left of the dashed curve (blue) and those which lie to the right (red). The (red) points that lie to the right of the dashed curve display the initial ϵ which give subsequent evolution of c, a, b and ϵ such that a critical point given by (4.29) collides with the unit ζ-circle, at which point a cusp forms on the interface $\partial\Omega(t)$. All initial values that lie in the shaded region with

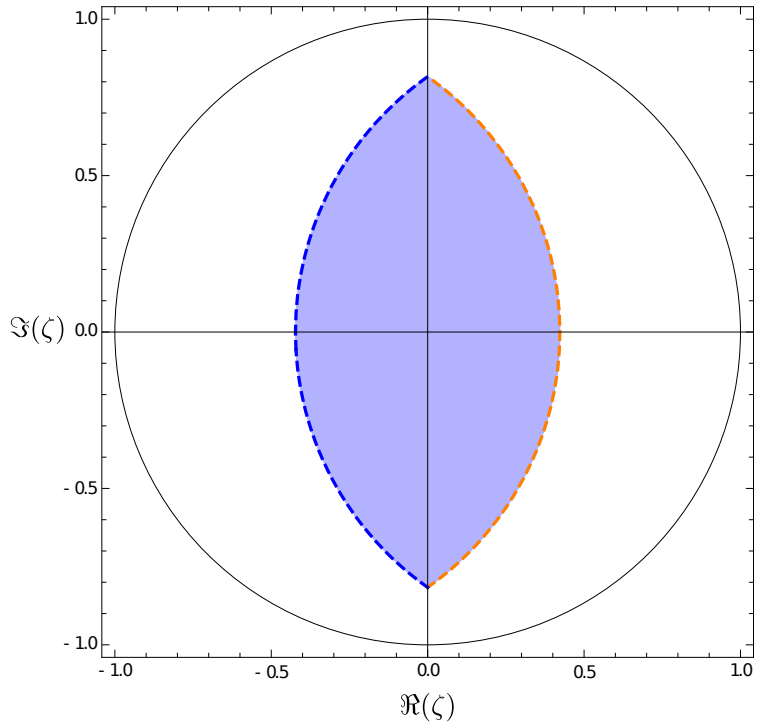

Figure 4.13: The shaded region describing possible values of complex ϵ inside D when $t = 0$, $a(0) = 1$, $b(0) = 1/3$, such that (4.18) remains univalent. The arcs of the circles described by the dashed lines mark the extremity of the shaded region and are given by (4.32).

$\arg(\epsilon(0)) < \pi/4$ are such that a critical point given by (4.29) collides with the unit ζ-circle and are not displayed. Figure 4.15 shows an example of the interface for such evolution. The corresponding evolution of the critical points given by (4.29) are displayed in figure 4.16(a).

The (blue) points lying to the left of the dashed curve in figure 4.14 display those initial ϵ where c, a, b and ϵ evolve in such a manner that ϵ and b decay to zero. An example of the evolution of the interface with such an initial condition is displayed in figure 4.17, where the bubble interface evolves to a circle as $t \to \infty$. In this case, the trajectory of ϵ in the ζ-plane is displayed in figure 4.18, where we see that ϵ loops on to the negative real axis, after which $\epsilon \to 0$ as $t \to \infty$. The corresponding trajectories of the critical points given by (4.29) are displayed in figure 4.16(b), where we see both critical points moving towards the origin for large time. Hence, it is demonstrated that for the class of solutions given by (4.18) that survives for all time for a ZST

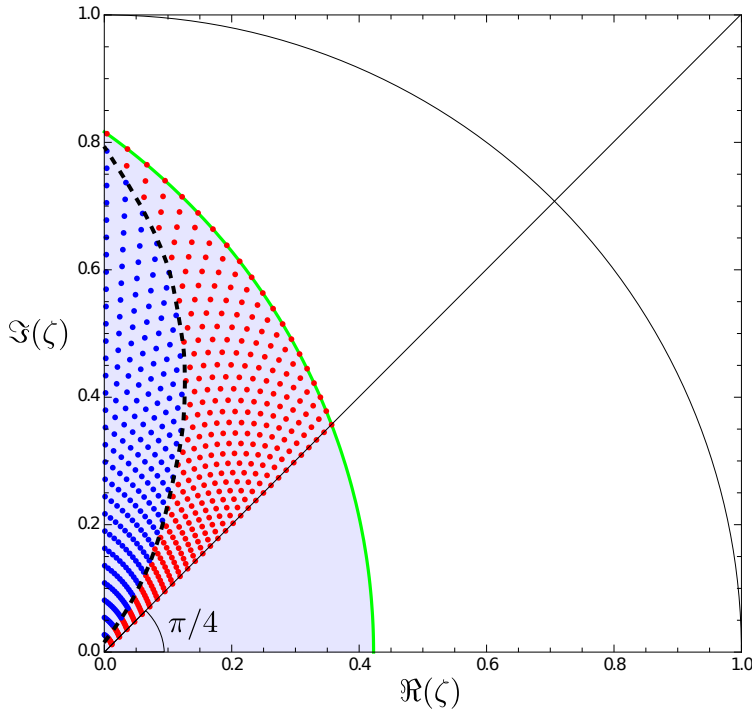

Figure 4.14: An example showing values of $\epsilon(0)$ (in the positive quadrant) such that (4.18) is univalent at $t = 0$ and (i) $\epsilon(t)$, $b(t)$ decay to zero as $t \to \infty$ (dots lying to the left of the dashed curve), (ii) $a(t)$, $b(t)$ and $\epsilon(t)$ evolve such that the critical points (4.29) collide with the the unit circle (dots lying to the right of the dashed curve). Here, c, a, b and ϵ of (4.18) evolve under the physics of a bubble in a uniform flow of unit speed at infinity with $c(0) = 0$, $a(0) = 1$ and $b(0) = 1/3$.

Hele-Shaw flow (by avoiding contact with the Schwarz function singularity) tend towards a circle traveling at speed $U = 2V$, otherwise the solution breaks down in finite time.

4.5 Summary

The stability of a steady shape elliptical bubble solution of the Hele-Shaw free boundary problem in an unbounded cell has been studied both analytically and numerically. In section 4.3.1 the numerical results demonstrate that for initially elliptical bubbles, the only (attractive) solution as $t \to \infty$ is a circular bubble travelling at a steady speed of twice the background flow V. Since surface tension effects are not included, the results are related to the analytical results of Vasconcelos and Mineev-Weinstein [149] for the selection problem in a channel geometry, where it is

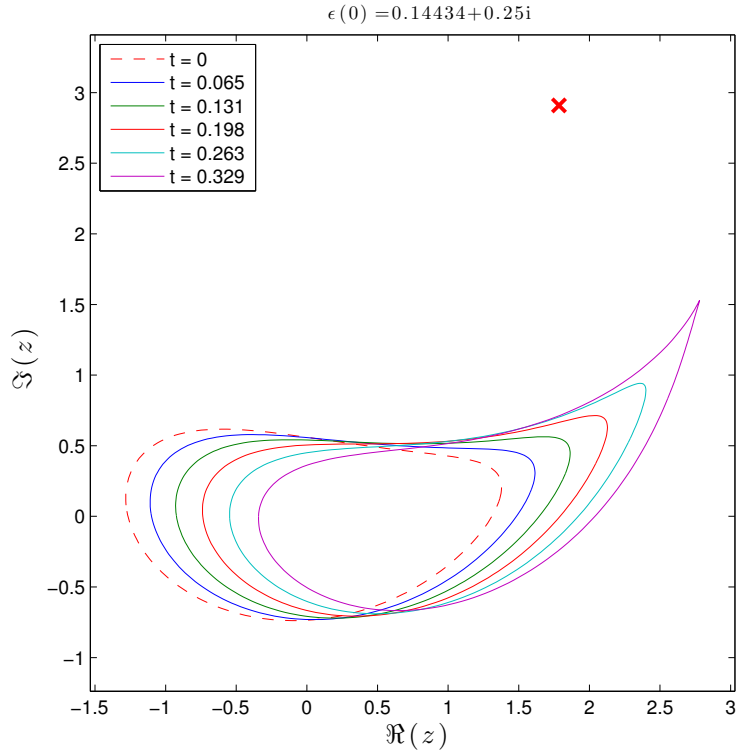

Figure 4.15: Snapshots of the evolution of a perturbed elliptical bubble given initially (dashed) by (4.18) with $c(0) = 0$, $a(0) = 1$ and $b(0) = 1/3$ and $\epsilon(0) = 0.14434 + 0.25i$. A cusp forms on the interface at $t = 0.329$. The singularity of the Schwarz function (4.19) is marked by a cross.

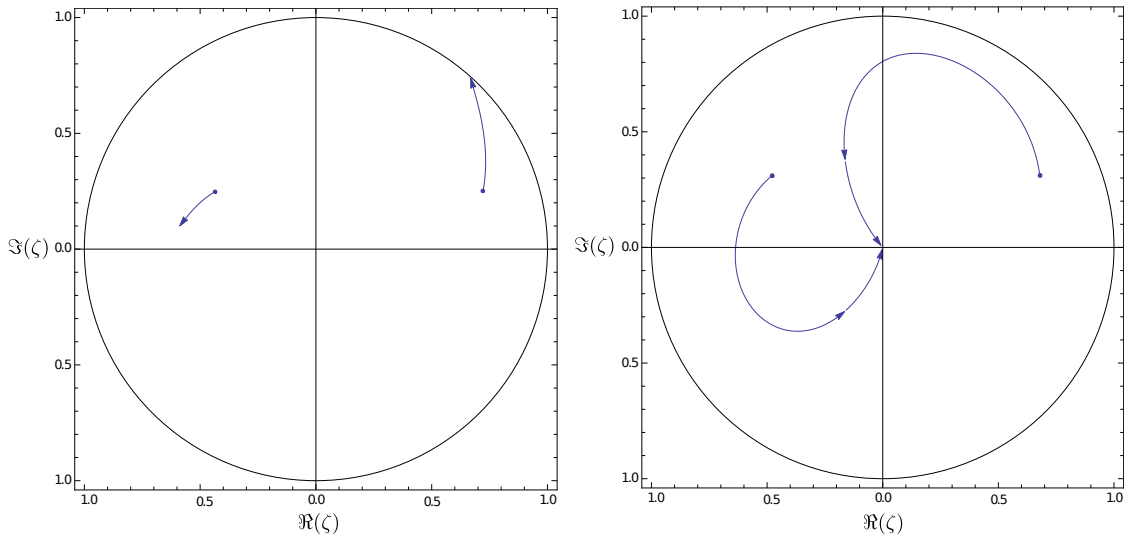

(a) (b)

Figure 4.16: Comparison of the trajectories of the critical points in the ζ-plane, given by (4.29), for the cases (a) corresponding to figure 4.15 with $0 \leq t \leq 0.329$ and (b) corresponding to figure 4.17 with $0 \leq t \leq 100$. The initial position of the critical points are marked by a dot.

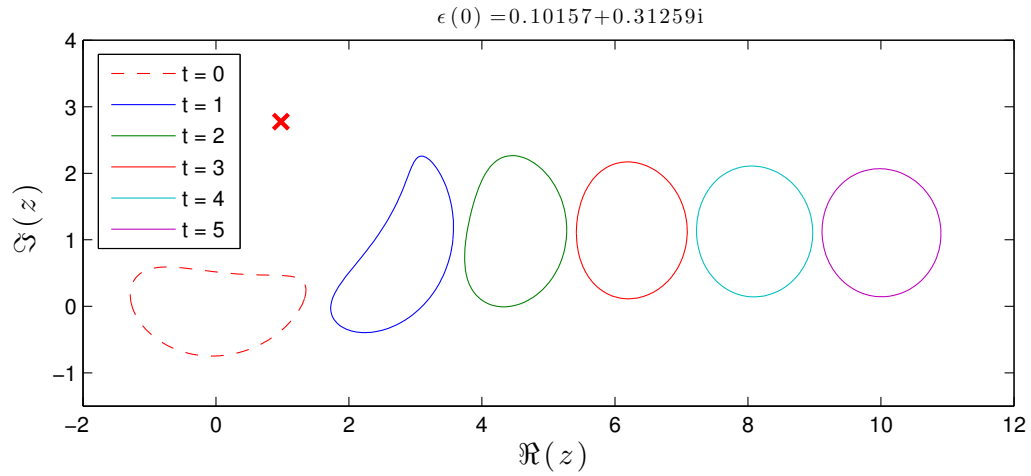

Figure 4.17: Snapshots of the evolution of a perturbed elliptical bubble given initially (dashed) by (4.18) with $c(0) = 0$, $a(0) = 1$ and $b(0) = 1/3$ and $\epsilon(0) = 0.10157 + 0.31259i$. The interface evolves smoothly to a circular interface as t increases. The singularity of the Schwarz function (4.19) is marked by a cross.

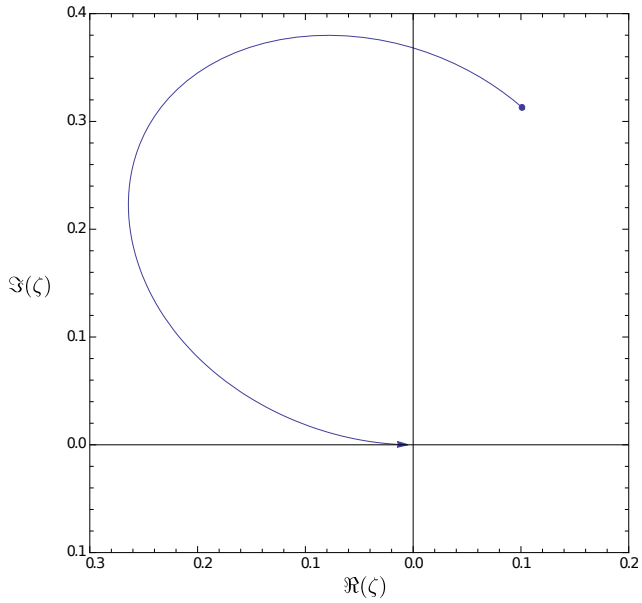

Figure 4.18: The trajectory of $\epsilon(t)$ in the ζ-plane for $0 \leq t \leq 100$ according to (4.27) with $c(0) = 0$, $a(0) = 1$ and $b(0) = 1/3$ and $\epsilon(0) = 0.10157 + 0.31259i$. The initial location of ϵ is marked by a dot and epsilon decays to zero along the negative axis for large t. The corresponding interface evolves smoothly to a circular interface as t increases, shown in figure 4.17.

shown that the selected bubble also propagates with speed $2V$. A stability argument in section 4.4 based on a perturbed ellipse provides further evidence the circular bubble with speed $U = 2V$ as being the stable attractor. However, it should be noted that the filtering method has a smoothing effect akin to surface tension. Thus it is not clear if the numerical results support the ZST selection mechanism, or if the

selection is a result of the filtering mechanism itself. In section 4.4 the extent of the domain for which solutions do not break down in finite time of the ZST problem has been calculated by solving the corresponding ODEs, i.e. (4.27), numerically.

In section 4.3.2 and 4.3.3 it is shown for some initial shapes of $\partial\Omega(0)$, it is possible that the evolution of $\partial\Omega(t)$ results in one of two types of topological change. In the former, the numerical results suggest the bubble may split, becoming multiply connected. In the latter, the bubble encloses a region of viscous fluid, i.e. a singly connected viscous fluid domain eventually becomes two disconnected regions. The numerical results suggest the singularities of the Schwarz function of the initial interface play an important role on the evolution of the interface, since mathematically the boundary cannot cross the singularity.

Chapter 5

Two-phase Hele-Shaw flows

5.1 Problem background and mathematical model

In this chapter we consider the 'general' problem of two-phase Hele-Shaw flows, otherwise known as the *Muskat problem* [103], where two viscous fluids with varying pressure are separated by a common interface $\partial\Omega(t)$. Most of the work regarding Hele-Shaw flows centres around the one-phase problem, and rightly so as there are many interesting problems that have been studied and are yet to be studied, as demonstrated in the preceding chapters of this thesis. In 2000, Howison [60] remarks that '*little progress has been made in the study when the viscosity of both phases are significant*'. Almost fifteen years later this statement is still largely valid. The difficulty being, the complex variable techniques which prove to be very useful in constructing exact solutions for the one-phase problem (used throughout chapters 1–4) are much more difficult to apply in the two-phase problem.

In the one-phase problem, conformal mappings are used in a variety of complex variable techniques, e.g. the Polubarinova-Galin equation [44, 112], the complex moment technique [116] or the Schwarz function method presented in this thesis.

The conformal mapping technique is particularly useful in the one-phase problem since the viscous phase, in most cases, can be mapped to a simple canonical domain, e.g. the interior of the unit disc (c.f. example 1.3.3 or 1.3.4) by virtue of the Riemann mapping theorem—see section 1.3.1. To use a similar conformal mapping technique in the two-phase problem, it would be required that the complement of the domain mapped in the one-phase problem be mapped to the secondary viscous fluid in the two-phase problem under the same one-to-one mapping function, e.g. mapping the interior of the unit disc to the domain occupied by the fluid with viscosity μ_1 *and* mapping the exterior of the unit disc to the domain occupied by the fluid with viscosity μ_2, under the same univalent map. In theory this is difficult to accomplish, however, it is possible to construct solutions in particular scenarios, see e.g. [20]. Some efforts have been made in the development of methods for the construction of exact solutions, e.g. [2, 20, 60], some of which are briefly discussed in section 5.3.1. The method presented by Crowdy [20] is followed in the construction of an exact solution presented in section 5.3.2.

Due to the difficulties in constructing exact solutions to the two-phase Hele-Shaw free boundary problem, various numerical methods have been developed, see e.g. [14,43,47,125], which include BIMs, e.g. [14]. In section 5.2, the BIM introduced in chapter 2 for one-phase Hele-Shaw flow is further developed to include two-phases, where the two fluids with finite, non-zero mobility (i.e. viscosity) ratio are separated by a simple closed curve $\partial\Omega(t)$.

Now we introduce the mathematical formulation of the general two-phase Hele-Shaw free boundary problem. Consider $\Omega_1(t)$ to be a finite domain, which will be referred to as the *inclusion*, and $\Omega_2(t)$ which will denote the infinite domain surrounding $\Omega_1(t)$, where $\Omega_1(t)$ and $\Omega_2(t)$ share the common interface $\partial\Omega(t)$—see figure 5.1. A fluid of viscosity μ_j occupies each domain $\Omega_j(t)$ and will be referred to as a *phase*. The fluids of each phase are governed by equations (1.11) and (1.12),

which can be derived as in section 1.2.1 for the one-phase problem. Using a subscript notation to distinguish between fluid properties in each phase, we write the Hele-Shaw equation as

$$\mathbf{u}_j = -\frac{h}{12\mu_j}\nabla p_j, \quad \mathbf{x} \in \Omega_j(t), \tag{5.1}$$

where μ_j denotes the viscosity of the fluid occupying the domain $\Omega_j(t)$, and the continuity equation in each phase is given by

$$\nabla \cdot \mathbf{u}_j = 0, \quad \mathbf{x} \in \Omega_j(t), \tag{5.2}$$

for $j = 1, 2$, except at a finite number of distributed hydrodynamic singularities that may exist in the either fluid domain—c.f. section 1.2.2. Following similar arguments to the derivation of the equations for the one-phase ZST Hele-Shaw free boundary problem with background fields (given in appendix B), in the two-phase problem, the dynamic boundary condition is

$$p_1 = p_2 + \Psi, \qquad \mathbf{x} \in \partial\Omega(t), \tag{5.3}$$

i.e the pressure across the interface is continuous and $\Psi(x, y, t)$ can be set appropriately for the given external field. The kinematic condition is

$$\mathbf{u}_1 \cdot \mathbf{n} = \mathbf{u}_2 \cdot \mathbf{n}, \qquad \mathbf{x} \in \partial\Omega(t), \tag{5.4}$$

i.e. the normal velocity of both phases is continuous on the interface, where $\mathbf{n}$ is the unit normal vector on $\partial\Omega(t)$ pointing from $\Omega_1(t)$ into $\Omega_2(t)$—see figure 5.1. Here, as in section 1.2.2, we write the free boundary problem described by (5.1)–(5.4) in terms of the velocity potential in each phase defined as

$$\phi_j(x, y, t) = -k_j p_j(x, y, t), \tag{5.5}$$

where $k_j = h^2/12\mu_j$ is the (constant) mobility of each fluid, $j = 1, 2$, and so the two-phase ZST Hele-Shaw free boundary problem can be written as

$$\nabla^2\phi_1 = 0, \qquad \mathbf{x} \in \Omega_1(t), \tag{5.6a}$$

$$\nabla^2\phi_2 = 0, \qquad \mathbf{x} \in \Omega_2(t), \tag{5.6b}$$

$$\phi_1 = \Lambda\left(\phi_2 - k_2\Psi\right), \qquad \mathbf{x} \in \partial\Omega(t), \tag{5.6c}$$

$$\frac{\partial\phi_1}{\partial n} = \frac{\partial\phi_2}{\partial n}, \qquad \mathbf{x} \in \partial\Omega(t). \tag{5.6d}$$

The constant Λ, defined as $\Lambda \coloneqq k_1/k_2 = \mu_2/\mu_1$, in (5.6c) is the mobility (or viscosity) ratio.

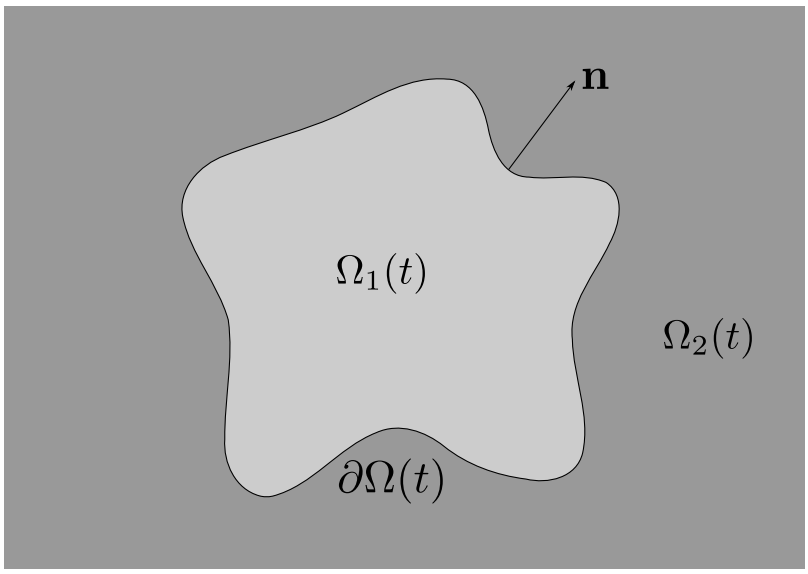

Figure 5.1: Sketch of the two-phase Hele-Shaw free boundary problem in an unbounded Hele-Shaw cell. The *inclusion*, i.e. the domain $\Omega_1(t)$ occupied by a viscous fluid with viscosity μ_1, is surrounded by an infinite expanse of another viscous fluid with viscosity μ_2. The direction of the normal vector on the interface $\partial\Omega(t)$ is displayed.

The stability of a planar front separating two fluids in an unbounded cell was first considered by Saffman and Taylor [123], where one fluid displaces the other. It is well understood that if fluid advances into another fluid of greater viscosity, the interface is unstable, as indicated in section 1.1. The mathematical solutions given in [123, 138] regarding fingers and bubbles in the Hele-Shaw cell are derived in the

limit where viscosity of one of the fluids is set to zero, i.e. the one-phase problem. However, some remarks are made on the two-phase problem in passing. For example, in [123], regarding the family of solutions for the Saffman-Taylor finger in a channel traveling at speed U, say, where the viscosity of the fluid inside the finger is taken to be zero, the equations of motion are considered for non-zero fluid viscosity inside the finger instead, where the finger now travels with speed U^*, say. The pressure condition in the two-phase scenario then reads $U^*/k_1 = |U|/k_2$, i.e. $U^* = \Lambda|U|$ and the authors remark that the width of the bubble remains unchanged, travelling with speed U^*.

In the following section we derive a numerical method for ZST two-phase Hele-Shaw flow, which is tested against known exact results in section 5.2.3, and new analytical results presented in section 5.3.

5.2 A numerical model for two-phase Hele-Shaw flows

Here, the BIM derived in chapter 2 is extended to the case when both fluids have non-zero viscosity. This requires Laplace's equation be satisfied in both phases. Namely, (5.6a)–(5.6b) are satisfied independently, and the velocity potentials in each phase are coupled through the boundary conditions (5.6c)–(5.6d).

5.2.1 Mathematical formulation

Suppose the two phases are separated by a simple closed curve, $\partial\Omega(t)$. In this chapter we restrict our attention to the evolution of $\partial\Omega(t)$ such that it remains a simple closed interface, for simplicity. The interface is driven by either a background field (as in section 2.5 for the one-phase problem) or hydrodynamic singularities,

which may exist in either fluid phase.

The velocity potential in each phase is decomposed as $\phi_j = \widetilde{\phi}_j + \widehat{\phi}_j$, $j = 1, 2$, where the velocity potentials due to the given background flow (e.g. due to hydrodynamic singularities in each phase) are $\widehat{\phi}_j(x, y, t)$, and $\widetilde{\phi}_j(x, y, t)$ are the potential parts due to the presence of the free boundary. The background flow field is given by $\widehat{\mathbf{u}}_j = \nabla\widehat{\phi}_j$. The velocity fields $\widetilde{\mathbf{u}}_j = \nabla\widetilde{\phi}_j(x, y, t)$ are solenoidal, irrotational vector fields which describe local evolution of the interface, $\partial\Omega(t)$, as a result of the background flow, and so $\widetilde{\phi}_j(x, y, t)$ are regular in $\Omega_j(t)$, for $j = 1, 2$, respectively. The total fluid velocity in each phase is then given by the sum $\mathbf{u}_j = \widetilde{\mathbf{u}}_j + \widehat{\mathbf{u}}_j$, $j = 1, 2$. In terms of the complex variable $z = x + iy$, $\widetilde{\phi}_j(x, y, t) \equiv \widetilde{\phi}_j(z, \bar{z}, t)$, and therefore, in terms of $\widetilde{\phi}_j$, the free boundary problem (5.6) can be written as

$$\nabla_z^2\widetilde{\phi}_1 = 0, \qquad z \in \Omega_1(t), \tag{5.7a}$$

$$\nabla_z^2\widetilde{\phi}_2 = 0, \qquad z \in \Omega_2(t), \tag{5.7b}$$

$$\widetilde{\phi}_1 + \widehat{\phi}_1 = \Lambda\left(\widetilde{\phi}_2 + \widehat{\phi}_2 - k_2\Psi\right), \qquad z \in \partial\Omega(t), \tag{5.7c}$$

$$\frac{\partial}{\partial n}\left(\widetilde{\phi}_1 + \widehat{\phi}_1\right) = \frac{\partial}{\partial n}\left(\widetilde{\phi}_2 + \widehat{\phi}_2\right), \qquad z \in \partial\Omega(t), \tag{5.7d}$$

where $\nabla_z^2 = 4\partial^2/\partial z\partial\bar{z} \equiv \partial^2/\partial x^2 + \partial^2/\partial y^2$, $\partial/\partial n = \Re\{(n_1 + in_2)(\partial_x - i\partial_y)\}$, and $\mathbf{n} = (n_1, n_2)$ is the unit normal vector on $\partial\Omega(t)$ pointing from $\Omega_1(t)$ in to $\Omega_2(t)$.

Let the interface be parameterised w.r.t. arc length, s, such that $\partial\Omega(t)$ is traversed in the anticlockwise direction, then the normal and tangential vectors are defined as (2.4a) and (2.4b). Let us define the *total* normal and tangential velocities of each fluid phase on the interface as

$$\begin{aligned} v_{nj} &= \mathbf{u}_j \cdot \mathbf{n} \\ &= u_j\frac{\mathrm{d}y}{\mathrm{d}s} - v_j\frac{\mathrm{d}x}{\mathrm{d}s} \end{aligned} \tag{5.8a}$$

and

$$\begin{aligned} v_{\tau j} &= \mathbf{u}_j \cdot \boldsymbol{\tau} \\ &= u_j \frac{\mathrm{d}x}{\mathrm{d}s} + v_j \frac{\mathrm{d}y}{\mathrm{d}s}, \end{aligned} \tag{5.8b}$$

where $\mathbf{u}_j = (u_j, v_j)$ is the fluid velocity vector in each phase $j = 1, 2$ and $\boldsymbol{\tau} = (\tau_1, \tau_2)$ is the unit tangent vector on $\partial\Omega(t)$. Taking the tangential derivative of the dynamic boundary condition (5.7c) yields

$$\frac{\partial \widetilde{\phi}_1}{\partial \tau} + \frac{\partial \widehat{\phi}_1}{\partial \tau} = \Lambda \left(\frac{\partial \widetilde{\phi}_2}{\partial \tau} + \frac{\partial \widehat{\phi}_2}{\partial \tau} - k_2 \frac{\partial \Psi}{\partial \tau} \right), \qquad z \in \partial\Omega(t), \tag{5.9}$$

i.e.

$$\widetilde{v}_{\tau 1} = -\widehat{v}_{\tau 1} + \Lambda(\widetilde{v}_{\tau 2} + \widehat{v}_{\tau 2} - k_2 \Psi_\tau), \qquad z \in \partial\Omega(t), \tag{5.10}$$

where $\Psi_\tau = \partial\Psi/\partial\tau = \boldsymbol{\tau} \cdot \nabla\Psi$. We shall write the kinematic boundary condition (5.7d) as

$$\widetilde{v}_{n1} = -\widehat{v}_{n1} + \widehat{v}_{n2} + \widetilde{v}_{n2}, \qquad z \in \partial\Omega(t). \tag{5.11}$$

Since the normal velocity on $\partial\Omega(t)$ must be continuous, the velocity of the interface shall be denoted by

$$V_n = v_{n1} = v_{n2}, \qquad z \in \partial\Omega(t). \tag{5.12}$$

Before we construct the BIEs on $\partial\Omega(t)$, first assume $\Omega_2(t)$ is enclosed by a large circular contour Γ_R, of radius R, centred at the centre of mass of $\Omega_1(t)$—see figure 5.2. We construct the function $F_j(z,t)$, $j = 1, 2$, such that

$$F_j(z,t) \coloneqq \frac{\partial \widetilde{w}_j / \partial z}{z - z_m}, \tag{5.13}$$

where $z_m \in \partial\Omega(t)$ and $\widetilde{w}_j = \widetilde{\phi}_j + i\widetilde{\psi}_j$ is the complex potential in the fluid region $\Omega_j(t)$ and $\widetilde{\psi}_j$ is the harmonic conjugate of $\widetilde{\phi}_j$, $j = 1, 2$. Now we consider two contour integral equations such that the contours enclose the domains $\Omega_j(t)$ lying to their

left. First we consider an equation concerning the complex potential in the inclusion, i.e. in the fluid domain $\Omega_1(t)$, given by

$$\frac{1}{2i\pi}\oint_{\partial\Omega(t)} F_1(z,t)\,\mathrm{d}z = \frac{1}{2}\left.\frac{\partial\widetilde{w}_1}{\partial z}\right|_{z_m}, \tag{5.14}$$

since $\partial\widetilde{w}_j/\partial z$ is an analytic function inside $\Omega_j(t)$, $j = 1, 2$. Making the change of variable as proposed in section 2.2.2, (5.14) can be written as

$$\fint_0^{L(t)} \frac{\widetilde{v}_{\tau 1}(s) + i\widetilde{v}_{n1}(s)}{z(s) - z(s_m)}\,\mathrm{d}s = i\pi\,(\widetilde{v}_{\tau 1} + i\widetilde{v}_{n1})\left.\left(\frac{\mathrm{d}z}{\mathrm{d}s}\right)^{-1}\right|_{s_m}, \tag{5.15}$$

where the integral on the left hand side is a Cauchy principal value integral, $L(t)$ is the total arc length of $\partial\Omega(t)$ and on the interface the identity

$$(\widetilde{u}_j - i\widetilde{v}_j)\frac{\mathrm{d}z}{\mathrm{d}s} = \widetilde{v}_{\tau j} + i\widetilde{v}_{nj}, \qquad j = 1, 2, \tag{5.16}$$

has been employed.

Now we consider the integral equation such that the contour is constructed to contain $\Omega_2(t)$ to its left. In order to achieve this, the contour considered is $\Gamma_R \cup z_A z_B \cup \partial\Omega(t) \cup z_B z_A$, as displayed in figure 5.2, and a change of sign is made in the integral equation to account for the reversal of the orientation such that $\Omega_2(t)$ does indeed lie to the left of the appropriately orientated contour. Hence, the integral equation considering the complex potential of the fluid occupying $\Omega_2(t)$ reads

$$-\frac{1}{2i\pi}\left(\oint_{\Gamma_R} + \int_{z_A z_B} + \oint_{\partial\Omega(t)} - \int_{z_A z_B}\right) F_2(z,t)\,\mathrm{d}z = \frac{1}{2}\left.\frac{\partial\widetilde{w}_2}{\partial z}\right|_{z_m}, \tag{5.17}$$

where $z_A z_B$ is the straight path joining the points $z_A \in \Gamma_R$ to $z_B \in \partial\Omega(t)$. Considering the limit in which $R \to \infty$, in an analogous manner to the derivation presented

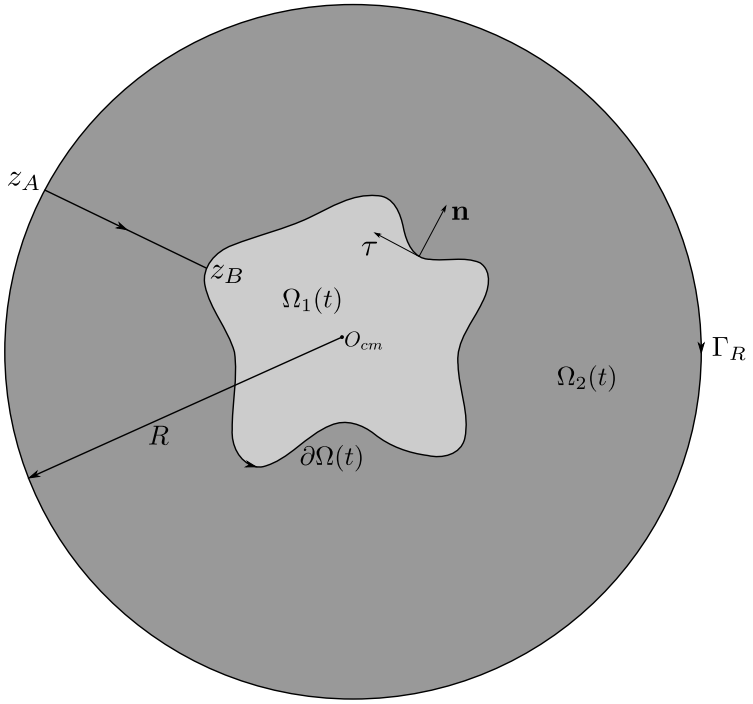

Figure 5.2: An inclusion $\Omega_1(t)$ surrounded by a finite fluid region, $\Omega_2(t)$, bounded by the curves $\partial\Omega(t)$ and Γ_R. The normal and tangential vectors along $\partial\Omega(t)$ are displayed. The choice of contours and their orientation in the calculation of the integral of (5.15) and (5.19) are also displayed, O_{cm} denotes the centre of mass of $\Omega_1(t)$ and R the radius of the circular contour Γ_R.

in section 2.6, (5.17) becomes

$$-\frac{1}{2i\pi}\oint_{\partial\Omega(t)} F_2(z,t)\,\mathrm{d}z = \frac{1}{2}\left.\frac{\partial\widetilde{w}_2}{\partial z}\right|_{z_m}. \tag{5.18}$$

In parametric from, w.r.t. arc length, and making use of the identity (5.16), (5.18) becomes

$$\int_0^{L(t)} \frac{\widetilde{v}_{\tau 2}(s) + i\widetilde{v}_{n2}(s)}{z(s) - z(s_m)}\,\mathrm{d}s = -i\pi\,(\widetilde{v}_{\tau 2} + i\widetilde{v}_{n2})\left.\left(\frac{\mathrm{d}z}{\mathrm{d}s}\right)^{-1}\right|_{s_m}. \tag{5.19}$$

Using the dynamic and kinematic conditions (5.10) and (5.11), the integral equations (5.15) and (5.19) are written in terms of the two unknown quantities of one of the fluid phases, i.e. $\widetilde{v}_{nj}$ and $\widetilde{v}_{\tau j}$ for $j = 1$ *or* 2. In what follows, we eliminate $\widetilde{v}_{\tau 1}$ and $\widetilde{v}_{n1}$ in favour of $\widetilde{v}_{\tau 2}$ and $\widetilde{v}_{n2}$ such that (5.15) and (5.19) give a system of coupled

integral equations, i.e.

$$\begin{aligned}\oint_0^{L(t)} \frac{-\widehat{v}_{\tau 1} + \Lambda\left[\widetilde{v}_{\tau 2}(s) + \widehat{v}_{\tau 2}(s) - k_2\Psi_\tau(s)\right]}{z(s) - z(s_m)}\,\mathrm{d}s \\ + i\oint_0^{L(t)} \frac{-\widehat{v}_{n1}(s) + \widetilde{v}_{n2}(s) + \widehat{v}_{n2}(s)}{z(s) - z(s_m)}\,\mathrm{d}s \\ = i\pi\left\{-\widehat{v}_{\tau 1} + \Lambda\left[\widetilde{v}_{\tau 2} + \widehat{v}_{\tau 2} - k_2\Psi_\tau\right] + i\left[-\widehat{v}_{n1} + \widetilde{v}_{n2} + \widehat{v}_{n2}\right]\right\}\left(\frac{\mathrm{d}z}{\mathrm{d}s}\right)^{-1}\Bigg|_{s_m},\end{aligned} \tag{5.20a}$$

and

$$\oint_0^{L} \frac{\widetilde{v}_{\tau 2}(s) + i\widetilde{v}_{n2}(s)}{z(s) - z(s_m)}\,\mathrm{d}s = -i\pi\left[\widetilde{v}_{\tau 2} + i\widetilde{v}_{n2}\right]. \tag{5.20b}$$

Re-arranging (5.20a) and (5.20b), we have

$$\left(\frac{\mathrm{d}z}{\mathrm{d}s}\right)\Bigg|_{s_m}\oint_0^{L(t)} \frac{\Lambda\widetilde{v}_{\tau 2}(s) + i\widetilde{v}_{n2}(s)}{z(s) - z(s_m)}\,\mathrm{d}s - i\pi\left[\Lambda\widetilde{v}_{\tau 2}(s_m) + i\widetilde{v}_{n2}(s_m)\right] = r(s_m), \tag{5.21a}$$

$$\left(\frac{\mathrm{d}z}{\mathrm{d}s}\right)\Bigg|_{s_m}\oint_0^{L(t)} \frac{\widetilde{v}_{\tau 2}(s) + i\widetilde{v}_{n2}(s)}{z(s) - z(s_m)}\,\mathrm{d}s + i\pi\left[\widetilde{v}_{\tau 2}(s_m) + i\widetilde{v}_{n2}(s_m)\right] = 0, \tag{5.21b}$$

where $z_m = z(s_m) \in \partial\Omega(t)$, and here $r(s_m)$ is a known function on the interface, given by

$$\begin{aligned}r(s_m) = \left(\frac{\mathrm{d}z}{\mathrm{d}s}\right)\Bigg|_{s_m}\oint_0^{L(t)} \frac{\widehat{v}_{\tau 1}(s) - \Lambda\left[\widehat{v}_{\tau 2}(s) - k_2\Psi_\tau(s)\right] - i\left[\widehat{v}_{n2}(s) - \widehat{v}_{n1}(s)\right]}{z(s) - z(s_m)}\,\mathrm{d}s \\ + i\pi\left\{-\widehat{v}_{\tau 1}(s_m) + \Lambda\left[\widehat{v}_{\tau 2}(s_m) - k_2\Psi_\tau(s_m)\right] + i\left[\widehat{v}_{n2}(s_m) - \widehat{v}_{n1}(s_m)\right]\right\}.\end{aligned} \tag{5.22}$$

The known tangential and normal velocities on the interface, i.e. $\widehat{v}_{\tau j}$ and $\widehat{v}_{nj}$, can be found given the background potential $\widehat{\phi}_j$ in each phase, $j = 1, 2$. The coupled equations (5.21) can be solved for $\widetilde{v}_{n2}$ and $\widetilde{v}_{\tau 2}$ from which the normal velocity of the of the interface, V_n, can be inferred according to (5.12) and recalling that $v_{n2} = \widetilde{v}_{n2} + \widehat{v}_{n2}$. Since the interface moves in the normal direction, the velocity of the interface is given

by

$$\mathbf{V}_{\partial\Omega} = V_n \mathbf{n}, \qquad \mathbf{x} \in \partial\Omega(t). \tag{5.23}$$

Therefore, the interface is advected according to

$$\frac{\mathrm{d}\mathbf{x}}{\mathrm{d}t} = \mathbf{V}_{\partial\Omega}, \qquad \mathbf{x} \in \partial\Omega(t). \tag{5.24}$$

This completes the formulation for the numerical method of the two-phase, ZST Hele-Shaw free boundary problem with external background fields. Equations (5.21)–(5.23) give the normal velocity of $\partial\Omega(t)$ at any instance, and (5.24) allows the interface to be advected in time.

5.2.2 Numerical procedure

In what follows, explicit time notation is suppressed for brevity. Equations (5.21) and (5.24) can be discretised in space and time, and the solutions $\widetilde{v}_{n2}$ and $\widetilde{v}_{\tau 2}$ can be approximated numerically. The interface is discretised according to (2.25)–(2.28), and the midpoints and derivatives are calculated according to (2.31) and (2.38), respectively, as presented in section 2.3. The unknown quantities to be found at the discrete mesh points, S_i, are

$$\alpha n_i = \widetilde{v}_n(S_i), \tag{5.25a}$$

$$\alpha \tau_i = \widetilde{v}_\tau(S_i), \tag{5.25b}$$

for $i = 1, \ldots, N$, with the periodic conditions

$$\alpha n_{N+1} = \alpha n_1, \tag{5.26a}$$

$$\alpha \tau_{N+1} = \alpha \tau_1. \tag{5.26b}$$

The BIEs (5.21a) and (5.21b) can be discretised as follows. The integrals are approximated via the trapezium rule, for example, the first integral in (5.21a) can be approximated as

$$\int_0^L \frac{\Lambda\widetilde{v}_{\tau 2}(s) + i\widetilde{v}_{n2}(s)}{z(s) - z(s_m)}\,\mathrm{d}s \approx \sum_{j=1}^{N} \frac{\Lambda\alpha\tau_j + i\alpha n_j}{Z_j - Z_{m+1/2}}\Delta S, \quad m = 1, \ldots, N. \tag{5.27}$$

The value of the solution at the midpoints $S_{i+1/2}$, for $i = 1, \ldots, N$, are calculated via a linear approximation, for example, $\alpha n(S_{i+1/2})$ is approximated as

$$\alpha n_{i+1/2} = \frac{1}{Z_{i+1} - Z_i}\left[\left(Z_{i+1} - Z_{i+1/2}\right)\alpha n_i + \left(Z_{i+1/2} - Z_i\right)\alpha n_{i+1}\right]. \tag{5.28}$$

Since the background normal and tangential velocities are known at the discrete points, i.e. $\widehat{v}_{n2}(S_i)$ and $\widehat{v}_{\tau 2}(S_i)$, and midpoints, i.e. $\widehat{v}_{n2}(S_{i+1/2})$ and $\widehat{v}_{\tau 2}(S_{i+1/2})$, the function $r(s_m)$ can be approximated using the trapezium rule and we write $r(s_m) = r(S_{m+1/2}) \approx R_m$, $m = 1, \ldots, N$. Hence, as in chapter 2, choosing s_m to coincide with the midpoints $S_{m+1/2}$, the BIEs (5.21a) and (5.21b) each provide N linear, algebraic equations.

Let us write the right hand side of (5.21a) and (5.21b) as one vector, i.e. $\mathbf{R} = (R_1, \ldots, R_N, R_{N+1}, \ldots, R_{2N})^\top$, where $R_i = 0$, for $i = N+1, \ldots, 2N$, i.e. the right hand side of (5.21b). Then, constructing a solution vector $\boldsymbol{\alpha}$, such that $\boldsymbol{\alpha} = (\boldsymbol{\alpha}\mathbf{n}, \boldsymbol{\alpha}\boldsymbol{\tau})^\top$, where $\boldsymbol{\alpha}\mathbf{n} = (\alpha n_1, \ldots, \alpha n_N)^\top$ and $\boldsymbol{\alpha}\boldsymbol{\tau} = (\alpha\tau_1, \ldots, \alpha\tau_N)^\top$ are the normal and tangential velocities at the N mesh points, a matrix equation can be written in the form

$$\boldsymbol{M}\boldsymbol{\alpha} = \mathbf{R}, \tag{5.29}$$

giving a $2N \times 2N$ system of linear equations. The elements M_{kj} of $\boldsymbol{M}$ and R_k of $\mathbf{R}$ are calculated appropriately, according to (5.21), in a similar manner to (2.44)–(2.46) presented in section 2.3.1. Following the filtering method proposed in the numerical

solution to the one-phase problem, as presented in 2.4, the matrix system (5.29) is modified by considering errors in approximating the right hand side of (5.21b). Assuming $\widetilde{v}_{n2}(s)$ and $\widetilde{v}_{\tau 2}(s)$ are smooth periodic functions on $\partial\Omega(t)$, the modification incorporates the condition that the integral of the square of the second derivatives for $\widetilde{v}_{n2}(s)$ and $\widetilde{v}_{\tau 2}(s)$ must be minimised, independently. The modified matrix equation reads

$$(\boldsymbol{M}^\top \boldsymbol{M} + \gamma \boldsymbol{P})\alpha = \boldsymbol{M}^\top \mathbf{R}, \tag{5.30}$$

where $\boldsymbol{P}$ is the block diagonal matrix

$$\boldsymbol{P} = \begin{pmatrix} \boldsymbol{H} & \mathbf{0} \\ \mathbf{0} & \boldsymbol{H} \end{pmatrix}, \tag{5.31}$$

and the $N \times N$ matrix $\boldsymbol{H}$ is the matrix representation of a third order difference operator [144] and γ denotes the smoothing parameter, where $0 < \gamma < \infty$ (see section 2.4 for further detail).

It remains to compute the evolution of $\partial\Omega$ in time after computing the solution vector α from (5.30) at time t_j. The evolution can be approximated at the following time step $t_{j+1} = t_j + \Delta t$ by

$$\Re(Z_i^{\text{new}}) = \Re(Z_i) + \mathcal{U}(S_i, t_j)\Delta t, \quad i = 1, \ldots, N, \tag{5.32}$$

$$\Im(Z_i^{\text{new}}) = \Im(Z_i) + \mathcal{V}(S_i, t_j)\Delta t, \quad i = 1, \ldots, N, \tag{5.33}$$

where $Z_i^{\text{new}} \in \partial\Omega^{\text{new}}$, which is the new position of the interface $\partial\Omega$ at $t = t_j + \Delta t$, $\mathcal{U}(S_i, t_j) = \Im\{V_n(S_i, t)\mathrm{d}Z_i/\mathrm{d}s\}$, $\mathcal{V}(S_i, t_j) = -\Re\{V_n(S_i, t)\mathrm{d}Z_i/\mathrm{d}s\}$, $V_n(S_i, t_j) = \widetilde{v}_n(S_i, t_j) + \widehat{v}_n(S_i, t_j)$ and $(\mathcal{U}, \mathcal{V}) = \mathbf{V}_{\partial\Omega}$ as in (5.24). A modified Euler (i.e. a second order Runge-Kutta) method is employed, as in [8] and chapter 2, such that the time stepping method is approximately $\mathcal{O}((\Delta t)^2)$ accurate.

When $\partial\Omega^{\text{new}}$ is found, the new total arc length L^{new} is computed from the mesh

points Z_i^{new}, $i = 1, \ldots, N+1$, which are then redistributed to an equispaced mesh by cubic spline interpolation. Setting $Z_i = Z_i^{\text{new}}$ (after interpolation to the equispaced mesh), i.e. setting $\partial\Omega = \partial\Omega^{\text{new}}$ and $L = L^{\text{new}}$, applying the above procedure again completes the algorithm for computing $\partial\Omega$ at later times.

5.2.3 Testing and results

Example 5.2.1 (Elliptical inclusion in a straining flow)

Here we consider the exact solution derived by Crowdy [20] for an elliptical inclusion, $\Omega_1(t)$, inside a steady straining background flow in $\Omega_2(t)$. The derivative of the complex potential in the phase occupying $\Omega_2(t)$, in terms of the notation of section 5.2.1, is given by

$$\frac{\partial \widehat{w}_2}{\partial z} = \sigma_{st} z, \tag{5.34}$$

as $z \to \infty$ where σ_{st}, a given constant, is the strength of the purely straining flow. Here we have $\Psi \equiv 0$. Following the solution presented in [20], the interface $\partial\Omega(t)$ is mapped from the unit ζ-circle ∂D by

$$z = \frac{a}{\zeta} + b\zeta, \tag{5.35}$$

where $a(t)$ and $b(t)$ are real time-dependent parameters given by the solution

$$a = \frac{1}{\sqrt{1 - |e|^2}}, \tag{5.36}$$

$$b = ea, \tag{5.37}$$

and $e(t)$ represents eccentricity of the ellipse and is given by the solution to the equation

$$\Lambda \tanh^{-1} e - \frac{\Lambda - 1}{2} e = \sigma_{st} t. \tag{5.38}$$

Figures 5.3(a) and 5.3(b) show comparison between numerical results and the exact solution described by (5.35)–(5.38) for $\Lambda = 0.5$ and 2, respectively. There is excellent agreement between numerical and explicit solutions.

Example 5.2.2 (Expanding circular inclusion)

Here we consider the explicit solution of example 5.3.1 for a circular inclusion, $\Omega_1(t)$, centred on the origin, driven by a point source of strength Q_1 located at at the origin. In this example, we make use of the external field Ψ to cater for the sink at infinity, in $\Omega_2(t)$, by setting $\Psi = (-Q_1/2\pi k_1)\log|z|$ in (5.22) and the background fields in $\Omega_1(t)$ and $\Omega_2(t)$ are given by $\widehat{\phi}_1 = (Q_1/2\pi)\log|z|$ and $\widehat{\phi}_2 = 0$, respectively. This satisfies the condition $\Psi = p_1 - p_2$ on $\partial\Omega(t)$.

Figure 5.4(a) shows comparison between the exact solution (derived in example 5.3.1 in section 5.3) and numerical solution of the interface. Figure 5.4(b) shows the relative error, (2.78), between the area of the inclusion calculated explicitly, given in example 5.3.1, and numerically, according to (2.76). There is excellent agreement between the numerical and exact solutions.

5.3 Exact solutions

Here we present steady solutions for translating inclusions in a uniform steady background flow in the case of an ellipse, with major axis inclined at an arbitrary angle to the direction of the background flow, and for a circle, where a relationship between the propagation speed of the inclusion and the mobility ratio is derived.

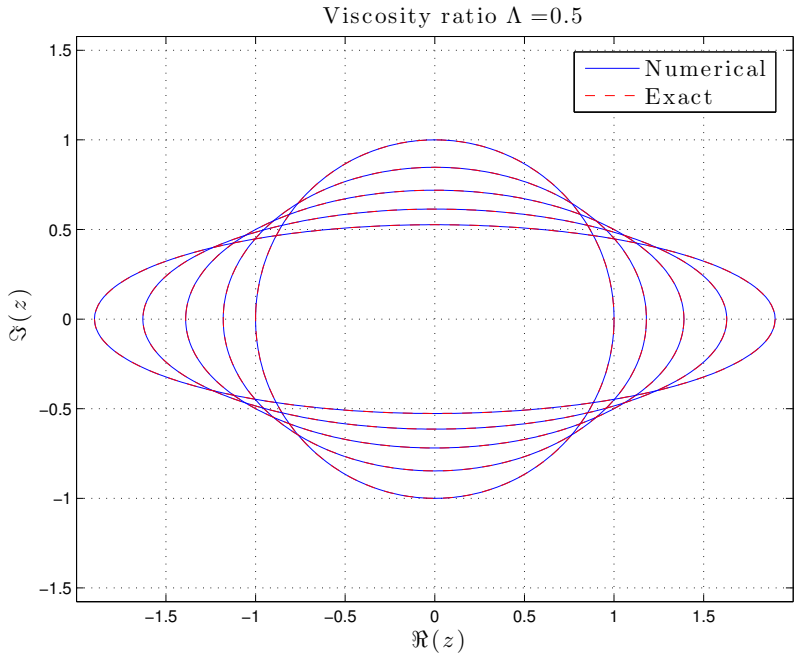

(a)

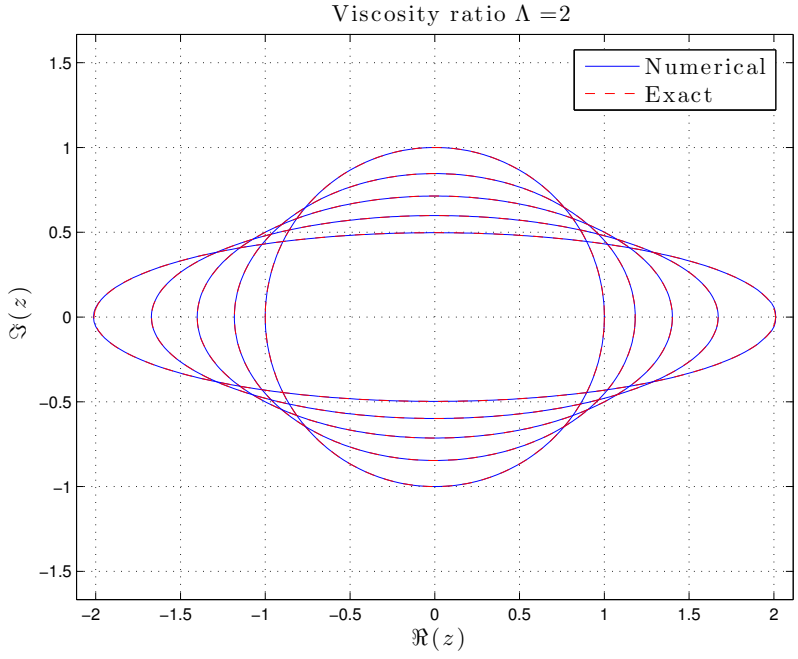

(b)

Figure 5.3: Superposition of the numerical and exact solutions of the interface at time (a) $t = 0$, 0.25, 0.5, 0.75 and 1, and (b) $t = 0$, 0.125, 0.25, 0.375 and 0.5. Results presented for an initially circular inclusion subject to a straining background flow with $\sigma_{st} = 1$ and viscosity ratios (a) $\Lambda = 0.5$ and (b) $\Lambda = 2$. Here there are $N = 300$ mesh points on the free boundary and step-size $\Delta t = 10^{-3}$. The initial circular interface is given by (5.35) with $a(0) = 1$ and $b(0) = 0$, i.e. $e(0) = 0$.

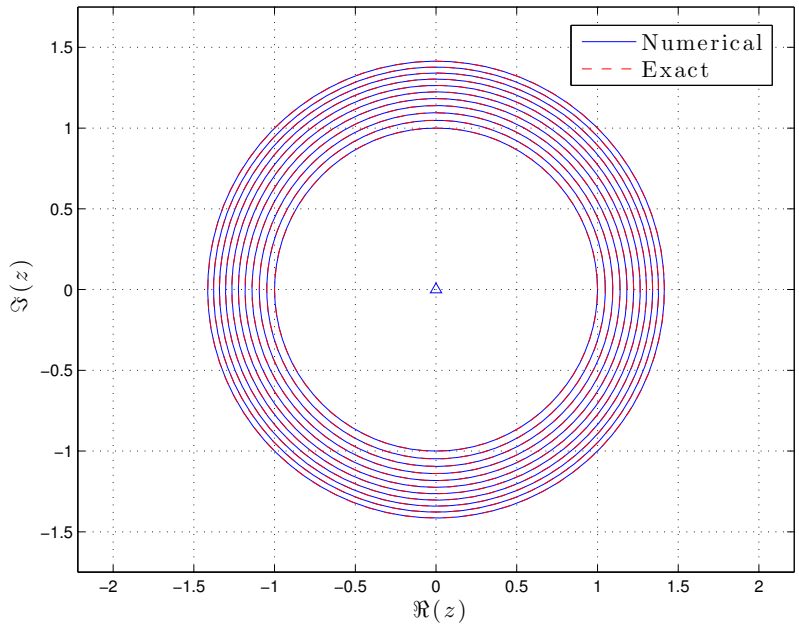

(a)

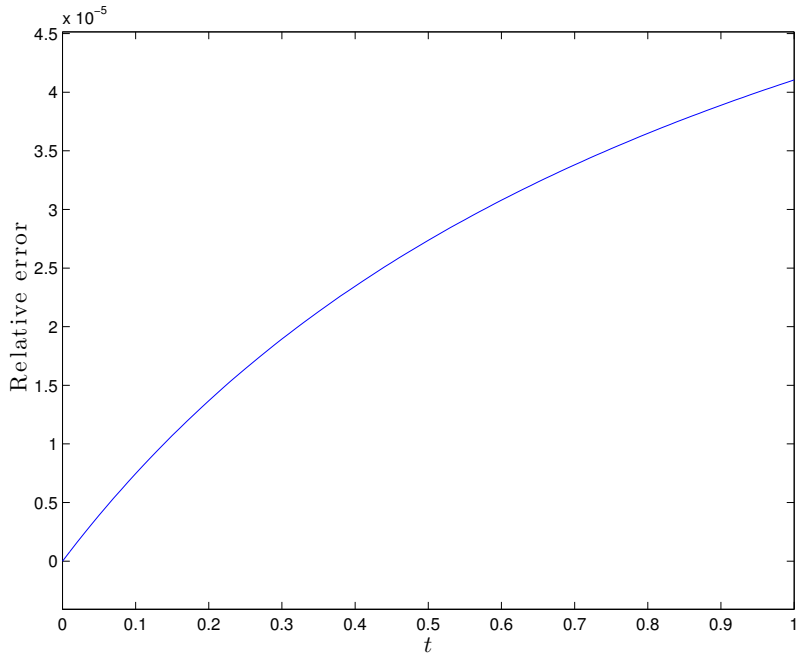

(b)

Figure 5.4: Superposition of the numerical and exact solutions of the interface at time $t = 0$, 0.1, 0.2, 0.3, 0.4, 0.5, 0.6, 0.7, 0.8, 0.9 and 1.0 shown in (a). The relative error of inclusion area, $0 \leq t \leq 1$, is shown in (b). Results are presented for an an initially circular inclusion subject to point source of strength $Q_1 = \pi$ located at the origin, marked by a triangle in (a), and viscosity ratio $\Lambda = 0.5$. Here there are $N = 100$ mesh points on the free boundary and step-size $\Delta t = 10^{-3}$. The initial circular interface is given by (5.46) with $R(0) = R_0 = 1$.

This theoretical result is compared with results from simulations computed using the numerical method presented in section 5.2.

5.3.1 Solution methods

As discussed in section 5.1, little work on exact solutions to the two-phase problem exists due to the difficulties of applying complex variable methods. Below we briefly discuss two solution methods suggested in the literature. First we give an account of the method suggested by Howison [60].

In [60], a solution method in an 'inverse manner' is presented, motivated by the comments on the two-phase finger solution made by Saffman and Taylor [123]. The following steps are suggested.

(i) Construct the complex potential, w_1, in $\Omega_1(t)$ to be an analytic function in the entire complex plane (not just inside the inclusion). The idea is to analytically continue w_1 away from the initial interface between the two-phases, $\partial\Omega(0)$, assuming no additional singularities exist. That is, considering the one-phase problem with, $\phi_2 \equiv 0$ in $\Omega_2(t)$, then the complex potential w_1 satisfies the Schwarz function equation (1.46), i.e. $2\partial w_1/\partial z = \partial g/\partial t$. Therefore, assuming w_1 can be analytically continued away from $\partial\Omega(0)$ implies g, the Schwarz function of the initial interface, has no additional singularities.

(ii) Assume the fluid inside $\Omega_1(t)$ occupies all of the complex plane and then follow the evolution of $\partial\Omega(0)$ in $\mathbb{C}$ as a material curve under the action of w_1, with time, i.e. use the kinematic boundary condition (5.12) according to w_1. Therefore, the complex conjugate velocity of $\partial\Omega(t)$ is given by the derivative of the complex potential w_1. Writing the equation of the interface according

to (1.29) we have

$$\begin{aligned}\frac{\partial w_1}{\partial z} &= \frac{\mathrm{d}\bar{z}}{\mathrm{d}t} \\ &= \frac{\mathrm{d}g}{\mathrm{d}t} \\ &= \frac{\partial g}{\partial z}\frac{\mathrm{d}z}{\mathrm{d}t} + \frac{\partial g}{\partial t},\end{aligned} \tag{5.39}$$

hence

$$\frac{\partial w_1}{\partial z} = \frac{\partial g}{\partial z}\frac{\partial \overline{w_1}}{\partial z} + \frac{\partial g}{\partial t}, \tag{5.40}$$

where $\overline{w_1} = \overline{w_1}(\bar{z}, z, t) = \overline{w_1}(g(z,t), z, t)$ is analytic in $\Omega_1(t)$ since w_1 is. Equation (5.40) has characteristics from which it is found that $\varpi_2 - w_2 =$ constant along the characteristics, an equation which must be satisfied for a valid solution to the two-phase problem.

(iii) Finally, find the complex potential w_2 (by writing $w_2 = (k_2/k_1)w_1 + \varpi_2$, where ϖ_2 is the additional correction required) catering for the fluid of viscosity μ_2 in $\Omega_2(t)$, which must satisfy the dynamic boundary boundary condition (5.3) on $\partial\Omega(t)$, as well as the kinematic boundary condition (5.4). Writing $\Re(\varpi_2) = \varphi_2$, then the velocity potential of w_2 is given by $\Re(w_2) = \phi_2 = \phi_1 + \varphi_2$ and $\Re(w_1) = \phi_1$ is known from steps (i) and (ii). Then, φ_2 must satisfy the pseudo one-phase free boundary problem

$$\nabla_z^2 \varphi_2 = 0, \qquad z \in \Omega_2(t), \tag{5.41a}$$

$$\varphi_2 = 0, \qquad z \in \partial\Omega(t), \tag{5.41b}$$

$$\frac{\partial \varphi_2}{\partial n} = \frac{k_1 - k_2}{k_1}\frac{\partial \phi_1}{\partial n}, \qquad z \in \partial\Omega(t), \tag{5.41c}$$

where the Schwarz function equation (1.46) can be applied and, in this case, would be written as $2\partial\varpi_2/\partial z = \partial g/\partial t$.

Using the method above, Howison [60] gives examples of constructing exact solutions, e.g. travelling wave, straining flow, and also derives the solution of Jacquard

and Séguier [65] of growing fingers in a channel, which is the same (for a particular value of finger width) as given by Saffman in [122]. Crowdy [20] notes that the solution obtained by Jacquard and Séguier [65] is somewhat fortuitous and that the above solution method of Howison [60] is a systematic alternative.

Crowdy [20] also suggests a solution method of finding explicit solutions of the two-phase Hele-Shaw free boundary problem in the following manner, relying on two main steps when the interface $\partial\Omega(t)$ is given in the form of a parametric map for a particular class of time-dependent flows.

(i) First write the velocity potential in each phase in complex form as $\phi_j = \Re\{w_j(z,t)\} = \{w_j(z,t) + \overline{w_j(z,t)}\}/2,\ j = 1,2.$ Hence, applying the dynamic condition (5.3) and kinematic condition (5.4), a relationship between the derivative of the complex potential in $\Omega_2(t)$ can be written in terms of the complex potential in $\Omega_1(t)$, known a priori, i.e. to find explicitly the derivative of the complex potential in $\Omega_2(t)$ due to the presence (and pressure inside) of $\Omega_1(t)$ [20] by

$$\frac{\partial w_2}{\partial z} = \frac{(\Lambda^{-1}+1)}{2}\frac{\partial w_1}{\partial z} + \frac{(\Lambda^{-1}-1)}{2}\overline{\frac{\partial w_1}{\partial z}}\frac{\mathrm{d}g}{\mathrm{d}z}, \qquad z \in \partial\Omega(t). \tag{5.42}$$

(ii) Secondly, the kinematic condition, written in the form $\Im\{(\partial w_1/\partial z)(\mathrm{d}z/\mathrm{d}s)\} = -\Im\{(\mathrm{d}z/\mathrm{d}t)(\mathrm{d}\bar{z}/\mathrm{d}s)\}$ [20] is employed and the kinematic boundary condition (5.7d) can be written as

$$\frac{\partial w_2}{\partial z} - \overline{\frac{\partial w_2}{\partial z}}\frac{\mathrm{d}g}{\mathrm{d}z} = \frac{\partial w_1}{\partial z} - \overline{\frac{\partial w_1}{\partial z}}\frac{\mathrm{d}g}{\mathrm{d}z}, \qquad z \in \partial\Omega(t). \tag{5.43}$$

Equation (5.43) can then be used to determine the evolution of the interface, as the parameters of the map of $\partial\Omega(t)$ are found as the solution to a system of ODEs.

In fact, Crowdy [20] derives exact solutions assuming $\Omega_1(t)$ is elliptical for all time, subject to background flows such that $\partial w_1/\partial z$ is a linear function of z. In section 5.3.2 and 5.3.3, we consider a class of flows such that the derivative of the complex potential inside $\Omega_1(t)$ is assumed constant, i.e. we consider translating inclusions as a result of a uniform background flow in $\Omega_2(t)$. Crowdy [20] remarks that the elliptical shape of $\partial\Omega(t)$ and the linear flow in $\Omega_1(t)$ is a 'special case', and the analysis presented there cannot be extended easily to other interface shapes. A particular reason being that the derivative of the Schwarz function, i.e. $\partial g/\partial z$ in (5.42), should not exhibit any singularities for w_2 to be analytic throughout the complex plane.

Below we present a straight forward example of finding an exact solution based on the method suggested in [20].

Example 5.3.1 (Expanding circular inclusion)

Consider a circular inclusion $\Omega_1(t)$ expanding due to a point source of strength $Q_1 > 0$, located at the centre of $\Omega_1(t)$, taken to be the origin w.l.o.g., for which the complex potential in $\Omega_1(t)$ is given by

$$w_1 \to \frac{Q_1}{2\pi}\log z, \qquad \text{as } z \to 0. \tag{5.44}$$

In the outer fluid, i.e. in $\Omega_2(t)$, the complex potential behaves like

$$w_2 \to \frac{Q_2}{2\pi}\log z, \qquad \text{as } z \to \infty, \tag{5.45}$$

where fluid is removed to conserve mass ($Q_2 > 0$), i.e. there exists a sink at infinity.

Let the circular interface $\partial\Omega(t)$ be given by the map

$$z = \frac{R}{\zeta}, \tag{5.46}$$

which, in fact, is a conformal map from the interior of the unit ζ-disc, D, to the exterior of the circular inclusion, i.e. $\Omega_2(t)$. Taking the complex conjugate of (5.46), and differentiating w.r.t. z, we find the derivative of the Schwarz function of $\partial\Omega(t)$ to be

$$\frac{\mathrm{d}g}{\mathrm{d}z} = -\frac{R^2}{z^2}. \tag{5.47}$$

Therefore, applying (5.42) we have

$$\frac{Q_2}{2\pi}\frac{1}{z} = \frac{\Lambda^{-1}+1}{2}\frac{Q_1}{2\pi}\frac{1}{z} - \frac{\Lambda^{-1}-1}{2}\frac{Q_1}{2\pi}\frac{1}{\bar{z}}\frac{R^2}{z^2} \tag{5.48}$$

$$= \frac{\Lambda^{-1}+1}{2}\frac{Q_1}{2\pi}\frac{1}{z} - \frac{\Lambda^{-1}-1}{2}\frac{Q_1}{2\pi}\frac{z}{R^2}\frac{R^2}{z^2}, \tag{5.49}$$

and comparing terms of $\mathcal{O}(z^{-1})$ we find the strength of the sink at infinity to be

$$Q_2 = Q_1. \tag{5.50}$$

Now we apply the kinematic condition (5.6d), which can be written in the form (see equations (5.71)–(5.73) in section 5.3.2)

$$\Im\left(-i\frac{Q_1}{2\pi}\frac{1}{z}\frac{R}{\zeta}\right) = -\Im\left(i\frac{\dot{R}}{\zeta}R\zeta\right). \tag{5.51}$$

Using (5.46) on the interface, (5.51) yields

$$\frac{1}{2}\frac{\mathrm{d}}{\mathrm{d}t}(R^2) = \frac{Q_1}{\pi}, \tag{5.52}$$

that is, the area of the circular inclusion $\Omega_1(t)$ is given by $A = \pi R^2 = Q_1 t + \pi R_0^2$, as expected, with radius $R = \sqrt{R_0^2 + (Q_1 t/\pi)}$.

5.3.2 Rotated elliptical inclusion in a uniform flow

Consider a fluid of viscosity μ_1 separated from a fluid of viscosity μ_2 by a simple closed free boundary, $\partial\Omega(t) := \Omega_1(t) \cap \Omega_2(t)$, in an unbounded Hele-Shaw cell, where $\Omega_1(t)$ is of infinite expanse surrounding the inclusion $\Omega_1(t)$. The governing equations in each fluid phase are given by (5.1)–(5.4) which can be written in terms of the free boundary problem (5.6).

Suppose the free boundary (and thus the inclusion) is driven by a uniform background flow in $\Omega_2(t)$ of speed V in the positive x direction, then, the complex potential in $\Omega_2(t)$ is given by

$$w_2 \to Vz, \qquad \text{as } z \to \infty. \tag{5.53}$$

This implies $\Omega_1(t)$ propagates downstream with speed $U(t) = U_R(t) + iU_I(t)$, say, where the $U_I(t)$ allows for additional cross stream velocity. Suppose $\partial\Omega(t)$ is given by an ellipse whose semi-major axis is inclined at an angle $\theta_e(t)$ to the real axis. The mapping from the unit ζ-circle, ∂D, to the interface, $\partial\Omega(t)$, is given by

$$z = d + e^{i\theta_e}\left(\frac{a}{\zeta} + b\zeta\right), \tag{5.54}$$

i.e. it is assumed $\Omega_1(t)$ is elliptical for all time. Using the solution method presented in [20]—discussed in section 5.3.1 above—we check whether (5.54) yields a solution to the two-phase problem, and we seek the appropriate components of the velocity of the inclusion, i.e. (U_R, U_I). In fact, (5.54) describes a conformal map from the interior of the unit ζ-dsic, D, to the exterior of the ellipse, i.e. $\Omega_2(t)$, hence, we assume $a \neq 0$, and that $a(t)$, $b(t) \in \mathbb{R}$ and $d(t) \in \mathbb{C}$, are parameters to be found.

Assuming the fluid inside the inclusion $\Omega_1(t)$ propagates uniformly inside an elliptical boundary with speed $U = U_R + iU_I$, where U_R, $U_I \in \mathbb{R}$, then the complex

potential in $\Omega_1(t)$ is given by $w_1 = \overline{U}z$. Therefore, (5.42) gives

$$\frac{\partial w_2}{\partial z} = \frac{(\Lambda^{-1}+1)}{2}\overline{U} + \frac{(\Lambda^{-1}-1)}{2}U\frac{\mathrm{d}g}{\mathrm{d}z}, \qquad z \in \partial\Omega(t). \tag{5.55}$$

The function $\bar{z}$ on $\partial\Omega(t)$, i.e. when $\zeta \in \partial D$, is equivalent to the Schwarz function g of the interface, and from (5.54) we have that for the rotated elliptical interface

$$g = \overline{d} + e^{-i\theta_e}\left(a\zeta + \frac{b}{\zeta}\right). \tag{5.56}$$

From (5.54) we also note that

$$\frac{1}{\zeta} = \frac{e^{-i\theta_e}}{a}(z-d) - \frac{b}{a}\zeta, \tag{5.57}$$

and so (5.56) can be written as

$$g = \overline{d} - \frac{bd}{a}e^{-2i\theta_e} + \frac{b}{a}e^{-2i\theta_e}z + \frac{e^{-i\theta_e}}{a}\left(|a|^2 - |b|^2\right)\zeta. \tag{5.58}$$

Differentiating (5.58) w.r.t. z yields

$$\begin{aligned}\frac{\mathrm{d}g}{\mathrm{d}z} &= \frac{\overline{b}}{a}e^{-2i\theta_e} + \frac{e^{-i\theta_e}}{a}\left(|a|^2 - |b|^2\right)\frac{1}{\mathrm{d}z/\mathrm{d}\zeta} \\ &= \frac{\overline{b}}{a}e^{-2i\theta_e} + \frac{e^{-i\theta_e}}{a}\left(|a|^2 - |b|^2\right)\frac{\zeta^2}{b\zeta^2 - a}.\end{aligned} \tag{5.59}$$

Therefore, substituting (5.59) in (5.55) we have

$$\frac{\partial w_2}{\partial z} = \frac{(\Lambda^{-1}+1)}{2}\overline{U} + \frac{(\Lambda^{-1}-1)}{2}U\left[\frac{\overline{b}}{a}e^{-2i\theta_e} + \frac{e^{-i\theta_e}}{a}\left(|a|^2 - |b|^2\right)\frac{\zeta^2}{b\zeta^2 - a}\right], \tag{5.60}$$

which is a complex equation valid on the interface, i.e. for $z \in \partial\Omega(t)$. Note that $\mathrm{d}z/\mathrm{d}\zeta$, in this case, has no zeros inside the unit ζ-disc, D, which in turn implies that the right hand side of (5.55) is analytic for all $z \in \Omega_2(t)$, since $|a/b| > 1$.

From (5.54), as $\zeta \to 0$, i.e. $z \to \infty$, we find that

$$\frac{1}{\zeta} = \frac{e^{-i\theta_e}}{a}(z-\gamma) + \mathcal{O}(z^{-1}), \tag{5.61}$$

and

$$\zeta = ae^{i\theta_e}\frac{1}{z} + a\gamma e^{i\theta_e}\frac{1}{z^2} + \mathcal{O}(z^{-3}). \tag{5.62}$$

As $z \to \infty$, the complex potential in $\Omega_2(t)$ is given by (5.53). Hence, by analytic continuation, and expanding the right hand side of (5.60) as $z \to \infty$, we have

$$V = \frac{(\Lambda^{-1}+1)}{2}\overline{U} + \frac{(\Lambda^{-1}-1)}{2}U\left[\frac{\overline{b}}{a}e^{-2i\theta_e} + \left(|a|^2 - |b|^2\right)\frac{1}{z^2}\right] + \mathcal{O}(z^{-3}). \tag{5.63}$$

Comparing terms of $\mathcal{O}(1)$, (5.63) yields

$$2V = (\Lambda^{-1}+1)(U_R - iU_i) + (\Lambda^{-1}-1)(U_R + iU_i)\frac{b}{a}e^{-2i\theta_e}. \tag{5.64}$$

Taking the real and imaginary parts of (5.64) gives

$$2V = (\Lambda^{-1}+1)U_R + (\Lambda^{-1}-1)\frac{b}{a}(U_R\cos 2\theta_e + U_i \sin 2\theta_e) \tag{5.65a}$$

and

$$0 = -(\Lambda^{-1}+1)U_I + (\Lambda^{-1}-1)\frac{b}{a}(U_I\cos 2\theta_e - U_R \sin 2\theta_e), \tag{5.65b}$$

respectively. From (5.65b), re-arranging yields

$$\frac{U_I}{U_R} = \frac{(b/a)(\Lambda^{-1}-1)\sin 2\theta_e}{(b/a)(\Lambda^{-1}-1)\cos 2\theta_e - (\Lambda^{-1}+1)}, \tag{5.66}$$

which gives the angle of propagation of the inclusion $\Omega_1(t)$ as a function of the angle of tilt of the ellipse, θ_e, and the mobility ratio, Λ. Eliminating U_I between (5.66)

and (5.65a) we find

$$U_R = \frac{2V[-(\Lambda^{-1}+1)+(b/a)(\Lambda^{-1}-1)\cos 2\theta_e]}{(b/a)^2(\Lambda^{-1}-1)^2-(\Lambda^{-1}+1)^2}, \tag{5.67}$$

and thus, from (5.66), we may write U_I explicitly as

$$U_I = \frac{2V(b/a)(\Lambda^{-1}-1)\sin 2\theta_e}{(b/a)^2(\Lambda^{-1}-1)^2-(\Lambda^{-1}+1)^2}. \tag{5.68}$$

It now remains to calculate the evolution of the interface of the form (5.54) according to the kinematic condition (5.43), i.e. by (5.6d). First consider the identity

$$\begin{aligned} \mathrm{d}s^2 &= \mathrm{d}x^2+\mathrm{d}y^2 \\ &= \mathrm{d}z\mathrm{d}\bar{z}, \end{aligned} \tag{5.69}$$

therefore, we may write the derivative of z w.r.t. s as

$$\begin{aligned} \frac{\mathrm{d}z}{\mathrm{d}s} &= \frac{1}{\mathrm{d}\bar{z}/\mathrm{d}s} \\ &= \frac{\mathrm{d}z/\mathrm{d}s}{|\mathrm{d}z/\mathrm{d}s|^2} \\ &= \frac{(\mathrm{d}z/\mathrm{d}\zeta)(\mathrm{d}\zeta/\mathrm{d}s)}{|\mathrm{d}z/\mathrm{d}\zeta|^2|\mathrm{d}\zeta/\mathrm{d}s|^2}, \end{aligned} \tag{5.70}$$

hence

$$\frac{\mathrm{d}z}{\mathrm{d}s} = \frac{(\mathrm{d}z/\mathrm{d}\zeta)}{|\mathrm{d}z/\mathrm{d}\zeta|^2(\mathrm{d}\bar{\zeta}/\mathrm{d}s)}. \tag{5.71}$$

On $\partial\Omega(t)$, having parameterised w.r.t. arc length, s, we may write $\zeta = e^{is}$, hence $\mathrm{d}\bar{\zeta}/\mathrm{d}s = -ie^{-is}$, therefore

$$\frac{\mathrm{d}z}{\mathrm{d}s} = i\zeta\frac{\mathrm{d}z/\mathrm{d}\zeta}{|\mathrm{d}z/\mathrm{d}\zeta|^2} \tag{5.72a}$$

and

$$\frac{\mathrm{d}\bar{z}}{\mathrm{d}s} = -i\frac{\mathrm{d}\bar{z}/\mathrm{d}\zeta}{\zeta|\mathrm{d}z/\mathrm{d}\zeta|^2}. \tag{5.72b}$$

From (5.43), the kinematic condition can be written as

$$\Im\left(w_1'\frac{\mathrm{d}z}{\mathrm{d}s}\right) = -\Im\left(\frac{\mathrm{d}z}{\mathrm{d}t}\frac{\mathrm{d}\bar{z}}{\mathrm{d}s}\right). \tag{5.73}$$

Since $w_1 = \overline{U}z$, using (5.72), (5.73) becomes

$$\Im\left(\overline{U}i\zeta\frac{\mathrm{d}z}{\mathrm{d}\zeta}\right) = -\Im\left(-\frac{\mathrm{d}z}{\mathrm{d}t}\frac{i}{\zeta}\frac{\mathrm{d}\bar{z}}{\mathrm{d}\zeta}\right), \tag{5.74}$$

which is valid on the interface and may be written as

$$\Re\left(\overline{U}\zeta\frac{\mathrm{d}z}{\mathrm{d}\zeta}\right) = \Re\left(\frac{\mathrm{d}z}{\mathrm{d}t}\frac{1}{\zeta}\frac{\mathrm{d}\bar{z}}{\mathrm{d}\zeta}\right), \qquad z \in \partial\Omega(t). \tag{5.75}$$

From (5.54) we find that

$$\frac{\mathrm{d}z}{\mathrm{d}\zeta} = e^{i\theta_e}\left(-\frac{a}{\zeta^2} + b\right), \tag{5.76}$$

hence

$$\frac{\mathrm{d}\bar{z}}{\mathrm{d}\zeta} = e^{-i\theta_e}\left(-a\zeta^2 + b\right), \tag{5.77}$$

and

$$\frac{\mathrm{d}z}{\mathrm{d}t} = \frac{\mathrm{d}d}{\mathrm{d}t} + i\frac{\mathrm{d}\theta_e}{\mathrm{d}t}e^{i\theta_e}\left(\frac{a}{\zeta} + b\zeta\right) + e^{i\theta}\left(\frac{1}{\zeta}\frac{\mathrm{d}a}{\mathrm{d}t} + \frac{\mathrm{d}b}{\mathrm{d}t}\zeta\right). \tag{5.78}$$

Therefore, (5.75) reads

$$\Re\left[(U_R - iU_I)e^{i\theta_e}\left(-\frac{a}{\zeta} + b\zeta\right)\right] = \Re\left[e^{-i\theta_e}\left(-a\zeta + \frac{b}{\zeta}\right)\left(\frac{\mathrm{d}d}{\mathrm{d}t} + i\frac{\mathrm{d}\theta_e}{\mathrm{d}t}e^{i\theta_e}\left(\frac{a}{\zeta} + b\zeta\right) + e^{i\theta_e}\left(\frac{1}{\zeta}\frac{\mathrm{d}a}{\mathrm{d}t} + \frac{\mathrm{d}b}{\mathrm{d}t}\zeta\right)\right)\right], \quad (5.79)$$

where $\zeta \in \partial D$, i.e. $\zeta\overline{\zeta} = 1$. Writing $e^{i\theta_e} = \cos\theta_e + i\sin\theta_e$ and $\zeta = e^{i\alpha} = \cos\alpha + i\sin\alpha$, from (5.79) we have that

$$B(b-a)\cos\alpha - C(a+b)\sin\alpha = b\frac{\mathrm{d}b}{\mathrm{d}t} - a\frac{\mathrm{d}a}{\mathrm{d}t} + D(b-a)\cos\alpha + E(a+b)\sin\alpha + 2\frac{\mathrm{d}\theta_e}{\mathrm{d}t}ab\sin 2\alpha + (b\frac{\mathrm{d}a}{\mathrm{d}t} - a\frac{\mathrm{d}b}{\mathrm{d}t})\cos 2\alpha, \quad (5.80)$$

where

$$B = U_R\cos\theta_e + U_I\sin\theta_e, \qquad C = U_R\sin\theta_e - U_I\cos\theta_e,$$
$$D = \frac{\mathrm{d}d_R}{\mathrm{d}t}\cos\theta_e + \frac{\mathrm{d}d_I}{\mathrm{d}t}\sin\theta_e, \qquad E = \frac{\mathrm{d}d_I}{\mathrm{d}t}\cos\theta_e - \frac{\mathrm{d}d_R}{\mathrm{d}t}\sin\theta_e.$$

Comparing terms of $\mathcal{O}(1)$, $\mathcal{O}(\cos 2\alpha)$ and $\mathcal{O}(\sin 2\alpha)$ in (5.80) yields

$$\frac{1}{2}\frac{\mathrm{d}}{\mathrm{d}t}\left(b^2 - a^2\right) = 0, \quad (5.81a)$$
$$\frac{\mathrm{d}}{\mathrm{d}t}\left(\log a - \log b\right) = 0, \quad (5.81b)$$
$$2ab\frac{\mathrm{d}\theta_e}{\mathrm{d}t} = 0. \quad (5.81c)$$

From (5.81b) we see that a/b = constant and (5.81a) implies $a^2 - b^2$ = constant, i.e. area conservation. Therefore, a and b are constant. Hence, (5.81c) implies θ_e = constant. Considering terms of $\mathcal{O}(\cos\alpha)$ and $\mathcal{O}(\sin\alpha)$ in (5.80) gives

$$(b-a)(U_R\cos\theta_e + U_I\sin\theta_e) = (b-a)\left(\frac{\mathrm{d}d_R}{\mathrm{d}t}\cos\theta_e + \frac{\mathrm{d}d_I}{\mathrm{d}t}\sin\theta_e\right), \quad (5.82)$$
$$-(a+b)(U_R\sin\theta_e - U_I\cos\theta_e) = -(a+b)\left(\frac{\mathrm{d}d_R}{\mathrm{d}t}\sin\theta_e - \frac{\mathrm{d}d_I}{\mathrm{d}t}\cos\theta_e\right), \quad (5.83)$$

which imply

$$\frac{\mathrm{d}d}{\mathrm{d}t} = U, \tag{5.84}$$

i.e. $d = Ut + d(0)$, since a, b and θ_e are constant. That is, an interface of shape given by (5.54)—i.e. a rotated ellipse—is a steady shape solution of the two-phase Hele-Shaw free boundary problem with uniform background flow, where the inclusion (and interface) propagates with speed $U = U_R + iU_I$ given by (5.67)–(5.68). The solution (5.67)–(5.68) has various limiting cases, given in table 5.1.

To summarise, the kinematic condition formulated in (5.73) is consistent with the equation derived on the interface, (5.55), and gives the evolution of the time-dependent map (5.54), i.e. the evolution of $\partial\Omega(t)$. The result shows that steady solutions of the two-phase Hele-Shaw flow problem, in particular elliptical solutions, are rotationally invariant, a generalisation of the one-phase counterpart considered in [140].

5.3.3 Circular inclusion in a uniform flow

Now consider the problem (a special case of the solution presented in section 5.3.2) in which the interface $\partial\Omega(t)$ is given by

$$z = d + \frac{R}{\zeta}, \tag{5.85}$$

a conformal map from ∂D to $\partial\Omega(t)$, where $R(t)$ and $d(t)$ are real parameters to be found. That is, we consider the geometric limit of item (iv) in table 5.1, i.e. $b \equiv 0$, $R \equiv a$ and so we may also set $\theta_e \equiv 0$ in (5.54) w.l.o.g.

Suppose $\partial\Omega(0)$ is given by a circle of radius $R(0) = R_0$ centred at the origin, i.e. we set $d(0) = 0$ w.l.o.g. An expression for the 'drift' speed, i.e. the speed of propagation, of the circular inclusion is found by setting $b = 0$ in (5.67) and (5.68),

	Viscosity ratio	Inclusion speed	Description
(i)	$\Lambda = 1$, $\mu_1 = \mu_2$.	$U_R = V$, $U_I = 0$.	The interface is a passive tracer, i.e. all fluid in $\Omega_1 \cup \Omega_2$ moves with velocity V.
(ii)	$\Lambda \to 0$, $\mu_1 \to \infty$.	$U_R = 0$, $U_I = 0$.	The case of a very viscous inner fluid, akin to flow past a solid elliptical object.
(iii)	$\Lambda \to \infty$, $\mu_1 \to 0$.	$U_R = \dfrac{2V[1 + (b/a)\cos 2\theta_e]}{1 - (b/a)^2}$, $U_I = \dfrac{2V(b/a)\sin 2\theta_e}{1 - (b/a)^2}$.	The case of an inviscid inclusion, i.e. a translating elliptical bubble [140].
(iv)	$\forall\Lambda$, $b = 0$.	$U_R = \dfrac{2V}{1 + \Lambda^{-1}}$, $U_I = 0$.	The case of a translating patch of fluid with circular boundary—c.f. solution (5.86) in section 5.3.3.

Table 5.1: Characteristic limits describing the flow regime for an elliptical inclusion, translating in a uniform background flow with propagation speed given by the solutions (5.67) and (5.68). The limits in (i)–(iii) are for viscosity ratio Λ, and the limit in (iv) is a geometric limit.

giving

$$U = \frac{2V}{1 + \Lambda^{-1}}, \tag{5.86}$$

where the drift speed $U = U_R$ is purely real since $U_I \equiv 0$. It now remains to calculate the evolution of the interface according to the kinematic condition. From (5.81a) and (5.84) we find $R = R_0 =$ constant and $d = Ut$. That is, the interface

$\partial\Omega(t)$ propagates as a circle of constant radius with speed U given by (5.86), which is a relationship between the speed of the inclusion, U, the background flow speed, V, and mobility ratio, Λ. The flow regime can be categorised in particular limits of viscosity ratio, given in table 5.2.

	Viscosity ratio	Inclusion speed	Description
(i)	$\Lambda \to 0$, $\mu_1 \to \infty$.	$U = 0$.	Flow past a cylinder.
(ii)	$\Lambda = 1$, $\mu_1 = \mu_2$.	$U = V$.	The interface is a passive tracer.
(iii)	$\Lambda \to \infty$, $\mu_1 \to 0$.	$U = 2V$.	A translating circular bubble.

Table 5.2: Characteristic limits of viscosity ratio Λ which describe the flow regime for a circular inclusion translating in a uniform background flow, where the drift speed of the inclusion is given in (5.86).

Furthermore, since (5.85) represents a conformal map from the unit ζ-disc, D, to the exterior of the circular inclusion, i.e. $\Omega_2(t)$, the complex potential in $\Omega_2(t)$ can be computed as follows. The derivative of the Schwarz function of $\partial\Omega(t)$ can be found from (5.85), given by

$$\begin{aligned} \frac{\mathrm{d}g}{\mathrm{d}z} &= \frac{\partial g}{\partial \zeta}\frac{\mathrm{d}\zeta}{\mathrm{d}z} \\ &= -\zeta^2 \\ &= \frac{R^2}{(z-d)^2}. \end{aligned} \tag{5.87}$$

Employing (5.87) and $w_1 = Uz$ in (5.42) yields

$$\frac{\partial w_2}{\partial z} = \frac{(\Lambda^{-1}+1)}{2}U + \frac{(\Lambda^{-1}-1)}{2}U\frac{\mathrm{d}g}{\mathrm{d}z}, \qquad z \in \partial\Omega(t). \tag{5.88}$$

Hence, integrating and using (5.86) gives

$$w_2 = Vz + \frac{(\Lambda^{-1} - 1)UR^2}{2(z - d)}, \tag{5.89}$$

and taking the real part, the velocity potential is

$$\phi_2 = Vx + \frac{(\Lambda^{-1} - 1)UR^2}{2\left[(x - d)^2 + y^2\right]}(x - d). \tag{5.90}$$

In the case $\Lambda^{-1} - 1 < 0$, i.e. the case where the inclusion has lower viscosity than the outer fluid, the complex potential (5.89) is that of a flow past an anti-dipole (e.g. a bubble when $\Lambda^{-1} \equiv 0$) at any instance, and the streamlines intersect $\partial\Omega(t)$ at right angles—see figure 5.5(c).

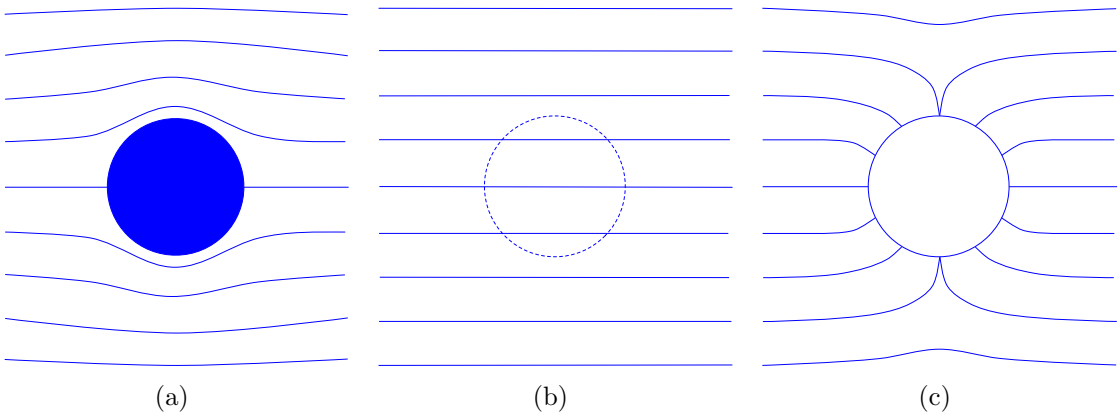

Figure 5.5: Sketches of the streamlines in $\Omega_2(t)$ observed in a stationary frame when the inclusion $\Omega_1(t)$ has viscosity such that $\partial\Omega(t)$ describes the perimeter of (a) a cylinder, i.e. $\Lambda \to 0$, (b) a passive tracer, i.e. $\Lambda \equiv 1$, and (c) a bubble, i.e. $\Lambda \to \infty$. The sketches (a), (b) and (c) correspond to the cases (i), (ii) and (iii) in table 5.2, respectively.

Figures 5.6 shows comparison, for a range of viscosity ratios, between numerical results and the analytic prediction (5.86). Numerical results are found using the algorithm given in section 5.2, where the initial interface is given by a circle of unit radius centred at the origin. In the results presented, $N = 80$ mesh points are taken on the interface for each viscosity ratio, where on the interval $10^{-3} \leq \Lambda \leq 40$, 200 equally spaced points are taken. Each simulation is run for one time unit with step

size $\Delta t = 10^{-3}$. The speed of the translating circular inclusion is calculated from numerical results by averaging the speed of the centre of mass over all time steps. The solution presented here is for background flow speed $V = 1$. There is excellent agreement between the exact and numerical solutions.

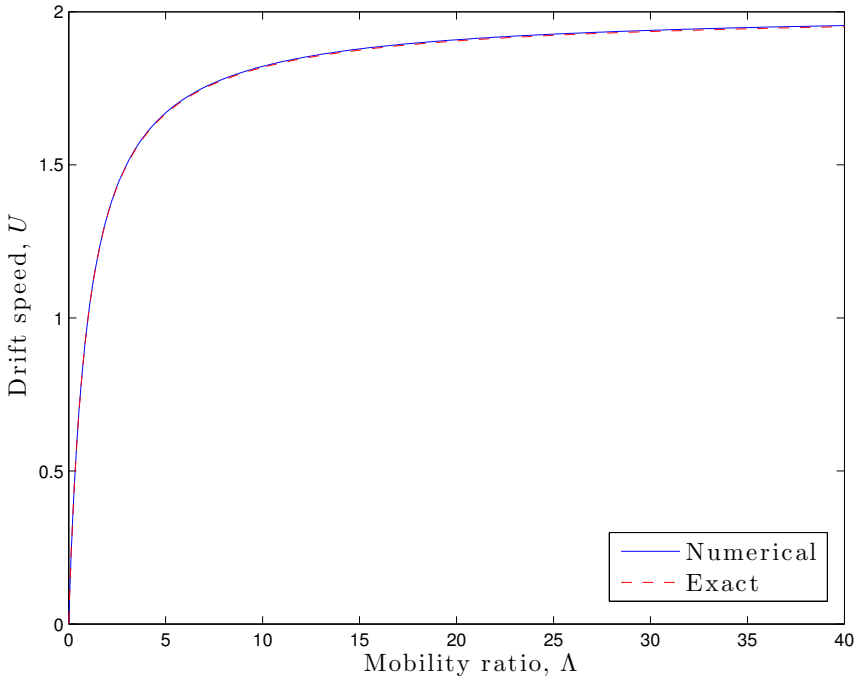

Figure 5.6: Comparison between numerical results and the analytical prediction of the exact solution (5.86) for the drift speed for a circular inclusion of viscosity μ_1 surrounded by a fluid of viscosity μ_2, due to a uniform background flow of speed $V = 1$ and $10^{-3} \leq \Lambda \leq 40$. $\Lambda = \mu_1/\mu_2$ denotes the viscosity ratio.

5.3.4 On the remarks made by Taylor and Saffman (1959) regarding two-phase solutions

In the original work of Taylor and Saffman [138] on the Taylor-Saffman bubble solutions in a channel geometry (and also for the Saffman-Taylor finger discussed in section 5.1) the authors remark on corresponding two-phase solutions to the one-phase problem studied. In [138] the governing equations of the one-phase problem

in the channel are presented as

$$\psi_2 = \pm 1 \quad \text{on } y = \pm V, \quad \phi_2 \to x, \quad x \to \pm\infty, \tag{5.91a}$$

$$\phi_2 = 0 \quad \text{on the interface,} \tag{5.91b}$$

$$\psi_2 = Uy \quad \text{on the interface,} \tag{5.91c}$$

which are updated for the two-phase problem—analogous to (5.6)—to

$$\psi_2 = \pm V \quad \text{on } y = \pm 1, \quad \phi_2 \to Vx, \quad x \to \pm\infty, \tag{5.92a}$$

$$\phi_1/k_1 = \phi_2/k_2 \quad \text{on the interface,} \tag{5.92b}$$

$$\psi_1 = \psi_2 = Uy \quad \text{on the interface.} \tag{5.92c}$$

Equation (5.92c) implies the bubble propagates with speed U, and therefore, in the two-phase problem one then takes $\phi_1 = Ux$ and $\psi_1 = Uy$ inside the inclusion (i.e. bubble). In [138], the complex potential ('*after some algebra*') is given in the form

$$W = \frac{\phi_2 + i\psi_2 - U^* z}{V - U^*} \tag{5.93}$$

and the authors remark that (5.93) satisfies (5.91), where $U^* = \mu_1 U/\mu_2 = k_2 U/k_1 = U/\Lambda$, and replacing U with $U' = (U - U^*)/(V - U^*)$ in the solutions to the one-phase problem gives solutions to the two-phase problem. They go on to say '*it is noted that the family of possible shapes are independent of the physical properties of the fluid*' and that 'U^* *is the velocity fluid moves around the bubble*' under the action of the pressure, i.e. ϕ_1, inside the bubble (or inclusion). Note that the second statement in their observation may not be correct since in the case of $\mu_1 = 0$ this implies the relative velocity is infinite, which cannot be true. In fact, the relative velocity should be V when $\mu_2 = 0$, i.e. equal to the background flow speed as this would be equivalent to flow around a solid object, and zero when $\mu_1 = 0$.

Now let us turn our attention to the family of solutions given by Taylor and Saffman [138] in the unbounded cell, i.e. their 'small bubble limit' in the channel, given by their equation (14), for which the corresponding velocity potential is given in the equation immediately after. In particular, the complex potential (for the one-phase problem, i.e. the Taylor-Saffman bubble), is given by the equation

$$Vz = \frac{U-V}{U}(w_2^2 + U^2R^2)^{1/2} + \frac{Vw_2}{U}, \tag{5.94}$$

where R here is equivalent to the maximum half width of the bubble defined in [138]. The solution in their equation (14) can be recovered by setting $\psi_2 = Uy$, $\phi_2 = 0$ in (5.94), where re-arranging and taking the real part gives

$$\left(\frac{Vx}{U-V}\right)^2 + y^2 = R^2, \tag{5.95}$$

describing the shape of the interface in Cartesian coordinates. Equation (5.95) is a solution to the problem described in (5.91).

We are particularly interested in the circular solution, which is achieved by setting $U = 2V$ in (5.95), i.e. a bubble travelling at speed twice the background flow giving a circular interface with radius R—the solution derived in example 1.3.6. Now, considering the remarks on the two-phase problem made in [138], in particular employing (5.93) in (5.94), i.e. setting $w_2 = W$ and replacing U by $U' = (U - U^*)/(V - U^*)$, as suggested, we have

$$\left(\frac{x}{U'-1}\right)^2 + y^2 = R^2, \tag{5.96}$$

a solution to the two-phase problem corresponding to (5.95). Again, since we are

interested in the circular solution, this occurs when $U' = 2$, i.e.

$$\begin{aligned} 2 &= \frac{U - U^*}{V - U^*} \\ &= \frac{U - U/\Lambda}{V - U/\Lambda}. \end{aligned} \tag{5.97}$$

Re-arranging (5.97) for U, the speed of propagation of the circular inclusion, we find that

$$U = \frac{2V}{1 + \Lambda^{-1}}, \tag{5.98}$$

which agrees with the result given in (5.86).

Now consider the velocity potential derived in (5.90). The coefficient of the second term, when $|z-d| = \sqrt{(x-d)^2 + y^2} = R$, can be viewed as the relative velocity of the fluids in both phases. The coefficient of the second term in (5.90) on the interface, $\partial\Omega(t)$, is

$$\begin{aligned} \frac{(\Lambda^{-1} - 1)U}{2} &= \frac{(\Lambda^{-1} - 1)2V}{2(1 + \Lambda^{-1})} \\ &= \frac{\mu_1 - \mu_2}{\mu_1 + \mu_2} V. \end{aligned} \tag{5.99}$$

Hence, when $\mu_1 = 0$, the relative velocity of fluid just outside the inclusion $\Omega_1(t)$ is $-V$ since the inclusion (in this case a bubble) is moving at speed twice that of the background flow. When $\mu_2 = 0$, the inclusion is at rest (analogous to the case of a solid cylinder) and the relative velocity of the passing fluid is V. When $\mu_1 = \mu_2$, the relative velocity of the two phases is zero, as expected, since $\mu_1 = \mu_2$ is the case in which $\partial\Omega(t)$ describes a passive tracer—see table 5.2.

5.4 Summary

In section 5.3, methods of finding exact solutions are discussed and an exact solution for an elliptical inclusion is derived. In section 5.2, a BIM is proposed

with which the two-phase problem can be solved numerically, and results are tested against exact solutions. The solution for a circular propagating solution is also derived in section 5.3.3, where the speed of propagation is given explicitly as a function of mobility ratio and the background flow speed, and is used to further test the numerical algorithm. It is also shown that, in fact, this solution is implicit in the work of Taylor and Saffman [138]. Finally, comments regarding two-phase solutions made in [123, 138] are considered, and the correct relative velocity of the two-phases in the case of propagating elliptical inclusions is given, albeit in an unbounded Hele-Shaw cell.

Chapter 6

Conclusions and further study

In this thesis three main topics have been explored, namely, the Hele-Shaw free boundary problem of a simple closed curve where a conducting fluid is subject to an external electric field in chapter 3; the motion of an unsteady bubble in an unbounded Hele-Shaw in chapter 4; and the two-phase Hele-Shaw free boundary problem in chapter 5. Throughout this thesis the ZST problem is considered. A numerical model is formulated for the one-phase problem in chapter 2 and is applied in chapters 3 and 4. The numerical model is revised for the two-phase problem in chapter 5 and is verified against exact solutions.

On the numerical method and formulation

A numerical model of the Hele-Shaw free boundary problem for one-, and two-phase flows are presented in chapters 2 and 5, respectively. The one-, and two-phase problems are formulated by considering the decomposition of the velocity potential into the background flow plus a 'local' solenoidal part. The stability of the numerical model is discussed in section 2.4 and is demonstrated in example 2.7.1. The numerical instability observed is similar to that previously mentioned in the literature, see e.g. [1, 85]. The instability, when no filtering is applied, is described and appropriate treatment is employed, following methods suggested in [109] and [144]. Numerical

results are tested against exact solutions in section 2.7 and 5.2.3 where excellent agreement is found, with errors in the numerical solutions behaving as expected.

The BIE which forms the basis of the numerical model, e.g. (2.15) for the one-phase problem, is a Cauchy singular integral equation. Taking the real part of the BIE, as is done, gives an integral equation which is similar to a Fredholm integral equation of the second kind. In [7] there is discussion and references to [12] and [6] on the solution to such integral equations and their stability, which may be applicable to the BIE derived in section 2.4. There is also reference to [84], where singular Fredholm integral equaltions with unbounded kernels, specifically Abel's equation, are studied. Callum [12] specifically mentions a minimisation problem of the error in the numerical solution to Fredholm integral equations of the first and second kind, similar to the minimisation problem suggested by Phillips [109] and Twomey [144] which is employed in this thesis. These techniques may be useful in seeking solutions to the BIEs presented in this thesis by, for example, a collocation method—see e.g. [37]. Exploring such solution methods may provide superior accuracy, however, for the purposes of this thesis, the accuracy of the current algorithm is sufficient.

On the one-phase problem with external fields

The Hele-Shaw equation and the Hele-Shaw free boundary problem including arbitrary conservative background fields are derived in appendix B which are applicable in various Hele-Shaw flows, see e.g. [39, 89]. The one-phase numerical model is modified to include external fields in section 2.5, which is tested against an existing exact solution in section 2.7 and a new solution derived in chapter 3.

In chapter 3 the Hele-Shaw free boundary problem for a conducting fluid subject to an external electric field is derived. It is shown analytically that the interface of a fluid blob is unstable for a positive point charge, where the external potential is defined in (3.17). Furthermore, it is shown that the interface is stable for a negative

point charge where, over time, the interface becomes symmetric about the point charge, i.e. the interface becomes circular with centre coinciding with the location of the point charge. The stability of existing steady solutions are then checked numerically, where it is found that the interface is indeed unstable, locally, near a positive point charge (if lying in the fluid domain) or negative point charge (if lying outside the fluid domain).

On the motion of an unsteady bubble in an unbounded Hele-Shaw cell

In chapter 4, the stability of a propagating elliptical bubble and bubble breakup is considered.

A boundary integral formulation and numerical method for the study of Hele-Shaw bubble evolution in an unbounded cell is presented in section 2.6. In section 4.3.1 the numerical results demonstrate that for initially elliptical bubbles, the only (attractive) solution as $t \to \infty$ is a circular bubble travelling at a steady speed twice that of the background flow. These results are compatible with the analytical results of Vasconcelos and Mineev-Weinstein [149] for the selection problem in a channel geometry, where it is shown that the bubble eventually propagates with speed twice that of the background flow. A stability argument is presented in section 4.4 for a perturbed ellipse, providing further evidence that the circular bubble with speed $U = 2V$ is a stable attractive solution.

Usually, the formation of cusps in the un-regularised Hele-Shaw free boundary problem are deemed unphysical and are treated by the inclusion of surface tension, see e.g. [26, 67, 132]. This helps model, mathematically, what is observed in the real world. For example, when modelling sink driven flows, in the un-regularised model cusps form in finite time at which point the fluid velocity becomes infinite—see example 1.3.3 and section 3.4.2. The trend has been to then, based on the above

argument, to include surface tension, which has been the case in the study of the selection problem. However, this limits the understanding of instabilities on the interface and their effects on the selection problem as they are eliminated by surface tension. In this thesis, the un-regularised problem, albeit with numerical filtering, is modelled mathematically and solved numerically in which we observe the selection of the bubble with shape such that it travels at speed twice the background flow.

Concerning bubble breakup, a simple analysis is presented by which the breakup of a single bubble may be predicted, given the initial interface and the driving hydrodynamics, by studying the mathematical structure of the Schwarz function equation and hence the evolution of $\partial\Omega(t)$. In section 4.3.2 and 4.3.3 it is shown for some initial shapes $\partial\Omega(0)$ that the evolution of $\partial\Omega(t)$ may result in one of two types of topological change. In section 4.3.2 the numerical results suggest that the bubble may split, becoming multiply connected. In section 4.3.3 the bubble evolves to enclose a region of viscous fluid, i.e. a singly connected viscous fluid domain eventually becomes two disconnected regions. The numerical results suggest that the singularities of the Schwarz function of the initial interface play an important role on the evolution of the interface, since, mathematically, the boundary cannot cross the singularity.

On numerical simulation of a bubble near a wall in a steady uniform flow and interaction with other boundaries

Here we present some preliminary numerical results simulating the motion of a bubble near a solid, straight wall in a semi-infinite Hele-Shaw cell. Symmetric bubbles in a channel geometry have been previously studied where some exact steady solutions have been found, see e.g. [45, 46, 148], and also a specific class of temporal solutions have been found for initially symmetric and asymmetric bubbles (about the channel centreline), see e.g. [149]. In the latter, the interface of the bubble evolves to

the Taylor-Saffman bubble (travelling at speed twice that of the background flow). The author is not aware of exact temporal solutions of the one-phase Hele-Shaw free boundary problem for a single bubble travelling close to a solid wall. There exist steady solutions for symmetric bubbles propagating in an unbounded Hele-Shaw cell given by Crowdy [21], where the (vertically aligned) two-bubble solution is of interest here, and the stability of this steady shape solution is tested numerically. By the method of images, the case of two symmetric bubbles is equivalent to the case of a single bubble where the wall coincides with the line of symmetry. As mentioned in chapter 3, there is a vast array of applications of Hele-Shaw flows in microfluidic devices. Here, motivation can be found from experimental results of single, and multiple droplets (e.g. oil-in-water [127] and water-in-oil [10] droplets) injected into a uniform background flow [10, 127]. Although the viscosity ratios between the droplet and the surrounding fluid in [10,127] are finite, where the theory presented in chapter 5 would be applicable, in this section we consider the simpler case in which the pressure remains constant within the droplet region, i.e. the droplet describes a bubble.

Assume that the the upper half complex plane is filled with a viscous fluid. Consider an initially circular bubble of unit radius in a semi-infinite Hele-Shaw cell with its centre at a distance $d_w > 0$ away from a solid wall which coincides with the the $\Re(z)$ axis. Suppose that the bubble—and thus $\partial\Omega(t)$—is driven by a uniform background flow, of speed V, in the positive $\Re(z)$ direction. Here, we employ the method of images together with the extension to multiple interface problems of the one-phase Hele-Shaw numerical model derived in section 2.8 to simulate the motion of $\partial\Omega(t)$. More precisely, the upper half plane is reflected in $\Im(z) = 0$, where now we investigate the motion of two identical bubbles in an unbounded Hele-Shaw cell—see figure 6.1.

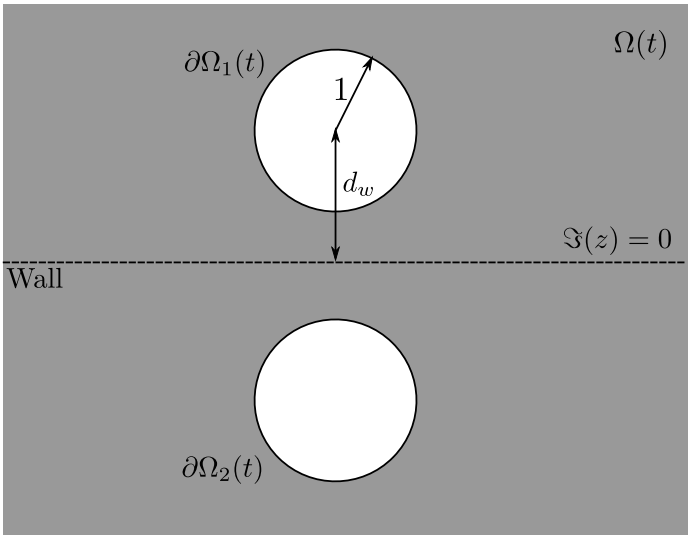

Figure 6.1: A sketch showing a circular bubble with interface $\partial\Omega_1(t)$ and its image, whose interface is denoted by $\partial\Omega_2(t)$, reflected in a wall coinciding with $\Im(z) = 0$. The sketch shows the equivalent problem of studying the motion two symmetric bubbles in an unbounded Hele-Shaw cell with the viscous fluid occupying the domain $\Omega(t)$, to the problem of a single bubble near a wall, where the viscous fluid occupies the upper half plane.

Let the interface of the bubble above the wall be denoted by $\partial\Omega_1(t) \equiv \partial\Omega(t)$, and it's image, below the wall, by $\partial\Omega_2(t)$. Hence, the BIE (2.92) applies, with $\Upsilon = 2$, whose solution gives the normal velocity on each interface denoted by $\widetilde{v}_{n\jmath}$, $\jmath = 1, 2$. Since $\partial\Omega_2(t)$ is a reflection of $\partial\Omega_1(t)$ in $\Im(z) = 0$, the BIE can be simplified and written in terms of the the normal velocity on $\partial\Omega_1(t)$ alone by enforcing the symmetry conditions $\partial\Omega_2(t) \coloneqq \{\overline{z} : z \in \partial\Omega_1(t)\}$ and that the complex velocity on $\partial\Omega_2(t)$ be given by $\overline{\widetilde{u} + i\widetilde{v}}$, where $\widetilde{u} + i\widetilde{v}$ is the complex velocity on $\partial\Omega_1(t)$. Hence, in this case, the BIE (2.92) can be written as

$$\left(\frac{\mathrm{d}z}{\mathrm{d}s}\right)\Big|_{z_m} \left(-\fint_0^{L_1} \frac{i\widetilde{v}_{n1}}{z - z_m}\,\mathrm{d}s + \int_0^{L_1} \frac{i\widetilde{v}_{n1}}{\overline{z} - z_m}\,\mathrm{d}s\right) + \pi\, \widetilde{v}_{n1}|_{z_m} = \left(\frac{\mathrm{d}z}{\mathrm{d}s}\right)\Big|_{z_m} \left(\fint_0^{L_1} \frac{\widehat{v}_{\tau 1}}{z - z_m}\,\mathrm{d}s + \int_0^{L_1} \frac{\widehat{v}_{\tau 1}}{\overline{z} - z_m}\,\mathrm{d}s\right) - i\pi\, \widehat{v}_{\tau 1}|_{z_m}\,, \quad (6.1)$$

where $z_m \in \partial\Omega_1(t)$, and $L_1(t)$ denotes the total arc length of $\partial\Omega_1(t)$. Equation (6.1) can be discretised and approximated in a similar fashion to (2.96)—see section 2.8—with N distinct mesh points chosen along $\partial\Omega_1(t)$. Whence, (6.1) yields N algebraic

equations where the second integral on the left, and right hand side of (6.1) account for the existence of the image bubble.

Figures 6.2–6.7 show numerical results for an initially unit circular bubble at distance $d_w = 2$ from the wall, with centre $2i$, which is subject to a uniform background flow of speed $V = 1$. Figure 6.2 shows the evolution of the x and y components of the centre of mass, and figure 6.3 displays the evolution of the speed of the centre of mass. The centre of mass, z_{cm}, is calculated using the formula

$$z_{cm} = \frac{1}{A}\left(\iint_{\mathrm{int}(\partial\Omega_1(t))} x\,\mathrm{d}x\mathrm{d}y + i\iint_{\mathrm{int}(\partial\Omega_1(t))} y\,\mathrm{d}x\mathrm{d}y\right), \tag{6.2}$$

where Green's theorem is applied and the resulting (surface) integrals are discretised and approximated by the trapezium rule, in a similar manner to (2.32), and A is the area of the bubble which can be calculated numerically by the formula given in (2.76). The speed of the centre of mass, $v_{cm} = |\dot{z}_{cm}|$, is calculated by using the formula given in (4.10). In the numerical results shown, $N = 60$ mesh points are taken on the interface. In figures 6.2(a), 6.2(b) and 6.3(a), a range of curves are presented for decreasing step size Δt.

It is interesting to note that for small time, for all values of Δt, the centre of mass of the bubble transverse to the wall follow almost the same trajectory—see figure 6.4(b). In figure 6.5 we see snapshots of the evolution of the bubble for $0 \leq t \leq 2$, where it can also be seen that the interface does not remain circular. The centre of mass of the bubble arcs away then towards the wall whilst the interface changes shape, before moving away from the wall as time increases. A similar (small time) motion is observed experimentally in [127], however, the experiments are conducted for droplets that are more viscous than the surrounding fluid confined in a finite width channel, and the interface of the droplets remain circular. As the interface remains circular, the droplets (and thus the centre of mass) undergo oscillations close to the wall.

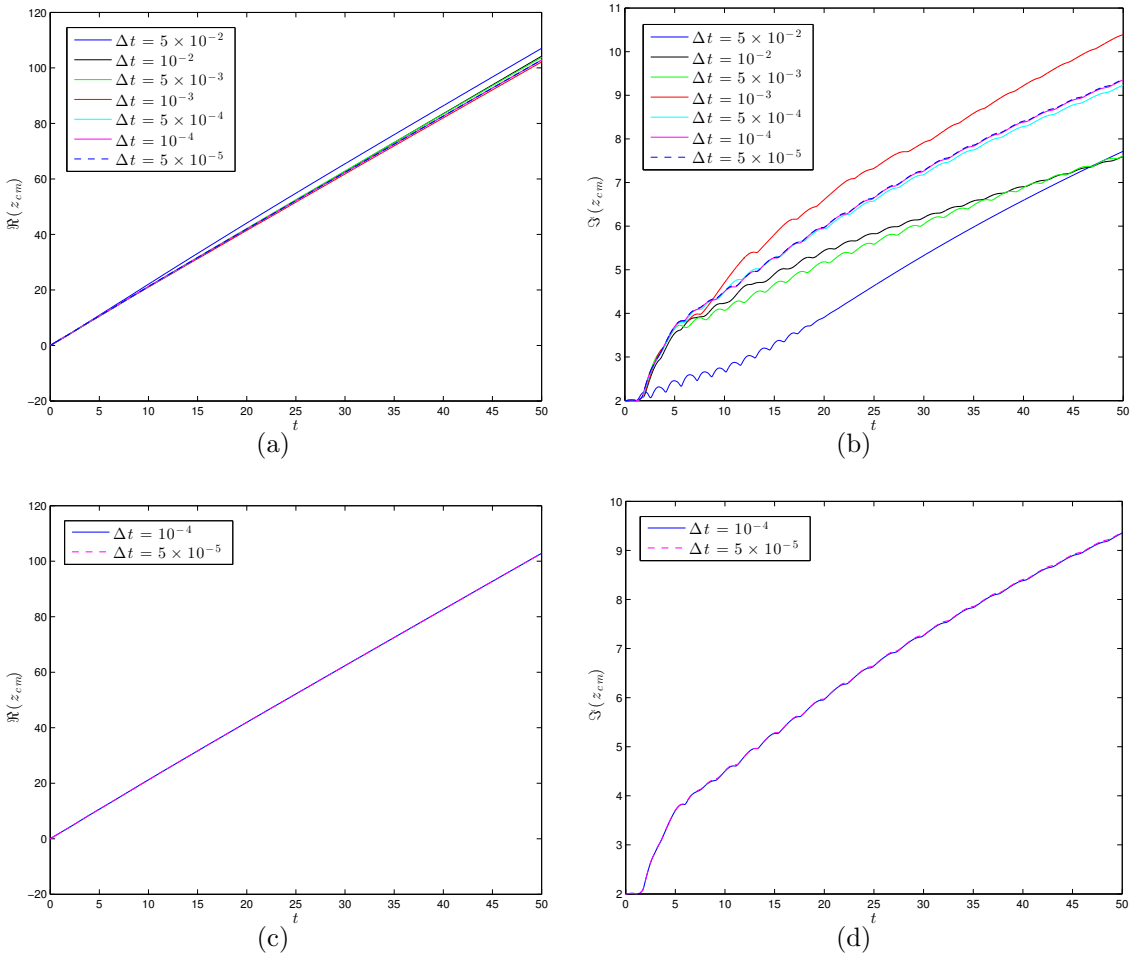

Figure 6.2: The evolution of $\Re(z_{cm})$ and $\Im(z_{cm})$ for $0 \leq t \leq 50$ are plotted for various values of Δt in (a) and (b), respectively. In (c) and (d) the curves corresponding to the two smallest values of Δt are plotted, where the solutions have good agreement for all t. In the results presented, $N = 60$, $d_w = 2$ and the background flows speed is $V = 1$.

In figure 6.3(b), it can be seen that the speed of the centre of mass converges to a particular solution, which appears to oscillate towards $v_{cm} = 2$. Figure 6.2(d) show's the y component of the centre of mass also converging towards a particular solution and shows that the centre of mass of the bubble progressively moves away from the wall. Figure 6.2(c) shows the x component of the centre of mass converging towards the line with gradient 2. That is, the bubble diverges away from the wall such that it becomes a steady circular bubble moving with speed twice that of the background flow. For $\Delta t = 5 \times 10^{-5}$, the maximum size of the spacial step ΔS throughout the simulation was calculated to be 1.047×10^{-1}. The relative error in bubble area was

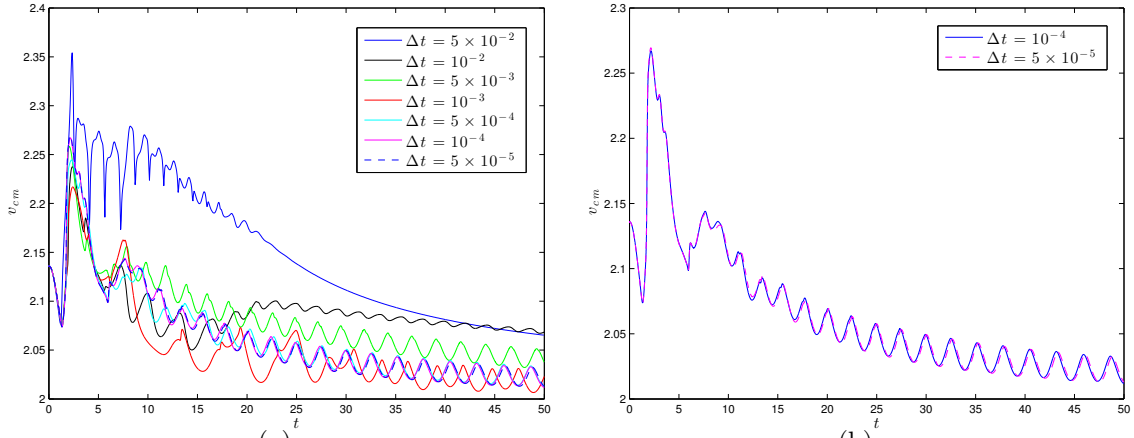

Figure 6.3: The evolution of v_{cm} for $0 \leq t \leq 50$ is plotted for various values of Δt in (a). In (b) the curves corresponding to the two smallest values of Δt are plotted, where the solutions have good agreement for all t. In the results presented, $N = 60$, $d_w = 2$ and the background flows speed is $V = 1$.

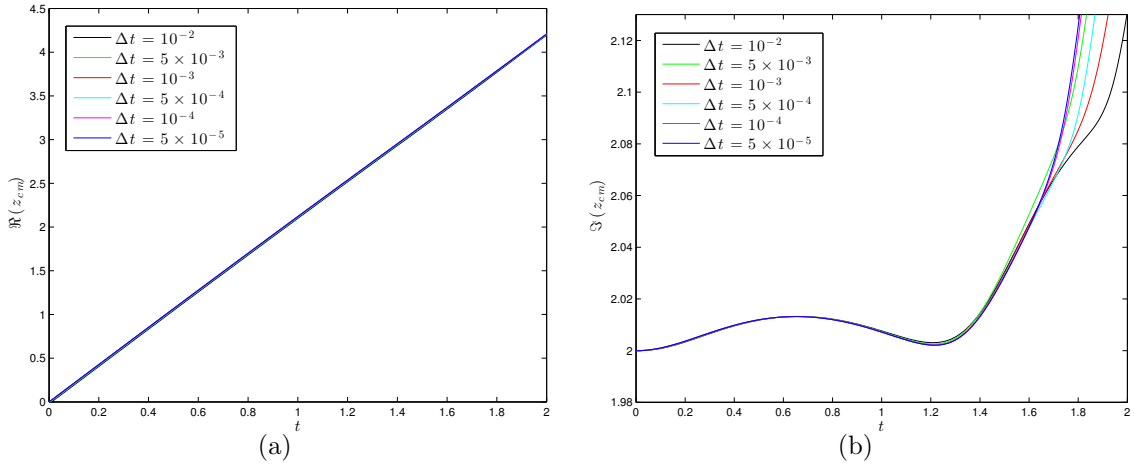

Figure 6.4: Plots showing the short time ($0 \leq t \leq 2$) evolution of $\Re(z_{cm})$ and $\Im(z_{cm})$ for various values of Δt. In the results presented, $N = 60$, $d_w = 2$ and the background flows speed is $V = 1$.

calculated at each time step by the formula given in (2.78), where the exact bubble area is $A = \pi$ (since the initial bubble is a circle of unit radius). The maximum relative error in bubble area throughout the simulation was $\mathcal{O}(10^{-3})$, as expected, since the area is calculated numerically using (2.76) which employs the trapezium rule approximation and is $\mathcal{O}((\Delta S)^3)$ accurate. Since appreciable differences between solutions shown in figures 6.2 and 6.3 decrease as Δt decreases, it is concluded that the results are reliable for $\Delta t = \mathcal{O}(10^{-4})$. The interface of the bubble is shown at the final time step (of the simulation) in figure 6.6. Figure 6.7 shows evolution of

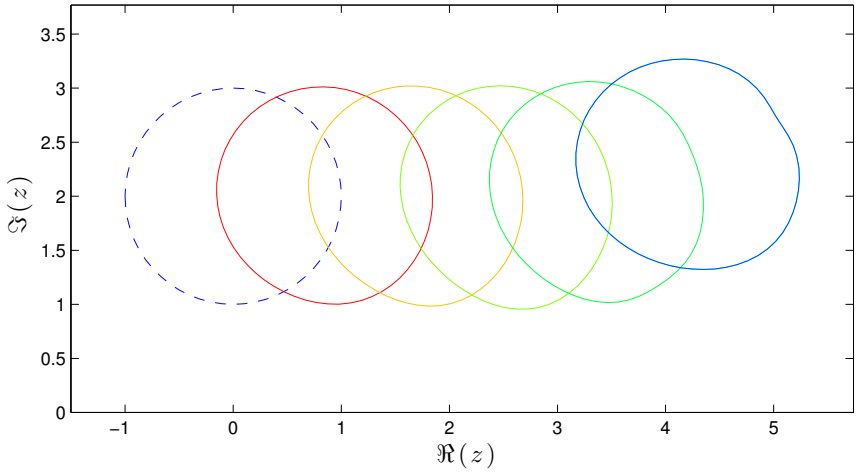

Figure 6.5: Snapshots of the evolution of the bubble near a wall (coinciding with $\Im(z) = 0$) shown at times $t = 0$, 0.4, 0.8, 1.2, 1.6 and 2. The initial bubble interface (dashed) is given by a unit circle such that $d_w = 2$. In the results presented, $N = 60$, $\Delta t = 5 \times 10^{-5}$ and the background flow speed is $V = 1$.

the interface up to this time. It is speculated that $v_{cm} \to 2$ as $t \to \infty$, where the interface becomes circular as the bubble propagates to a large distance away from the wall, i.e. relaxing to the same steady state reported in sections 4.3.1, 4.3.2 and 4.4.

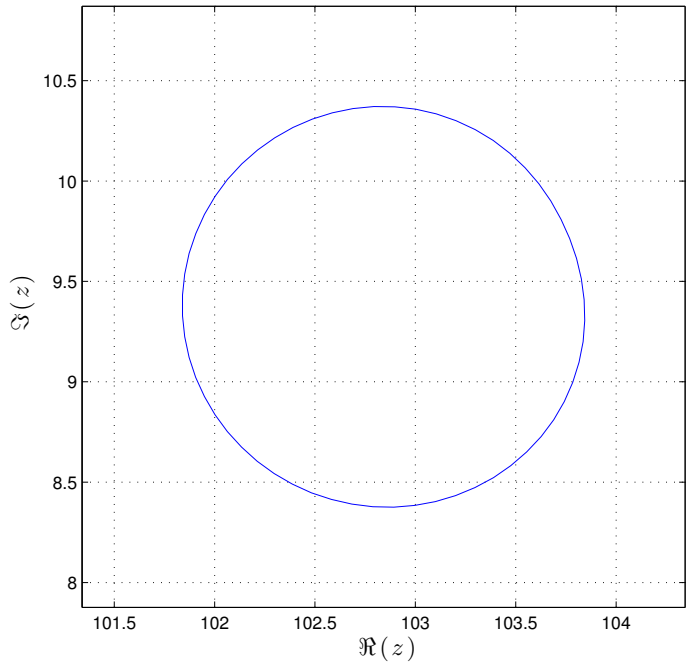

Figure 6.6: The interface of a bubble at time $t = 50$. The bubble was initially circular with centre $2i$, i.e. located at a distance $d_w = 2$ from a wall coinciding with $\Im(z) = 0$. In the result presented, $N = 60$, $\Delta t = 5 \times 10^{-5}$ and the background flow speed is $V = 1$.

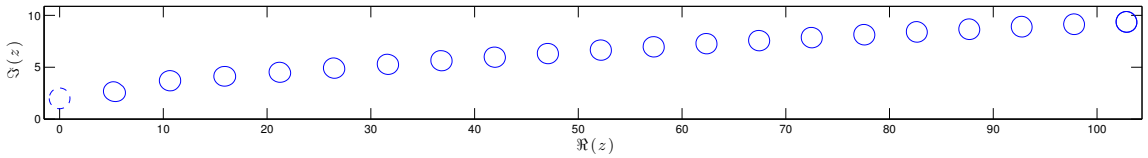

Figure 6.7: Snapshots of the evolution of an initially circular bubble (dashed) located at a distance $d_w = 2$ from a wall coinciding with $\Im(z) = 0$. The snapshots are shown from $t = 0$ to 50 in 2.5 unit increments. In the result presented, $N = 60$, $\Delta t = 5 \times 10^{-5}$ and the background flow speed is $V = 1$.

The results suggest that the bubble will diverge away from the wall where the speed of the bubble tends to twice that of the background flow. The long time oscillations of the speed of the centre of mass are of particular interest which resemble a similarity to experimental results in [127], albeit of droplets in a relatively less viscous surrounding fluid. Given the recent experiments in [127], it would be of interest to extend the multiple interface model of section 2.8 to the two-phase problem, where the method of images may be applied and the effect of mobility ratio on the motion of the droplet (or inclusion) can be studied.

The steady solution reported by Crowdy [21] is also tested, in particular the symmetric solution given by the map

$$z = \frac{ia}{\sqrt{\rho}}\left[K\left(-\frac{i\zeta}{\sqrt{\rho}},\rho\right) - K\left(-1,\rho\right) + \left(1-\frac{2}{U}\right)\left(K\left(-i\zeta\sqrt{\rho},\rho\right) - K\left(-\rho,\rho\right)\right)\right], \quad (6.3)$$

where the interior of a punctured unit ζ-disc is mapped to the flow domain $\Omega(t)$, $K(\zeta,\rho)$ is a Schottky-Klein prime function (details of which can be found in [21,22]) and the background flow speed is taken to be $V = 1$. In figure 6.8, the evolution of $\partial\Omega(t)$ is shown for $0 \leq t \leq 2$ where the results suggest that the interface does not remain steady and instead, like the case of a circular bubble, propagates away from the wall where it is expected that the interface will become circular for large time, as in figure 6.7.

The parameters chosen for the results presented in figure 6.8 are $\rho = 0.3$, $a = 0.5783$ and $U = 2$, i.e. $V = 1$. Note, these parameters correspond to the steady pair of symmetric bubbles (or equivalently a single bubble near a wall that coincides with the real axis) propagating at speed twice that of the background flow. These

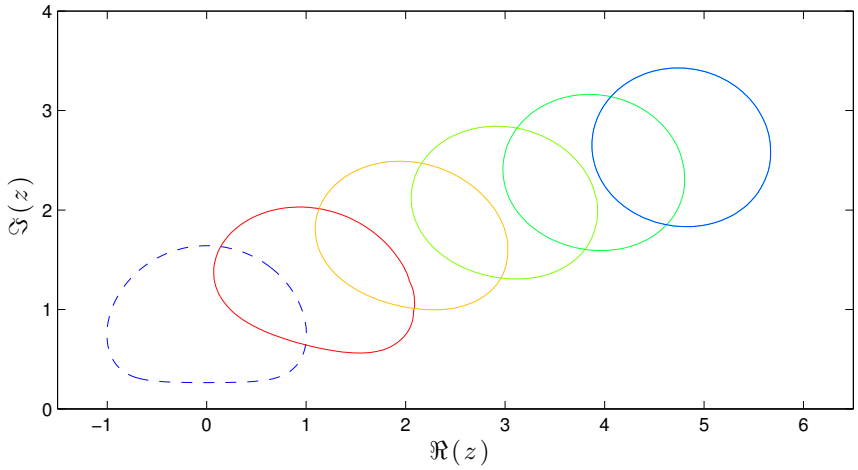

Figure 6.8: Snapshots of the evolution of a bubble near a wall (coinciding with $\Im(z) = 0$) shown at times $t = 0$, 0.4, 0.8, 1.2, 1.6 and 2. The initial bubble interface (dashed) is given by (6.3) with $\rho = 0.3$ and $a = 0.5783$. In the results presented, $N = 200$, $\Delta t = 10^{-4}$ and the background flow speed is $V = 1$.

preliminary results suggest that the steady solution given by (6.3) is not stable. In fact, there is a continuous family of possible shapes for which the bubble (or pair of symmetric bubbles) will travel at speed $U = 2V$—see figure 6.9. These shapes are admitted from the map (6.3) for $0 < \rho < 1$. As $\rho \to 0$, the bubble becomes circular and is located at large distance from the wall, i.e. from the real axis. The parameter a in (6.3) can be found by fixing the area of the bubble. The numerical results here suggest that the circular solution far from the wall is a stable, attractive solution. It is conjectured that, given a bubble of arbitrary shape initially close to a wall, as long as the solution exists for all time, the bubble will become circular and attain speed $U = 2V$ as $t \to \infty$ whilst propagating far away from the wall. The possibility of more than one $U = 2V$ solution is interesting and this problem merits further investigation, both analytically and numerically.

There also exist temporal exact and numerical solutions for the growth of blobs and fingers in a wedge for both the ZST [48, 118, 119] and regularised [5] problems. Furthermore, there are numerical solutions of Hele-Shaw flows past or near obstacles, see e.g. [88], for which there are no known exact solutions. It would be of interest to model one-, and two-phase flows interacting with boundaries such as walls, plates

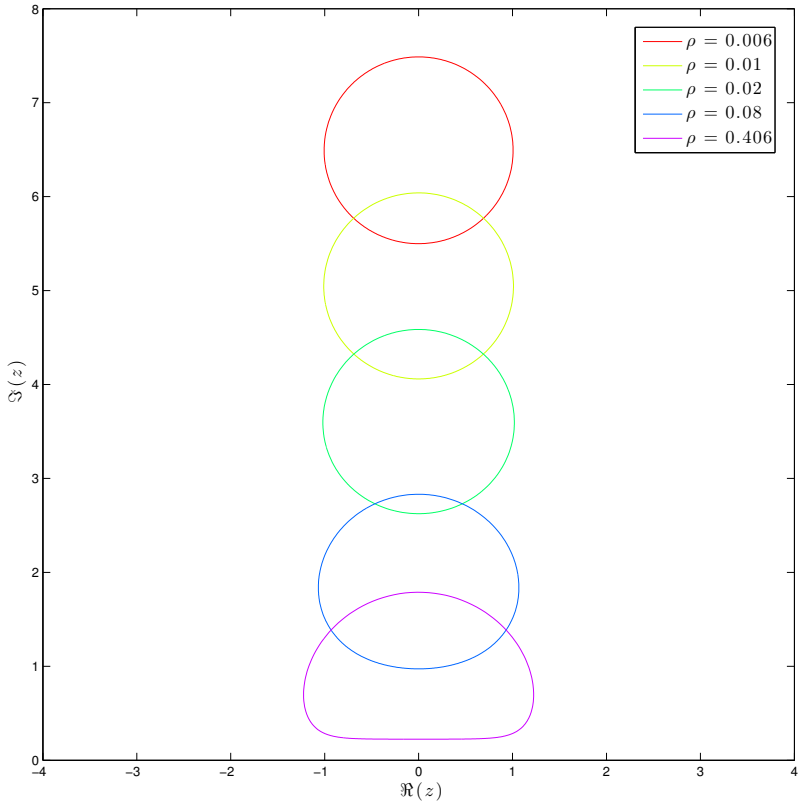

Figure 6.9: Displaying a discrete set of bubble shapes (from a continuous family of shapes) such that the bubble near a wall (or equivalently the pair of symmetric bubbles) travel at a steady speed, $U = 2$. As $\rho \to 0$, the interface, given by the map (6.3), tends to a circle at large distance from the wall that coincides with $\Im(z) = 0$. As $\rho \to 1$, the bubble touches the wall. Here, the area of all bubbles is fixed to π and the parameter $a = 0.9939$, 0.9899, 0.9798, 0.9175 and 0.5720 for increasing ρ.

and a wedge which may be compared to solutions in the literature mentioned above.

On numerical simulation of an initially elliptical inclusion in a steady uniform flow in the two-phase problem

In chapter the 5 the two-phase Hele-Shaw free boundary problem is presented and a numerical model to solve the problem is given in section 5.2. The numerical model is tested against known exact solutions in section 5.2.3 where excellent agreement is found. Two existing methods of finding exact solutions [20, 60] are discussed in section 5.3 and the method of [20] is used to derive an exact steady solution for a rotated elliptical inclusion in a uniform background flow which, in fact, is implicit in [20]. An explicit relation is given between the drift speed and mobility ratio

for the special case of a translating circular inclusion which is used to further test the numerical model. In section 5.3.4, remarks of Taylor and Saffman [138] are discussed and a correct expression is given for relative velocity of the translating circular inclusion and the outer flow.

Following the numerical results presented in section 4.3.1, a natural question to ask would be; how long does it take for an elliptical inclusion of mobility ratio Λ to evolve to an inclusion with a circular interface? More precisely, does the interface evolve to a circle, and if so, how does the value of Λ affect its evolution. The results of section 4.3.1 strongly suggest similar behaviour will exist in two-phase numerical experiments. Some preliminary results have been computed and are presented in figure 6.10.

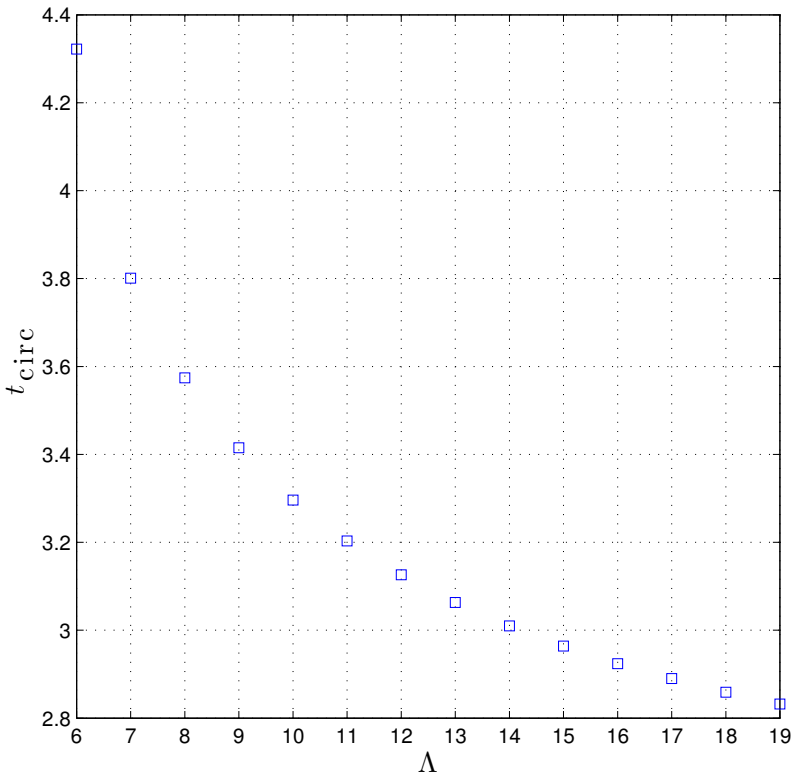

Figure 6.10: A plot showing the time taken against mobility ratio for an elliptical inclusion to become 'sufficiently circular', i.e. $\partial\Omega(t_{\mathrm{circ}})$ satisfies the condition (6.5) where $\delta_T = 0.05$, in a uniform background flow of speed $V = 1$. Data points are marked by squares for $6 \leq \Lambda \leq 19$. In each simulation, the initial shape of the interface, $\partial\Omega(0)$, is given by (5.54) with $d = 0$, $\theta_e = 0$, $b = 1$ and $a = 0.2$. Results are presented for $N = 200$ and $\Delta t = 10^{-3}$.

The results show the time taken for an initially elliptical inclusion to become sufficiently circular, a condition computed as follows. Let z_{cm} denote the centre of mass of the inclusion at time $t = t_j$, say, i.e. the centre of mass of $\Omega_1(t_j)$, which can be calculated by the formula

$$z_{cm} = \frac{1}{A}\left(\iint_{\Omega_1(t_j)} x\,\mathrm{d}x\mathrm{d}y + i\iint_{\Omega_1(t_j)} y\,\mathrm{d}x\mathrm{d}y\right), \tag{6.4}$$

where Green's theorem is applied and the resulting integrals along $\partial\Omega(t)$ are discretised and approximated by the trapezium rule, in a similar manner to (2.32). Here, A is the area of the inclusion $\Omega_1(t_j)$ which can also be calculated numerically by the formula given in (2.76). Now, let the distance from the i-th mesh point on $\partial\Omega(t_j)$ to the centre of mass, z_{cm}, be given by $\lambda_i = |z_{cm} - z(S_i)|$, and let $R_{\text{circ}} = \sqrt{A/\pi}$ where A is the area of the inclusion calculated numerically. Then, if

$$\max_i \left|\frac{\lambda_i}{R_{\text{circ}}} - 1\right| < \delta_T, \quad i = 1, \ldots, N, \tag{6.5}$$

is satisfied for some chosen value of tolerance, δ_T, we assume $\partial\Omega(t_{\text{circ}})$ is sufficiently circular, where $t = t_{\text{circ}}$ is the time the interface satisfies the condition (6.5). In the simulations that produced the data of figure 6.10, the tolerance is chosen to be $\delta_T = 0.05$, i.e. the radius of the approximately circular interface does not vary more than 5% between all mesh points on $\partial\Omega(t_{\text{circ}})$. The initial interface, $\partial\Omega(0)$, is given by (5.54) with $d = 0$, $\theta_e = 0$, $b = 1$ and $a = 0.2$, for all values of Λ, i.e. we start with precisely the same shape interface in all simulations. The value t_{circ} corresponding to the value $\delta_T = 0.05$ that satisfies (6.5) in the one-phase case (i.e. the case of a bubble for which $\Lambda \to \infty$) is computed as $t_{\text{circ}} \approx 1.193$, where, the smoothing parameter is taken to be $\gamma = 1$. The data in figure 6.10 suggest decay to a particular value of t_{circ}, however, more simulations have to be carried out, in particular for $\Lambda > 19$, to be confident that the value of t_{circ} will evolve smoothly to $t_{\text{circ}} \approx 1.193$ as Λ increases, if

indeed it does. In all simulations, $N = 200$ mesh points are taken on on the interface and time step $\Delta t = 10^{-3}$ is chosen.

The results are only given here as preliminary results as the smoothing parameter, γ—see (5.30)—is chosen to be a relatively high value (namely $\gamma = 8000$ in these two-phase simulations) compared with all other one-phase numerical results presented in this thesis. The high smoothing parameter was chosen to counteract numerical instability of the type discussed in section 2.7 and example 2.7.1, which appear prominently at the rear of the elliptical interface (with respect to flow direction). Currently, the author is not aware of the cause of these numerical instabilities and why they appear at the rear of the interface, as apposed to the front, as one may expect. An example of the evolution of the interface from a simulation corresponding to $\Lambda = 10$ with $\gamma = 8000$ is shown in figure 6.11 up to time $t = t_{\text{circ}}$. The evolution of an initially elliptical inclusion, studied numerically, warrants further investigation.

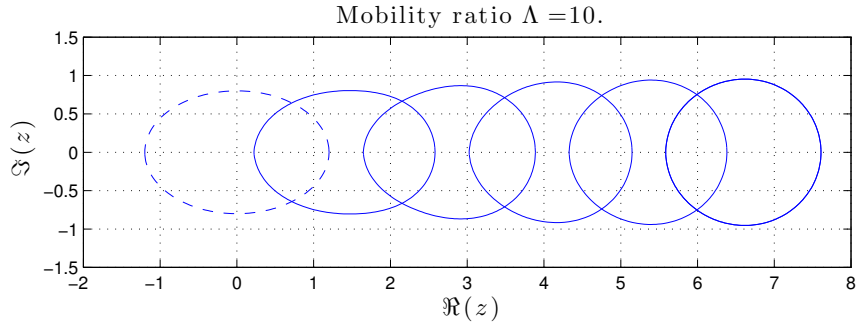

Figure 6.11: Snapshots of the evolution of $\partial\Omega(t)$ for $0 \leq t \leq 3.296$ in the case $\Lambda = 10$, where the smoothing parameter $\gamma = 8000$ is chosen in this simulation. The initial interface (dashed) is given by (5.54) with $d = 0$, $\theta_e = 0$, $b = 1$ and $a = 0.2$. Results are presented for $N = 200$ and $\Delta t = 10^{-3}$. The interface is shown at times $t = 0$, 0.6592, 1.3184, 1.9776, 2.6368 and 3.296. Here, the interface is driven by a uniform flow in $\Omega_2(t)$ in the positive $\Re(z)$ direction of speed $V = 1$.

In the numerical results presented in section 5.3.3, numerical instabilities are also observed, which are treated with a modest smoothing parameter value of $\gamma = 15$, which is sufficient for all simulations. For $\mathcal{O}(1)$ smoothing parameter, e.g. $\gamma = 1$, on the interval $0 \leq t \leq 1$, numerical instabilities are observed on $\partial\Omega(t)$ at the front of the circular interface, which are consequently picked up by the underlying physics

and develop into prominent fingering instabilities. Figure 6.12 shows comparison between the same simulation with $\gamma = 1$ and $\gamma = 15$. In figure 6.12(a) we see the so called fingering instability taking over, whereas in figure 6.12(b) the interface remains smooth and circular, with drift speed U agreeing with the exact solution (5.86).

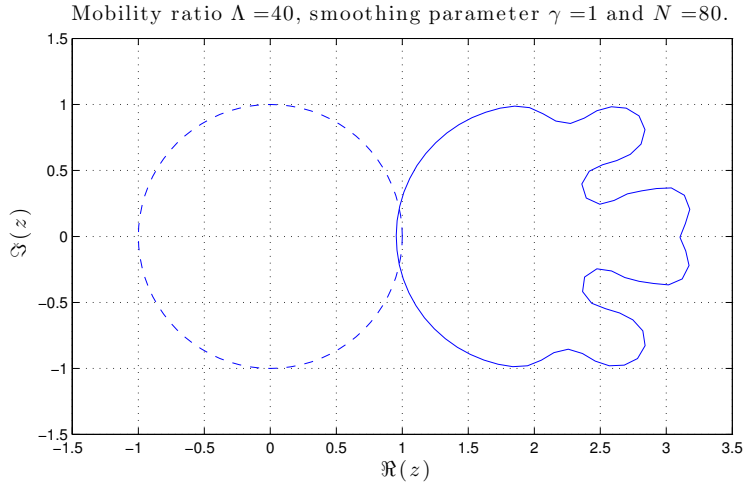

(a)

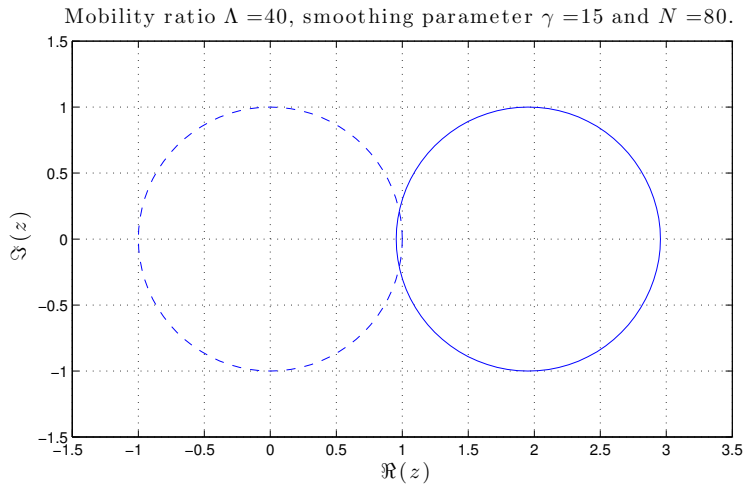

(b)

Figure 6.12: Comparison between numerical simulations of an initially unit circular interface (dashed) of an the inclusion $\Omega_1(t)$ driven by a uniform flow in $\Omega_2(t)$ of speed $V = 1$ in the positive $\Re(z)$ direction. Here the mobility ratio $\Lambda = 40$. The final shape of the interface (solid) is shown at $t = 1$. In (a) a smoothing parameter of $\gamma = 1$ is chosen and in (b) $\gamma = 15$. Results are presented for $N = 80$ and $\Delta t = 10^{-3}$.

Furthermore, when the number of mesh points, N, is increased, smaller wavelength instabilities appear, which grow faster with time, as expected—demonstrated in figure 6.13. This agrees with the discussion presented in section 2.4 and [1]. The

development of these instabilities (due to the physics) mainly appear when $\Lambda > 1$, as expected, since these values of mobility ratio describe the case of a fluid moving through a relatively more viscous fluid and therefore correspond to the instabilities discussed in [123]. The initial instabilities appear, here, due to numerical error. For $\Lambda < 1$, it is conjectured that similar fingering instability should appear at the rear of the circular inclusion, however, these were not observed in any numerical tests performed. This may be since $\Lambda < 1$ describes a physically stable situation, as compared with $\Lambda > 1$, and in the limit $\Lambda \to 0$ the results should replicate flow passed a fixed solid cylinder—this is apparent from the results presented in figure 5.6.

The instabilities observed in the two-phase problem of the type shown in figure 6.13 seem counterintuitive since the two-phase problem is a generalisation of the one-phase counterpart, where such instabilities are not observed. The author's initial thoughts were that the boundary condition (5.6c) would provide a regulatory affect on the interface. In fact, in one-phase simulations, disturbances on the interface appear to decay rapidly, even for small smoothing parameter compared with $\gamma = 1$ (results not shown here), and the interface remains circular for large time. The long-time stable behaviour of the interface is demonstrated by the numerical results presented earlier in this chapter (of a bubble propagating near a wall). These results, in the author's view, support the idea that the solution $U = 2V$ (corresponding to a circular bubble in an unbounded Hele-Shaw cell) is selected as a stable attractive solution in a dynamical sense, since here, it is the ZST Hele-Shaw free boundary problem that is studied, and modelled numerically. However, it should be noted that the filtering method has a smoothing effect akin to surface tension. Thus it is not clear if the numerical results support the ZST selection mechanism, or if the selection is a result of the filtering mechanism itself. This requires further investigation.

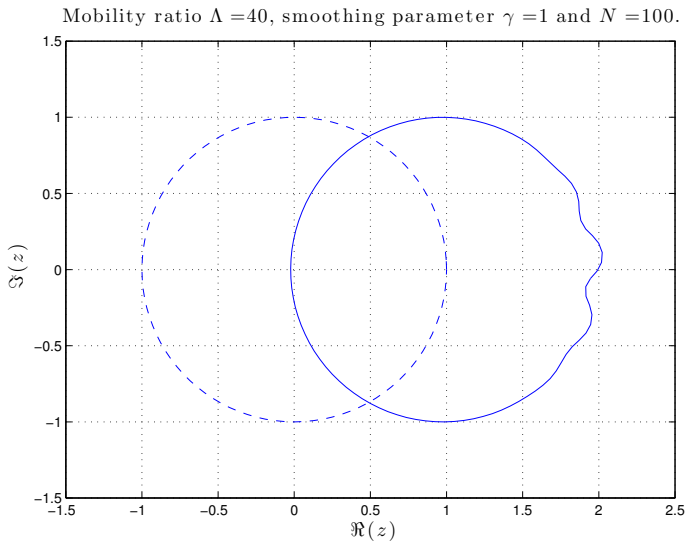

(a)

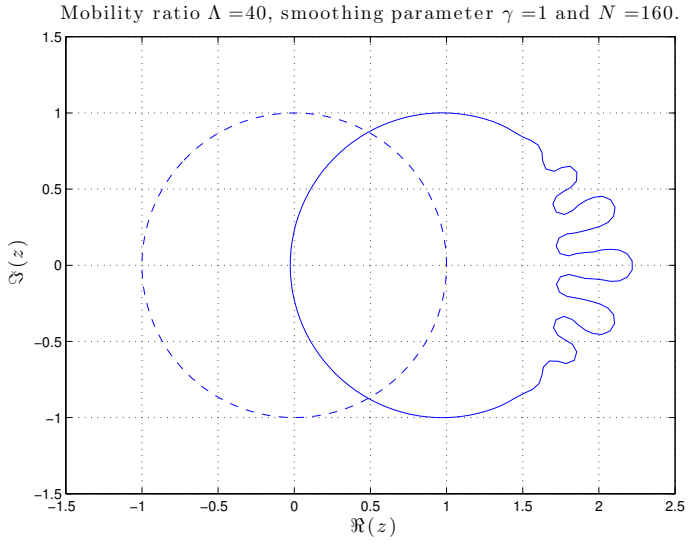

(b)

Figure 6.13: Comparison between the evolution of $\partial\Omega(t)$ of an initially circular interface (dashed) in a uniform background flow of speed $V = 1$ in the positive $\Re(z)$ direction. Here the mobility ratio $\Lambda = 40$. The final shape of the interface (solid) is shown at $t = 0.5$. In (a) $N = 100$ mesh points are taken on the interface, and in (b) $N = 160$. Results presented here are for $\Delta t = 10^{-3}$, and in both cases $0 \leq t \leq 0.5$ with $\gamma = 1$.

Appendix A

Complex moment description of Hele-Shaw flows

In 1972, Richardson [116] introduced a 'complex moment' description which demonstrates that there is an infinite number of invariants (i.e. conserved quantities) of motion in Hele-Shaw free boundary flows. To derive these infinite conservation laws (a consequence of the geometric property of Hele-Shaw flows) we consider the case of an injection driven free boundary. That is, the free boundary evolution of a fluid blob driven by a source of strength $Q_1 > 0$ located at $\mathbf{x} = \mathbf{x}_1$, i.e. $z = z_1 = x_1 + iy_1$, inside the fluid domain, $\Omega(t)$. Let us define the complex moment

$$M_k := \iint_{\Omega(t)} z^k \, \mathrm{d}x\mathrm{d}y, \tag{A.1}$$

where the complex variable is $z = x + iy$. Suppose that the fluid domain $\Omega(t)$ has boundary $\partial\Omega(t)$ given by a simple closed contour in $\mathbb{C}$ which encloses z_1. Then, by the Riemann mapping theorem, there exists a conformal map from the unit ζ-disc D in the ζ-plane to the fluid blob in the physical z-plane given by $z = f(\zeta, t)$—see e.g. [48].

Consider any analytic function $\mathcal{L}(z)$ on $\Omega(t)$. The rate of change of the integral

of $\mathcal{L}(z)$ over the fluid domain is (by the Reynolds Transport Theorem [48])

$$\frac{\mathrm{d}}{\mathrm{d}t}\iint\limits_{\Omega(t)} \mathcal{L}(z)\,\mathrm{d}x\mathrm{d}y = \oint_{\partial\Omega(t)} \mathcal{L}(z)v_n\,\mathrm{d}s, \tag{A.2}$$

where the normal velocity on $\partial\Omega(t)$ is $v_n = \mathbf{u}\cdot\mathbf{n}$ and $\mathbf{n}$ is the unit normal vector on $\partial\Omega(t)$. Since the velocity can be described as the gradient of a potential function, i.e. $\mathbf{u} = \nabla\phi$, with the boundary data $\phi = 0$ on $\partial\Omega(t)$, then (A.2) can be written as

$$\frac{\mathrm{d}}{\mathrm{d}t}\iint\limits_{\Omega(t)} \mathcal{L}(z)\,\mathrm{d}x\mathrm{d}y = \oint_{\partial\Omega(t)} \frac{\partial}{\partial n}(\mathcal{L}(z)\phi)\,\mathrm{d}s. \tag{A.3}$$

Applying Green's theorem and noting that $\nabla_z^2\mathcal{L} = 0$ since $\mathcal{L}(z)$ is analytic, then we have

$$\oint_{\partial\Omega(t)} \frac{\partial}{\partial n}(\mathcal{L}(z)\phi)\,\mathrm{d}s = \iint\limits_{\Omega(t)} \mathcal{L}(z)\nabla^2\phi\,\mathrm{d}x\mathrm{d}y. \tag{A.4}$$

Since $\nabla^2\phi = \delta_0(\mathbf{x}-\mathbf{x}_1)$ in the fluid domain $\Omega(t)$, where $\delta_0(\mathbf{x}-\mathbf{x}_1)$ is the Dirac distribution defined in (1.18), (A.4) can be written as

$$\begin{aligned}\iint\limits_{\Omega(t)} \mathcal{L}(z)\nabla^2\phi\,\mathrm{d}x\mathrm{d}y &= \iint\limits_{\Omega(t)} \mathcal{L}(z)\left[Q\delta_0(x-x_1)\delta_0(y-y_1)\right]\,\mathrm{d}x\mathrm{d}y \\ &= Q\mathcal{L}(z_1).\end{aligned} \tag{A.5}$$

Now, letting $\mathcal{L}(z) = z^k$ we have

$$\frac{\mathrm{d}}{\mathrm{d}t}M_k = Q\delta_{0k}, \tag{A.6}$$

for $k = 0, 1, 2, \ldots$, where δ_{0k} represents the *Kronecker delta*. This implies that *all*

moments, $k \geq 1$, are constant and the zeroth moment is

$$\begin{aligned} \frac{\mathrm{d}}{\mathrm{d}t} M_0 &= \frac{\mathrm{d}}{\mathrm{d}t} \iint\limits_{\Omega(t)} \mathrm{d}x\mathrm{d}y \\ &= Q, \end{aligned} \tag{A.7}$$

which is equal to the rate of injection of fluid mass due to the point source, i.e. the rate of change of fluid blob area. That is, (A.6) gives an infinite number of conservation laws, $k = 0, 1, 2, \ldots$, where M_0 is proportional to the fluid blob area at time t, $M_0 = Qt + M_0(0)$.

The complex moment description (A.6) can be used to derive equations that describe the evolution of the free boundary, $\partial\Omega(t)$. More precisely, given a parametric map $f(\zeta, t)$ with K parameters, (A.6) provide K equations, $k = 0, 1, \ldots, K-1$. This is an alternative method to find exact solutions to the Hele-Shaw free boundary problem described in section 1.3.4. The link between the set of ODEs governing a parametric map found via the Polubarinova-Galin equation (see appendix C) and the complex moment description described above was highlighted by Mineev-Weinstein [99], by which the link to integrable hierarchies in other areas of study become apparent.

Appendix B

Hele-Shaw flows with external potential fields

B.1 The Hele-Shaw equation with background conservative forcing

Here we derive the Hele-Shaw free boundary problem in the case when the fluid mass is subject to a *conservative* background body force, e.g. gravity, centrifugal force, or electromagnetic forces on conducting fluids—see chapter 3. Conservative forces can be described as the gradient of a scalar potential function $\Psi(x_1, x_2, x_3, t)$, i.e. we write

$$\mathbf{f}_b = \nabla\Psi, \tag{B.1}$$

where $\nabla = (\partial_{x_1}, \partial_{x_2}, \partial_{x_3})$.

Following the assumptions of Hele-Shaw flow i.e. neglecting any vertical fluid motion perpendicular to the plates and assuming $\partial\mathbf{u}/\partial t = 0$, from (1.2), the momentum equations are then

$$\rho u_1 \frac{\partial u_1}{\partial x_1} + \rho u_2 \frac{\partial u_1}{\partial x_2} = -\frac{\partial p}{\partial x_1} + \mu\nabla^2 u_1 + \frac{\partial \Psi}{\partial x_1}, \tag{B.2a}$$

$$\rho u_1 \frac{\partial u_2}{\partial x_1} + \rho u_2 \frac{\partial u_2}{\partial x_2} = -\frac{\partial p}{\partial x_2} + \mu \nabla^2 u_2 + \frac{\partial \Psi}{\partial x_2}, \tag{B.2b}$$

$$0 = -\frac{\partial p}{\partial x_3} + \frac{\partial \Psi}{\partial x_3}. \tag{B.2c}$$

Now, assuming the length scale L_d in the x_1x_2-plane is much greater than the length scale h (cell gap) in the x_3 direction, i.e. $h/L_\mathrm{d} \ll 1$, then the above equations reduce to

$$0 = -\frac{\partial p}{\partial x_1} + \mu \frac{\partial^2 u_1}{\partial x_3^2} + \frac{\partial \Psi}{\partial x_1}, \tag{B.3a}$$

$$0 = -\frac{\partial p}{\partial x_2} + \mu \frac{\partial^2 u_2}{\partial x_3^2} + \frac{\partial \Psi}{\partial x_2}, \tag{B.3b}$$

$$0 = -\frac{\partial p}{\partial x_3} + \frac{\partial \Psi}{\partial x_3}. \tag{B.3c}$$

Equations (B.3a) and (B.3b) represent Stokes flow in 2D, where the flow is driven by the gradient of the scalar function $P = p - \Psi$. Therefore, (B.3c) implies the function P is independent of x_3, i.e. $P = P(x_1, x_2, t)$. Thus, integrating (B.3a) and (B.3b) w.r.t. x_3 and taking the average over the cell gap, the mean 2D velocity is given by

$$\overline{u}_1 = -\frac{h^2}{12\mu}\left(\frac{\partial p}{\partial x_1} - \frac{\partial \Psi}{\partial x_1}\right), \tag{B.4a}$$

$$\overline{u}_2 = -\frac{h^2}{12\mu}\left(\frac{\partial p}{\partial x_2} - \frac{\partial \Psi}{\partial x_2}\right). \tag{B.4b}$$

Dropping the bar notation, (B.4) in vector form is

$$\mathbf{u} = -\frac{h^2}{12\mu}\left(\nabla p - \nabla \Psi\right) \tag{B.5}$$

$$= -\frac{h^2}{12\mu}\nabla P, \tag{B.6}$$

where here ∇ now represents the 2D differential operator $(\partial_{x_1}, \partial_{x_2})$.

B.2 Boundary effects leading to updated boundary conditions

Assume that $\Psi = \Psi(x_1, x_2, t)$, the external potential, is purely 2D and that the Hele-Shaw cell is filled with a viscous fluid occupying the domain $\Omega(t)$ surrounded by a secondary inviscid fluid over the domain $\Omega_{\text{inv}(t)}$, forming an interface $\partial\Omega(t)$. Let the pressure and external potential in $\Omega_{\text{inv}}(t)$ be denoted by p_{inv} and Ψ_{inv}, respectively. The boundary conditions are then

$$p = p_{\text{inv}}, \quad \mathbf{x} \in \partial\Omega(t) \tag{B.7a}$$

and

$$\Psi = \Psi_{\text{inv}}, \quad \mathbf{x} \in \partial\Omega(t), \tag{B.7b}$$

where $\mathbf{x}$ is the 2D position vector (x_1, x_2). Let us also assume that the external forces are such that the external potential permeates through the inviscid fluid without change, e.g. gravity forces remain the same over the viscous and inviscid fluids. Therefore, the external forces are given by (B.1) in the entire plane. Hence, the applied external field exerts a pressure on the interface $\partial\Omega(t)$. In the inviscid fluid the pressure distribution is related to the external potential and is such that

$$p_{\text{inv}} \sim \Psi, \quad \mathbf{x} \in \Omega_{\text{inv}}(t). \tag{B.8}$$

Since the pressure exterior to the viscous fluid is given by the external field in the inviscid region, the dynamic boundary condition must satisfy

$$p = \Psi, \qquad \mathbf{x} \in \partial\Omega(t). \tag{B.9}$$

The kinematic boundary condition remains unchanged from (1.16). That is, the

normal velocity of $\partial\Omega(t)$ must be equal to the normal velocity of the fluid on the interface, i.e.

$$v_n = \mathbf{u} \cdot \mathbf{n}, \qquad \mathbf{x} \in \partial\Omega(t), \tag{B.10}$$

where $\mathbf{n}$ is the unit normal vector on $\partial\Omega(t)$.

B.3 The Hele-Shaw free boundary problem driven by an external electric field

Writing $\phi(x_1, x_2, t) = -kp(x_1, x_2, t)$, where $k = h^2/12\mu$, and considering the continuity equation, $\nabla \cdot \mathbf{u} = 0$, the free boundary problem can be written in terms of the scalar potential function $\phi(x_1, x_2, t)$ as

$$\nabla^2\phi = 0, \qquad \mathbf{x} \in \Omega(t), \tag{B.11a}$$

$$\phi = -k\Psi, \quad \mathbf{x} \in \partial\Omega(t), \tag{B.11b}$$

$$v_n = \frac{\partial\phi}{\partial n}, \qquad \mathbf{x} \in \partial\Omega(t). \tag{B.11c}$$

The case of $\Psi \equiv 0$ recovers the classical Hele-Shaw free boundary problem described in section (1.2.2). Often, the external potential is re-normalised such that $\Psi(x_1, x_2, t) \equiv -k\Psi(x_1, x_2, t)$ and the dynamic boundary condition (B.11b) is written $\phi = \Psi$, $\mathbf{x} \in \partial\Omega(t)$, as presented in the literature—see e.g. [39, 89].

Appendix C

The Polubarinova-Galin equation

In the mid 1940s, Polubarinova-Kochina and Galin proposed a complex variable technique to tackle Hele-Shaw free boundary problems by the use of conformal mappings. They consider the following Hele-Shaw free boundary problem [44, 112]: let a viscous fluid occupy a simply connected domain $\Omega(t)$ with free boundary $\partial\Omega(t)$. Suppose the free boundary is driven by a source or sink located at $\mathbf{x}_1 = (x_1, y_1)$ of strength Q_1, where $Q_1 > 0$ for injection and $Q_1 < 0$ for extraction. The pressure surrounding the fluid is held constant, and is taken to be $p = 0$, so the dynamic boundary condition is

$$\phi(z, \bar{z}, t) = 0 \quad \text{on } \partial\Omega(t). \tag{C.1}$$

The function $\phi(z, \bar{z}, t)$ is harmonic in $\Omega(t) \setminus \{\mathbf{x}_1\}$, and from the continuity equation we have

$$\nabla^2\phi = Q_1\delta_0(\mathbf{x} - \mathbf{x_1}), \tag{C.2}$$

where $\delta_0(\mathbf{x} - \mathbf{x}_1)$ is the Dirac distribution defined in (1.18). The motion of the free boundary is given by the fluid velocity on $\partial\Omega(t)$ i.e. the kinematic condition

$$v_n = \frac{\partial\phi}{\partial n} \quad \text{on } \partial\Omega(t), \tag{C.3}$$

where v_n denotes the normal velocity of $\partial\Omega(t)$. Now, since the complex potential is given by $w = \phi + i\psi$—an analytic function in $\Omega(t)$—where $\psi(x, y, t) \equiv \psi(z, \bar{z}, t)$ is the harmonic conjugate of $\phi(x, y, t) \equiv \phi(z, \bar{z}, t)$, then $\partial w/\partial z = u - iv$. The complex potential in the vicinity of the point source (or sink) takes the form

$$w = \frac{Q_1}{2\pi} \log(z - z_1), \quad \text{as } z \to z_1. \tag{C.4}$$

The Riemann mapping theorem guarantees existence of a conformal map $z = f(\zeta, t)$ from the unit ζ-disc D in the ζ-plane to $\Omega(t)$, where the unit ζ-circle, ∂D, maps to the free boundary $\partial\Omega(t)$ in the z-plane [48]. In terms of the function $f(\zeta, t)$, the free boundary is given by

$$\partial\Omega(t) = \{f(e^{i\theta}, t) : \theta \in [0, 2\pi)\}, \tag{C.5}$$

and the outward normal to $\Omega(t)$ is given by

$$\mathbf{n} = \zeta \frac{f'}{|f'|}, \qquad \zeta \in \partial D, \tag{C.6}$$

where the prime denotes derivative w.r.t. the first argument. Hence, we can write the normal velocity v_n on $\partial\Omega(t)$ as

$$v_n = \Re \left\{ \frac{\partial w}{\partial z} \zeta \frac{f'}{|f'|} \right\}. \tag{C.7}$$

Due to the invariance of the Laplacian under a conformal mapping, we can write the superposition

$$(w \circ f)(\zeta, t) = \frac{Q}{2\pi} \log(\zeta). \tag{C.8}$$

Since $(w \circ f)(\zeta, t) = w(f(\zeta, t), t)$, the derivative of the complex potential w.r.t. z, as

$z \to z_1$, is

$$\frac{\partial w}{\partial z}\frac{\partial f}{\partial \zeta} = \frac{Q_1}{2\pi\zeta}. \tag{C.9}$$

Now, since $\partial\Omega(t)$ is given by $f(\zeta, t)$ such that $|\zeta|^2 = 1$, the normal velocity on the free boundary can be calculated as

$$\begin{aligned} v_n &= \Re\left\{\frac{\partial f}{\partial t}\overline{\mathbf{n}}\right\} \\ &= \Re\left\{\frac{\partial f}{\partial t}\zeta\overline{\frac{f'}{|f'|}}\right\}. \end{aligned} \tag{C.10}$$

Finally, combing (C.7), (C.9) and (C.10) we have

$$\Re\left\{\frac{\partial f}{\partial t}\zeta\overline{\frac{\partial f}{\partial \zeta}}\right\} = \frac{Q_1}{2\pi} \quad \text{on } \partial D. \tag{C.11}$$

More generally, equating the two expressions for v_n, namely (C.7) and (C.10), and noting that $|f'|^2 = f'\overline{f}$ on ∂D, we have

$$\Re\left\{\frac{\dot{f}}{\zeta f'}\right\} = \frac{1}{|f'|^2}\Re\left\{\zeta\frac{\partial w}{\partial z}\frac{\partial f}{\partial \zeta}\right\} \quad \text{on } \partial D. \tag{C.12}$$

Here, the dot denotes differentiation w.r.t. time. Equation (C.12) is known as the *Polubarinova-Galin* equation, or P-G equation for short, which gives the Hele-Shaw free boundary problem as differential functional equation governing the motion of the interface.

Example C.1 (Perturbed circular blob)

Consider the fluid blob occupying the domain $\Omega(t)$ with free boundary $\partial\Omega(t)$ given by the conformal map

$$z = a\zeta + b\zeta^2, \tag{C.13}$$

from the unit ζ-disc D where $a(t)$ and $b(t)$ are real time-dependent parameters to

be found, and the free boundary is driven by a point sink located at the origin, i.e. $z_1 = 0$. Hence, applying (C.11) in the case of a point sink of strength Q_1 gives

$$\Re\left\{\left(\zeta\frac{\mathrm{d}a}{\mathrm{d}t}+\zeta^2\frac{\mathrm{d}b}{\mathrm{d}t}\right)\frac{1}{\zeta}\left(a+\frac{2b}{\zeta}\right)\right\}=\frac{Q_1}{2\pi}. \tag{C.14}$$

Writing $\zeta = e^{i\theta}$ on ∂D and comparing terms of $\mathcal{O}(1)$ and $\mathcal{O}(\cos\theta)$, (C.14) yields

$$\frac{\mathrm{d}}{\mathrm{d}t}\left(a^2 b\right)=0, \tag{C.15a}$$

$$\frac{\mathrm{d}}{\mathrm{d}t}\left(\frac{a^2}{2}+b^2\right)=\frac{Q_1}{2\pi}, \tag{C.15b}$$

a set of coupled differential equations governing the evolution of a and b. Integrating (C.15), a and b are given by the solution to the set of equations

$$a^2 b = a_0^2 b_0, \tag{C.16a}$$

$$\frac{a^2}{2}+b^2=\frac{Q_1 t}{2\pi}+\frac{a_0^2}{2}+b_0^2, \tag{C.16b}$$

where $a_0 = a(0)$ and $b_0 = b(0)$. This is the same problem considered in example 1.3.3, for $n = 2$, and the solution to (C.16) agree with the solution to (1.67).

Appendix D

An alternative derivation of the Schwarz function equation

Let $g(z,t)$ be the Schwarz function of $\partial\Omega(t)$ as defined in (1.29), i.e. $\bar{z} = g(z,t)$, $z \in \partial\Omega(t)$. Taking the time derivative of $\bar{z}$ we have

$$\frac{\mathrm{d}\bar{z}}{\mathrm{d}t} = \frac{\partial g}{\partial z}\frac{\mathrm{d}z}{\mathrm{d}t} + \frac{\partial g}{\partial t}. \tag{D.1}$$

Since $\dot{z} = u + iv$, then $\dot{\bar{z}} = u - iv$, where the dot denotes differentiation w.r.t. time. Assuming there exists some background force $\mathbf{f}_b = -\nabla\Psi/k$ then $\phi(x,y,t) = \Psi(x,y,t)$ on the free boundary and so the tangential velocity along $\partial\Omega(t)$ is $\partial\Psi/\partial s$, where s denotes the arc length parameter along the free boundary. Hence, we have

$$\Re\left[(u - iv)\frac{\mathrm{d}z}{\mathrm{d}s}\right] = \frac{\partial\Psi}{\partial s}, \tag{D.2}$$

which can be written as

$$\frac{1}{2}\left[\frac{\mathrm{d}\bar{z}}{\mathrm{d}t}\frac{\mathrm{d}z}{\mathrm{d}s} + \frac{\mathrm{d}z}{\mathrm{d}t}\frac{\mathrm{d}\bar{z}}{\mathrm{d}s}\right] = \frac{\partial\Psi}{\partial s}. \tag{D.3}$$

From (1.34) we have that $\partial z/\partial s = \left(\sqrt{g'}\right)^{-1}$, and it can be shown that [30, p. 111]

$$\frac{\partial \bar{z}}{\partial s} = \sqrt{\frac{\partial g}{\partial z}}. \tag{D.4}$$

Hence, (D.3) becomes

$$\frac{\mathrm{d}\bar{z}}{\mathrm{d}t} + \frac{\mathrm{d}z}{\mathrm{d}t}\frac{\partial g}{\partial z} = 2\frac{\partial \Psi}{\partial z}. \tag{D.5}$$

Thus, adding (D.1) and (D.5) we have

$$2\frac{\mathrm{d}\bar{z}}{\mathrm{d}t} = \frac{\partial g}{\partial t} + 2\frac{\partial \Psi}{\partial z}. \tag{D.6}$$

Now, since $\dot{\bar{z}} = \partial w/\partial z$, i.e. the derivative of the complex potential, we can write (D.6) as

$$\frac{\partial w}{\partial z} = \frac{1}{2}\frac{\partial g}{\partial t} + \frac{\partial \Psi}{\partial z}. \tag{D.7}$$

This is precisely the generalised Schwarz function equation (1.79).

Appendix E

Role of the Kelly-Hinch procedure for translating bubbles

Consider the boundary integral equation (2.70), i.e.

$$\fint_0^L \frac{\widetilde{v}_\tau(s) + i\widetilde{v}_n(s)}{z(s) - z(s_m)}\,\mathrm{d}s = -i\pi\left[\widetilde{v}_\tau(s_m) + i\widetilde{v}_n(s_m)\right]\left(\frac{\mathrm{d}z}{\mathrm{d}s}\right)^{-1}\Bigg|_{s_m}. \tag{E.1}$$

The tangential velocity due to the background flow, on the interface, can be approximated at each mesh point S_i, $i = 1, \ldots, N$, by

$$\begin{aligned}\widehat{v}_\tau(S_i) &= \widehat{u}(S_i)\left.\frac{\mathrm{d}x}{\mathrm{d}s}\right|_{S_i} + \widehat{v}(S_i)\left.\frac{\mathrm{d}y}{\mathrm{d}s}\right|_{S_i} + \varepsilon_E(S_i)\\ &= \widehat{v}^*_\tau(S_i) + \varepsilon_E(S_i),\end{aligned} \tag{E.2}$$

where the derivatives in (E.2) are approximated using a finite difference formula and so $\varepsilon_E(S_i)$ denotes the error from the approximation at each mesh point. Therefore, in general, $\varepsilon_E = \varepsilon_E(s)$. Applying boundary condition (2.8) in (E.1) gives the equation for the unknown quantity $\widetilde{v}_n(s)$, i.e.

$$\fint_0^L \frac{-\widehat{v}_\tau(s) + i\widetilde{v}_n(s)}{z(s) - z(s_m)}\,\mathrm{d}s = -i\pi\left[-\widehat{v}_\tau(s_m) + i\widetilde{v}_n(s_m)\right]\left(\frac{\mathrm{d}z}{\mathrm{d}s}(s_m)\right)^{-1}\Bigg|_{s_m}, \tag{E.3}$$

and re-arranging gives

$$\left.\frac{\mathrm{d}z}{\mathrm{d}s}\right|_{s_m} \fint_0^L \frac{i\widetilde{v}_n(s)}{z(s)-z(s_m)}\,\mathrm{d}s + \pi\widetilde{v}_n(s_m) = \left.\frac{\mathrm{d}z}{\mathrm{d}s}\right|_{s_m} \fint_0^L \frac{\widehat{v}_\tau(s)}{z(s)-z(s_m)}\,\mathrm{d}s - i\pi\widehat{v}_\tau(s_m). \quad \text{(E.4)}$$

Replacing $\widehat{v}_\tau(s)$ with $\widehat{v}^*_\tau(s)$, i.e. the approximation $\widehat{v}_\tau(s) - \varepsilon_E(s)$ in (E.4), we have

$$\left.\frac{\mathrm{d}z}{\mathrm{d}s}\right|_{s_m} \fint_0^L \frac{i\widetilde{v}^*_n(s)}{z(s)-z(s_m)}\,\mathrm{d}s + \pi\widetilde{v}^*_n(s_m) = \left.\frac{\mathrm{d}z}{\mathrm{d}s}\right|_{s_m} \fint_0^L \frac{\widehat{v}_\tau(s)-\varepsilon_E(s)}{z(s)-z(s_m)}\,\mathrm{d}s - i\pi\widehat{v}_\tau(s_m) - \varepsilon_E(s_m), \quad \text{(E.5)}$$

where if $\widetilde{v}_n(s)$ is the solution corresponding to $\widehat{v}_\tau$, then the solution corresponding to $\widehat{v}^*_\tau = \widehat{v}_\tau(s) - \varepsilon_E(s)$ is $\widetilde{v}^*_n(s)$, say. Let us assume that the error, $\varepsilon_E(S_i)$, is approximately the same constant at each mesh point, $i = 1, \ldots, N$. Therefore $\varepsilon_E(s) \approx \epsilon_E =$ constant, since the same finite difference formula is employed at each mesh point and so the error is expected to be of the same order at each mesh point.

Now, consider the relation between $\widetilde{v}_n(s)$ and $\widetilde{v}^*_n(s)$, i.e. the affect of the error $\varepsilon_E(s)$. From (2.15) we see that $\widetilde{u} - i\widetilde{v} + c$ is a solution to

$$\frac{1}{2i\pi}\oint_{\partial\Omega(t)} \frac{\widetilde{u}(z) - i\widetilde{v}(z) + c}{z - z_m}\,\mathrm{d}z = -\frac{\widetilde{u}(z_m) - i\widetilde{v}(z_m) + c}{2}, \quad \text{(E.6)}$$

where, in general, c is a complex constant, i.e. $c = c_R + ic_I$ and c_R, $c_I \in \mathbb{R}$. Note that

$$\begin{aligned}(\widetilde{u} - i\widetilde{v} + c)\frac{\mathrm{d}z}{\mathrm{d}s} &= \widetilde{v}_\tau + i\widetilde{v}_n + (c_R + ic_I)\frac{\mathrm{d}z}{\mathrm{d}s} \\ &= \widetilde{v}_\tau + i\widetilde{v}_n + c_R\frac{\mathrm{d}x}{\mathrm{d}s} - c_I\frac{\mathrm{d}y}{\mathrm{d}s} + i\left(c_R\frac{\mathrm{d}y}{\mathrm{d}s} + c_I\frac{\mathrm{d}x}{\mathrm{d}s}\right) \quad \text{(E.7)} \\ &= \widetilde{v}_\tau + i\widetilde{v}_n + c_A + ic_B,\end{aligned}$$

where

$$c_A = c_R \frac{\mathrm{d}x}{\mathrm{d}s} - c_I \frac{\mathrm{d}y}{\mathrm{d}s} \tag{E.8a}$$

and

$$c_B = c_R \frac{\mathrm{d}y}{\mathrm{d}s} + c_I \frac{\mathrm{d}x}{\mathrm{d}s}. \tag{E.8b}$$

Parameterising w.r.t. arc length, (E.6) can be written as

$$\int_0^L \frac{\widetilde{v}_\tau(s) + c_A + i(\widetilde{v}_n(s) + c_B)}{z(s) - z(s_m)} \,\mathrm{d}s = - i\pi \left[\widetilde{v}_\tau(s_m) + c_A + i\widetilde{v}_n(s_m) + ic_B\right] \left(\frac{\mathrm{d}z}{\mathrm{d}s}\right)^{-1}\Bigg|_{s_m}. \tag{E.9}$$

The constant c is fixed by imposing the dynamic boundary condition in (E.9). For example, for the solution corresponding to (2.8), $c_A = 0$, which implies $c_B = 0$ and so $c = 0$. That is, if $\widehat{v}_\tau$ is known exactly, then this corresponds to $c = 0$. Now, assume that $\widehat{v}_\tau$ is not known exactly, i.e. $\widehat{v}_\tau = \widehat{v}_\tau^* + \epsilon_E$, where ϵ_E is the error in approximating $\widehat{v}_\tau$ and $\widehat{v}_\tau^*$ is the approximation. Then, if we assume $\widehat{v}_\tau$ has some constant error, this error is related to the constant c_A by the dynamic boundary condition, i.e.

$$\widetilde{v}_\tau(s) + c_A = -(\widehat{v}_\tau - \epsilon_E). \tag{E.10}$$

Hence, when written in terms of the tangential and normal velocities, (E.6) gives the solution $\widetilde{v}_n$ corresponding to $\widetilde{v}_\tau = -\widehat{v}_\tau^*$ on $\partial\Omega(t)$, where $c_A = \epsilon_E$. Therefore if $\epsilon_E \neq 0$, then $c_A \neq 0$ and so $c_B \neq 0$. Since x_s, y_s, c_R and c_I are all real, then so too is c_B. Therefore, the solution to (E.5) is $\widetilde{v}_n + c_B$. Hence, if we substitute $\widetilde{v}_\tau = -(\widehat{v}_\tau - \epsilon_E) = -\widehat{v}_\tau^*$ in (E.1), then the expected solution $\widetilde{v}_n(s)$ will be superimposed with some constant function K, say. This constant, $K = c_B$, is merely a shift of the solution $\widetilde{v}_n(s)$ on the vertical axis. These effects are exhibited most prominently in

the numerical solution of travelling bubbles.

If the desired solution $\widetilde{v}_n(s)$ is shifted by constant K due to the error ϵ_E in approximating $\widehat{v}_\tau(s)$ on $\partial\Omega(t)$, and if it is known that the total fluid flux across $\partial\Omega(t)$ should be zero, then the average flux of $\widetilde{v}_n(s)$ should also zero. Therefore, the average flux of $\widetilde{v}_n(s) + K$ across $\partial\Omega$ will be K. Now consider the Kelly-Hinch procedure proposed in [68] and described in section 2.3. The procedure is to 'perturb' the solution according to the formula

$$\widetilde{v}_n(s) \to \widetilde{v}_n - \text{'average flux across } \partial\Omega(t)\text{'}, \tag{E.11}$$

i.e.

$$\widetilde{v}_n(s) \to \widetilde{v}_n - \left(\oint_{\partial\Omega(t)} \widetilde{v}_n(s)\,\mathrm{d}s\right)\left(\oint_{\partial\Omega(t)} \mathrm{d}s\right)^{-1}. \tag{E.12}$$

Therefore, if the average flux of the solution is zero, then no perturbation takes place and we have the solution we were seeking, i.e. the error $\varepsilon_E(s) = 0$. If the average flux of the computed solution is K, then

$$\widetilde{v}_n(s) \to (\widetilde{v}_n + K) - K, \tag{E.13}$$

and we retrieve the desired solution $\widetilde{v}_n$ with zero fluid flux across $\partial\Omega(t)$. Therefore, assuming the observed shift in the solution owes to the error in approximating $\widehat{v}_\tau$, which is of the form $\varepsilon_E(s) \approx \epsilon_E =$ constant for all s, and since $\widetilde{v}_\tau = -\widehat{v}_\tau$ on the interface, then the solution to (E.1) is the desired solution $\widetilde{v}_n(s)$ with at most an error of constant shift K. Hence, applying the procedure (E.12) to the shifted solution restores the desired solution.

Appendix F

Alternative BIE and method of computing the normal velocity

Consider the integral equation (2.14) in the derivation of the BIE (2.20) of the one-phase Hele-Shaw free boundary problem for a fluid blob with interface $\partial\Omega(t)$. There, the function $F(z,t)$ is constructed using the derivative of the complex potential, $\widetilde{w}(z,t)$, i.e. the conjugate complex velocity, in which case the resulting BIE (2.20) can be solved directly for the unknown normal velocity $\widetilde{v}_n$ on the interface.

Instead, choosing to construct the function $F(z,t)$ in terms of the complex potential, i.e.

$$F(z,t) \coloneqq \frac{\widetilde{w}(z,t)}{z - z_m}, \tag{F.1}$$

then the contour integral over the interface of the blob reads

$$\frac{1}{2i\pi} \oint_{\partial\Omega(t)} F(z,t)\,\mathrm{d}z = \frac{\widetilde{w}(z_m,t)}{2}, \tag{F.2}$$

where $z_m \in \partial\Omega(t)$. Since $\widetilde{w} = \widetilde{\phi} + i\widetilde{\psi}$, where $\widetilde{\phi}$ and $\widetilde{\psi}$ are the velocity potential and stream function of the velocity field $\widetilde{\mathbf{u}}$, respectively, (F.2) gives

$$\oint_{\partial\Omega(t)} \frac{\widetilde{\phi} + i\widetilde{\psi}}{z - z_m}\,\mathrm{d}z = i\pi \left(\widetilde{\phi} + i\widetilde{\psi}\right)\Big|_{z_m}. \tag{F.3}$$

Parametrising $\partial\Omega(t)$ with arc length, (F.3) becomes

$$\int_0^{L(t)} \frac{\widetilde{\phi}(s) + i\widetilde{\psi}(s)}{z(s) - z(s_m)} \frac{\mathrm{d}z}{\mathrm{d}s}\,\mathrm{d}s = i\pi\left(\widetilde{\phi}(s_m) + i\widetilde{\psi}(s_m)\right). \tag{F.4}$$

Applying the dynamic boundary condition (2.3b), i.e. $\widetilde{\phi} = -\widehat{\phi}$ on $\partial\Omega(t)$, (F.4) can be written in terms of the unknown stream function, $\widetilde{\psi}(s)$, on $\partial\Omega(t)$, in the form

$$\int_0^{L(t)} \frac{i\widetilde{\psi}(s)}{z(s) - z(s_m)}\,\mathrm{d}s + \pi\widetilde{\psi}(s_m) = \int_0^{L(t)} \frac{\widehat{\phi}(s)}{z(s) - z(s_m)}\,\mathrm{d}s - i\pi\widehat{\phi}(s_m). \tag{F.5}$$

Once $\widetilde{\psi}(s)$ is found from (F.5), the normal velocity on $\partial\Omega(t)$ due to the regular part of the flow field can be found by differentiating $\widetilde{\psi}(s)$ w.r.t. s since

$$\begin{aligned}
\frac{\mathrm{d}\widetilde{\psi}}{\mathrm{d}s} &= \frac{\partial\widetilde{\psi}}{\partial x}\frac{\mathrm{d}x}{\mathrm{d}s} + \frac{\partial\widetilde{\psi}}{\partial y}\frac{\mathrm{d}y}{\mathrm{d}s} \\
&= -\widetilde{v}\frac{\mathrm{d}x}{\mathrm{d}s} + u\frac{\mathrm{d}y}{\mathrm{d}s} \\
&= \widetilde{\mathbf{u}}\cdot\mathbf{n} \\
&= \widetilde{v}_n.
\end{aligned} \tag{F.6}$$

Equations (F.5) and (F.6) can be discretised, and (F.5) can be solved using the methods described in sections 2.3 and 2.4. Therefore, given $\widehat{\phi}(x, y, t)$, the total normal velocity of the interface can be found since $V_n = \widetilde{v}_n + \widehat{v}_n$, and the interface can be advected according to (2.23)–(2.24).

Using the approach described here allows for an extra parameter in the model for multiple interfaces, e.g. when there exist two or more bubbles in an unbounded Hele-Shaw cell. In particular, the BIE of the form (F.5) allows for mismatched constant pressure in each bubble. For example, the case of two bubbles with interfaces $\partial\Omega_1(t)$ and $\partial\Omega_2(t)$ such that $\phi = c_1$ on $\partial\Omega_1(t)$ and $\phi = c_2$ on $\partial\Omega_2(t)$. Then, using a similar formulation for multiple bubbles presented in section 2.8, the boundary integral

equation for the unknown stream function on the interfaces can be written as

$$\sum_{\ell=1}^{2} \fint_0^{L_\ell(t)} \frac{i\widetilde{\psi}_\ell(s)}{z(s)-z(s_m)}\,\mathrm{d}s - \pi\widetilde{\psi}_\jmath(s_m) = \\ -\sum_{\ell=1}^{2} \fint_0^{L_\ell(t)} \frac{c_\ell - \widehat{\phi}_\ell(s)}{z(s)-z(s_m)}\,\mathrm{d}s - i\pi\left[c_\jmath - \widehat{\phi}_\jmath(s_m)\right], \quad \text{(F.7)}$$

when $z_m = z(s_m) \in \partial\Omega_\jmath(t)$, $\jmath = 1$ or 2. Here, $\widetilde{\psi}_\ell$ and $\widehat{\phi}_\ell$ denote the stream function and velocity potential, respectively, on each bubble interface $\partial\Omega_\ell(t)$, and $L_\ell(t)$ denotes the total arc length of each interface, $\ell = 1, 2$.

Appendix G

An exact rational map solution for a translating bubble

Here we derive an exact solution for a bubble in a uniform flow where the interface is given by a rational map such that the Schwarz function, defined in (1.29), exhibits a singularity in the flow domain at a finite distance from the free boundary. Consider a finite bubble region bounded by the curve $\partial\Omega(t)$ in an unbounded Hele-Shaw cell, where viscous fluid occupies the region exterior of the bubble, denoted by $\Omega(t)$. Let us consider consider the conformal map, $z(\zeta, t)$, of the form (4.11), i.e.

$$z = \frac{a_0 + a_1\zeta + a_2\zeta^2}{\zeta + b_0}, \tag{G.1}$$

from the *interior* of the unit ζ-disc, D, to the domain $\Omega(t)$. For univalency and desired initial crescent bubble shape, we require $a_0 < 0$, $a_1 < 0$, $a_2 > 0$ and $|b_0| < 1$, where a_0, a_1, a_2 and b_0 are real, time-dependent parameters to be found.

The Schwarz function of (G.1) is given by

$$\begin{aligned} g &= \frac{a_0\zeta^2 + a_1\zeta + a_2}{\zeta(\zeta + b_0)} \\ &= \frac{a_0\zeta}{1 + b_0\zeta} + \frac{a_1}{1 + b_0\zeta} + \frac{a_2}{1 + b_0\zeta}. \end{aligned} \tag{G.2}$$

Note, since $|1/b_0|> 1$, (G.2) has only one relevant singularity, the singularity which lies inside the unit ζ-disc at $\zeta = 0$ and is mapped to the viscous fluid domain. From (G.1), we find that the Schwarz function singularity in the viscous domain lies at

$$z_0 = \frac{a_0}{b_0}. \tag{G.3}$$

Varying b_0 about zero places the singularity at a finite distance to the left or to the right of the bubble interface, on the $\Re(z)$ axis, whilst altering the shape of the interface.

As $\zeta \to 0$, from (G.1) we have

$$\frac{1}{\zeta} = \left(\frac{a_1}{b_0} - \frac{a_0}{b_0^2}\right)\frac{1}{z - z_0} + \mathcal{O}(1). \tag{G.4}$$

Assuming that the interface, $\partial\Omega(t)$, is driven by a uniform bounded flow at infinity of constant speed V in the positive $\Re(z)$ direction, then, as $z \to \infty$, the complex potential behaves like $w \to Vz$. Therefore, expanding g as $\zeta \to 0$ yields

$$\begin{aligned} g &= a_0\zeta(1 - b_0\zeta) + a_1(1 - b_0\zeta + b_0^2\zeta^2) + \frac{a_2}{\zeta}(1 - b_0\zeta + b_0^2\zeta^2 - b_0^3\zeta^3) + \mathcal{O}(\zeta^3) \\ &= \frac{a_2}{\zeta} + \mathcal{O}(1) \\ &= a_2\left(\frac{a_1}{b_0} - \frac{a_0}{b_0^2}\right)\frac{1}{z - z_0} + \mathcal{O}(1). \end{aligned} \tag{G.5}$$

The Schwarz function equation governing the evolution of a conformal map is given by (1.46). That is, as $z \to z_0$, comparing terms of $\mathcal{O}((z - z_0)^{-1})$ and $\mathcal{O}((z - z_0)^{-2})$ we have

$$\frac{\mathrm{d}}{\mathrm{d}t}\left[\frac{a_2a_1}{b_0} - \frac{a_2a_0}{b_0^2}\right] = 0, \tag{G.6}$$

$$\frac{\mathrm{d}}{\mathrm{d}t}\left[\frac{a_0}{b_0}\right] = 0. \tag{G.7}$$

Now let us consider the expansion of g as $\zeta \to -b_0$, i.e as $z \to \infty$. From (G.1), as $\zeta \to -b_0$, we have

$$\begin{aligned}\zeta &= (a_0 - a_1 b_0 + a_2 b_0^2)\frac{1}{z} - b_0 + \mathcal{O}(z) \\ &= \frac{K}{z} - b_0 + \mathcal{O}(z),\end{aligned} \tag{G.8}$$

where $K = a_0 - a_1 b_0 + a_2 b_0^2 = \text{constant}$. Hence, from (G.2), as $\zeta \to -b_0$

$$\begin{aligned}g &= \frac{a_0\left([K/z] - b_0\right)^2 + a_1\left([K/z] - b_0\right) + a_2 + \mathcal{O}(z)}{\left([K/z] - b_0\right)\left([Kb_0/z] - b_0^2 + 1\right) + \mathcal{O}(z)} \\ &= \frac{-(a_0 b_0^2 - a_1 b_0 + a_2)}{b_0(1 - b_0^2)} - \left[\frac{(a_1 K - 2b_0 a_0 K)}{b_0(1 - b_0^2)}\right. \\ &\qquad \left. + \frac{K(1 - 2b_0^2)(a_0 b_0^2 - a_1 b_0 + a_2)}{b_0^2(1 - b_0^2)^2}\right]\frac{1}{z} + \mathcal{O}(z^{-2}).\end{aligned} \tag{G.9}$$

Therefore, applying (1.46) as $z \to \infty$ yields

$$\frac{\mathrm{d}}{\mathrm{d}t}\left[\frac{-(a_0 b_0^2 - a_1 b_0 + a_2)}{b_0(1 - b_0^2)}\right] = 2V, \tag{G.10}$$

$$\frac{\mathrm{d}}{\mathrm{d}t}\left[\frac{(a_1 K - 2b_0 a_0 K)}{b_0(1 - b_0^2)} + \frac{K(1 - 2b_0^2)(a_0 b_0^2 - a_1 b_0 + a_2)}{b_0^2(1 - b_0^2)^2}\right] = 0. \tag{G.11}$$

The area of the bubble, A, can be calculated using Green's theorem with integration around the unit ζ-circle, ∂D, to yield

$$\begin{aligned}A &= \frac{1}{2i}\oint_{\partial D} \overline{z} z' \mathrm{d}\zeta \\ &= \frac{1}{2i}\oint_{\partial D}\left[\frac{a_0\zeta^2 + a_1\zeta + a_2}{\zeta(\zeta + b_0)}\right]\left\{\frac{a_1 + 2a_2\zeta^2}{\zeta + b_0} - \frac{a_0 + a_1\zeta + a_2\zeta^2}{(\zeta + b_0)^2}\right\}\mathrm{d}\zeta,\end{aligned} \tag{G.12}$$

where prime denotes differentiation w.r.t. the first argument. Expressing the integrand as partial fractions we find

$$A = \frac{1}{2i}\oint_{\partial D} \frac{a_0 a_2}{b_0} + \frac{(a_0 - a_1 b_0 + a_2 b_0^2)(a_2 - a_1 b_0 + a_0 b_0^2)}{b_0(1 - b_0^2)(\zeta + b_0)^2}$$

$$+\frac{a_2a_1b_0-a_2a_0}{b_0^2\zeta}-\frac{(a_0-a_1b_0+a_2b_0^2)(a_2-a_0b_0^2-2a_2b_0^2+a_1b_0^3)}{b_0^2(1-b_0^2)^2(1+b_0\zeta)}$$
$$+\frac{(a_0-a_1b_0+a_2b_0^2)(a_2-a_0b_0^2-2a_2b_0^2+a_1b_0^3)}{b_0^2(1-b_0^2)^2(\zeta+b_0)}\,\mathrm{d}\zeta, \quad \text{(G.13)}$$

and by Cauchy's integral formula we have

$$\begin{aligned}\frac{A}{\pi}&=\left[\frac{a_2a_1}{b_0}-\frac{a_2a_0}{b_0^2}+\frac{(a_0-a_1b_0+a_2b_0^2)(a_2-a_0b_0^2-2a_2b_0^2+a_1b_0^3)}{b_0^2(1-b_0^2)^2}\right]\\&=\left[\frac{a_2a_1}{b_0}-\frac{a_2a_0}{b_0^2}+\frac{K(a_2-a_0b_0^2-2a_2b_0^2+a_1b_0^3)}{b_0^2(1-b_0^2)^2}\right].\end{aligned} \quad \text{(G.14)}$$

Therefore, conservation of bubble area is given by

$$\frac{\mathrm{d}}{\mathrm{d}t}\left[\frac{a_2a_1}{b_0}-\frac{a_2a_0}{b_0^2}+\frac{K(a_2-a_0b_0^2-2a_2b_0^2+a_1b_0^3)}{b_0^2(1-b_0^2)^2}\right]=0. \quad \text{(G.15)}$$

It can be verified that (G.11) is a linear combination of (G.15) and (G.6). Thus, the evolution of the parameters in (G.1) are governed by (G.6), (G.7), (G.10) and (G.15), which can be solved numerically.

The critical points of (G.1), i.e. the points ζ_* such that $z'(\zeta_*,t)=0$, are given by

$$(a_1+2a_2\zeta_*^2)(\zeta_*+b_0)-a_0+a_1\zeta_*+a_2\zeta_*^2=0, \quad \text{(G.16)}$$

therefore

$$\zeta_*=-b_0\pm\sqrt{b_0^2-\frac{a_1b_0-a_0}{a_2}}. \quad \text{(G.17)}$$

Figure G.1 shows an example of the evolution of the interface with Schwarz function singularity (G.3) lying downstream, i.e. to the right, of the initial bubble interface. Figure G.2 shows the corresponding motion of the critical points in the ζ-plane. As the critical points collide with the unit ζ-disc, cusps form on the interface, beyond which the solution breaks down. The above example shows the evolution

of a 'crescent' shaped bubble, where the solution breaks down before the Schwarz function singularity is approached, i.e. the bubble interface never crosses the location of the singularity.

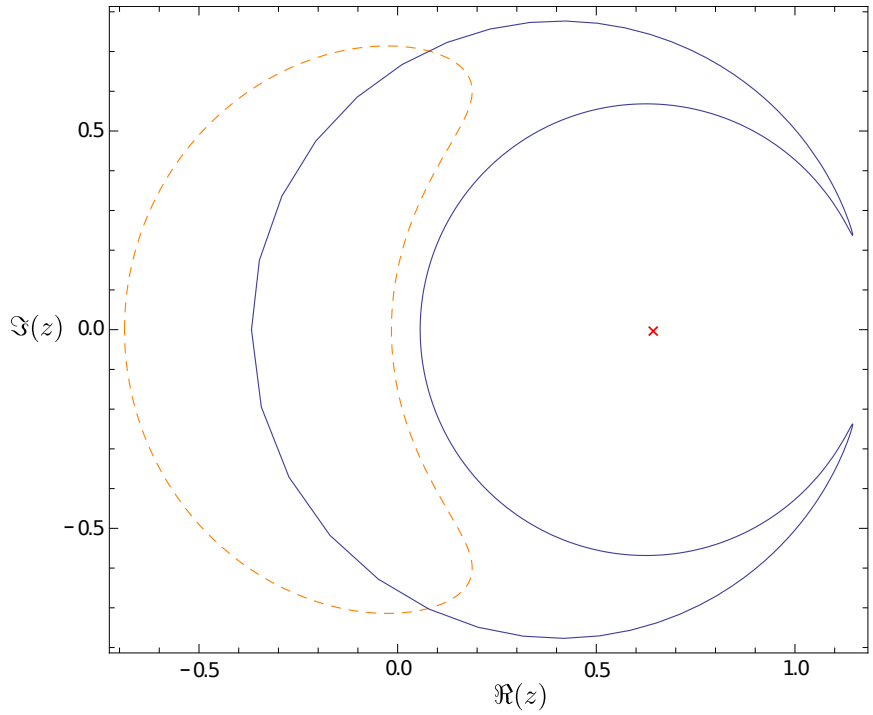

Figure G.1: Snapshots of the bubble interface at $t = 0$ (dashed) and at $t = 0.172$ (solid) where the initial interface is given by (G.1) with $a_0(0) = -0.375$, $a_1(0) = -0.15$, $a_2(0) = 0.25$, $b_0(0) = -0.5$. The Schwarz function singularity is marked by the cross, downstream of the initial bubble.The final interface shape (solid) is shown at $t = 0.172$, where formation of cusps on the interface are visible.

The above class of solution can also be derived by mapping the *exterior* of the unit ζ-disc to the fluid domain. Consider the map from D_{ext} to the viscous fluid domain, $\Omega(t)$, given by (4.11). Note that the map (4.11) can be written in the form

$$\begin{aligned} z &= c + \frac{a}{\zeta} + \frac{b}{\zeta - e} \\ &= \frac{(b - ce) + (c - ae)\zeta + a\zeta^2}{\zeta - e} \\ &= \frac{a_0 + a_1\zeta + a_2\zeta^2}{\zeta + b_0}, \end{aligned} \tag{G.18}$$

where it is required that $b < 0$, $a > 0$ and $|a| > |b|$ for univalency. This map has the same form of the map given by (4.18) in section 4.4. Here, c, a, b and e are

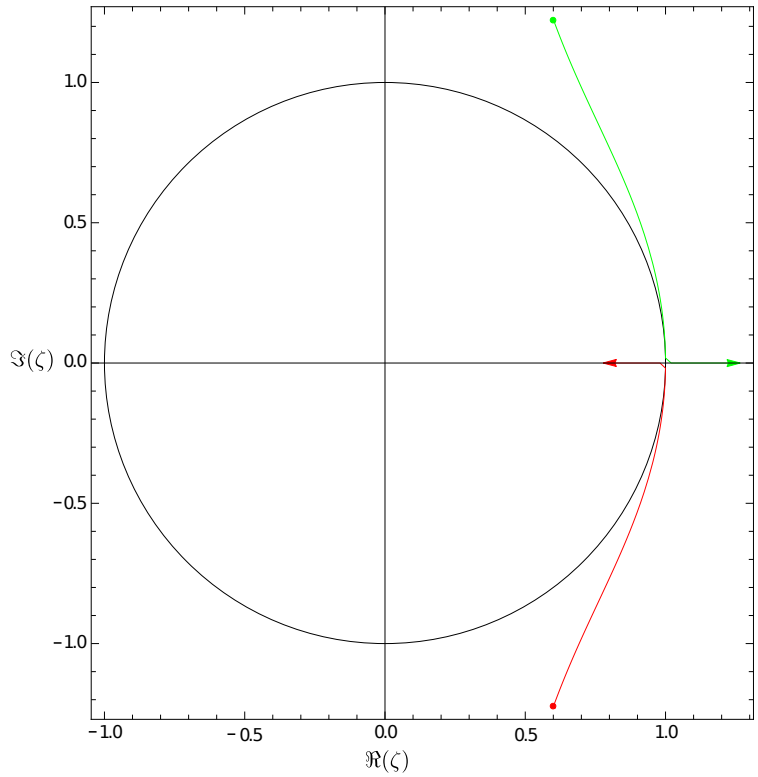

Figure G.2: Motion of the critical points (G.17) corresponding to an initial bubble whose interface is given by (G.1) with $a_0(0) = -0.375$, $a_1(0) = -0.15$, $a_2(0) = 0.25$, $b_0(0) = -0.5$, where $0 \leq t \leq 0.18$. The initial location of the critical points are marked by a dot.

real, time-dependent parameters to be found. The Schwarz function of the bubble interface is given by

$$g = c + \frac{a}{\zeta} - \frac{b}{e} + \frac{b}{e}\frac{1}{1 - e\zeta}. \tag{G.19}$$

Therefore, as before, there exists only one relevant Schwarz function singularity at $\zeta = 1/e$, which is mapped to the the point $z_0 = z(e^{-1})$ in the viscous domain, i.e.

$$z_0 = c + \frac{a}{e} + \frac{be}{1 - e^2}. \tag{G.20}$$

The critical points of (G.18) are given by

$$\zeta_* = e \pm \sqrt{\frac{b}{a}}. \tag{G.21}$$

Following the derivation for a perturbed ellipse (c.f. section 4.4) the parameters c,

a, b and e of the map (G.18) are governed by the coupled set of differential equations given by

$$\frac{\mathrm{d}}{\mathrm{d}t}\left(c - \frac{b}{e}\right) = 2V, \tag{G.22a}$$

$$\frac{\mathrm{d}}{\mathrm{d}t}\left(a^2 - \frac{ab}{e^2}\right) = 0, \tag{G.22b}$$

$$\frac{\mathrm{d}}{\mathrm{d}t}\left(c + \frac{a}{e} + \frac{be}{1-e^2}\right) = 0, \tag{G.22c}$$

$$\frac{\mathrm{d}}{\mathrm{d}t}\left(a^2 - \frac{b^2}{[1-e^2]^2}\right) = 0. \tag{G.22d}$$

Figure G.3 shows an example of the evolution of the interface with Schwarz function singularity (G.20) lying downstream of the initial bubble, where the coupled equations (G.22a)–(G.22d) have been solved numerically. Figure G.4 shows the corresponding motion of the critical points in the ζ-plane. As the critical points collide with the unit ζ-circle, cusps form on the bubble interface at $t \approx 0.9385$, at which point the solution breaks down.

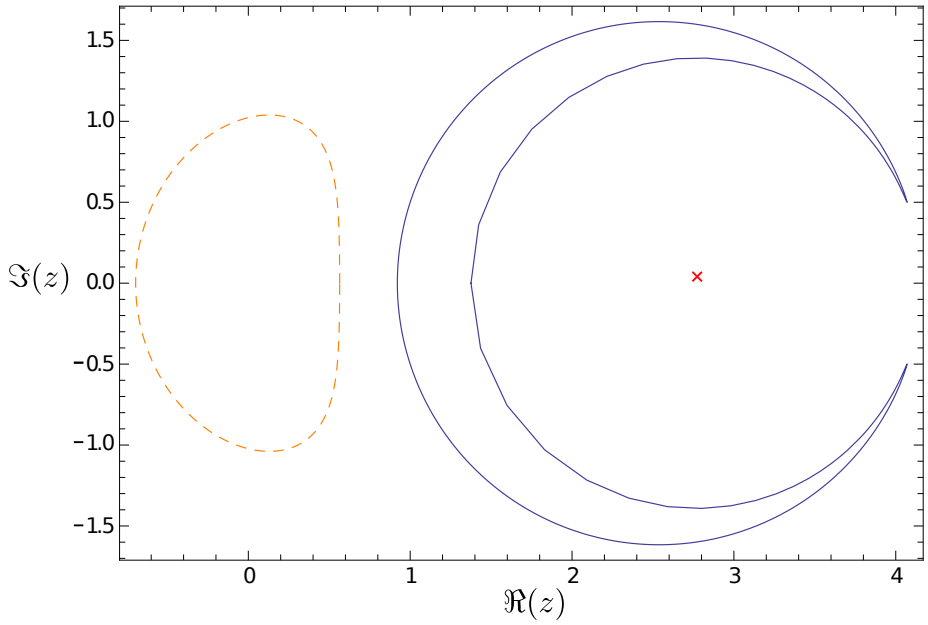

Figure G.3: Snapshots of the bubble interface at $t = 0$ (dashed) and at $t = 0.935$ (solid) where the initial interface is given by (G.18) with $c(0) = 0$, $a(0) = 0.85$, $b(0) = -0.2$, $e(0) = 0.3$. The Schwarz function singularity is marked by the cross. At $t = 0.935$ (solid line), the formation of the cusps on the interface are visible, beyond which the solution breaks down.

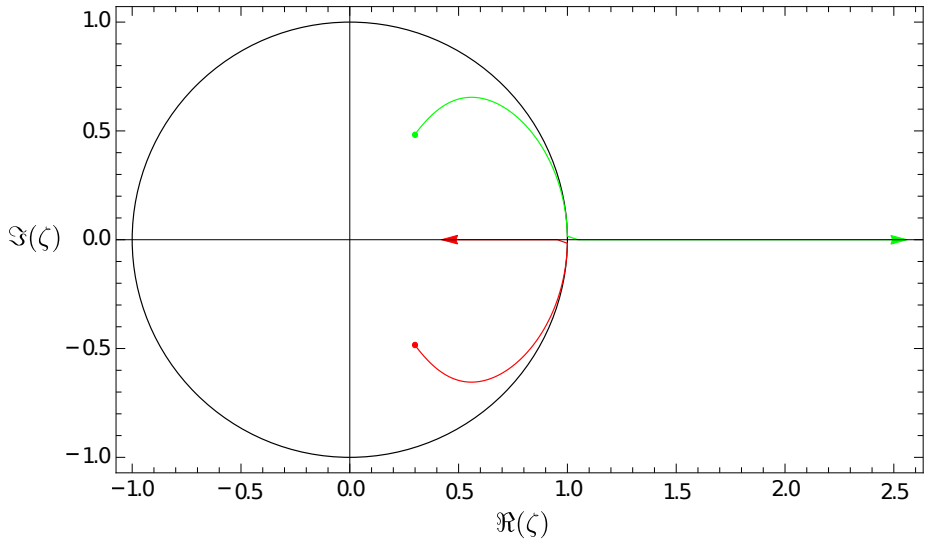

Figure G.4: Motion of the critical points given by (G.21), $0 \leq t \leq 1$, for an initial bubble with interface given by (G.18) and $c(0) = 0$, $a(0) = 0.85$, $b(0) = -0.2$, $e(0) = 0.3$, where the initial location of the critical points are marked by a dot.

Bibliography

[1] J. M. Aitchison and S. D. Howison. Computation of Hele-Shaw flows with free boundaries. *J. Comput. Phys.*, 60(9):376–390, 1985.

[2] M. M. Alimov. Construction of exact solutions to the Muskat problem. *Lobachevskii J. Math.*, 32(4):404–413, 2011.

[3] R. F. Almgren. Comment on "Selection of the Saffman-Taylor finger width in the absence of surface tension: An exact result". *Phys. Rev. Lett.*, 81(26):5951, 1998.

[4] E. Alvarez-Lacalle, J. Casademunt and J. Eggers. Pinch-off singularities in rotating Hele-Shaw flows at high viscosity contrast. *Phys. Rev. E*, 80(056306):1–10, 2009.

[5] M. B. Amar, V. Hakim, M. Mashaal and Y. Couder. Self-dilating viscous fingers in wedge-shaped Hele–Shaw cells. *Phys. Fluids A*, 3(7):1687–1690, 1991.

[6] R. S. Anderssen and P. Bloomfield. Numerical differentiation procedures for non-exact data. *Numer. Math.*, 22(3):157–182, 1974.

[7] K. E. Atkinson. *The Numerical Solution of Integral Equations of the Second Kind*. Cambridge University Press, Cambridge, 1st edition, 1997.

[8] G. R. Baker. A test of the method of Fink & Soh for following vortex-sheet motion. *J. Fluid. Mech.*, 100(1):209–220, 1980.

[9] G. K. Batchelor. *An Introduction To Fluid Dynamics*. Cambridge Mathematical Library. Cambridge University Press, Cambridge, 2000.

[10] T. Beatus, R. H. Bar-Ziv and T. Tlusty. The physics of 2D microfluidic droplet ensembles. *Physics Reports*, 516(3):103–145, 2012.

[11] G. Birkhoff. Helmholtz and Taylor instability. *Proc. Symp. Appl. Maths. Soc.*, 13:55–76, 1962.

[12] J. Callum. Numerical differentiation and regularization. *SIAM J. Numer. Anal.*, 8(2):254–265, 1971.

[13] J. Casademunt and F. X. Magdaleno. Comment on "Selection of the Saffman-Taylor finger width in the absence of surface tension: An exact result". *Phys. Rev. Lett.*, 81(26):5950, 1998.

[14] H. D. Ceniceros, T. Y. Hou and H. Si. Numerical study of Hele-Shaw flow with suction. *Phys. Fluids*, 11(9):2471–2486, 1999.

[15] S. J. Chapman and J. R. King. The selection of Saffman-Taylor fingers by kinetic undercooling. *J. Eng. Math.*, 46(1):1–32, 2003.

[16] M. L. Cordero, D. R. Burnham, C. N. Baroud and D. McGloin. Thermocapillary manipulation of droplets using holographic beam shaping: Microfluidic pin ball. *Appl. Phys. Lett.*, 93(034107):1–3, 2008.

[17] Y. Couder, O. Cardoso, D. Dupuy, P. Tavernier and W. Thom. Dendritic growth in the Saffman-Taylor experiments. *Europhys. Lett.*, 2(6):437–443, 1986.

[18] D. Crowdy. Circulation-induced shape deformations of drops and bubbles: Exact two-dimensional models. *Phys. Fluids*, 11(10):2836–2845, 1999.

[19] D. Crowdy. On a class of geometry driven free boundary problems. *SIAM J. Appl. Math.*, 62(3):945–964, 2002.

[20] D. Crowdy. Exact solutions to the unsteady two-phase Hele-Shaw problem. *Q. J. Mech. Appl. Math.*, 59(4):475–485, 2006.

[21] D. Crowdy. Multiple steady bubbles in a Hele-Shaw cell. *Proc. R. Soc. Lond. A*, 465(2102):421–435, 2009.

[22] D. Crowdy and J. Marshall. Computing the Schottky-Klein Prime Function on the Schottky Double of planar domains. *Comput. Meth. Funct. Th.*, 7(1):293–308, 2007.

[23] D. Crowdy and A. Surana. Contour dynamics in complex domains. *J. Fluid Mech. Mech.*, 593:235–254, 2007.

[24] L. J. Cummings, Y. E. Hohlov, S. D. Howison and K. Kornev. Two-dimensional solidification and melting in potential flows. *J. Fluid Mech.*, 378:1–18, 1999.

[25] L. J. Cummings, S. D. Howison and J. R. King. Two-dimensional Stokes and Hele-Shaw flows with free surfaces. *Euro. J. Appl. Math.*, 10(6):635–680, 1999.

[26] M. Dallaston. *Mathematical Models of Bubble Evolution in a Hele–Shaw Cell.* PhD thesis, Queensland University of Technology, Brisbane, 2013.

[27] M. Dallaston and S. McCue. Numerical solution to the Saffman-Taylor finger problem with kinetic undercooling regularisation. *ANZIAM J.*, 52:C124–C138, 2011.

[28] M. Dallaston and S. McCue. Bubble extinction in Hele-Shaw flow with surface tension and kinetic undercooling regularization. *Nonlinearity*, 26(6):1639–1665, 2014.

[29] H. Darcy. *Les Fontaines Publiques de la Ville de Dijon.* Victor Dalmont, Paris, 1856.

[30] P. J. Davis. *The Schwarz function and its applications.* Number 17 in The Carus Mathematical Monographs. The Mathematical Association of America, Rhode Island, 1974.

[31] P. J. Davis and P. Rabinowitz. *Methods of Numerical Integration.* Academic Press, Inc., Orlando, 2nd edition, 1984.

[32] R. de Ruiter, A. M. Pit, V. M. de Oliveira, M. H. G. Duits, D. van den Ende and F. Mugele. Electrostatic potential wells for on-demand drop manipulation in microchannels. *Lab Chip.*, 14(5):883–891, 2014.

[33] G. S. Deem and N. J. Zabusky. Vortex waves: stationary "V States," interactions, recurrence and breaking. *Phys. Rev. Lett.*, 40(13):859–862, 1978.

[34] A.J. Degregoria and L.W. Schwartz. A boundary-integral method for 2-phase displacement in Hele–Shaw cells. *J. Fluid Mech.*, 164:383–400, 1986.

[35] D. G. Dritschel. The nonlinear evolution of rotating configurations of uniform vorticity. *J. Fluid Mech.*, 172:157–182, 1986.

[36] N. Dubash and A. J. Mestel. Behaviour of a conducting drop in a highly viscous fluid subject to an electric field. *J. Fluid Mech.*, 581:469–493, 2007.

[37] D. Elliott. A comprehensive approach to the approximate solution of singular integral equations over the arc (-1,1). *J. Integral Equations Appl.*, 2(1):59–94, 1989.

[38] V. Entov and P. Etingof. On the breakup of air bubbles in a Hele-Shaw cell. *Euro. J. Appl. Math.*, 22(2):125–149, 2011.

[39] V. M. Entov and P. Etingof. On a generalized two-fluid Hele-Shaw flow. *Euro. J. Appl. Math.*, 18(1):103–128, 2007.

[40] V. M. Entov, P. Etingof and D. Ya. Kleinbock. Hele-Shaw flows with a free boundary produced by multipoles. *Euro. J. Appl. Math.*, 4(2):97–120, 1993.

[41] V. M. Entov, P. Etingof and D. Ya. Kleinbock. On nonlinear interface dynamics in Hele-Shaw flows. *Euro. J. Appl. Math.*, 6(5):399–420, 1995.

[42] L. Euler. Principes généraux du mouvement des fluides. *Mem. de l'acad. d. sc. de Berlin*, 11:274–315, 1757.

[43] R. Folch, J. Casademunt, A. Henández-Machado and L. Ramírez-Piscina.

Phase-field model for Hele-Shaw flows with arbitrary viscosity contrast. II. Numerical study. *Phys. Rev. E*, 60(2):1734–1740, 1999.

[44] L. A. Galin. Unsteady filtration with a free surface. *Dokl. Akad. Nauk S.S.S.R*, 47:246–249, 1945.

[45] C. C. Green. *Mathematical techniques for free boundary problems with multiple boundaries*. PhD thesis, Imperial College London, London, 2013.

[46] C. C. Green and G. L. Vasconcelos. Multiple steadily translating bubbles in a Hele-Shaw channel. *Proc. R. Soc. Lond. A*, 470(2163):1–14, 2014.

[47] J. M. Guevara-Jordan and J. Glimm. A mixed finite element method for Hele-Shaw cell equations. *Computat. Geosci.*, 1(1):35–58, 1997.

[48] B. Gustafsson and A. Vasiliev. *Conformal and Potential Analysis in Hele-Shaw Cells*. Advances in Mathematical Fluid Mechanics. Birkhäuser, Basel, 2006.

[49] H. S. Hele-Shaw. Experiments on the nature of the surface resistance in pipes and ships. In *Transactions of the Royal Institution of Naval Architecture*, volume 39, pages 145–153, London, 1898. Henry Sotheran & Co.

[50] H. S. Hele-Shaw. The flow of water. *Nature*, 58(1489):34–36, 1898.

[51] H. S. Hele-Shaw. Flow of water. *Nature*, 59(1523):222–223, 1899.

[52] H. von Helmholtz. On discontinuous movements of fluids. *Phil. Mag. S. 4*, 36(244):337–346, 1868.

[53] G. M. Homsy. Viscous fingering in porous media. *Ann. Rev. Fluid Mech.*, 19(1):271–311, 1987.

[54] T. Y. Hou, Z. Li, S. Osher and H. Zhao. A hybrid method for moving interface problems with application to the Hele–Shaw flow. *J. Comput. Phys.*, 134(2):236–252, 1997.

[55] T. Y. Hou, J. S. Lowengrub and M. J. Shelley. Boundary Integral Meth-

ods for Multicomponent Fluids and Multiphase Materials. *J. Comput. Phys.*, 169(1):302–362, 2001.

[56] S. D. Howison. Cusp development in Hele-Shaw flow with a free surface. *SIAM J. Appl. Math.*, 46(1):20–26, 1986.

[57] S. D. Howison. Bubble growth in porous media and Hele–Shaw cells. *Proc. R. Soc. Eding. A-Ma.*, 102(1–2):141–148, 1986.

[58] S. D. Howison. Fingering in Hele-Shaw cells. *J. Fluid Mech.*, 167:439–453, 1986.

[59] S. D. Howison. Complex variable methods in Hele-Shaw moving boundary problems. *Euro. J. Appl. Math.*, 3(3):209–224, 1992.

[60] S. D. Howison. A note on the two-phase Hele-Shaw problem. *J. Fluid Mech.*, 409:243–249, 2000.

[61] S. D. Howison. http://people.maths.ox.ac.uk/howison/Hele-Shaw, 2014.

[62] S. D. Howison, J. R. Ockendon and A. A. Lacey. Singularity development in moving-boundary problems. *Q. J. Mech. Appl. Math.*, 38(3):343–360, 1985.

[63] C. Huntingford. An Exact Solution to the One-Phase zero-surface-tension Hele-Shaw free-boundary problem. *Computers Math. Applic.*, 29(10):45–50, 1995.

[64] V. I. Ivanov and M. K. Trubetskow. *Handbook of Conformal Mapping with Computer-Aided Visualization*. CRC Press Inc., Florida, 1st edition, 1995.

[65] P. Jacquard and P. Séguier. Mouvement de deux fluides en contact dans un mileu poreux. *Journal de Mécanique*, 1(4):367–394, 1962.

[66] T. Kambe. *Elementary fluid mechanics*. World Scientific Publishing Co. Pte. Ltd., Singapore, 2007.

[67] E. D. Kelly and E. J. Hinch. Numerical simulations of sink flow in the Hele-Shaw cell with small surface tension. *Euro. J. Appl. Math.*, 8(6):533–550, 1997.

[68] E. D. Kelly and E. J. Hinch. Numerical solution of Hele-Shaw flows driven by a quadrupole. *Euro. J. Appl. Math.*, 8(6):551–566, 1997.

[69] D. A. Kessler, J. Koplik and H. Levine. Pattern selection in fingered growth phenomena. *Adv. Phys.*, 37(3):255–339, 1988.

[70] D. A. Kessler and H. Levine. Microscopic selection of fluid fingering patterns. *Phys. Rev. Lett.*, 86(20):4532–4535, 2001.

[71] A. H. Khalid, N. R. McDonald and J.-M. Vanden-Broeck. Hele-Shaw flow driven by an electric field. *Euro. J. Appl. Math.*, 25(4):425–447, 2014.

[72] A. H. Khalid, N. R. McDonald and J.-M. Vanden-Broeck. On the motion of unsteady translating bubbles in an unbounded Hele-Shaw cell. *Phys. Fluids*, 27(1):1–21, 2015.

[73] B. J. Kirby. *Micro- and Nanoscale Fluid Mechanics, Transport in Microfluidic Devices*. Cambridge University Press, Cambridge, 2010.

[74] G. Kirchhoff. Zur Theorie freier Flüssigkeitsstrahlen. *J. Reine Angew. Math.*, 70(4):289–298, 1869.

[75] P. Ya. Kochina and N. N. Kochina. On an oil-field contour. *J. Appl. Math. Mechs.*, 60(6):953–957, 1996.

[76] R. Krasny. A study of singularity formation in a vortex sheet by the point-vortex approximation. *J. Fluid Mech.*, 167:65–93, 1986.

[77] A. A. Lacey. Moving boundary problems in the flow of liquid through porous media. *J. Austral. Math. Soc. B*, 24(2):171–193, 1982.

[78] L. D. Landau and E. M. Lifshitz. *Electrodynamics of continuous media*, volume 8 of *Course of Theoretical Physics*. Pergamon Press, Oxford, 1st English edition, 1960.

[79] L. D. Landau and E. M. Lifshitz. *The Classical Theory of Fields*, volume 2 of

Course of Theoretical Physics. Pergamon Press, Oxford, 3rd revised English edition, 1971.

[80] S. Y. Lee, E. Bettelheim and P. Wiegmann. Bubble break-off in Hele-Shaw flows: singularities and integrable structures. *Physica D*, 219(1):23–34, 2006.

[81] L. S. Leibenzon. Ob odnom sluchae izoterminicheskogo techeniya vyazkogo gaza v grunte i o debete gazovykh skvazhin. *Azerb. neft. khoz-vo*, 4:109–113, 1923.

[82] L. S. Leibenzon. The motion of a gas in a porous medium, complete works. *Acad. Sci. URSS, Moscow*, 2, 1953.

[83] D. Li, editor. *Electrokinetics in microfluidics*, volume 2 of *Interface Science and Technology*. Elsevier Ltd., Amsterdam, 2004.

[84] P. Linz. *Analytical and Numerical Methods for Volterra Equations*. SIAM Studies in Applied Mathematics. Society for Industrial and Applied Mathematics, Philadelphia PA, 1985.

[85] M. S. Longuet-Higgins and E. D. Cokelet. The Deformation of Steep Surface Waves on Water. I. A Numerical Method of Computation. *Proc. R. Soc. Lond. A.*, 350(9):1–26, 1976.

[86] F. Malloggi, S. A. Vanapalli, H. Gu, D. van den Ende and F. Mugele. Electrowetting-controlled droplet generation in a microfluidic flow-focusing device. *J. Phys.: Condens. Matter*, 19(46):1–7, 2007.

[87] T. Maxworthy. Bubble formation, motion and interaction in a Hele-Shaw cell. *J. Fluid. Mech.*, 173:95–114, 1986.

[88] N. R. McDonald. Computation of Hele-Shaw free boundary priblems near obstacles. *Theor. Comput. Fluid Dyn.*, 24(6):537–550, 2010.

[89] N. R. McDonald. Generalised Hele-Shaw flow: A Schwarz function approach. *Euro. J. Appl. Math.*, 22(6):517–532, 2011.

[90] J. W. McLean and P. G. Saffman. The effect of surface tension on the shape of fingers in a Hele–Shaw cell. *J. Fluid Mech.*, 102:455–469, 1981.

[91] R. F. Millar. An inverse moving boundary problem for Laplace's equation. In G. F. Roach, editor, *Proc. Workshop on Inverse Problems and Imaging*, pages 103–126, London, 1989. Pitman-Longman.

[92] R. F. Millar. Bubble motion along a channel in a Hele–Shaw cell: a Schwarz function approach. *Complex Variables, Theory and Application: An International Journal*, 18(1–2):13–25, 1992.

[93] M. B. Mineev. A finite polynomial solution of the two-dimensional interface dynamics. *Physica D*, 43(2–3):288–292, 1990.

[94] M. Mineev-Weinstein. Mineev-Weinstein replies. *Phys. Rev. Lett.*, 81(20):4529, 1998.

[95] M. Mineev-Weinstein. Mineev-Weinstein replies. *Phys. Rev. Lett.*, 81(26):5952, 1998.

[96] Mark Mineev-Weinstein. Selection of the Saffman-Taylor finger width in the absence of surface tension: An exact result. *Phys. Rev. Lett.*, 80(10):2113–2116, 1998.

[97] M. Mineev-Weinstein, G. D. Doolen, J. E. Pearson and S. P. Dawson. Formation and pinch-off of viscous droplets in the absence of surface tension: An exact result. In *eprint arXiv:patt-sol/9912006*, pages 1–4, 1999.

[98] M. Mineev-Weinstein, M. Putinar and R. Teodorescu. Random matrices in 2D, Laplacian growth and operator theory. *J. Phys. A: Math. Theor.*, 41(26):1–74, 2008.

[99] M. Mineev-Weinstein, P. B Wiegmann and A. Zabrodin. Integrable structure of interface dynamics. *Phys. Rev. Lett.*, 84(22):5106–5109, 2000.

[100] M. Mineev-Weinstein and A. Zabrodin. Whittam-Toda Hierarchy in the Laplacian Growth Problem. *J. Nonlinear Math. Phys.*, 8(1):212–218, 2001.

[101] J. R. Moore, A. Boleve, J. W. Sanders and S. D. Glaser. Self-potential investigation of moraine dam seepage. *J. Appl. Geophys.*, 74(4):277–286, 2011.

[102] F. Mugele and J. C. Baret. Electrowetting: from basics to applications. *J. Phys.: Condens. Matter*, 17(28):705–774, 2005.

[103] M. Muskat. Two fluid systems in porous media. The encroachment of water into an oil sand. *J. Appl. Phys.*, 5(9):250–264, 1934.

[104] M. Muskat. *The flow of homogeneous fluids through porous media.* McGraw-Hill, New York, 1937.

[105] C.-L. M. H. Navier. Mémoire sur les lois du mouvement des fluids. *Mem. Acad. Sci. Inst. Fr.*, 6:389–440, 1823.

[106] Z. Nehari. *Conformal Mapping.* McGraw-Hill, New York, 1952.

[107] J. R. Ockendon and S. D. Howison. Kochina and Hele-Shaw in modern mathematics, natural science and industry. *J. Appl. Math. Mech.*, 66(3):505–512, 2002.

[108] M. F. Pettigrew and H. Rasmussen. Numerical solutions for unstable Hele-Saw flows. *J. Comput. Appl. Math.*, 47(2):253–266, 1993.

[109] D. L. Phillips. A technique for the numerical solution of certain integral equations of the first kind. *J. ACM.*, 9(1):84–97, 1962.

[110] P. Ya. Polubarinova-Kochina. Concerning unsteady motions in the theory of filtration. *Prikl. Mathem. Mech.*, 9(1):79–90, 1945.

[111] P. Ya. Polubarinova-Kochina. On a problem of the motion of the contour of a petroleum shell. *Dokl. Akad. Nauk S.S.S.R*, 47:254–257, 1945.

[112] P. Ya. Polubarinova-Kochina. On the motion of the oil contour. *Dokl. Akad. Nauk S.S.S.R*, 47:254–257, 1945.

[113] M. Prakash and N. Gershenfeld. Microfluidic bubble logic. *Science*, 315(5813):832–835, 2007.

[114] J. E. Pringle and A. R. King. *Astrophysical Flows*. Cambridge University Press, Cambridge, 2007.

[115] A. Ramos. Electrohydrodynamic pumping in microsystems. In A. Ramos, editor, *Electrokinetics and Electrohydrodynamics in Microsystems*, volume 530 of *CISM Courses and Lectures*, pages 127–175. Springer, Vienna, 2011.

[116] S. Richardson. Hele-Shaw flows with a free boundary produced by the injection of fluid into a narrow channel. *J. Fluid Mech.*, 56:609–618, 1972.

[117] S. Richardson. Hele-Shaw flows with time-dependent free boundaries in which the fluid occupies a multiply-connected region. *Euro. J. Appl. Math.*, 5(2):97–122, 1994.

[118] S. Richardson. Hele-Shaw flows with free boundaries in a corner or around a wedge Part I: Liquid at the vertex. *Euro. J. Appl. Math.*, 12(6):665–676, 2001a.

[119] S. Richardson. Hele-Shaw flows with free boundaries in a corner or around a wedge Part II: Air at the vertex. *Euro. J. Appl. Math.*, 12(6):677–688, 2001b.

[120] V. F. Riegels. Zur kritik des Hele-Shaw-Versuchs. *ZAMM*, 18(2):95–106, 1938.

[121] N. Rott. Diffraction of a weak shock with vortex generation. *J. Fluid Mech.*, 1:111–128, 1956.

[122] P. G. Saffman. Exact solutions for the growth of fingers from a flat interface between two fluids in a porous medium or Hele-Shaw cell. *Q. Jl Mech. Appl. Math*, 12(2):146–150, 1959.

[123] P. G. Saffman and G. Taylor. The penetration of a fluid into a porous medium or Hele-Shaw cell containing a more viscous liquid. *Proc. R. Soc. Lond. A*, 245(1242):312–333, 1958.

[124] A. Sarkissian and H. Levine. Comment on "Selection of the Saffman-Taylor finger width in the absence of surface tension: An exact result". *Phys. Rev. Lett.*, 81(20):4528, 1998.

[125] L. W. Schwartz and A. J. Degregoria. Two-phase flow in Hele-Shaw cells: numerical studies of sweep efficieny in a five-spot pattern. *J. Austral. Math. Soc. Ser. B*, 29(4):275–400, 1988.

[126] M. J. Shelley, F. R. Tian and K. Wlodarski. Hele-Shaw flow and pattern formation in a time-dependent gap. *Nonlinearity*, 10(6):1471–1495, 1997.

[127] B. Shen, M. Leman, M. Ressat and P. Tabeling. Dynamics of a small number of droplets in microfluidic Hele-Shaw cells. *Exp. Fluids*, 55(1728):1–10, 2014.

[128] M. Siegel and S. Tanveer. Singular perturbations of smoothly evolving Hele-Shaw solutions. *Phys. Rev. Lett.*, 76(3):419–422, 1996.

[129] T. M. Squires and M. Z. Bazant. Induced-charge electro-osmosis. *J. Fluid Mech.*, 509:217–252, 2004.

[130] G. G. Stokes. On the theories of the internal friction of fluids in motion. *Trans. Cambridge Philos. Soc.*, 8:287–305, 1845.

[131] J. Strain. A boundary integral approach to unstable solidification. *J. Comput. Phys.*, 85(2):342–389, 1989.

[132] S. Tanveer. The effect of surface tension on the shape of a Hele–Shaw cell bubble. *Phys. Fluids*, 29(11):3537–3548, 1986.

[133] S. Tanveer. Analytic theory for the selection of a symmetric Saffman-Taylor finger in a Hele-Shaw cell. *Phys. Fluids*, 30(6):1589–1605, 1987.

[134] S. Tanveer. New solutions for steady bubbles in a Hele-Shaw cell. *Phys. Fluids*, 30(3):651–658, 1987.

[135] S. Tanveer. Evolution of Hele-Shaw interface for small surface tension. *Phil. Trans. R. Soc. Lond. A*, 343(1668):155–204, 1993.

[136] S. Tanveer. Surprises in viscous fingering. *J. Fluid Mech.*, 409:273–308, 2000.

[137] A. Tatulchenkov and A. Cebers. Complex bubble dynamics in a vertical Hele-Shaw cell. *Phys. Fluids*, 17(10):1–9, 2005.

[138] G. Taylor and P. G. Saffman. A note on the motion of bubbles in a Hele-Shaw cell and porous medium. *Quart. J. Mech. Appl. Math.*, 12(3):266–279, 1959.

[139] F. R. Tian. On the Breakdown of Hele-Shaw Solutions with Nonzero Surface Tension. *J. Nonlinear Sci.*, 5:479–484, 1995.

[140] F. R. Tian and G. L. Vasconcelos. Rotation invariance for steady Hele-Shaw flows. *Phys. Fluids A*, 5(8):1863–1865, 1993.

[141] G. A. Tokaty. *A History and Philosophy of Fluid Mechanics*. Dover Publications Inc., New York, 1994.

[142] U. Tristan. MATLAB file available for download from www.mathworks.com/matlabcentral/fileexchange/35488-connect-randomly-ordered-2d-points-into-a-minimal-nearest-neighbor-closed-contour, 2012.

[143] G. Tryggvason and H. Aref. Numerical experiments on Hele-Shaw flow with a sharp interface. *J. Fluid Mech.*, 136:1–30, 1983.

[144] S. Twomey. On the numerical solution of Fredholm integral equations of the first kind by the inversion of the linear system produced by quadrature. *J. ACM.*, 10(1):97–101, 1963.

[145] J.-M. Vanden-Broeck. Fingers in a Hele-Shaw cell with surface tension. *Phys. Fluids*, 26(8):2033–2034, 1983.

[146] J.-M. Vanden-Broeck. Steep solitary waves in water of finite depth with constant vorticity. *J. Fluid. Mech.*, 274:339–348, 1994.

[147] J.-M. Vanden-Broeck. *Gravity-capillary free-surface flows*. Cambridge Monographs on Mechanics. Cambridge University Press, Cambridge, 2010.

[148] G. L. Vasconcelos. Exact solutions for steady bubbles in a Hele-Shaw cell with rectangular geometry. *J. Fluid Mech.*, 444:175–198, 2001.

[149] G. L. Vasconcelos and Mark Mineev-Weinstein. Selection of the Taylor-Saffman bubble does not require surface tension. *Phys. Rev. E*, 89(061003):1–5, 2014.

[150] Alexander Vasil'ev. From the Hele-Shaw experiment to integrable systems: A historical overview. *Complex Anal. Oper. Theory*, 3(2):551–585, 2009.

[151] N. Whitaker. Numerical solution of the Hele-Shaw equations. *J. Comput. Phys.*, 90(1):176–199, 1990.

[152] P. K. Wong, T. H. Wang, J. H. Deval and C. M. Ho. Electrokinetics in micro devices for biotechnology applications. *IEEE/ASME Trans. Mechanotronics*, 9(2):366–376, 2004.